DESIGN AND PERFORMANCE ANALYSIS OF INDEX-MODULATED AFFINE FREQUENCY DIVISION MULTIPLEXING WAVEFORMS USING VARIATIONAL BAYESIAN AND MESSAGE PASSING FRAMEWORKS

ANOOP A
2022PHD22006



Indian Institute of Information Technology Kottayam

DESIGN AND PERFORMANCE ANALYSIS OF INDEX-MODULATED AFFINE FREQUENCY DIVISION MULTIPLEXING WAVEFORMS USING VARIATIONAL BAYESIAN AND MESSAGE PASSING FRAMEWORKS

Thesis

Submitted in Partial Fulfillment of the

Requirements for the Degree of

Doctor of Philosophy

by

ANOOP A

2022PHD22006



DEPARTMENT OF ELECTRONICS AND COMMUNICATION ENGINEERING

INDIAN INSTITUTE OF INFORMATION TECHNOLOGY KOTTAYAM

PALA - 686635, KERALA, INDIA

September 2026

भारतीय सूचना प्रौद्योगिकी संस्थान कोट्टायम
INDIAN INSTITUTE OF INFORMATION TECHNOLOGY KOTTAYAM
(An Institution under Ministry of Education, Govt. of India governed by an Act of Parliament)
Tel: 04822-202 100 (office), 202135 (Academics), 202110 (Security), 202102 (Accounts)
Email: registrar@iitkotayam.ac.in, Website: www.iitkottayam.ac.in

CERTIFICATE

Date: / / 2026

This is to certify that the thesis entitled **Design and Performance Analysis of Index-Modulated Affine Frequency Division Multiplexing Waveforms Using Variational Bayesian and Message Passing Frameworks** submitted by **Anoop A (2022PHD22006)** to the **Indian Institute of Information Technology Kottayam** is a record of bonafide research work carried out by him under our supervision and is worthy of consideration for the award of the degree of **Doctor of Philosophy** of the Institute. The results contained in this Thesis have not been submitted in part or full to any other university or institute for any Degree or Diploma.

Guide	**Co-Guide**
Dr. Kala S	**Dr. J. V. Bibal Benifa**
Assistant Professor	*Assistant Professor*
Department of ECE	Department of CSE
IIIT Kottayam	IIIT Kottayam

DECLARATION

I declare that

(a) the work contained in the thesis is original and has been done by me under the guidance of my supervisors;

(b) the work has not been submitted to any other institute for any degree or diploma;

(c) I have followed the guidelines provided by the Institute in preparing the thesis;

(d) I have conformed to ethical norms and guidelines while writing the thesis;

(e) whenever I have used materials (data, models, figures, and text) from other sources, I have given due credit to them by citing them in the text of the thesis, giving their details in the references, and taking permission from the copyright owners of the sources, if necessary, and;

(f) whenever I have quoted written materials from other sources, I have put them under quotation marks and given due credit to the sources by citing them and providing required details in the references.

(g) The thesis has been checked for plagiarism with the tool recommended by the institute and has been found to conform the plagiarism policy of the institute.

Place: IIIT Kottayam

Date: / / 2026

Anoop A

2022PHD22006

Department of ECE

© Copyright 2026 by Indian Institute of Information Technology Kottayam
All rights reserved

Acknowledgments

I am deeply indebted to numerous individuals whose support and encouragement have been instrumental throughout my doctoral journey at IIIT Kottayam. The successful completion of this work would not have been possible without the assistance and cooperation of many, and I would like to express my sincere gratitude to all those who contributed to my progress and growth over the course of this research.

First and foremost among them is my supervisor, Dr. Kala S, Assistant Professor in the Department of ECE whose invaluable guidance, encouragement, and unwavering support have been instrumental throughout the course of this research. I am profoundly grateful for the opportunity to pursue my research under her guidance in the Department of Electronics and Communication Engineering. Her approachability and positive demeanor fostered a collaborative and intellectually stimulating research environment, making my association with the Intelligent Integrated Circuits and Systems (I^2CS) Research Lab both productive and enriching. Her research intuition and unwavering commitment to excellence greatly inspired me, and her insightful feedback and high standards for technical writing significantly shaped the quality and productivity of my PhD work.

I would also like to express my sincere gratitude to my co-guide, Dr. J. V. Bibal Benifa, Assistant Professor in the Department of CSE, whose constructive suggestions, technical expertise, and continuous support played a crucial role in strengthening my research and in bringing this thesis to completion.

I would like to sincerely thank my Doctoral Committee members, Dr. Ananth A, Assistant Professor in the Department of ECE and Dr. Dhanyamol M V, Assistant Professor in the Department of Computational Science and Humanities, for their encouragement and constructive input at various stages of my research work. Their critical evaluation during the progress seminars helped refine the direction and presentation of this research.

I would like to thank Prof. Prasad Krishna, Director (Additional Charge), IIIT Kottayam, Dr. M. Radhakrishnan, Registrar, IIIT Kottayam, Prof. Ashok S, Professor In-Charge (Academics), IIIT Kottayam, and Dr. Divya Sindhu Lekha, Associate Dean (PhD Academics) and Assistant Professor in the Department of CSE, IIIT Kottayam, for the administrative support extended throughout the course of this work. I also thank all the faculty members of the Department of

ECE for their co-operation during my PhD program.

Heartfelt thanks are due to my fellow scholars and friends from the I^{2}CS Research Lab and to my PhD batchmates from the January 2022 admission cohort, whose companionship, technical discussions, and shared sense of purpose carried me through the difficult phases of this work. Their support, technical exchanges, and friendship sustained me throughout the program, and many of the ideas in this thesis were sharpened in the conversations we shared along the way.

I am deeply grateful to my research collaborator and mentor, Dr. Christo Kurisummoottil Thomas, Assistant Professor in the Department of Electrical and Computer Engineering, Worcester Polytechnic Institute, Massachusetts, USA, for his consistent encouragement and exceptional technical mentorship throughout this research journey. The numerous discussions with him greatly contributed to shaping the message passing and variational inference framework that underpins this thesis, and his insights during the preparation of our joint research papers were invaluable. His belief in this work, often expressed at moments when I was least sure of it, has been a source of motivation that I will carry with me well beyond this thesis. I remain sincerely indebted to him for his exceptional mentorship and collaborative support. I am also thankful to Dr. Walid Saad, Professor in the Department of Electrical and Computer Engineering, Virginia Tech, Virginia, USA, for the collaborative support that enriched the dual-mode and multi-mode index modulation work presented in this thesis.

I sincerely acknowledge Oil and Natural Gas Corporation Limited (ONGC), my employer, for the institutional and administrative support extended throughout this doctoral program. I am particularly thankful to the senior officers and the management of ONGC who granted me the leave of absence required to attend the mandatory course work at IIIT Kottayam and who issued the No Objection Certificate that made the registration possible. Pursuing a PhD while working in the upstream oil and gas industry would not have been feasible without their understanding and trust, and I am genuinely grateful for the consideration shown to me at every stage.

On a personal note, I would like to express my deepest gratitude to my wife, Roshni Murali, for standing by me through every phase of this journey. The decision to pursue a PhD while continuing in service required her to accept long periods of academic absence and demanding stretches of work alongside professional responsibilities. She accepted all of it without complaint, kept our home running through every stretch I disappeared into research, and remained the steady presence that made the rest of this possible. This thesis is as much hers as it is mine. To my children, Niveditha Anoop and Adidev Anoop, who grew up alongside this thesis

and shared their father with it on many evenings and weekends, I owe a debt of love and time that I hope to repay in the years ahead.

I also extend my heartfelt gratitude to my parents for the values, the education, and the unwavering encouragement that brought me to this point, and to my extended family for their persistent support during my PhD program. Finally, I cannot forget thanking the Almighty for making me stronger and more perseverant in the difficult situations that this journey demanded.

The research concepts, methodology, derivations, analysis, and findings presented in this thesis are entirely my own original work. Generative AI tools were used only to assist with grammar checking and language refinement of text I had already written. I take full responsibility for the entire content of this thesis.

Anoop A

Dedicated to my wife Roshni Murali, whose patience and quiet strength carried this work alongside her own, to my children Niveditha and Adidev, who shared their father with this thesis on countless evenings, and to my parents, whose belief in education made this journey possible...

Abstract

The next generation of wireless systems is being shaped by the demands of high-mobility scenarios such as high-speed rail, vehicle-to-everything communication, low-Earth-orbit satellite links, and unmanned aerial vehicle networks. In these environments the wireless channel becomes doubly dispersive in both time and frequency, and the orthogonality of the subcarriers used by conventional Orthogonal Frequency Division Multiplexing (OFDM) breaks down, leading to severe inter-carrier interference and a sharp degradation in error performance. Orthogonal Time Frequency Space (OTFS) modulation partially addresses this problem by operating in the delay-Doppler domain, but its two-dimensional frame structure introduces high pilot overhead and substantial detection complexity. Affine Frequency Division Multiplexing (AFDM), a chirp-based waveform built on the Discrete Affine Fourier Transform (DAFT), has emerged as a strong candidate for high-mobility transmission, achieving full delay-Doppler diversity through a one-dimensional transform with substantially lower pilot overhead and detection complexity than OTFS. This research investigates the design and performance analysis of index-modulated AFDM waveforms together with the Variational Bayesian and message passing detection frameworks needed to demodulate them under doubly dispersive channels. The early phase of the work develops two index modulation schemes on the OTFS waveform that establish the design template the AFDM chapters build upon, namely an enhanced spatial modulation scheme and a generalized dual-mode index modulation scheme. ESM-OTFS is demodulated by a Variational Bayesian Inference detector that jointly recovers the active indices and the modulation symbols through closed-form Gaussian and Gamma updates, while OTFS-GDM-IM is demodulated by ML and LLR detectors.

Three Bayesian and message passing detectors are then developed for the conventional AFDM waveform. A Vector Approximate Message Passing detector with preconditioned conjugate gradient linear estimation reduces the equalization cost from cubic to quadratic in the frame length, a multi-path parallel interference cancellation detector exploits the per-path sparsity of the DAFT-domain effective channel matrix at near-linear complexity, and a Variational Bayesian detector for AFDM receivers with low-resolution analog-to-digital converters uses a truncated Gaussian likelihood to eliminate the bit error rate saturation floor under coarse quantization. Building on this detection foundation, three index modulation

schemes are then developed on AFDM together with a sparse Bayesian detector tuned to the structured sparsity of the AFDM-IM transmit vector. AFDM with generalized index modulation allows the number of active subcarriers per subblock to vary across a permitted set, AFDM with quadrature index modulation extends subcarrier index modulation to operate independently on the in-phase and quadrature components and is supported by a pairwise error probability analysis, and a Variational Bayesian Sparse Bayesian Learning detector exploits the structured sparsity of the AFDM-IM transmit vector through a hierarchical Gaussian-Gamma prior with closed-form iterative updates that avoid matrix inversion and deliver substantial bit error rate gains over MMSE detection in high-Doppler channels.

The thesis then develops dual-mode and multi-mode index modulation on AFDM. AFDM-DM-IM activates every subcarrier of a subblock through two disjoint constellation alphabets and is detected by three baseline schemes (ML, MMSE-ML, MMSE-LLR) and two proposed message passing detectors that jointly infer the symbols and the activation patterns through an inline belief propagation module. The VAMP-DMDIM detector adapts the preconditioned conjugate gradient VAMP framework to the dual-mode prior, while the GAMP-DMDIM detector replaces the conjugate gradient step with direct output and input message updates augmented by adaptive damping, variance flooring, an Onsager bypass at high SNR, and a divergence-detection reset, consistently outperforming MMSE-LLR and VAMP-DMDIM in bit error rate. AFDM-MM-IM further generalizes the construction by modulating every subcarrier with a symbol drawn from one of several distinct constellations, with the full permutation of modes carrying factorial-order index information, demodulated by an LLR-based greedy detector, a Viterbi-based trellis detector, and a sphere decoding based near-ML detector. A pairwise error probability analysis of the average bit error rate is derived for both schemes using the moment generating function of the codeword difference correlation matrix. Simulations over the doubly dispersive channel confirm that the proposed schemes significantly outperform classical AFDM, AFDM-IM, OFDM-MM, and OTFS-MM in bit error rate at comparable spectral efficiencies, establishing a coherent family of index-modulated AFDM schemes for next-generation high-mobility wireless communication.

Keywords: Affine frequency division multiplexing, doubly dispersive channels, high-mobility wireless communication, index modulation, dual-mode index modulation, multi-mode index modulation, variational Bayesian inference, message passing detection, pairwise error probability.

Contents

Abstract **xvii**

List of Figures **xxv**

List of Tables **xxix**

Nomenclature **xxxi**

Acronyms **xxxvi**

1 Introduction **1**

1.1 The Mobility Problem in Wireless Communications 2
1.2 Towards Delay-Doppler Waveforms 4
1.3 Index Modulation in Multicarrier Systems 5
1.4 Detection of Index-Modulated Waveforms 7
1.5 Low-Resolution Analog-to-Digital Conversion 8
1.6 Contribution of Thesis 9
1.7 Organization of Thesis 12

2 Background and Literature Review **14**

2.1 From OFDM to Delay-Doppler Waveforms 14
2.1.1 OFDM and its Limitations 14
2.1.2 Orthogonal Time Frequency Space Modulation 15
2.1.3 Affine Frequency Division Multiplexing 17
2.2 Index Modulation Techniques 18
2.2.1 The Index Modulation Concept 18
2.2.2 OFDM with Index Modulation and its Variants 19
2.2.3 OTFS with Index Modulation 20
2.2.4 Current State of AFDM with Index Modulation 21
2.3 Detection Algorithms 21
2.3.1 Classical and Linear Detectors 22

2.3.2 Message Passing and Approximate Message Passing 22
2.3.3 Variational Bayesian Methods 24
2.4 Low-Resolution ADC Receivers 25
2.5 Background on the DAFT and AFDM System Model 26
2.6 Gaps Addressed in This Thesis 27

3 OTFS Based Index Modulation 29
3.1 OTFS System Model 30
3.1.1 OTFS Modulation and Demodulation 30
3.1.2 Delay-Doppler Channel and Input-Output Relation 31
3.1.3 MIMO-OTFS Signal Representation 33
3.2 Enhanced Spatial Modulation Based OTFS 34
3.2.1 Enhanced Spatial Modulation 34
3.2.2 ESM-OTFS Transmitter and Frame Structure 35
3.2.3 MMSE Detector for ESM-OTFS 38
3.2.4 Variational Bayesian Inference Based Detector for ESM-OTFS 39
3.2.5 Spectral Efficiency of ESM-OTFS 42
3.2.6 Computational Complexity of ESM-OTFS 43
3.3 Generalized Dual-Mode Index Modulation Based on OTFS 44
3.3.1 OTFS Based Dual-Mode Index Modulation 44
3.3.2 OTFS-GDM-IM Transmitter and Signal Model 45
3.3.3 ML Detector for OTFS-GDM-IM 47
3.3.4 LLR Detector for OTFS-GDM-IM 48
3.3.5 Spectral Efficiency of OTFS-GDM-IM 50
3.3.6 Computational Complexity of OTFS-GDM-IM 51
3.4 Simulation Results 51
3.4.1 ESM-OTFS Performance 51
3.4.2 OTFS-GDM-IM Performance 57
3.5 Summary 59

4 AFDM with Advanced Bayesian and Message Passing Detectors 61
4.1 AFDM System Model 62
4.1.1 Discrete Affine Fourier Transform 62
4.1.2 AFDM Modulation 62
4.1.3 Doubly Dispersive Channel 63
4.1.4 DAFT-Domain Representation 64
4.1.5 Parameter Selection 65
4.1.6 Right Orthogonal Invariance of AFDM Channel 66

4.2 Standard VAMP Detector with SVD 67
4.2.1 VAMP Framework 67
4.2.2 MMSE Denoising 68
4.2.3 SVD-Based LMMSE Estimation 69
4.3 Low-Complexity VAMP Detector with Conjugate Gradient 70
4.3.1 Problem Formulation 70
4.3.2 Diagonal Preconditioning 71
4.3.3 Preconditioned Conjugate Gradient Solver 72
4.3.4 Simultaneous Trace Estimation 73
4.3.5 VAMP Parameter Updates 74
4.3.6 Denoiser Module 74
4.3.7 Convergence Properties 75
4.3.8 Complexity of VAMP-CG 75
4.4 Multi-Path Parallel Interference Cancellation Detector 77
4.4.1 Problem Formulation 77
4.4.2 Factorized Gaussian Approximation 78
4.4.3 Multi-Path Parallel Interference Cancellation 78
4.4.4 Bayesian Symbol Estimation 79
4.4.5 Reliability-Weighted Decision Statistics Combining 80
4.4.6 Computational Complexity of MP-PIC 81
4.4.7 Convergence Analysis 83
4.5 Variational Bayesian Detector for Quantized AFDM 85
4.5.1 Quantization Model 86
4.5.2 Probabilistic Model Construction 87
4.5.3 Mean-Field Variational Approximation 88
4.5.4 Gaussian Approximation of Interference 89
4.5.5 Truncated Gaussian Likelihood Evaluation 90
4.5.6 Symbol Probability Update 91
4.5.7 ELBO Monotonicity 93
4.5.8 Computational Complexity of VB-Quantized AFDM 93
4.6 Simulation Results 94
4.6.1 VAMP-CG Performance 94
4.6.2 MP-PIC Performance 98
4.6.3 VB Detector for Quantized AFDM Performance 101
4.7 Complexity Comparison 105
4.8 Summary 106

5 AFDM with Index Modulation Schemes and Sparse Bayesian Detection 108
5.1 AFDM-IM Baseline . . . 109
5.2 AFDM with Generalized Index Modulation . . . 110
5.2.1 Generalization of AFDM-IM . . . 110
5.2.2 Example Implementation . . . 112
5.2.3 AFDM-GIM Receiver and Equalization . . . 114
5.2.4 Energy Detection Based Detector . . . 114
5.2.5 LLR Based Detector . . . 115
5.2.6 Spectral Efficiency of AFDM-GIM . . . 116
5.2.7 Computational Complexity of AFDM-GIM . . . 116
5.3 AFDM with Quadrature Index Modulation . . . 117
5.3.1 AFDM-QIM Transmitter . . . 117
5.3.2 AFDM-QIM Receiver Model . . . 119
5.3.3 MMSE-ML Detector . . . 119
5.3.4 ML Detector . . . 120
5.3.5 Spectral Efficiency of AFDM-QIM . . . 120
5.3.6 Computational Complexity of AFDM-QIM . . . 121
5.4 Pairwise Error Probability Analysis for AFDM-QIM . . . 122
5.4.1 Conditional Pairwise Error Probability . . . 122
5.4.2 Unconditional Pairwise Error Probability . . . 123
5.4.3 Chernoff Bound and Average Bit Error Rate . . . 123
5.5 Variational Bayesian Sparse Bayesian Learning Detector for AFDM-IM 124
5.5.1 Sparse Signal Recovery Formulation . . . 124
5.5.2 Hierarchical Gaussian-Gamma Prior . . . 124
5.5.3 Mean-Field Variational Approximation . . . 125
5.5.4 Iterative VB Updates . . . 126
5.5.5 Energy Detection Based Demodulation . . . 127
5.5.6 Computational Complexity of VB-SBL Detector . . . 128
5.6 Simulation Results . . . 128
5.6.1 AFDM-GIM Performance . . . 128
5.6.2 AFDM-QIM Performance . . . 131
5.6.3 VB-SBL Detector Performance . . . 135
5.7 Summary . . . 137

6 AFDM with Dual-Mode Index Modulation and Message Passing Detection 139
6.1 AFDM-DM-IM System Model . . . 140

6.2 Baseline Detectors for AFDM-DM-IM . . . 142
6.2.1 ML Detector . . . 142
6.2.2 MMSE-ML Detector . . . 143
6.2.3 MMSE-LLR Detector . . . 143
6.3 VAMP-DMDIM Detector . . . 144
6.3.1 Detection Problem and Dynamic Mixed Prior . . . 144
6.3.2 MMSE Denoiser . . . 145
6.3.3 Subblock Belief Propagation . . . 145
6.3.4 CG-Based LMMSE Estimation . . . 146
6.3.5 Hard Decision . . . 146
6.4 GAMP-DMDIM Detector . . . 147
6.4.1 Output Linear Update . . . 148
6.4.2 Input Linear Update . . . 148
6.4.3 MMSE Denoiser with Dynamic Mixed Prior . . . 149
6.4.4 Subblock Belief Propagation . . . 149
6.4.5 Adaptive Damping Schedule . . . 149
6.4.6 Divergence Detection and Reset . . . 150
6.4.7 Hard Decision . . . 150
6.5 Pairwise Error Probability Analysis . . . 151
6.5.1 Conditional Pairwise Error Probability . . . 151
6.5.2 Unconditional Pairwise Error Probability . . . 152
6.5.3 Chernoff Bound and Average Bit Error Rate . . . 152
6.6 Spectral Efficiency . . . 153
6.7 Computational Complexity Summary . . . 153
6.8 Simulation Results . . . 154
6.8.1 AFDM-DM-IM Performance with Baseline Detectors . . . 154
6.8.2 Message Passing Detector Performance . . . 157
6.9 Summary . . . 161

7 AFDM with Multi-Mode Index Modulation and Permutation-Based Detection 163
7.1 AFDM-MM-IM System Model . . . 164
7.1.1 Look-Up Table Method . . . 165
7.1.2 Factorial Permutation Method . . . 165
7.1.3 Transmit Signal and Channel Model . . . 166
7.1.4 MMSE Equalization and Joint ML Decoding . . . 167
7.2 LLR-Based Greedy Detector . . . 168
7.3 Viterbi-Based Trellis Detector . . . 170

7.3.1 Trellis Construction 170
7.3.2 Cost Matrix and Dynamic Programming 170
7.4 Sphere Decoding Based Near-ML Detector 174
7.5 Pairwise Error Probability Analysis 176
7.5.1 Conditional Pairwise Error Probability 176
7.5.2 Unconditional Pairwise Error Probability 177
7.5.3 Average Bit Error Probability 178
7.6 Spectral Efficiency 178
7.7 Computational Complexity Summary 180
7.8 Simulation Results 181
7.9 Summary 189

8 Conclusion and Future Work **191**
8.1 Conclusions 191
8.2 Future Directions 193

List of Publications **195**

References **199**

Curriculum Vitae **207**

List of Figures

1.1 Evolution of wireless communication generations and their mobility, data rate, latency, and application targets, from 1G analog voice in the 1980s to 6G envisioned for 2030 2

3.1 Block diagram of the ESM-OTFS system 36
3.2 Block diagram of the OTFS-DM-IM system used as the baseline for OTFS-GDM-IM 45
3.3 BER performance of ESM-OTFS, QSM-OTFS, SM-OTFS, and SIMO-OTFS systems based on MMSE detector with $M = 4$, $N = 4$ for 4 BPCU 52
3.4 BER performance of ESM-OTFS, QSM-OTFS, SM-OTFS, and SIMO-OTFS systems based on MMSE detector with $M = 4$, $N = 4$ for 6 BPCU 53
3.5 BER performance of ESM-OTFS using ZF, MMSE, and VBI detectors with $M = 4$, $N = 4$ for 8 BPCU 53
3.6 BER performance of ESM-OTFS using ZF, MMSE, and VBI detectors with $M = 4$, $N = 4$ for 10 BPCU 54
3.7 BER performance of ESM-OTFS at different velocities $M = 16$, $N = 16$ for 4 BPCU 55
3.8 BER performance of ESM-OTFS at different velocities $M = 16$, $N = 16$ for 6 BPCU 55
3.9 Trade-off between detector complexity and BPCU in ESM-OTFS systems 56
3.10 BER performance of OTFS-GDM-IM under high Doppler environments 57
3.11 BER performance of OTFS-GDM-IM with other OTFS based index modulation systems 58
3.12 BER performance comparison of OTFS-GDM-IM with OTFS-DM-IM with the same system parameters 58
3.13 BER performance comparison of OTFS-GDM-IM detectors 59

4.1 BER performance comparison of VAMP-CG, VAMP-SVD, and MMSE detectors . . . 95
4.2 BER performance of the proposed VAMP-CG detector across multiple modulation orders . . . 95
4.3 Impact of system dimension on VAMP-CG detector performance with varying number of subcarriers and channel parameters . . . 96
4.4 BER of the proposed VAMP-CG detector under integer and fractional Doppler for AFDM with $N = 64$ and modulation orders $M = 2, 4, 8, 16$ . . . 97
4.5 BER of the proposed VAMP-CG detector under imperfect CSI for QPSK AFDM with $N = 64$, with change in the estimation error variance scaled by β . . . 98
4.6 BER performance of the MP-PIC detector with $N = 20$ and $P = 5$ paths . . . 99
4.7 BER performance of the MP-PIC detector with $N = 20$ and $P = 10$ paths . . . 99
4.8 BER performance comparison of the MP-PIC detector at $N = 20$ across different path counts $P = 4, 8, 10, 12$ . . . 100
4.9 BER performance comparison of the MP-PIC detector at $N = 40$ across different path counts $P = 4, 8, 10, 12$ . . . 101
4.10 NMSE performance of the VB detector for quantized AFDM using BPSK . . . 102
4.11 NMSE performance of the VB detector for quantized AFDM using QPSK . . . 102
4.12 BER performance of the VB detector for quantized AFDM using BPSK and QPSK modulation . . . 103
4.13 NMSE performance comparison of various detectors for quantized AFDM using BPSK . . . 104
4.14 NMSE performance comparison of various detectors for quantized AFDM using QPSK . . . 104
4.15 BER performance comparison of various detectors for quantized AFDM using BPSK . . . 105

5.1 Block diagram of the AFDM-GIM system . . . 111
5.2 Block diagram of the AFDM-QIM system . . . 118
5.3 Spectral efficiency variation with the permitted active subcarriers in AFDM-GIM . . . 129

5.4 BER performance comparison of AFDM-GIM with AFDM-IM and conventional AFDM at the same spectral efficiency 130
5.5 BER performance of AFDM-GIM with different spectral efficiencies and detection techniques 131
5.6 Comparison between the theoretical BER analysis and the simulated BER performance for AFDM-QIM using ML detector 132
5.7 BER performance comparison of AFDM-QIM and AFDM-IM under two different spectral efficiency values 132
5.8 BER performance comparison of AFDM-QIM under different values of $K = \{1, 2, 3\}$ and $M = 2$ 133
5.9 BER performance comparison of AFDM-QIM under different values of $K = \{1, 2, 3\}$ and $M = 4$ 134
5.10 BER performance comparison of MMSE and VB-SBL detector for AFDM-IM with $L = 4$ 135
5.11 BER performance comparison of MMSE and VB-SBL detector for AFDM-IM with $L = 8$ 136
5.12 BER performance of the VB-SBL based AFDM-IM detector across different modulation schemes 136

6.1 Block diagram of the AFDM-DM-IM system 141
6.2 BER comparison of AFDM-DM-IM and AFDM-IM under high Doppler 155
6.3 Comparison between the theoretical BER upper bound and the simulated BER for AFDM-DM-IM using the ML detector 156
6.4 BER performance of AFDM-DM-IM under different spectral efficiency values 156
6.5 BER comparison of AFDM-DM-IM and OTFS-DM-IM 157
6.6 BER versus SNR for two spectral efficiency configurations with $L = 4$, $K = 2$ over the EVA channel 158
6.7 BER versus SNR for two values of $\alpha_{\max}$ over the EVA channel with disjoint BPSK dual-mode alphabets 159
6.8 BER versus SNR for $L = 8$ over the EVA channel, comparing $K = 3$ and $K = 5$ 160
6.9 BER versus SNR for $L = 16$ over the EVA channel, comparing $K = 1$ and $K = 3$ 160

7.1 Block diagram of the AFDM-MM-IM system 165
7.2 Trellis diagram for $n = 4$ used in mode-order detection for multi-mode index modulation 171

7.3 BER performance of AFDM-MM-IM using n-mode constellations under the AWGN channel with BPSK 181
7.4 BER performance of AFDM-MM-IM using n-mode constellations under the doubly dispersive channel with BPSK 182
7.5 BER performance of AFDM-MM-IM using n-mode constellations under the doubly dispersive channel with QPSK 183
7.6 BER performance of AFDM-MM-IM with $n = 4$ under different detection schemes with BPSK modulation 184
7.7 BER performance of AFDM-MM-IM with $n = 4$ under different detection schemes with QPSK modulation 184
7.8 Comparison of the theoretical BER upper bound and the simulated BER of AFDM-MM-IM with $n = 3$, BPSK, and ML detection for different P 185
7.9 Comparison of AFDM-MM-IM, AFDM-DM-IM, and classical AFDM at comparable spectral efficiencies 186
7.10 BER performance comparison of AFDM-MM and OTFS-MM for different subblock lengths under the high-Doppler channel 187
7.11 BER performance comparison of AFDM-MM, OTFS-MM, and OFDM-MM for $n = 4$ under the high-Doppler channel 187
7.12 Spectral efficiency comparison for AFDM-based schemes with $n = 4$, $K = 2$, and constellation size 4 188

List of Tables

3.1 ESM, $N_T = 2$ transmit antennas, four BPCU 35
3.2 ESM mapping rule for $N_T = 2$ and QPSK as primary constellation . 37
3.3 A look-up table for dual-mode index modulation with $g_1 = 2$, $L = 4$, $K = 2$ 45

4.1 Computational complexity comparison of AFDM detectors with N subcarriers, $|\mathcal{A}|$ constellation size, L_p effective channel taps per symbol, K_{it} outer VAMP iterations, K_{CG} inner CG iterations, $t_{\max}$ MP-PIC iterations, and $T_{\max}$ VB iterations. 106

6.1 Look-up table for dual-mode index modulation with $g_1 = 2$, $L = 4$, $K = 2$ 141
6.2 Computational complexity of AFDM-DM-IM detectors with N subcarriers, G subblocks, L subblock length, K active subcarriers, alphabet sizes M_A and M_B, combined alphabet size $Q = M_A + M_B$, pattern count $N_p = \binom{L}{K}$, T message passing iterations, K_{CG} inner CG iterations, and n_{probe} trace probes 154

7.1 Permutation mapping for $n = 4$ using factorial expansion 166
7.2 Computational complexity of AFDM-MM-IM detectors 180

Nomenclature

$(\cdot)^*$	Complex conjugate
$(\cdot)^H$	Hermitian transpose
$(\cdot)^T$	Transpose
$[n]_N$	n modulo N
α_i	Integer part of ν_i
α_k	Divergence of the VAMP denoiser
$\alpha_{\max}$	Maximum normalized integer Doppler shift
$\bar{x}_m$	Posterior mean of symbol m
$\mathbf{\Delta}_{\nu_i}$	Diagonal Doppler matrix for the i^{th} path
$\mathbf{\Gamma}_{\text{CPP},i}$	Chirp-periodic prefix correction matrix for the i^{th} path
$\mathbf{\Lambda}_c$	Diagonal chirp matrix with entries $e^{-j2\pi cn^2}$
$\mathbf{\Phi}$	Error correlation matrix, $\mathbf{\Phi} = \mathbf{e}\mathbf{e}^H$
$\mathbf{\Pi}$	Cyclic forward-shift permutation matrix
$\boldsymbol{Q}_k, \boldsymbol{b}_k$	Linear system matrix and right-hand side in VAMP-CG
Δf	Subcarrier spacing
δ	Squared Euclidean distance between codewords under the channel
$\delta(\cdot)$	Dirac delta function or Kronecker delta
Δ_q	Quantization step size
γ_k	VAMP denoiser precision at iteration k
γ_w	Noise precision, $\gamma_w = 1/\sigma^2$

$\hat{\mathbf{x}}$	Estimate of the transmit vector
λ_i	Eigenvalues of $\mathbf{K}$ or of the channel correlation matrix
$\Lambda_{k,m}(a)$	Log-likelihood contribution in the VB detector
$\mathbb{1}(\cdot)$	Indicator Function
$\mathbb{E}[\cdot]$	Expectation operator
$\mathbf{A}$	DAFT matrix, $\mathbf{A} = \mathbf{\Lambda}_{c_2}\mathbf{F}\mathbf{\Lambda}_{c_1}$
$\mathbf{A}^H$	Inverse DAFT matrix
$\mathbf{C}$	Channel correlation matrix
$\mathbf{e}$	Error vector, $\mathbf{e} = \mathbf{x} - \hat{\mathbf{x}}$
$\mathbf{e}^q$	Quantization error vector
$\mathbf{F}$	Normalized N-point DFT matrix
$\mathbf{H}_{\text{eff}}$	Effective channel matrix in the DAFT (or DD) domain
$\mathbf{H}_{\text{td}}$	Time-domain channel matrix
$\mathbf{K}$	Codeword difference correlation matrix
$\mathbf{r}$	Time-domain received signal after CPP removal
$\mathbf{r}^q$	Quantized time-domain received signal
$\mathbf{r}_k$	VAMP denoiser input at iteration k
$\mathbf{s}$	Time-domain transmit signal
$\mathbf{w}$	Additive white Gaussian noise vector in the time domain
$\mathbf{x}$	Transmit symbol vector in the DAFT (or DD) domain
$\mathbf{y}$	Received signal in the DAFT (or DD) domain
$\mathbf{y}^q$	Quantized signal in the DAFT domain
$\mathcal{A}$	Constellation alphabet (generic)
$\mathcal{B}$	Second constellation alphabet for dual-mode index modulation
$\mathcal{CN}(\boldsymbol{\mu}, \boldsymbol{\Sigma})$	Circularly symmetric complex Gaussian distribution

$\mathcal{J}^{(g)}$	Index pattern of the g^{th} subblock
$\mathcal{J}_A^{(g)}, \mathcal{J}_B^{(g)}$	Index subsets for alphabets $\mathcal{A}$ and $\mathcal{B}$ in DM-IM
$\mathcal{P}^{(g)}$	Mode permutation of the g^{th} subblock in MM-IM
$\mathcal{Q}(\cdot)$	Uniform scalar quantizer
$\text{diag}(\cdot)$	Diagonal of a matrix, or diagonal matrix formed from a vector
$\text{Tr}(\cdot)$	Trace of a matrix
ν_i	Normalized Doppler shift of the i^{th} path, $\nu_i = \alpha_i + a_i$
$\odot$	Element-wise (Hadamard) product
$\otimes$	Kronecker product
$\pi_{m,a}$	Probability that symbol m takes value a
$\text{Re}(\cdot), \text{Im}(\cdot)$	Real and imaginary parts of a complex variable
σ^2	Noise variance
$\tilde{\mathbf{r}}_k, \tilde{\gamma}_k$	Onsager-corrected denoiser output and precision
$\tilde{\mathbf{w}}$	Noise vector in the DAFT (or DD) domain
ξ_ν	Spread parameter for fractional Doppler in the DAFT domain
$\{\mathcal{M}_1, \ldots, \mathcal{M}_n\}$	Set of distinct constellations for multi-mode index modulation
a_i	Fractional part of ν_i, $a_i \in (-1/2, 1/2]$
b	Total bits per frame
b_q	ADC resolution in bits
c_1, c_2	AFDM chirp parameters
$d_H(\cdot,\cdot)$	Hamming distance between bit sequences
f_c	Carrier frequency
f_i	Doppler frequency of the i^{th} path
$F_{\boldsymbol{\alpha}}(\cdot)$	Moment generating function
G	Number of subblocks in a frame, $G = N/L$

g	Total bits per subblock, $g = g_1 + g_2$
g_1	Number of index bits per subblock
g_2	Number of modulation bits per subblock
h_i	Complex gain of the i^{th} propagation path
K	Number of active subcarriers per subblock in single-mode index modulation, or number of subcarriers in the primary alphabet in dual-mode index modulation
K_{CG}	Number of inner conjugate gradient iterations
K_{it}	Number of outer VAMP iterations
L	Subblock length in index modulation
l_i	Integer delay of the i^{th} path
L_p	Effective number of channel taps per symbol in the DAFT domain
L_{cp}	Length of the chirp-periodic prefix
$L_{\max}$	Maximum delay spread in samples
M	Number of delay bins in an OTFS frame
M_A, M_B	Sizes of $\mathcal{A}$ and $\mathcal{B}$ in dual-mode index modulation
N	Total number of subcarriers in an AFDM frame
n	Number of subcarriers per subblock in multi-mode index modulation
N_0	Noise power spectral density
N_{ofdm}	Number of OFDM symbols in an OTFS frame
P	Number of multipath components
P_{ABER}	Average bit error probability
q	Number of distinct nonzero eigenvalues
$Q(\cdot)$	Gaussian Q-function
T	OFDM symbol duration
u_j, c_j	Quantization thresholds and output levels
v_m	Posterior variance of symbol m

Acronyms

1G First Generation

2G Second Generation

3G Third Generation

3GPP 3rd Generation Partnership Project

4G Fourth Generation

5G Fifth Generation

6G Sixth Generation

ABER Average Bit Error Rate

ADC Analog-to-Digital Converter

AFDM Affine Frequency Division Multiplexing

AFDM-DM-IM AFDM with Dual-Mode Index Modulation

AFDM-GIM AFDM with Generalized Index Modulation

AFDM-IM AFDM with Index Modulation

AFDM-MM-IM AFDM with Multi-Mode Index Modulation

AFDM-QIM AFDM with Quadrature Index Modulation

AMP Approximate Message Passing

AMPS Advanced Mobile Phone System

AWGN Additive White Gaussian Noise

BER Bit Error Rate

BP Belief Propagation

CG Conjugate Gradient

CNN Convolutional Neural Network

CP Cyclic Prefix

CPEP Conditional Pairwise Error Probability

CPP Chirp-Periodic Prefix

CSI Channel State Information

DAFT Discrete Affine Fourier Transform

DD Delay-Doppler

DFT Discrete Fourier Transform

DL Deep Learning

DNN Deep Neural Network

ED Energy Detection

EDGE Enhanced Data Rates for GSM Evolution

ELBO Evidence Lower Bound

EPA Extended Pedestrian A

ESM Enhanced Spatial Modulation

ESM-OTFS Enhanced Spatial Modulation based OTFS

ETU Extended Typical Urban

EVA Extended Vehicular A

GAMP Generalized Approximate Message Passing

GPRS General Packet Radio Service

GSM Global System for Mobile Communications

ICI Inter-Carrier Interference

IDAFT Inverse Discrete Affine Fourier Transform

IM Index Modulation

IMT-2000 International Mobile Telecommunications 2000

IoT Internet of Things

ISFFT Inverse Symplectic Finite Fourier Transform

ISI Inter-Symbol Interference

ITU International Telecommunication Union

KL Kullback-Leibler

LEO Low-Earth Orbit

LLR Log-Likelihood Ratio

LMMSE Linear Minimum Mean Square Error

LSTM Long Short-Term Memory

LTE Long-Term Evolution

LTV Linear Time-Varying

MAP Maximum A Posteriori

MIMO Multiple-Input Multiple-Output

ML Maximum Likelihood

MMSE Minimum Mean Square Error

MP Message Passing

MP-PIC Multi-Path Parallel Interference Cancellation

NMSE Normalized Mean Squared Error

NOMA Non-Orthogonal Multiple Access

NR New Radio

OCDM Orthogonal Chirp Division Multiplexing

OFDM Orthogonal Frequency Division Multiplexing

OFDM-IM OFDM with Index Modulation

OTFS Orthogonal Time Frequency Space

OTFS-DM-IM OTFS with Dual-Mode Index Modulation

OTFS-GDM-IM OTFS with Generalized Dual-Mode Index Modulation

OTFS-IIM OTFS with Improved Index Modulation

OTFS-IM OTFS with Index Modulation

PAPR Peak-to-Average Power Ratio

PCG Preconditioned Conjugate Gradient

PEP Pairwise Error Probability

PIC Parallel Interference Cancellation

QSM Quadrature Spatial Modulation

QSM-OTFS Quadrature Spatial Modulation based OTFS

RWDSC Reliability-Weighted Decision Statistics Combining

SAVE Space Alternating Variational Estimation

SBL Sparse Bayesian Learning

SE Spectral Efficiency

SFFT Symplectic Finite Fourier Transform

SIMO Single-Input Multiple-Output

SM Spatial Modulation

SM-OTFS Spatial Modulation based OTFS

SNR Signal-to-Noise Ratio

TDMA Time Division Multiple Access

TF Time-Frequency

UAV Unmanned Aerial Vehicle

UE User Equipment

UMTS Universal Mobile Telecommunications System

UPEP Unconditional Pairwise Error Probability

V2X Vehicle-to-Everything

VAMP Vector Approximate Message Passing

VB Variational Bayesian

VBI Variational Bayesian Inference

ZF Zero-Forcing

Chapter 1

Introduction

The evolution of wireless communication from analog voice to fully digital broadband networks has been driven by the simultaneous expansion of two performance requirements, namely the data rate available to each user and the mobility profile under which that rate must be sustained. Fig. 1.1 summarizes this trajectory across approximately five decades. The first generation (1G), introduced in the early 1980s, supported analog voice transmission at approximately 2.4 Kbps for pedestrian users. The second generation (2G) introduced digital voice through GSM, GPRS, EDGE, and TDMA at 50 Kbps and added text messaging, while supporting stationary or low-mobility users. The third generation (3G), realized through UMTS and IMT-2000, increased the data rate to 21 Mbps and enabled multimedia services on mobile handsets. The fourth generation (4G) Long-Term Evolution (LTE) delivered data rates up to 100 Mbps with latency near 10 ms and supported mobility up to 350 km/h, enabling mobile television and mobile Internet at vehicular speeds. The fifth generation (5G) New Radio achieved peak data rates of 20 Gbps with a latency of 1 ms and a mobility ceiling of 500 km/h, supporting wearable devices, the Internet of Things, and smart city deployments.

The sixth generation (6G), targeted for commercial deployment around 2030, departs substantially from this evolutionary pattern. Data rates exceeding 1 Tbps, latencies in the 10 to 100 μs range, and mobility profiles beyond 1000 km/h are

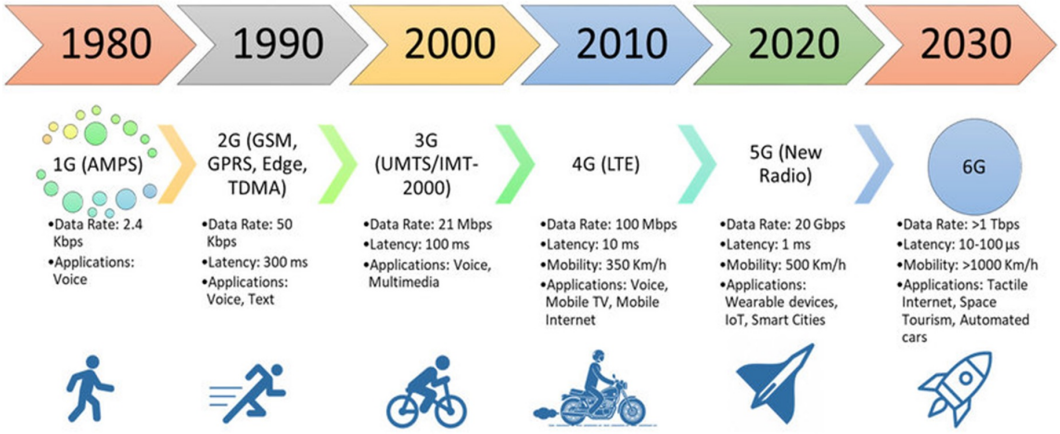


Figure 1.1: Evolution of wireless communication generations and their mobility, data rate, latency, and application targets, from 1G analog voice in the 1980s to 6G envisioned for 2030

envisioned to support applications such as the tactile Internet, autonomous vehicle networks, and space tourism. As illustrated in Fig. 1.1, the mobility requirement increases substantially from pedestrian speeds in 1G to aerospace velocities in 6G, and this increase imposes significant additional constraints on the physical layer. Each step along the mobility axis imposes increasingly stringent requirements on the waveform, the channel estimator, and the detector, to the extent that OFDM, the waveform used in 4G and 5G, loses its subcarrier orthogonality as mobility increases, resulting in inter-carrier interference. This thesis addresses the physical-layer design challenges that arise in this regime.

1.1 The Mobility Problem in Wireless Communications

Conventional wireless communication system design has long relied on the assumption that the channel varies slowly relative to the symbol duration. Although wireless channels are inherently time-varying due to multipath fading, shadowing, and large-scale path loss, the rate of variation has historically been sufficiently slow that the channel could be treated as essentially time-invariant over the span

of a single symbol or a single OFDM frame. The orthogonal frequency division multiplexing (OFDM) waveform underlying both 4G LTE and 5G NR is fundamentally based on this quasi-static channel assumption, since subcarrier orthogonality is preserved only when the channel response remains constant over the symbol duration. This assumption ceases to hold in emerging high-mobility scenarios. Next-generation wireless systems are being designed for operating conditions in which mobility is a central rather than incidental factor, including vehicle-to-everything (V2X) communication at highway speeds, high-speed railways operating above 500 km/h, unmanned aerial vehicles maneuvering through three-dimensional space, and low-earth-orbit (LEO) satellite links where Doppler shifts can reach hundreds of kilohertz. These constitute the principal use cases around which 6G is being designed [1, 2]. In each of these scenarios, the channel varies rapidly within a single transmission and the quasi-static channel assumption is no longer valid.

The mathematical signature of high mobility is the doubly dispersive channel, which spreads transmitted signals along two axes simultaneously, namely the delay axis due to multipath propagation and the Doppler axis due to relative motion between the transmitter and the receiver. A propagation path with delay τ_i and Doppler shift ν_i introduces both a time shift and a frequency shift in the received signal. When multiple paths coexist, each with distinct (τ_i, ν_i) coordinates, the receiver observes a superposition that cannot be effectively separated using waveforms designed for one-dimensional dispersion. OFDM exhibits a specific and well-understood limitation in this regime. Its subcarriers remain orthogonal in the frequency domain only when the channel response is constant over the symbol duration. A Doppler shift disrupts this orthogonality by rotating each subcarrier at a slightly different rate, producing inter-carrier interference (ICI) that scales with the maximum Doppler shift $\nu_{\max}$ and subcarrier spacing Δf as $\nu_{\max}^2/(\Delta f)^2$. At a vehicle velocity of 500 km/h and a carrier frequency of 4 GHz, the maximum Doppler shift is approximately 1.85 kHz, which represents a substantial fraction of

a 15 kHz subcarrier spacing and gives rise to significant ICI. In addition, OFDM achieves only diversity order one over a multipath channel regardless of the number of available paths, since each subcarrier observes essentially a single frequency-domain channel tap. The diversity inherent in the multipath structure is therefore not exploited [3, 4]. These limitations are structural in nature and cannot be resolved through parameter adjustment alone. The waveform itself, that is, the choice of basis functions over which information is multiplexed, must be redesigned.

1.2 Towards Delay-Doppler Waveforms

Two waveforms have emerged as principal candidates for high-mobility communication, and both are based on the same underlying principle, namely that the doubly dispersive channel admits a simple representation in an appropriately chosen domain rather than requiring direct compensation in the time-frequency domain. Orthogonal Time Frequency Space (OTFS) modulation, introduced by Hadani *et al.* [5], multiplexes information symbols on a two-dimensional grid in the delay-Doppler (DD) domain. The transmitter applies an inverse symplectic finite Fourier transform (ISFFT) followed by a Heisenberg transform, and the receiver performs the inverse operations. A channel that appears rapidly time-varying in the time-frequency domain becomes sparse and quasi-static in the DD domain, with each propagation path contributing a single point at coordinates (τ_i, ν_i) [6, 7]. Each transmitted symbol is spread across the entire time-frequency plane, and consequently each symbol benefits from the full delay-Doppler diversity of the channel. OTFS has been studied extensively in recent years and has demonstrated significant advantages. It has been shown to outperform OFDM by a substantial margin in high-mobility scenarios [8, 9], channel estimation in the DD domain requires fewer pilots than the corresponding time-frequency approach [10, 11], and the peak-to-average power ratio (PAPR) is well-controlled [12]. However, the two-dimensional nature of OTFS introduces several practical costs. The pilot

overhead in a two-dimensional grid is non-negligible, since a typical OTFS pilot region occupies $(4\nu_{\max}+1)(2\tau_{\max}+1)$ resource elements, which reduces the available data payload when the channel exhibits substantial delay-Doppler spread [13, 14]. The transmit and receive processing also requires an additional two-dimensional transform beyond the standard OFDM front-end. Furthermore, the DD-domain channel matrix, although sparse, exhibits a quasi-diagonal structure that is not always amenable to low-complexity detector designs [15].

Affine Frequency Division Multiplexing (AFDM), introduced by Bemani *et al.* [16, 17], addresses these limitations. AFDM is based on the discrete affine Fourier transform (DAFT), which generalizes the discrete Fourier transform (DFT) through two chirp parameters c_1 and c_2. With these parameters tuned to the delay-Doppler profile of the channel, AFDM achieves full diversity over the doubly dispersive channel using a one-dimensional frame structure. Each transmitted symbol still experiences the combined effect of all propagation paths, and the achievable diversity order matches that of OTFS, while the transceiver architecture resembles that of OFDM with two additional diagonal phase rotations. The practical consequences of this structure are significant. AFDM retains OFDM compatibility, requires approximately half the pilot overhead of OTFS [17], and produces an effective channel matrix in the DAFT domain that is sparse and banded rather than quasi-diagonal. The banded structure of the AFDM channel matrix enables low-complexity detection, and a substantial portion of this thesis is devoted to exploiting this structural property.

1.3 Index Modulation in Multicarrier Systems

Beyond the choice of waveform, a second design dimension that has attracted considerable research attention is index modulation (IM). In addition to the information conveyed through the amplitude and phase of modulated symbols, IM transmits additional bits through the selection of active resources such as subcarri-

ers, antennas, or time slots [18, 19]. The activation pattern itself thereby acts as an additional information-bearing dimension.The appeal of this dimension is twofold. Because part of the information is now carried by the choice of which resources are activated, a given data rate can be met with a smaller signal constellation than conventional signaling would require; the wider spacing between constellation points that results improves error performance at no change in rate, and conversely the same constellation can be made to carry more bits. Just as importantly, confining the active resources to a chosen pattern imposes a known, structured sparsity on the transmitted vector, so that detection reduces to jointly identifying this active support and the symbols carried on it, a problem for which the message passing and Bayesian methods developed in this thesis are naturally suited. Index modulation is therefore not merely a means of raising spectral efficiency but a way of shaping the transmitted signal so that it is more readily recovered.

The most widely studied variant is OFDM with index modulation (OFDM-IM), in which only a subset of subcarriers within each subblock is activated and the activation pattern encodes the index bits [20]. OFDM-IM provides measurable improvements in spectral and energy efficiency, but it leaves a portion of the subcarriers inactive, which represents an inefficient use of available resources. Dual-mode OFDM-IM [21] addresses this inefficiency by replacing the inactive subcarriers with symbols drawn from a second, distinguishable constellation. Multi-mode variants [22] extend this approach further by assigning permutations of distinct constellations across subcarriers.

Analogous developments have been carried out for OTFS, including OTFS with index modulation (OTFS-IM) [23], OTFS with improved IM [24], dual-mode OTFS-IM [25], and multi-mode OTFS-IM [26], each occupying a different position on the spectral-efficiency to reliability trade-off curve. For AFDM, the corresponding literature is considerably sparser. AFDM with index modulation (AFDM-IM) has been investigated in [27,28], but the more sophisticated variants, namely dual-mode,

generalized, quadrature, and multi-mode index modulation tailored to AFDM, were largely unexplored at the outset of this work. Given the strong fundamentals of AFDM as a delay-Doppler waveform, this represents a substantive gap in the literature, and a major component of this thesis is directed toward addressing this gap.

1.4 Detection of Index-Modulated Waveforms

A delay-Doppler waveform combined with index modulation requires an effective detector for its practical realization, and this requirement presents significant difficulties. Maximum likelihood (ML) detection is optimal in principle but exhibits complexity that grows exponentially with the number of subcarriers, rendering it infeasible for any frame of practical size. Linear receivers such as the minimum mean-square error (MMSE) detector provide a reasonable performance baseline but require an $N \times N$ matrix inversion at a cost of $\mathcal{O}(N^3)$ operations per channel realization, and they do not exploit the discrete structure of the constellation. Between these two extremes lies a family of message passing and Bayesian inference algorithms that exploit the sparse structure of the channel matrix to achieve near-optimal performance at substantially lower computational cost. Approximate message passing (AMP) [29] performs well for independent and identically distributed Gaussian measurement matrices but is prone to divergence on the structured matrices that arise in AFDM and OTFS. Vector AMP (VAMP) [30] relaxes the i.i.d. requirement to right-orthogonal invariance, a condition that AFDM channels approximately satisfy. VAMP provides strong convergence guarantees, but its standard formulation requires a singular value decomposition of the channel matrix at a cost of $\mathcal{O}(N^3)$ per channel realization. Generalized AMP (GAMP) [31] extends the framework to accommodate arbitrary priors and likelihoods, including the nonlinear quantization effects that arise when low-resolution analog-to-digital converters are employed at the receiver.

Variational Bayesian (VB) inference provides an additional inference framework. By approximating the intractable posterior distribution with a factorized variational distribution and maximizing the evidence lower bound (ELBO), VB methods incorporate sparsity priors, quantization constraints, and discrete constellation structure in a principled manner [32, 33]. The mean-field factorization reduces the complexity from exponential to linear in the frame size, which renders the approach computationally tractable. None of these inference tools were originally developed for AFDM or for AFDM with index modulation, and their adaptation, together with the development of new variants where required, constitutes a substantial portion of the contributions presented in this thesis.

1.5 Low-Resolution Analog-to-Digital Conversion

A further practical consideration concerns the use of low-resolution analog-to-digital converters (ADCs) in modern wireless receivers, particularly in massive MIMO and millimeter-wave systems. The motivation for low-resolution conversion is power consumption, since ADC power consumption scales approximately as 2^b for b-bit resolution, and a reduction from 12 bits to 3 or 4 bits yields substantial power savings [34, 35]. However, low-resolution quantization is a nonlinear operation, and conventional linear receivers do not accommodate this nonlinearity effectively. The Bussgang decomposition [36] provides a linear approximation that performs adequately at moderate resolutions but degrades significantly at 3 bits or below, where the bit error rate (BER) floor remains essentially constant with increasing signal-to-noise ratio (SNR). To overcome this floor, the detector must explicitly model the truncated-Gaussian likelihood induced by quantization. Variational Bayesian methods are well-suited to this requirement, and one of the contributions of this thesis is a VB detector developed specifically for AFDM with low-resolution ADCs.

1.6 Contribution of Thesis

This thesis contributes to the design of waveforms and receivers for high-mobility wireless communication, with particular emphasis on index modulation schemes built on AFDM and the detection algorithms required to recover information from them. The work is motivated by the observation that AFDM, despite its strong fundamentals as a delay-Doppler waveform, has received considerably less attention than OTFS in the context of index modulation. This represents a substantive gap in the literature, since several established techniques from the OFDM-IM and OTFS-IM literatures, including dual-mode, multi-mode, generalized, and quadrature variants, have not been systematically extended to AFDM. This thesis addresses this gap through the contributions outlined below. Two index modulation schemes for OTFS are developed as foundational work that supports the AFDM-focused chapters that follow. An enhanced spatial modulation variant of OTFS (ESM-OTFS) is proposed, which combines the delay-Doppler diversity of OTFS with the spectral and energy efficiency of spatial modulation. Two detectors are developed for ESM-OTFS, namely an MMSE-based linear detector that serves as a baseline and a Variational Bayesian inference detector that exploits the sparsity of the transmit vector and jointly recovers the active antenna pattern and the modulated symbols within a single inference procedure. In addition, a generalized dual-mode index modulation scheme for OTFS (OTFS-GDM-IM) is proposed, accompanied by ML and log-likelihood ratio (LLR) detectors. These OTFS contributions are independently meaningful and additionally provide the framework upon which several of the AFDM detectors developed in subsequent chapters are constructed.

The AFDM detection problem is then addressed through three detectors of progressively increasing structural complexity. A Vector AMP detector incorporating preconditioned conjugate gradient iterations is developed to replace the standard singular value decomposition, reducing the per-iteration complexity from cubic to quadratic in the frame size while preserving the detection performance of standard

VAMP. A multi-path parallel interference cancellation detector is also developed that exploits a structural property unique to AFDM, namely the complete delay-Doppler separation of propagation paths in the DAFT-domain channel matrix, by constructing independent Bayesian estimates from each path and subsequently combining them through interference cancellation. A Variational Bayesian detector is additionally developed for AFDM with low-resolution ADCs. This detector models the truncated-Gaussian likelihood induced by quantization directly rather than relying on the linearizing Bussgang approximation, and consequently maintains effective operation at 3-bit and 4-bit ADC resolutions where Bussgang-based receivers exhibit a pronounced BER floor.

Generalized and quadrature index modulation schemes for AFDM are proposed together with a sparse Bayesian detector for the AFDM-IM family. Generalized AFDM-IM (AFDM-GIM) relaxes the fixed-activation constraint of conventional AFDM-IM by allowing the number of active subcarriers in each subblock to vary, which enlarges the pattern space and increases the spectral efficiency. Quadrature AFDM-IM (AFDM-QIM) encodes index bits independently on the in-phase and quadrature components, which doubles the index-bit capacity for a given active-subcarrier count. For the baseline AFDM-IM, a Variational Bayesian detector employing a hierarchical Gaussian-Gamma sparsity prior is developed. The prior captures the structured sparsity of the index-modulated transmit vector, and the inference procedure jointly recovers the active pattern and the symbol values. A dual-mode index modulation scheme for AFDM (AFDM-DM-IM) is then proposed that activates all subcarriers within each subblock. The inactive subcarriers that are inherent to AFDM-IM and represent an inefficiency are eliminated by modulating each subcarrier with one of two disjoint constellations, where the index pattern determines which constellation is applied to each subcarrier and all subcarriers thus carry information. Three detectors are developed for this scheme. An MMSE-ML detector is presented as a baseline. A low-complexity MMSE-LLR detector is

developed for practical frame sizes where ML detection becomes infeasible. The principal contribution in this context is a pair of message passing detectors, namely VAMP-DMDIM and GAMP-DMDIM, that jointly estimate the symbols and the mode assignments through an inline belief propagation module, and that achieve performance close to ML detection while maintaining complexity comparable to MMSE.

A multi-mode index modulation framework for AFDM (AFDM-MM-IM) is then developed that employs full permutations of distinct constellations across the subcarriers of each subblock. The factorial growth in the number of index patterns provides spectral efficiency that exceeds what dual-mode and single-mode variants can support. Three detectors are developed to span a range of complexity-performance trade-offs. A greedy LLR-based detector operates at the lowest complexity level. A Viterbi-style trellis detector occupies an intermediate position, and a sphere decoding detector approaches ML performance with a complexity that grows only moderately with the frame size. A closed-form average BER bound is derived using the pairwise error probability framework, which enables analytical comparison against the simulation results. Across these chapters, the thesis develops a coherent body of work on AFDM-based index modulation and the associated detection problems. The proposed schemes include AFDM-GIM, AFDM-QIM, AFDM-DM-IM, and AFDM-MM-IM, together with the OTFS-based ESM-OTFS and OTFS-GDM-IM schemes that serve as foundational work. The detectors developed range from low-complexity Bayesian and message passing variants to sphere-decoding and trellis-based near-ML detectors, and they include a variational Bayesian receiver tailored to low-resolution ADC scenarios. Collectively, these contributions establish AFDM as a strong candidate waveform for 6G high-mobility communication and provide a set of design tools that can be applied or extended in subsequent research.

1.7 Organization of Thesis

The thesis is organized into eight chapters. Chapter 2 surveys the literature on which the subsequent work builds, covering high-mobility waveforms such as OTFS and AFDM, the index modulation techniques developed for OFDM and OTFS, the detection algorithms used to recover information from index-modulated waveforms, and the practical considerations arising from low-resolution analog-to-digital conversion. The chapter concludes by identifying the specific gaps in the AFDM literature that the subsequent chapters address. Chapter 3 develops two index modulation schemes for OTFS that serve as foundational work for the AFDM-focused chapters. An enhanced spatial modulation variant of OTFS (ESM-OTFS) is proposed and supported by an MMSE baseline detector and a Variational Bayesian inference detector. A generalized dual-mode index modulation scheme (OTFS-GDM-IM) is also presented, together with ML and LLR detectors. The OTFS framework and the variational inference machinery introduced in this chapter are carried over to the AFDM setting in the chapters that follow.

Chapter 4 introduces the AFDM system model in detail and develops three Bayesian and message passing detectors, namely a low-complexity Vector AMP detector that replaces the singular value decomposition step with preconditioned conjugate gradient iterations, a multi-path parallel interference cancellation detector that exploits the delay-Doppler path separation property of AFDM, and a Variational Bayesian detector tailored to AFDM with low-resolution ADCs. Chapters 5 through 7 build on this detection framework and present the principal index modulation contributions of the thesis. Chapter 5 proposes generalized and quadrature index modulation schemes for AFDM (AFDM-GIM and AFDM-QIM) and a sparse Bayesian detector for the AFDM-IM family based on a hierarchical Gaussian-Gamma sparsity prior. Chapter 6 develops a dual-mode index modulation scheme (AFDM-DM-IM) that activates all subcarriers within each subblock and supports it with MMSE-ML, MMSE-LLR, and message passing detectors based on

VAMP and GAMP. Chapter 7 develops a multi-mode index modulation framework (AFDM-MM-IM) employing full permutations of distinct constellations across subcarriers, together with greedy LLR, Viterbi-trellis, and sphere decoding detectors and a closed-form pairwise error probability bound. Chapter 8 concludes the thesis with a summary of the principal findings, a discussion of their implications for AFDM as a candidate waveform for 6G high-mobility systems, and an outline of directions for future research.

Chapter 2

Background and Literature Review

This chapter reviews the body of work on which the rest of the thesis builds. The survey is organized around four themes: the waveforms developed for high-mobility communication, the index modulation techniques overlaid on these waveforms, the detection algorithms used to recover the transmitted information, and the practical issues introduced by low-resolution analog-to-digital converters. The aim is not to be exhaustive. The wireless literature on each of these topics is large, but the point here is to characterize the relevant prior work in enough detail that the specific gaps addressed in later chapters become clear.

2.1 From OFDM to Delay-Doppler Waveforms

2.1.1 OFDM and its Limitations

Orthogonal Frequency Division Multiplexing has been the dominant multicarrier scheme in wireless systems for two decades. Its underlying principle, namely the decomposition of a frequency-selective channel into parallel approximately flat subchannels via a discrete Fourier transform, works well when the channel is

approximately static within the symbol duration. This assumption has held for 4G LTE and 5G NR in most practical deployments, and the resulting modulation scheme underlies most contemporary wireless infrastructure.

OFDM degrades when the channel varies rapidly. Doppler shifts cause subcarriers to lose orthogonality, and the resulting inter-carrier interference grows with the square of the normalized Doppler spread. Hwang *et al.* [3] surveyed OFDM and its wireless applications and identified these limitations. More recent assessments have argued that as wireless systems progress towards 6G, with its emphasis on high-mobility scenarios, OFDM performance will become a binding constraint [2,4].

Several modifications have been proposed to make OFDM more robust to mobility. Pulse shaping, ICI self-cancellation, and decision-feedback equalization [37] have all been explored. These help, but none of them recover the diversity inherent in the multipath structure. OFDM remains diversity-order-one regardless of the number of propagation paths, because each subcarrier sees only one tap of the frequency-domain channel.

A separate line of work explored alternative chirp-based waveforms. Orthogonal Chirp Division Multiplexing (OCDM), introduced by Ouyang and Zhao [38], uses chirp signals generated via the discrete Fresnel transform. OCDM is more resilient to multipath than OFDM, but its fixed chirp rate limits how much delay-Doppler diversity it can exploit. This limitation motivated waveforms with tunable chirp parameters.

2.1.2 Orthogonal Time Frequency Space Modulation

OTFS was introduced by Hadani *et al.* in 2017 [5], and the subsequent years have produced a substantial body of work on it. The central idea is that a doubly dispersive channel, while it appears rapidly time-varying in the time-frequency domain, is essentially time-invariant in the delay-Doppler domain. Each propagation path contributes a single point in the DD plane, and the channel response over

many transmitted symbols is characterized by a small number of complex gains at distinct delay-Doppler coordinates.

OTFS exploits this by multiplexing symbols on a two-dimensional grid in the DD domain. The transmitter applies an inverse symplectic finite Fourier transform (ISFFT) to convert DD symbols to the time-frequency domain, followed by a Heisenberg transform to produce the time-domain signal. The receiver reverses these operations. Each transmitted symbol is spread across the entire time-frequency plane, so each symbol experiences the diversity of all propagation paths, achieving full delay-Doppler diversity.

Performance studies have confirmed the predicted benefits. Hadani *et al.* [8] evaluated OTFS in millimeter-wave systems and reported significant BER gains over OFDM. Surabhi *et al.* [39] analyzed the diversity of uncoded OTFS rigorously and showed that with appropriate symbol mappings, OTFS achieves diversity order equal to the number of paths. Raviteja *et al.* developed practical detectors [7, 11] and showed how OTFS could be implemented as an OFDM overlay with pre- and post-processing modules. The PAPR properties were studied by Surabhi *et al.* [12]. Channel estimation methods using embedded pilots were proposed by Raviteja *et al.* [40] and developed further in subsequent work [10].

The two-dimensional structure of OTFS enables full diversity but also introduces overhead. The pilot region required for channel estimation occupies a 2D patch of resource elements, typically $(4\nu_{\max}+1)(2\tau_{\max}+1)$ symbols, which can be a substantial fraction of the frame in channels with large delay and Doppler spread. The transceiver requires a 2D transform in addition to standard OFDM processing, which adds implementation cost. The effective channel matrix in the DD domain, while sparse and structured, has a quasi-diagonal pattern that does not always admit the simplest detector designs.

MIMO extensions of OTFS have been studied extensively [9, 13–15]. These add implementation complexity but also further diversity. Channel estimation for

MIMO-OTFS, particularly in the massive MIMO regime, has been a major focus.

2.1.3 Affine Frequency Division Multiplexing

AFDM was introduced by Bemani *et al.* in 2021 [16] and developed more fully in their 2023 paper [17]. The underlying idea is that the discrete affine Fourier transform (DAFT), which generalizes the DFT through two chirp parameters c_1 and c_2, can be adapted to a specific channel's delay-Doppler profile more flexibly than the DFT. With the parameters chosen appropriately, the effective channel matrix in the DAFT domain becomes sparse and banded, with each propagation path occupying a distinct set of entries.

What distinguishes AFDM is that it achieves the same full diversity as OTFS using a one-dimensional frame structure. The transmitter resembles an OFDM transmitter with two additional diagonal phase rotations applied before and after the DFT. The chirp-periodic prefix replaces the cyclic prefix and serves the same function, making the multipath channel effectively circular for the DAFT operation, but with a phase correction that accounts for the quadratic-phase character of the AFDM signal.

The pilot overhead in AFDM is approximately half that of OTFS [17], because the embedded pilot needs only a one-dimensional guard region rather than a two-dimensional one. Channel estimation methods have been developed by Bemani *et al.* [17] and refined in subsequent work [41, 42] to handle fractional Doppler shifts.

The structure of the DAFT-domain effective channel matrix has been studied in detail. With $c_1 = (2\alpha_{\max} + 1)/(2N)$,where $\alpha_{\max}$ denotes the maximum Doppler shift normalised to the subcarrier spacing and c_2 chosen as an irrational number or a rational with denominator larger than $2N$, each propagation path contributes to a distinct set of column indices in the effective channel matrix [17]. For integer Doppler shifts, each path contributes exactly one non-zero per row. For fractional Doppler, the non-zeros spread over $2\xi_\nu + 1$ columns, where ξ_ν is the integer guard

parameter that bounds the number of adjacent columns retained on either side of the nominal path location, but the path separation property still holds approximately.

Comparative studies of AFDM and OTFS have been carried out in several works [43], and the general finding is that AFDM matches OTFS in diversity performance while offering lower pilot overhead and simpler implementation. This makes AFDM a strong candidate for 6G high-mobility systems, and a growing body of work has explored extensions: AFDM with sparse code multiple access (AFDM-SCMA) [44] for massive connectivity, integrated sensing and communication using AFDM [45, 46], and DFT-based modulation and demodulation schemes for backward compatibility with OFDM [47].

Low-complexity detection for AFDM has been an active area. Bemani *et al.* [48] proposed two detectors that exploit the sparsity of the effective channel matrix. Subsequent work has developed message passing methods [49, 50] and orthogonal AMP variants tailored to the AFDM channel structure. The detection problem is still an open area, and a substantial part of the present thesis contributes to it.

2.2 Index Modulation Techniques

2.2.1 The Index Modulation Concept

Index modulation conveys information through the selection of which resources are activated for transmission, in addition to or in place of the conventional modulation of those resources. The resources can be subcarriers, antennas, time slots, spreading codes, or other discrete entities. Mao *et al.* [18] provide a thorough survey of the field, and Basar *et al.* [19] cover the next-generation perspective.

IM offers two main advantages. It increases spectral efficiency without resorting to higher-order constellations, which would otherwise reduce minimum Euclidean distance and degrade BER. And by activating only a fraction of available resources at any given time, IM reduces energy consumption and inter-carrier interference.

The trade-offs are non-trivial. Inactive resources represent unused capacity, and the detector has to recover the activation pattern in addition to the symbols. In many scenarios, however, the gains outweigh the costs.

2.2.2 OFDM with Index Modulation and its Variants

OFDM-IM was proposed by Basar *et al.* [20] as the original combination of OFDM with index modulation. In OFDM-IM, the N subcarriers are divided into subblocks of length L, and within each subblock K out of L subcarriers are activated to carry QAM symbols. The activation pattern conveys $\lfloor \log_2 \binom{L}{K} \rfloor$ index bits.

The original scheme leaves $L-K$ subcarriers idle per subblock, which is inefficient. Several variants address this. OFDM with Generalized IM [51] allows the number of active subcarriers to vary across subblocks, increasing the pattern space and hence the index bits. OFDM with In-phase/Quadrature IM [52] uses the I and Q components of complex symbols as independent index-modulation domains.

Dual-mode OFDM-IM (DM-OFDM) [21, 53] addresses the idle-subcarrier problem differently. Instead of leaving subcarriers inactive, it modulates them with symbols from a second, distinguishable constellation. The index pattern selects which constellation modulates which subcarrier, and all subcarriers are active. The total spectral efficiency increases, and the minimum Euclidean distance properties can be tuned by choosing the two constellations appropriately.

Multi-mode OFDM-IM (MM-OFDM-IM) [22] generalizes the dual-mode approach by using more than two distinguishable constellations and full permutations of them across subcarriers. The number of index patterns grows factorially with the subblock length, substantially increasing spectral efficiency. Composite generalizations that jointly optimize mode assignment and subcarrier grouping have been proposed [54].

IM has also been integrated with multiple access schemes. Index modulation multiple access (IMMA) [55] extends non-orthogonal multiple access (NOMA)

principles using IM for resource activation. Spatial modulation [56, 57] and its enhanced [58] and quadrature [59] variants apply the index modulation principle to transmit antennas. Multi-UAV cooperative NOMA with IM has been studied for air-ground networks [60].

2.2.3 OTFS with Index Modulation

The extension of IM to OTFS has been investigated in several papers. Liang *et al.* [23] introduced OTFS-IM, where a subset of DD-grid points are activated to carry QAM symbols. The performance was shown to exceed that of OFDM-IM in high-mobility scenarios, owing to the underlying diversity advantage of OTFS.

OTFS with improved IM (OTFS-IIM) [24] sends each index bit twice for error protection, trading spectral efficiency for reliability. Dual-mode OTFS-IM (OTFS-DM-IM) [25] activates all DD-grid points and assigns one of two constellations to each, removing the resource-waste penalty of OTFS-IM. Multi-mode OTFS-IM [26] uses permutations of multiple distinguishable constellations, achieving spectral efficiencies well beyond what dual-mode schemes can support.

A parallel line of work has used delay-Doppler indexing in different ways. Francis *et al.* [61] studied diversity and PAPR enhancements through indexing. Zhao *et al.* [62] extended dual-mode IM to fractional Doppler channels. The relationship between OTFS-IM and OTFS with subcarrier number modulation is explored in [63].

Detectors for OTFS-IM range from ML and LLR-based methods to deep learning approaches [23, 24]. Deep learning detectors specifically for OFDM-IM and DM-OFDM [64, 65] have been adapted to the OTFS setting, often with favorable complexity-performance trade-offs at the cost of training overhead.

2.2.4 Current State of AFDM with Index Modulation

The literature on AFDM-IM is considerably less developed than the corresponding OTFS and OFDM literatures, and this is one of the gaps the present thesis addresses.

Zhu *et al.* [27] developed AFDM-IM along the lines of OFDM-IM, with subcarrier activation patterns conveying index bits while active subcarriers carry QAM symbols. Tao *et al.* [28] presented a similar scheme with different design choices. Both works show that AFDM-IM inherits the full delay-Doppler diversity of AFDM while gaining the spectral efficiency benefits of index modulation.

Beyond these basic schemes, additional variants have been proposed but the coverage is incomplete. Integrating IM with repetition coding (IMRC-AFDM) [66] improves diversity at the cost of spectral efficiency. AFDM with pre-chirp index modulation (AFDM-PIM) [67] embeds information in chirp parameters rather than subcarrier indices. CDD-AFDM-IM [68] combines cyclic delay diversity with IM for multi-antenna systems.

What was largely missing when the present work began were the dual-mode, multi-mode, generalized, and quadrature variants that have proven effective in the OFDM and OTFS contexts. The structural properties of the AFDM effective channel matrix, sparse and banded but distinct in its precise form from OFDM and OTFS, raise specific questions about how these schemes should be adapted to AFDM and how they should be detected. Addressing these questions is the principal subject of Chapters 5, 6, and 7.

2.3 Detection Algorithms

The detection problem for index-modulated waveforms is harder than the corresponding problem for conventional waveforms, because the receiver must recover not only the transmitted symbols but also the index patterns. Several families

of detectors have been developed, each with different complexity-performance trade-offs.

2.3.1 Classical and Linear Detectors

The optimal detector is maximum likelihood (ML), which jointly searches over all valid combinations of index patterns and symbols. ML is computationally infeasible for realistic frame sizes because its complexity is exponential in the number of subcarriers, but it serves as a useful performance benchmark.

Linear receivers based on zero-forcing or minimum mean-squared error (MMSE) equalization are the standard choice for practical systems. Both require an $N \times N$ matrix inversion at cost $O(N^3)$ per channel realization. They produce a soft estimate of the transmitted vector that is then processed further, by energy detection, LLR computation, or hard-decision decoding, to recover both symbols and index patterns. The main limitation of linear receivers in the index-modulation context is that they treat the transmit vector as an unstructured Gaussian quantity, ignoring both the discrete constellation structure and the sparsity induced by index modulation. The resulting gap to ML at high SNR is substantial.

2.3.2 Message Passing and Approximate Message Passing

Message passing methods exploit the sparse structure of the effective channel matrix to achieve near-ML performance at much lower cost. The detection problem is formulated as inference on a factor graph, with messages passed iteratively between symbol nodes and observation nodes.

Approximate message passing (AMP), introduced by Donoho *et al.* [29], provides a rigorous instantiation of this idea for i.i.d. Gaussian measurement matrices. The state evolution analysis [69] characterizes the per-iteration MSE in the large-system limit. AMP achieves near-optimal performance in the i.i.d. Gaussian setting at $O(N^2)$ cost per iteration, where N is the number of subcarriers, equivalently the

length of the DAFT-domain frame.

The difficulty with AMP is that the i.i.d. Gaussian assumption is rarely satisfied in practice. The effective channel matrices that arise in OFDM, OTFS, and AFDM are structured rather than random, and AMP is prone to divergence on such matrices. Vector AMP (VAMP), proposed by Rangan *et al.* [30], relaxes the requirement to right-orthogonal invariance, which is much easier to satisfy. VAMP comes with rigorous convergence guarantees [70] and works on a much broader class of channel matrices.

The standard VAMP algorithm requires a singular value decomposition of the channel matrix in its LMMSE step, again at $O(N^3)$ cost per channel realization. For slowly varying channels this cost is amortized over many transmissions, but for fast-fading channels it can dominate the receiver complexity. One of the contributions of this thesis, in Chapter 4, is a VAMP variant that uses preconditioned conjugate gradient iterations in place of the SVD, reducing per-iteration complexity from $O(N^3)$ to $O(N^2)$.

Generalized AMP (GAMP) [31] extends the AMP framework to arbitrary priors and likelihoods, including discrete priors and nonlinear measurement models. This makes GAMP particularly applicable to systems with finite constellations and to low-resolution ADC scenarios. Orthogonal AMP (OAMP) [71] provides another variant with attractive convergence properties for structured matrices.

Recent message passing work specifically for OTFS and AFDM includes the matched-filter-based MP algorithm [49], the multi-block UAMP detector [50], and the orthogonal-AMP-based detector for AFDM [44]. Yuan *et al.* [72] developed a unitary AMP detector for OTFS with strong empirical performance. Sharma *et al.* [73] proposed expectation propagation for OTFS with fractional Doppler shifts.

2.3.3 Variational Bayesian Methods

Variational Bayesian (VB) inference provides another route to tractable approximate posteriors. The exact posterior over the unknowns is intractable, so VB approximates it with a factorized variational distribution and optimizes the parameters of that distribution by minimizing the Kullback-Leibler divergence to the true posterior. This is equivalent to maximizing the evidence lower bound (ELBO), and the optimization can be carried out with closed-form coordinate ascent updates in many cases.

VB methods are particularly well-suited to problems with hierarchical structure, where the prior on the signal of interest itself depends on hyperparameters that have to be estimated. The Gaussian-Gamma sparse Bayesian learning model of Tipping [33] is the canonical example: the signal is given a Gaussian prior with precision parameters drawn from a Gamma hyperprior, and the precisions are inferred along with the signal. Large posterior precisions correspond to inferred zero entries, which is how the model enforces sparsity. The space-alternating variational estimation (SAVE) algorithm of Thomas and Slock [32] provides an efficient implementation of this idea, and it forms the basis for several detectors developed in the present thesis.

VB methods have been applied to MIMO-OTFS by Liu *et al.* [74], who developed joint channel estimation and signal detection algorithms. The mean-field factorization underlying VB is closely related to the message passing framework, and the boundary between the two is not always sharp.

For low-resolution ADC systems, VB inference is particularly attractive because the truncated-Gaussian likelihood induced by quantization can be incorporated directly into the variational updates. Bussgang-based linear receivers [75] are the traditional approach but degrade significantly at very low resolutions. Nguyen *et al.* [76] developed VB methods for few-bit massive MIMO with significantly better performance than the Bussgang baselines.

2.4 Low-Resolution ADC Receivers

The shift towards low-resolution ADCs in wireless receivers is motivated by power efficiency. The Walden figure of merit [77] shows that ADC power consumption scales approximately as 2^b for b-bit resolution, so reducing from 12 bits to 3 or 4 bits delivers substantial power savings. This becomes critical in massive MIMO and millimeter-wave systems, where hundreds or thousands of RF chains are present and total ADC power can otherwise dominate the receiver power budget [34, 35].

The challenge is that quantization is a nonlinear operation, and conventional linear receiver designs do not accommodate this nonlinearity effectively. The Bussgang decomposition [36] provides a useful linear approximation by representing the quantizer output as a scaled version of the input plus an uncorrelated distortion term. Linear receivers such as B-MMSE [75] exploit this decomposition and work reasonably well at moderate resolutions, around 5 or 6 bits and above. At 1-bit and 2-bit resolutions the Bussgang approach exhibits clear limitations, and at very low SNR even high-resolution scenarios become difficult.

Several papers have developed channel estimation and detection methods specifically for one-bit and few-bit ADCs. Li *et al.* [75] analyzed channel estimation and detection performance for one-bit massive MIMO. Mo *et al.* [78] developed iterative algorithms for one-bit channel estimation. Spatial Sigma-Delta architectures [79] use noise-shaping to mitigate quantization effects in the spatial domain.

For AFDM and OTFS systems, the literature on low-resolution ADCs is sparse. Mehrotra *et al.* [80] developed sparse channel estimation for MIMO OTFS and OTSM systems with finite-resolution ADCs, but detection algorithms specifically tailored to quantized AFDM had not been developed when the present work began. Chapter 4 of this thesis addresses this gap with a VB detector that handles the truncated-Gaussian likelihood directly.

2.5 Background on the DAFT and AFDM System Model

A brief review of the AFDM system model is given here, since most of the subsequent chapters build on it.

The discrete affine Fourier transform (DAFT) is a unitary transformation parameterized by two chirp parameters $c_1, c_2 \in \mathbb{R}$. For a length-N signal $\boldsymbol{s}$, the DAFT is

$$S[m] = \frac{1}{\sqrt{N}} e^{-j2\pi c_2 m^2} \sum_{n=0}^{N-1} e^{-j2\pi(mn/N + c_1 n^2)} s[n]. \tag{2.1}$$

In matrix form, $\boldsymbol{S} = \boldsymbol{A}\boldsymbol{s} = \boldsymbol{\Lambda}_{c_2} \boldsymbol{F} \boldsymbol{\Lambda}_{c_1} \boldsymbol{s}$, where $\boldsymbol{F}$ is the DFT matrix and $\boldsymbol{\Lambda}_c = \mathrm{diag}(e^{-j2\pi c n^2})$ is a diagonal chirp matrix. The DAFT is unitary and reduces to the DFT when $c_1 = c_2 = 0$.

AFDM modulates the DAFT-domain symbol vector $\boldsymbol{x}$ as $\boldsymbol{s} = \boldsymbol{A}^H \boldsymbol{x}$. A chirp-periodic prefix of length $L_{cp} \geq l_{\max}$ is appended; this prefix has the form $s[n] = s[N + n] e^{-j2\pi c_1 (N^2 + 2Nn)}$, which preserves the quadratic-phase structure of the DAFT signal through the multipath channel. Here $l_{\max} = \lceil \tau_{\max} / T_s \rceil$ is the maximum path delay expressed in integer samples , where $\lceil \cdot \rceil$ represents the ceiling function, with $\tau_{\max}$ the maximum channel delay spread and T_s the sampling interval. The condition $L_{\mathrm{cp}} \geq l_{\max}$ ensures that the chirp-periodic prefix absorbs the entire delay spread, so that the linear convolution with the channel is rendered equivalent to a circular convolution for the DAFT operation. In practice L_{cp} is set to $l_{\max}$ for a known delay profile, or to the delay budget of the deployment scenario when the profile is unknown, the overhead L_{cp}/N being the quantity traded against robustness.

After the doubly dispersive channel and CPP removal, the received signal in the DAFT domain is

$$\boldsymbol{y} = \boldsymbol{H}_{\mathrm{eff}} \boldsymbol{x} + \tilde{\boldsymbol{w}}, \tag{2.2}$$

where $\boldsymbol{H}_{\mathrm{eff}} = \sum_{i=1}^{P} h_i \boldsymbol{A} \boldsymbol{\Gamma}_{\mathrm{CPP},i} \boldsymbol{\Delta}_{f_i} \boldsymbol{\Pi}^{l_i} \boldsymbol{A}^H$ collects the contributions of all P propa-

gation paths, $\tilde{\boldsymbol{w}}$ is the DAFT-domain noise, which is still circular complex Gaussian by unitarity of $\boldsymbol{A}$, h_i is the complex gain of the ith path, $\boldsymbol{\Gamma}_{\mathrm{CPP},i}$ is the diagonal phase-correction matrix introduced by the chirp-periodic prefix for that path, $\boldsymbol{\Delta}_{f_i}$ is the diagonal Doppler-shift matrix, $\boldsymbol{\Pi}^{l_i}$ is the l_i-fold cyclic delay permutation matrix, and $\boldsymbol{A}$ represents the DAFT matrix.

The structure of $\boldsymbol{H}_{\mathrm{eff}}$ is what makes AFDM tractable. For integer Doppler shifts and parameter choices $c_1 = (2\alpha_{\max}+1)/(2N)$ with c_2 irrational or small-rational, each path i contributes a non-zero entry to row p of $\boldsymbol{H}_{\mathrm{eff}}$ at column $[p+\mathrm{loc}_i]_N$ only, where loc_i is a path-specific location offset. The paths separate completely in the DAFT domain. For fractional Doppler shifts, each path contributes non-zeros over $2\xi_\nu+1$ adjacent columns, but the separation property still holds approximately.

The diversity order of AFDM under ML detection is P, equal to the number of paths, when the parameters c_1, c_2 are chosen correctly. This is shown in [17] through a pairwise error probability analysis. The key requirement is $\mathrm{loc}_i \neq \mathrm{loc}_j$ for all $i \neq j$, which the choice of c_1 ensures, together with the constraint $2\alpha_{\max} + l_{\max} + 2\alpha_{\max} l_{\max} < N$ on the channel-frame relationship.

This structural property, sparse banded $\boldsymbol{H}_{\mathrm{eff}}$ with completely or nearly separated path contributions, underlies all the detector designs developed in Chapters 4 through 7. The path separation enables multi-path Bayesian estimators (Chapter 4), the banded sparsity enables low-complexity VAMP iterations (Chapter 4), and the discrete constellation structure of the transmit vector combined with the structured sparsity of index modulation enables sparse Bayesian and variational detectors (Chapters 5 through 7).

2.6 Gaps Addressed in This Thesis

For AFDM, the corresponding literature is less developed. AFDM-IM in its basic form has been studied [27, 28], but the more sophisticated index modulation variants, namely dual-mode, multi-mode, generalized, and quadrature, have not

been carried over from the OFDM and OTFS contexts in any systematic way. Detection algorithms tailored to the AFDM channel structure, particularly those that exploit complete delay-Doppler path separation, are not as well developed as the corresponding methods for OTFS. The practical issue of low-resolution ADCs, which has been studied for massive MIMO and to some extent for OFDM, has barely been touched in the AFDM context.

The remainder of this thesis takes up these gaps. Chapter 4 develops three Bayesian and message passing detectors for AFDM that address different aspects of the detection problem: a low-complexity VAMP variant that replaces the SVD step with preconditioned conjugate gradient iterations, a multi-path interference cancellation scheme that exploits the delay-Doppler path separation of AFDM, and a variational Bayesian detector that handles the truncated-Gaussian likelihood induced by low-resolution ADCs. Chapters 5 through 7 develop generalized, quadrature, dual-mode, and multi-mode index modulation schemes for AFDM, each with detectors tuned to its particular structure. Chapter 3 provides foundation work in the OTFS setting on which several of the AFDM chapters build. The detailed technical contributions are presented chapter by chapter in what follows.

Chapter 3

OTFS Based Index Modulation

This chapter develops two index modulation schemes built on OTFS modulation, which we use as the foundation before moving to AFDM in the chapters that follow. We first establish the OTFS signal model, its delay-Doppler input-output relation, and the MIMO-OTFS extension required for the spatial domain contribution. We then propose Enhanced Spatial Modulation based OTFS (ESM-OTFS), which combines ESM with OTFS to improve spectral efficiency in high mobility MIMO settings, and develop an MMSE based linear detector and a Variational Bayesian Inference (VBI) based sparse detector for it. We then propose OTFS with Generalized Dual-Mode Index Modulation (OTFS-GDM-IM), which removes the fixed sub-block partitioning of dual-mode index modulation and allows a variable number of grid points to be modulated by each constellation alphabet. Maximum likelihood (ML) and log-likelihood ratio (LLR) detectors are derived for OTFS-GDM-IM. Spectral efficiency and computational complexity are derived alongside each proposed waveform, and simulation results for both schemes are presented at the end of the chapter.

3.1 OTFS System Model

3.1.1 OTFS Modulation and Demodulation

OTFS modulation [5,6] is a way of transmitting information symbols that is robust to Doppler shift. It works by multiplexing the data symbols in the delay-Doppler (DD) domain, which is another way of expressing the signal that is invariant to Doppler shift. This makes OTFS ideal for high-mobility applications. Let $\{u[l,k], l = 0,1,\ldots,M-1, k = 0,1,\ldots,N-1\}$ be a two dimensional information signal in the DD domain where M denotes the number of subcarriers and N denotes the number of OFDM symbols or time slots. The time-frequency (TF) domain signal $U[m,n]$ is obtained from $u[l,k]$ through the inverse symplectic finite Fourier transform (ISFFT) as

$$U[m,n] = \frac{1}{\sqrt{MN}} \sum_{l=0}^{M-1} \sum_{k=0}^{N-1} u[l,k]\, e^{j2\pi\left(\frac{nk}{N} - \frac{ml}{M}\right)}. \tag{3.1}$$

Using the Heisenberg transform along with a transmitter side pulse shaping signal $p_{tx}(t)$, $U[m,n]$ is converted to a time domain (TD) signal $s(t)$

$$s(t) = \sum_{m=0}^{M-1} \sum_{n=0}^{N-1} U[m,n]\, p_{tx}(t - mT)\, e^{j2\pi n\Delta f(t-mT)}, \tag{3.2}$$

where Δf and T represent the subcarrier spacing and the OFDM symbol period respectively, with $\Delta f = 1/T$.

At the receiver, the received signal $r(t)$ is matched with the receiver side pulse shaping signal $p_{rx}(t)$ and is converted to the TF domain using the Wigner transform, and the resulting cross-ambiguity $\Lambda_{p_{rx},r}(t,f)$ is given as

$$\Lambda_{p_{rx},r}(t,f) = \int r(t')\, p_{rx}(t'-t)\, e^{j2\pi f(t'-t)}\, dt'. \tag{3.3}$$

The resultant signal is sampled with subcarrier spacing Δf and frame duration T.

The received TF domain signal is given as

$$V[m,n] = \Lambda_{p_{rx},r}(t,f)\Big|_{t=nT,\, f=m\Delta f}. \tag{3.4}$$

The DD domain signal $v[l,k]$ is obtained from $V[m,n]$ by applying the symplectic finite Fourier transform (SFFT) and is given as

$$v[l,k] = \frac{1}{\sqrt{MN}} \sum_{m=0}^{M-1} \sum_{n=0}^{N-1} V[m,n]\, e^{-j2\pi\left(\frac{nk}{N} - \frac{ml}{M}\right)}. \tag{3.5}$$

3.1.2 Delay-Doppler Channel and Input-Output Relation

Consider a DD domain channel with P channel taps, each with a delay of τ_i, a Doppler shift of ν_i, and a fading channel gain of h_i [7]. The channel impulse response in the DD domain can be represented as

$$h(\tau,\nu) = \sum_{i=1}^{P} h_i\, \delta(\tau - \tau_i)\, \delta(\nu - \nu_i), \tag{3.6}$$

where $\delta(\cdot)$ denotes the Dirac delta function. The integer delay and Doppler indices of the ith path are obtained as

$$l_i = \tau_i M \Delta f, \qquad \alpha_i = \nu_i N T. \tag{3.7}$$

Given the TD input signal $s(t)$, the received signal is

$$r(t) = \int_{\nu}\int_{\tau} h(\tau,\nu)\, s(t-\tau)\, e^{j2\pi\nu(t-\tau)}\, d\tau\, d\nu + w(t), \tag{3.8}$$

where $w(t)$ is the additive white Gaussian noise in the TD. Substituting the DD impulse response and discretizing at the symbol rate yields

$$r[q] = \sum_{i=1}^{P} h_i\, s[q-l_i]\, e^{j\frac{2\pi}{N}\alpha_i(q-l_i)} + w[q], \tag{3.9}$$

for $q = 0, 1, \ldots, MN-1$.

The vectorized TD input-output relation can be written as

$$\mathbf{r} = \left(\sum_{i=1}^{P} h_i \, \mathbf{\Pi}^{l_i} \, \mathbf{\Delta}^{\alpha_i} \right) \mathbf{s} + \mathbf{w} = \breve{\mathbf{H}} \mathbf{s} + \mathbf{w}, \tag{3.10}$$

where $\mathbf{\Pi}$ is the cyclic forward-shift permutation matrix of dimension $MN \times MN$

$$\mathbf{\Pi} = \begin{bmatrix} 0 & \cdots & 0 & 1 \\ 1 & \ddots & 0 & 0 \\ \vdots & \ddots & \ddots & \vdots \\ 0 & \cdots & 1 & 0 \end{bmatrix}, \tag{3.11}$$

$\mathbf{\Delta}$ is the diagonal Doppler matrix with entries $\mathbf{\Delta} = \mathrm{diag}\{e^{j2\pi p/(MN)}\}_{p=0}^{MN-1}$, and $\breve{\mathbf{H}}$ is the TD channel matrix of dimension $MN \times MN$, with l_i and α_i assumed to be integers without loss of generality.

At the receiver, the received signal vector $\mathbf{r}$ is converted to the DD domain and the input-output relation in the DD domain [11] is given as

$$\mathbf{y} = \mathbf{H}_{\text{eff}} \mathbf{x} + \tilde{\mathbf{w}}, \tag{3.12}$$

where $\mathbf{x} \in \mathbb{C}^{MN \times 1}$ is the DD domain transmit vector obtained by vectorizing $u[l,k]$, $\mathbf{y} \in \mathbb{C}^{MN \times 1}$ is the corresponding receive vector, and $\tilde{\mathbf{w}}$ is the noise vector in the DD domain. With rectangular pulse shaping at the transmitter and receiver, the effective DD domain channel matrix is given as $\mathbf{H}_{\text{eff}} = (\mathbf{F}_N \otimes \mathbf{I}_M) \breve{\mathbf{H}} (\mathbf{F}_N^H \otimes \mathbf{I}_M)$, where $\mathbf{F}_N$ is the N-point DFT matrix, $\mathbf{F}_N^H$ is its inverse, $\mathbf{I}_M$ is the $M \times M$ identity matrix, and $\otimes$ denotes the Kronecker product.

3.1.3 MIMO-OTFS Signal Representation

We extend the single antenna OTFS model to a MIMO setting [9] with N_T transmit antennas and N_R receive antennas, since the ESM-OTFS scheme of Section 3.2 is equipped with N_T transmit antennas and N_R receive antennas. The transmit symbol matrix of the MIMO-OTFS frame is $\mathbf{X} \in \mathbb{C}^{MN \times N_T}$, where the ith column $\mathbf{x}_i$ is the DD domain vector transmitted from the ith transmit antenna. The TD signal transmitted from the ith antenna $\mathbf{s}_i$ is derived from $\mathbf{x}_i$ by passing it through the ISFFT unit and OFDM modulator, which simulates the Heisenberg transform, and is given as

$$\mathbf{s}_i = (\mathbf{F}_N^H \otimes \mathbf{I}_M)\mathbf{x}_i, \tag{3.13}$$

where $\mathbf{s}_i$ is the $MN \times 1$ dimensional column vector. The TD signal $\mathbf{s}_i$ is transmitted from the ith transmit antenna and travels through the multipath wireless channel. The received signal at the jth receive antenna from the ith transmit antenna passes through SFFT and OFDM demodulator, which simulates the Wigner transform. The DD domain signal received at the jth receive antenna is given as

$$\mathbf{y}_j = \sum_{i=1}^{N_T} \mathbf{H}_{\text{eff},j,i}\, \mathbf{x}_i + \mathbf{w}_j, \tag{3.14}$$

where $\mathbf{H}_{\text{eff},j,i} \in \mathbb{C}^{MN \times MN}$ is the effective DD domain channel from the ith transmit antenna to the jth receive antenna. The received signal in the DD domain considering all the receive antennas is

$$\mathbf{y} = \mathbf{H}_{\text{eff}}\mathbf{x} + \mathbf{w}, \tag{3.15}$$

where $\mathbf{y} = [\mathbf{y}_1^T, \ldots, \mathbf{y}_{N_R}^T]^T \in \mathbb{C}^{N_R MN \times 1}$, $\mathbf{x} = [\mathbf{x}_1^T, \ldots, \mathbf{x}_{N_T}^T]^T \in \mathbb{C}^{N_T MN \times 1}$, and $\mathbf{w}$ is the corresponding effective noise vector. The effective MIMO DD channel matrix

of dimension $N_R MN \times N_T MN$ is

$$\mathbf{H}_{\text{eff}} = \begin{bmatrix} \mathbf{H}_{\text{eff},1,1} & \mathbf{H}_{\text{eff},1,2} & \cdots & \mathbf{H}_{\text{eff},1,N_T} \\ \mathbf{H}_{\text{eff},2,1} & \mathbf{H}_{\text{eff},2,2} & \cdots & \mathbf{H}_{\text{eff},2,N_T} \\ \vdots & \vdots & \ddots & \vdots \\ \mathbf{H}_{\text{eff},N_R,1} & \mathbf{H}_{\text{eff},N_R,2} & \cdots & \mathbf{H}_{\text{eff},N_R,N_T} \end{bmatrix}. \tag{3.16}$$

3.2 Enhanced Spatial Modulation Based OTFS

3.2.1 Enhanced Spatial Modulation

Spatial modulation (SM) [56, 57] is a wireless communication technique based on Multiple Input Multiple Output (MIMO) that uses the transmit antenna index for transmitting information symbols. SM involves the activation of a single transmit antenna at any given moment in time, and that selected antenna is used to transmit a signal from a chosen constellation. If N_T is the number of transmit antennas and $s_a = 2^{n_a}$ is the size of the signal constellation, the number of bits transmitted in SM is $n_a + \log_2(N_T)$.

Enhanced spatial modulation [58] improves the efficiency and robustness of SM by transmitting different symbols from different constellations depending on the number of active antennas. This is done by first transmitting symbols from a primary constellation during single transmit antenna activation, just like conventional SM. When two transmit antennas are enabled, symbols are transmitted from a secondary constellation. The size of the secondary constellation is taken as half of the primary constellation so that the same number of information bits are transmitted during single antenna activation and double antenna activation periods. This allows for a higher diversity gain as the signal is transmitted from two different antennas, which makes it more robust to interference. In order to maximize the minimum Euclidean distance between transmitted signal vectors,

secondary constellations are created via geometric interpolation. This ensures that the symbols in the secondary constellations are as far apart as possible, which makes it more difficult for the receiver to make errors.

In conventional SM, the number of information bits transmitted depends on the number of transmit antennas and the size of the symbol constellation used for modulation. In ESM, it is decided by the antenna and constellation symbol combinations. An illustration of the ESM system with two transmit antennas, QPSK as the primary constellation and BPSK as the secondary constellation is depicted in Table 3.1. Here the number of transmitted bits or bits per channel use (BPCU) is four. QPSK $= \pm 1 \pm j$, and BPSK0 and BPSK1 are respectively given by BPSK0 $= \pm 1$ and BPSK1 $= \pm j$. The first two combinations C1 and C2 appear as transmission from one of the antennas and convey one of the symbols from the QPSK constellation. The last two combinations C3 and C4 correspond to transmissions of symbols from the secondary constellations BPSK0 or BPSK1 coming out of both antennas.

Table 3.1: ESM, $N_T = 2$ transmit antennas, four BPCU

	TX1	**TX2**
C1	QPSK	0
C2	0	QPSK
C3	BPSK0	BPSK0
C4	BPSK1	BPSK1

3.2.2 ESM-OTFS Transmitter and Frame Structure

The system model of the proposed ESM-OTFS is shown in Fig. 3.1. The ESM-OTFS system is equipped with N_T transmit antennas and N_R receive antennas. A random bit sequence $\mathbf{b} = [b_0, b_1, \ldots, b_{B_{\text{tot}}-1}]$ of an ESM-OTFS frame in the DD domain enters the ESM-OTFS system, where $B_{\text{tot}} = MN \log_2(\mathbb{C}_{\text{ESM}})$ and $\mathbb{C}_{\text{ESM}}$ is the size of the ESM constellation. The mapping rule of ESM modulation is

given in Table 3.2. For each $\log_2(\mathbb{C}_{\text{ESM}})$ incoming bits, an ESM transmit vector is selected as per the presented mapping rule. For each of the MN time slots of an ESM-OTFS frame, a constellation symbol is assigned to each of the N_T transmit antennas. These MN symbols enter the OTFS Block Creator unit of the corresponding transmit antenna and form the transmit DD domain vector for the respective antenna.

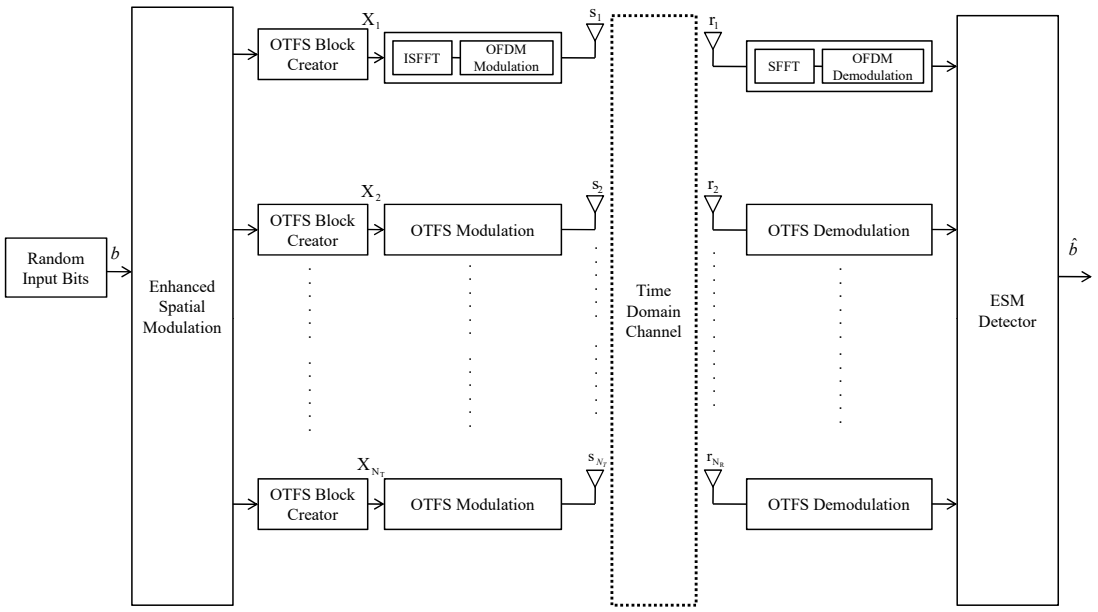


Figure 3.1: Block diagram of the ESM-OTFS system

The transmission rate of ESM-OTFS can be stated as $R_{\text{ESM-OTFS}} = MN \times \log_2(\mathbb{C}_{\text{ESM}})$, whereas under the same setup SM-OTFS has a transmission rate of $R_{\text{SM-OTFS}} = MN \log_2(s_a)$, where s_a is the order of the modulation used. Since the size of the ESM constellation formed by the combination of transmit antennas and primary and secondary constellation symbols is higher than the size of the modulation order used in SM, the transmission rate of ESM-OTFS is much better than that of SM-OTFS under the same MIMO environment. The dimension of the

Table 3.2: ESM mapping rule for $N_T = 2$ and QPSK as primary constellation

$\mathbb{C}_{\text{ESM}}$ bits	Transmit vector
0000	$[0+0j, -1+1j]$
0001	$[0+0j, -1-1j]$
0010	$[0+0j, +1+1j]$
0011	$[0+0j, +1-1j]$
0100	$[-1+1j, 0+0j]$
0101	$[-1-1j, 0+0j]$
0110	$[+1+1j, 0+0j]$
0111	$[+1-1j, 0+0j]$
1000	$[-1+0j, -1+0j]$
1001	$[-1+0j, +1+0j]$
1010	$[+1+0j, -1+0j]$
1011	$[+1+0j, +1+0j]$
1100	$[0-1j, 0-1j]$
1101	$[0-1j, 0+1j]$
1110	$[0+1j, 0-1j]$
1111	$[0+1j, 0+1j]$

data transmit matrix of an ESM-OTFS frame is $MN \times N_T$ and is given as

$$\mathbf{X}_{\text{ESM}} = \begin{bmatrix} \mathbf{x}_{0,0}^{1} & \cdots & \mathbf{x}_{0,0}^{i} & \cdots & \mathbf{x}_{0,0}^{N_T} \\ \mathbf{x}_{0,1}^{1} & \cdots & \mathbf{x}_{0,1}^{i} & \cdots & \mathbf{x}_{0,1}^{N_T} \\ \vdots & \ddots & \vdots & \ddots & \vdots \\ \mathbf{x}_{l,k}^{1} & \cdots & \mathbf{x}_{l,k}^{i} & \cdots & \mathbf{x}_{l,k}^{N_T} \\ \vdots & \ddots & \vdots & \ddots & \vdots \\ \mathbf{x}_{M-1,N-1}^{1} & \cdots & \mathbf{x}_{M-1,N-1}^{i} & \cdots & \mathbf{x}_{M-1,N-1}^{N_T} \end{bmatrix}. \tag{3.17}$$

$\mathbf{X}_i$ is the DD domain information matrix of dimension $M \times N$ transmitted from the ith transmit antenna and is formed by collecting all the elements of the ith column of $\mathbf{X}_{\text{ESM}}$. The received DD domain signal vector follows the MIMO-OTFS input-output model of (3.15).

3.2.3 MMSE Detector for ESM-OTFS

In order to bring down the complexity of detection, a detector combining MMSE equalization and minimum Euclidean distance detection is proposed for the detection of ESM-OTFS. First, an estimate of the transmitted signal $\hat{\mathbf{x}}_{\text{ESM}}^{\text{MMSE}}$ is obtained using an MMSE equalizer. The MMSE equalization is given as

$$\hat{\mathbf{x}}_{\text{ESM}}^{\text{MMSE}} = \left(\mathbf{H}_{\text{eff}}^{H} \mathbf{H}_{\text{eff}} + \frac{\mathbf{I}_{N_T MN}}{\rho_{\text{snr}}} \right)^{-1} \mathbf{H}_{\text{eff}}^{H} \mathbf{y}, \tag{3.18}$$

where $\mathbf{I}_{N_T MN}$ is the identity matrix of order $N_T MN \times N_T MN$ and ρ_{snr} is the average SNR in the DD domain. Now a minimum Euclidean distance detector is applied on each row of $\hat{\mathbf{X}}_{\text{ESM}}^{\text{MMSE}}$ against all the possible combinations of ESM constellation vectors $\mathcal{C}_{\text{ESM}}$. This can be formulated as

$$\left\{ \hat{\mathbf{X}}_{\text{ESM}}^{\eta} \right\} = \arg \min_{\mathbf{C}_{\text{ESM}} \in \mathcal{C}_{\text{ESM}}} \left| \hat{\mathbf{X}}_{\text{ESM}}^{\text{MMSE}}(\eta) - \mathbf{C}_{\text{ESM}} \right|^2, \quad 1 \leq \eta \leq MN, \tag{3.19}$$

where $\hat{\mathbf{X}}_{\text{ESM}}^{\text{MMSE}}(\eta)$ is the ηth row of the matrix $\hat{\mathbf{X}}_{\text{ESM}}^{\text{MMSE}}$. Then the ESM constellation vector with the minimum Euclidean distance is taken as the detected ESM-OTFS transmit vector for each time slot of the ESM-OTFS frame. Now an estimate of the original transmitted bits $\hat{\mathbf{b}}$ can be recovered by comparing each row of $\hat{\mathbf{X}}_{\text{ESM}}$ using the look-up table shown in Table 3.2. The steps involved in the detection of ESM-OTFS using the MMSE detector are summarized in Algorithm 3.1.

Algorithm 3.1 MMSE Detection of ESM-OTFS

Require: $\mathbf{y}$, $\mathbf{H}_{\text{eff}}$, $\mathcal{C}_{\text{ESM}}$
1: Compute $\hat{\mathbf{X}}_{\text{ESM}}^{\text{MMSE}}$ using (3.18)
2: Estimate the transmitted ESM vectors using (3.19) and form $\hat{\mathbf{X}}_{\text{ESM}}$
3: Retrieve the transmitted bits using the ESM mapping rule
4: **return** estimated bit sequence $\hat{\mathbf{b}}$

3.2.4 Variational Bayesian Inference Based Detector for ESM-OTFS

Since the computational complexity of the maximum likelihood detector increases exponentially with the number of transmit and receive antennas, we propose a detection algorithm based on the sparsity of the ESM-OTFS transmit frame. In ESM-OTFS, only one or two transmit antennas radiate at the same time and the others remain silent. This results in the formation of a data transmit matrix with most of the entries equal to zero, making the matrix sparse. The key idea behind the proposed detector is the sparse signal estimation of the received signal using Variational Bayesian Learning [32,33]. The problem of ESM-OTFS signal detection can be restated as

$$\mathbf{y} = \mathbf{H}_{\text{eff}}\mathbf{x} + \mathbf{w}, \tag{3.20}$$

where $\mathbf{x}$ and $\mathbf{y}$ are the transmit and receive signals of dimensions $N_T MN \times 1$ and $N_R MN \times 1$ respectively in the DD domain, $\mathbf{H}_{\text{eff}}$ is the effective DD domain channel matrix of dimension $N_R MN \times N_T MN$, and $\mathbf{w}$ is the Gaussian distributed white noise signal with zero mean and variance σ^2. The noise precision used in the VBI

updates is $\gamma_w = 1/\sigma^2$.

We assume a two-layer hierarchical prior for the transmit data signal $\mathbf{x}$ so that it motivates the sparsity property of $\mathbf{x}$. It is assumed that $\mathbf{x}$ follows a Gaussian distribution parameterized by $\boldsymbol{\alpha} = [\alpha_1, \alpha_2, \ldots, \alpha_{N_T MN}]$, where α_i is the inverse variance parameter of x_i and $\mathbf{x}$ is given as

$$p(\mathbf{x} \mid \boldsymbol{\alpha}) = \prod_{i=1}^{N_T MN} p(x_i \mid \alpha_i) = \prod_{i=1}^{N_T MN} \mathcal{N}(0, \alpha_i^{-1}). \tag{3.21}$$

A Gamma prior distribution is assumed for $\boldsymbol{\alpha}$

$$p(\boldsymbol{\alpha}) = \prod_{i=1}^{N_T MN} \Gamma^{-1}(a)\, b^a\, \alpha_i^{a-1}\, e^{-b\alpha_i}. \tag{3.22}$$

It is presumed that the noise precision γ_w is already known and that full DD domain channel state information is accessible at the receiver. The likelihood distribution of the received signal $\mathbf{y}$ is given as

$$p(\mathbf{y} \mid \mathbf{x}) = (2\pi)^{-N_R MN/2} \gamma_w^{N_R MN/2}\, e^{-\gamma_w \|\mathbf{y} - \mathbf{H}_{\text{eff}}\mathbf{x}\|^2/2}. \tag{3.23}$$

The estimation of the posterior distribution of the received signal is intractable. To address this, the variational Bayesian technique is applied, and the posterior distribution $p(\mathbf{x}, \boldsymbol{\alpha} \mid \mathbf{y})$ is approximated by a variational distribution

$$q(\mathbf{x}, \boldsymbol{\alpha}) = \prod_{i=1}^{N_T MN} q_{x_i}(x_i) \prod_{i=1}^{N_T MN} q_{\alpha_i}(\alpha_i). \tag{3.24}$$

The VBI technique calculates the factors of $q(\mathbf{x}, \boldsymbol{\alpha})$ by minimizing the Kullback-Leibler (KL) distance between the variational distribution and the true posterior. Minimization of the KL distance is equivalent to maximizing the evidence lower bound (ELBO), which results in

$$\ln q_i(\theta_i) = \langle \ln p(\mathbf{y}, \theta) \rangle_{k \neq i} + c_i, \tag{3.25}$$

where $\theta = \{\mathbf{x}, \boldsymbol{\alpha}\}$, θ_i denotes each scalar in θ, and $\langle\cdot\rangle_{k\neq i}$ denotes the expectation across the distributions q_k for all $k \neq i$. The joint probability distribution $p(\mathbf{y},\theta)$ can be represented as $p(\mathbf{y},\theta) = p(\mathbf{y} \mid \mathbf{x}, \boldsymbol{\alpha})\, p(\mathbf{x} \mid \boldsymbol{\alpha})\, p(\boldsymbol{\alpha})$. Expanding $\ln p(\mathbf{y},\theta)$ yields

$$\begin{aligned}\ln p(\mathbf{y},\theta) = {} & \tfrac{N_R MN}{2} \ln \gamma_w - \tfrac{\gamma_w}{2} \|\mathbf{y} - \mathbf{H}_{\text{eff}}\mathbf{x}\|^2 \\ & + \sum_{i=1}^{N_T MN} \left(\tfrac{1}{2} \ln \alpha_i - \tfrac{\alpha_i}{2} x_i^2 \right) \\ & + \sum_{i=1}^{N_T MN} \left((a-1) \ln \alpha_i + a \ln b - b\alpha_i \right) + \text{const.} \end{aligned} \tag{3.26}$$

Now using (3.25) and (3.26), we find the update expressions for $\ln q_{x_i}(x_i)$ and $\ln q_{\alpha_i}(\alpha_i)$. Applying (3.25) to x_i yields

$$\begin{aligned}\ln q_{x_i}(x_i) = {} & -\tfrac{\gamma_w}{2} \Big\{ \langle \|\mathbf{y} - \mathbf{H}_{\text{eff},\bar{i}} \mathbf{x}_{\bar{i}}\|^2 \rangle - (\mathbf{y} - \mathbf{H}_{\text{eff},\bar{i}} \langle \mathbf{x}_{\bar{i}} \rangle)^H \mathbf{H}_{\text{eff},i}\, x_i \\ & - x_i\, \mathbf{H}_{\text{eff},i}^H (\mathbf{y} - \mathbf{H}_{\text{eff},\bar{i}} \langle \mathbf{x}_{\bar{i}} \rangle) + \|\mathbf{H}_{\text{eff},i}\|^2 x_i^2 \Big\} \\ & - \tfrac{\langle \alpha_i \rangle}{2} x_i^2 + c_{x_i}, \end{aligned} \tag{3.27}$$

where $\mathbf{H}_{\text{eff}}\mathbf{x} = \mathbf{H}_{\text{eff},i} x_i + \mathbf{H}_{\text{eff},\bar{i}} \mathbf{x}_{\bar{i}}$, $\mathbf{H}_{\text{eff},i}$ denotes the ith column of $\mathbf{H}_{\text{eff}}$, $\mathbf{H}_{\text{eff},\bar{i}}$ is formed by removing the ith column of $\mathbf{H}_{\text{eff}}$, x_i is the ith element of $\mathbf{x}$, and $\mathbf{x}_{\bar{i}}$ is the vector formed by removing the ith element of $\mathbf{x}$. The expansion of $\ln q_{x_i}(x_i)$ is quadratic in x_i and can therefore be expressed as a Gaussian distributed random variable. The mean and variance of the subsequent Gaussian distribution are

$$\sigma_i^2 = \frac{1}{\gamma_w \|\mathbf{H}_{\text{eff},i}\|^2 + \langle \alpha_i \rangle}, \qquad \langle x_i \rangle = \mu_i = \sigma_i^2\, \mathbf{H}_{\text{eff},i}^H (\mathbf{y} - \mathbf{H}_{\text{eff},\bar{i}} \langle \mathbf{x}_{\bar{i}} \rangle) \gamma_w, \tag{3.28}$$

where μ_i is the point estimate of the ith element of the transmitted signal $\mathbf{x}$. In a similar way $\ln q_{\alpha_i}(\alpha_i)$ can be expressed as

$$\ln q_{\alpha_i}(\alpha_i) = (a - 1 + \tfrac{1}{2}) \ln \alpha_i - \alpha_i \left(\tfrac{\langle x_i^2 \rangle}{2} + b \right) + c_{\alpha_i}, \tag{3.29}$$

which is the log of a Gamma distribution. The mean of the resulting Gamma distribution is

$$\langle \alpha_i \rangle = \frac{a + \frac{1}{2}}{\frac{\langle x_i^2 \rangle}{2} + b}, \qquad \langle x_i^2 \rangle = \mu_i^2 + \sigma_i^2. \tag{3.30}$$

The equalized version of the transmitted signal matrix $\hat{\mathbf{X}}_{\text{ESM}}^{\text{VBI}}$ in the DD domain is formed by collecting all the point estimates μ_i for $i = 1, 2, \ldots, N_T MN$. The minimum Euclidean distance detector is then applied on each row of $\hat{\mathbf{X}}_{\text{ESM}}^{\text{VBI}}$ using (3.19) to obtain $\hat{\mathbf{X}}_{\text{ESM}}$. Each row of $\hat{\mathbf{X}}_{\text{ESM}}$ is decoded using the ESM mapping rule shown in Table 3.2 to retrieve an estimate of the original transmitted bits. The steps involved in the detection of ESM-OTFS using the VBI detector are summarized in Algorithm 3.2.

Algorithm 3.2 VBI Based ESM-OTFS Detection

Require: $\mathbf{y}$, $\mathbf{H}_{\text{eff}}$, $\mathcal{C}_{\text{ESM}}$, γ_w
1: Initialize $a, b \sim 10^{-10}$, $\alpha_i^0 = a/b$, $\sigma_i^{2,0} = 1/(\gamma_w \|\mathbf{H}_{\text{eff},i}\|^2 + \alpha_i^0)$, $\mathbf{x}^0 = \mathbf{0}$
2: **for** iteration $\ell = 0, 1, 2, \ldots$ until convergence **do**
3: Update $\sigma_i^{2,\ell+1}$ and $x_i^{\ell+1} = \mu_i$ from (3.28)
4: Compute $\langle x_i^{2,\ell+1} \rangle$ and update $\alpha_i^{\ell+1}$ from (3.30)
5: Check convergence using $\|\mathbf{x}^{\ell+1} - \mathbf{x}^{\ell}\|^2 / \|\mathbf{x}^{\ell}\|^2 \leq 10^{-18}$
6: **end for**
7: Form $\hat{\mathbf{X}}_{\text{ESM}}^{\text{VBI}}$ from the point estimates μ_i
8: Estimate the transmitted ESM vectors using (3.19) and form $\hat{\mathbf{X}}_{\text{ESM}}$
9: Retrieve the transmitted bits using the ESM mapping rule
10: **return** estimated bit sequence $\hat{\mathbf{b}}$

3.2.5 Spectral Efficiency of ESM-OTFS

The spectral efficiency (SE) of ESM-OTFS is defined as the ratio of the information rate to the total bandwidth occupied. The total time span of an ESM-OTFS frame is NT and the total bandwidth engaged by a frame is $M\Delta f$. The number of bits transmitted by an ESM-OTFS frame is $MN \log_2(\mathbb{C}_{\text{ESM}})$. The SE of ESM-OTFS is therefore

$$\text{SE}_{\text{ESM-OTFS}} = \frac{MN \log_2(\mathbb{C}_{\text{ESM}})}{NT \times M\Delta f} = \log_2(\mathbb{C}_{\text{ESM}}), \tag{3.31}$$

where $T\Delta f = 1$. The SE of SM-OTFS and QSM-OTFS [59] systems can be represented using the same parameters as

$$\mathrm{SE}_{\text{SM-OTFS}} = \log_2(M_{\text{mod}}) + \log_2(N_T), \tag{3.32}$$

$$\mathrm{SE}_{\text{QSM-OTFS}} = \log_2(M_{\text{mod}}) + 2\log_2(N_T), \tag{3.33}$$

where M_{mod} is the size of the modulation alphabet used. As an example, consider an ESM-OTFS system with QPSK as primary modulation and $N_T = 2$. The ESM constellation corresponding to this configuration is depicted in Table 3.2 and contains 16 distinct constellation vectors. The spectral efficiency of ESM-OTFS is therefore 4 BPCU. Under the same settings, the SE of SM-OTFS and QSM-OTFS are 3 and 4 BPCU respectively.

3.2.6 Computational Complexity of ESM-OTFS

The signal detection algorithm at the receiver is composed of two distinct components that contribute to its overall complexity. The first part is the computational complexity of the algorithm used for equalization and the second part is the complexity of the demodulation algorithm. The MMSE detector uses (3.18) for equalization, which has a computational complexity of $\mathcal{O}(M^3N^3N_T^3)$. The minimum Euclidean distance detector is used for the demodulation, which has a computational load of $\mathcal{O}(MN\mathbb{C}_{\text{ESM}})$, where $\mathbb{C}_{\text{ESM}}$ is the size of the ESM constellation. There is an additional search complexity of $\mathcal{O}(\mathbb{C}_{\text{ESM}})$ for decoding the bits.

The VBI based detector does not require any matrix inversion operation for the equalization step. It has a computational complexity of $\mathcal{O}(M^2N^2N_T^2I_{\text{VBI}})$, where I_{VBI} is the number of iterations required for convergence of the algorithm. Since the VBI based detector also uses Euclidean distance based detection for the demodulation, it has the same complexity in comparison to the MMSE detector for the demodulation step. The VBI detector therefore reduces the per iteration cost

from cubic to quadratic in MNN_T while exploiting the sparsity of the ESM-OTFS transmit vector at the cost of I_{VBI} iterations.

3.3 Generalized Dual-Mode Index Modulation Based on OTFS

3.3.1 OTFS Based Dual-Mode Index Modulation

We consider an OTFS-DM-IM system [25] as depicted in Fig. 3.2 with M subcarriers and N OFDM symbols. Δf denotes the subcarrier spacing and T represents the OFDM symbol duration. We consider a scenario where data is transmitted from one point to another, and b bits are transmitted between the points. The incoming b bits are split into G groups, where each group has g bits and is partitioned into g_1 bits and g_2 bits. These bit clusters are known as index bits and information bits respectively. Each group represents an OTFS subblock of length $L = MN/G$, where MN denotes the size of an OTFS frame. The index selector utilizes the first g_1 bits of the g bits to split the grid points of the OTFS subblock into two index subsets represented by $\mathcal{J}_{\mathcal{A}}$ and $\mathcal{J}_{\mathcal{B}}$. The functionality of the index selector can be observed in Table 3.3 for $g_1 = 2$, $L = 4$, and $K = 2$. There are two constellation alphabets in OTFS-DM-IM, $\mathcal{A}$ and $\mathcal{B}$, with sizes N_A and N_B respectively, provided $\mathcal{A} \cap \mathcal{B} = \varnothing$ [21]. As an example, $\mathcal{A} = \{-1-j, 1-j, 1+j, -1+j\}$ and $\mathcal{B} = \{3, 3j, -3, -3j\}$ represent two distinguishable QPSK modulation alphabets where $\mathcal{A} \cap \mathcal{B} = \varnothing$. The grid points corresponding to $\mathcal{J}_{\mathcal{A}}$ and $\mathcal{J}_{\mathcal{B}}$ are modulated by mappers A and B respectively. K grid points of the OTFS subblock are modulated by $\mathcal{A}$ and the remaining $L-K$ grid points are modulated by $\mathcal{B}$. g_1 and g_2 can be computed as $g_1 = \lfloor \log_2 \binom{L}{K} \rfloor$ and $g_2 = K \log_2 N_A + (L-K) \log_2 N_B$, where $\binom{L}{K}$ is the binomial coefficient and $\lfloor \cdot \rfloor$ represents the integer floor function. The information conveyed by an OTFS-DM-IM

subblock $g_{\text{OTFS-DM}}$ is

$$g_{\text{OTFS-DM}} = \lfloor \log_2 \binom{L}{K} \rfloor + K \log_2 N_A + (L-K) \log_2 N_B. \tag{3.34}$$

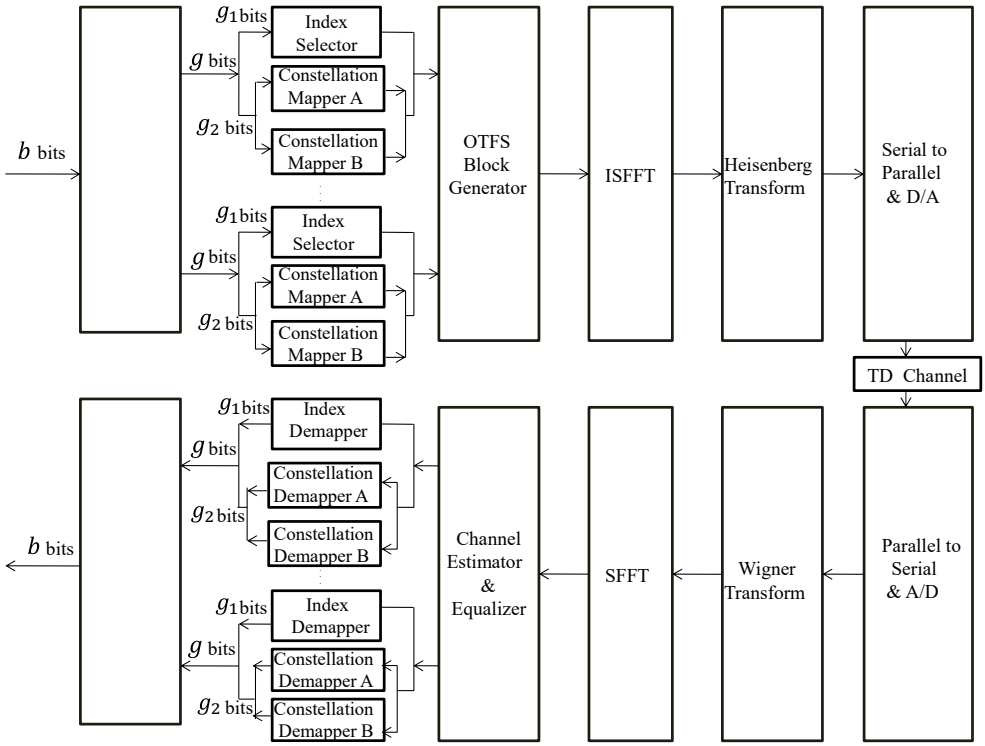


Figure 3.2: Block diagram of the OTFS-DM-IM system used as the baseline for OTFS-GDM-IM

Table 3.3: A look-up table for dual-mode index modulation with $g_1 = 2$, $L = 4$, $K = 2$

Index bits	Indices	Subblocks
$[0,0]$	$[1,2]$	$[\alpha_A^{(1)}, \alpha_A^{(2)}, \alpha_B^{(1)}, \alpha_B^{(2)}]$
$[0,1]$	$[1,3]$	$[\alpha_A^{(1)}, \alpha_B^{(1)}, \alpha_A^{(2)}, \alpha_B^{(2)}]$
$[1,0]$	$[2,3]$	$[\alpha_B^{(1)}, \alpha_A^{(1)}, \alpha_A^{(2)}, \alpha_B^{(2)}]$
$[1,1]$	$[3,4]$	$[\alpha_B^{(1)}, \alpha_B^{(2)}, \alpha_A^{(1)}, \alpha_A^{(2)}]$

3.3.2 OTFS-GDM-IM Transmitter and Signal Model

The size of $\mathcal{J}_{\mathcal{A}}$ is fixed in conventional OTFS-DM-IM. However, by incorporating variable sizes of $\mathcal{J}_{\mathcal{A}}$ in different subblocks, it is feasible to increase the number of

distinct OTFS subblock configurations, resulting in improved spectral efficiency [51]. Generalized dual-mode OTFS-IM (OTFS-GDM-IM) is proposed to enhance the spectral efficacy of OTFS-DM-IM. In OTFS-GDM-IM, the size of $\mathcal{J}_{\mathcal{A}}$ is no longer constant. The number of OTFS grid points modulated by $\mathcal{A}$ is now a variable and depends on the information bits. Since the size of $\mathcal{J}_{\mathcal{A}}$ is not fixed in a particular OTFS subblock, the size of $\mathcal{J}_{\mathcal{B}}$ is also a variable. For each OTFS subblock, $\mathcal{K}$ can be characterized as a set encompassing all possible realizations of $\mathcal{J}_{\mathcal{A}}$. This can be represented as

$$\mathcal{K} = \{K_1, K_2, \ldots, K_i, \ldots, K_T\}, \tag{3.35}$$

where T is the size of $\mathcal{K}$. Just like in conventional OTFS-DM-IM, the index bits are used to calculate the size of $\mathcal{J}_{\mathcal{A}}$, which is denoted as K_i. Then K_i OTFS grid points are modulated by $\mathcal{A}$ and the remaining $L - K_i$ grid points are modulated by $\mathcal{B}$. The total number of feasible OTFS subblock configurations is

$$n_{\text{GDM}} = \sum_{i=1}^{T} \binom{L}{K_i} N_A^{K_i} N_B^{L-K_i}. \tag{3.36}$$

The information transmitted by each OTFS-GDM-IM subblock is

$$g_{\text{OTFS-GDM}} = \left\lfloor \log_2 \left(\sum_{i=1}^{T} \binom{L}{K_i} N_A^{K_i} N_B^{L-K_i} \right) \right\rfloor. \tag{3.37}$$

Due to the higher number of potential realizations of OTFS subblocks in OTFS-GDM-IM, its spectral efficiency can be improved in comparison to conventional OTFS-DM-IM. As an illustration, consider OTFS subblocks of length $L = 4$ with two distinguishable BPSK modulations and $\mathcal{K} = \{1, 3\}$ and $\mathcal{K} = \{0, 1, 2, 3, 4\}$. Under this setting, the number of index bits conveyed by OTFS-GDM-IM is 3 and 4 bits respectively. The number of information bits is 4 in both cases. The total number of bits conveyed by OTFS-GDM-IM is 7 and 8 respectively, while the total number of bits carried by OTFS-DM-IM is 6. Clearly the number of bits transmitted by an OTFS subblock increases in the case of OTFS-GDM-IM compared to OTFS-DM-IM.

Increasing the size of $\mathcal{K}$ improves the spectral efficiency of OTFS-GDM-IM, with the highest spectral efficiency attained when $\mathcal{K} = \{0, 1, 2, \ldots, L\}$. OTFS-GDM-IM may experience a decline in performance and a significant rise in computational overhead as a result of a greater number of subblock realizations.

All the OTFS subblocks are passed through the OTFS block creator block as in OTFS-DM-IM to form the OTFS frame for OTFS-GDM-IM, $\mathbf{X}_{\text{GDM}} \in \mathbb{C}^{M \times N}$. OFDM based OTFS is used for the deployment of OTFS-GDM-IM. $\mathbf{X}_{\text{GDM}}$ is converted to the TF domain using ISFFT and then the Heisenberg transform along with rectangular pulse shaping is applied to obtain the time domain 2D matrix $\mathbf{S} \in \mathbb{C}^{M \times N}$. $\mathbf{S}$ is converted to the 1D time domain signal $\mathbf{s} \in \mathbb{C}^{MN \times 1}$. Then $\mathbf{s}$ propagates through the time-varying multipath wireless channel, and the time domain signal $\mathbf{r} \in \mathbb{C}^{MN \times 1}$ is picked up at the receiver. The Wigner transform along with rectangular pulse shaping and SFFT is applied to get the DD domain signal $\mathbf{Y}_{\text{GDM}} \in \mathbb{C}^{M \times N}$. An equalization method is applied on $\mathbf{Y}_{\text{GDM}}$ to remove the channel impairments. MMSE equalization is applied to estimate the transmitted symbols

$$\hat{\mathbf{y}}_{\text{GDM}} = \left(\mathbf{H}_{\text{eff}} \mathbf{H}_{\text{eff}}^{H} + \frac{\mathbf{I}_{MN}}{\sigma^2} \right)^{-1} \mathbf{H}_{\text{eff}}^{H} \mathbf{y}_{\text{GDM}}, \tag{3.38}$$

where σ^2 is the variance of the DD domain white noise. Then $\hat{\mathbf{y}}_{\text{GDM}}$ can be represented as $\hat{\mathbf{y}}_{\text{GDM}} = \{\hat{y}_1, \hat{y}_2, \ldots, \hat{y}_{MN}\}$. After the equalization, $\hat{\mathbf{y}}_{\text{GDM}}$ is separated into OTFS subblocks and these subblocks are passed on to the detector to retrieve the index and data information bits.

3.3.3 ML Detector for OTFS-GDM-IM

At the receiver, the ML detector can be utilized for the estimation of transmitted information. This is done by decoding each subblock of the equalized signal. For the ηth subblock, the ideal index sequence and transmitted symbols are retrieved by minimizing the ML construct. In the case of an ML detector, the search involves considering all potential subblock realizations by examining all feasible

index patterns $\mathcal{J}$ along with their accompanying symbol combinations $\mathcal{C}_{\mathbf{J}}$

$$\left\{\hat{\mathbf{J}}^{\eta}, \hat{\mathbf{X}}^{\eta}_{\mathrm{GDM}}\right\} = \arg \min_{\mathbf{J}\in\mathcal{J}, \mathbf{C}_{\mathbf{J}}\in\mathcal{C}_{\mathbf{J}}} \sum_{k=1}^{L} |\hat{y}_{\eta}(k) - \mathbf{C}_{\mathbf{J}}(k)|^2, \quad 1 \leq \eta \leq G, \tag{3.39}$$

where $\hat{\mathbf{J}}^{\eta}$ is the estimated index pattern of the ηth OTFS subblock and $\hat{\mathbf{X}}^{\eta}_{\mathrm{GDM}}$ is the estimated symbol vector. The demodulation of information bits is achieved by utilizing an index pattern mapping table and the two constellation alphabets, which map the information bits to the matching index pattern and constellation symbols. The computational load of the ML detector is of the order $\mathcal{O}(\sum_{i=1}^{T} \binom{L}{K_i} N_A^{K_i} N_B^{L-K_i})$, which grows exponentially as the variables N_A, N_B, L, and K_i rise in magnitude.

3.3.4 LLR Detector for OTFS-GDM-IM

The index bits represented in the DD domain constitute either 1 or 0. The natural logarithm of the ratio of the posterior probabilities between the OTFS grid points modulated with $\mathcal{A}$ and those modulated with $\mathcal{B}$ serves as a means to ascertain the index configuration of the grid. Employing an LLR-based detector for the detection of OTFS-GDM-IM can significantly simplify the detection complexity. Since the modulation of each grid point is done by either alphabet A or alphabet B, this approach allows for the determination of its constellation mode through LLR value computation

$$\zeta_n = \ln\left(\frac{\sum_{j=1}^{N_A} \Pr(\mathbf{x}_n^{\eta} = C_A(j) \mid \hat{y}_n^{\eta})}{\sum_{q=1}^{N_B} \Pr\left(\mathbf{x}_n^{\eta} = C_B(q) \mid \hat{y}_n^{\eta}\right)}\right), \tag{3.40}$$

where $1 \leq n \leq L$, $C_A(j) \in \mathcal{A}$, and $C_B(q) \in \mathcal{B}$. From (3.40), if the LLR value ζ_n of the nth grid point is positive, it has a higher possibility of being modulated by mapper A, and if ζ_n is negative, it has a higher possibility of being modulated by mapper B. Based on Bayes' theorem, $\sum_{j=1}^{N_A} \Pr(\mathbf{x}_n^{\eta} = C_A(j)) = K_i/L$ and $\sum_{q=1}^{N_B} \Pr(\mathbf{x}_n^{\eta} = C_B(q)) = (L - K_i)/L$. Since MMSE equalization is utilized for the equalization of the received DD domain signal, the noise variance gets modified. Representing $\mathbf{W}_{\mathrm{MMSE}} = (\mathbf{H}_{\mathrm{eff}}\mathbf{H}_{\mathrm{eff}}^H + \mathbf{I}_{MN}/\sigma^2)^{-1}\mathbf{H}_{\mathrm{eff}}^H$, the variance of the noise signal

after equalization is

$$\sigma^2_{\mathrm{MMSE}} = \mathrm{diag}\left(\mathbf{W}^H_{\mathrm{MMSE}}\mathbf{W}_{\mathrm{MMSE}}\right), \tag{3.41}$$

where diag$(\cdot)$ is the operator which gives the diagonal elements of the matrix as the output. We can expand the formula of ζ_n using the above results as

$$\begin{aligned}\zeta_n = &\ln\left(\frac{N_B K_i}{N_A(L-K_i)}\right)\\ &+\ln\left(\sum_{j=1}^{N_A}\exp\left(-\frac{|\hat{y}^\eta_n - C_A(j)|^2}{\sigma^2_{\mathrm{MMSE}}}\right)\right)\\ &-\ln\left(\sum_{q=1}^{N_B}\exp\left(-\frac{|\hat{y}^\eta_n - C_B(q)|^2}{\sigma^2_{\mathrm{MMSE}}}\right)\right).\end{aligned} \tag{3.42}$$

For each K_i with $1 \le i \le T$, LLR values for each grid point are calculated. If the LLR value is positive, the grid point has a higher possibility of being modulated by $\mathcal{A}$, and conversely if the LLR value is negative, it is less likely. The index pattern for each K_i can be obtained using the positive and negative LLR values and denoted as $\mathcal{J}_{A,K_i}$. Simply taking the positive and negative sign of the LLR value to determine whether a grid point is modulated by $\mathcal{A}$ or $\mathcal{B}$ results in wrong estimation of the index pattern due to the effect of channel noise. To address this issue, for each K_i, the K_i largest LLR values are considered in each OTFS subblock and those grid points have a higher possibility of being modulated by mapper A. For each K_i, the estimated symbols are derived using hard decision. The optimal index pattern and constellation symbols for the ηth OTFS subblock are obtained using the ML metric

$$\left\{\hat{\mathbf{J}}^\eta, \hat{\mathbf{X}}^\eta_{\mathrm{GDM}}\right\} = \arg \min_{\mathbf{J}\in\mathcal{J}_{K_i}, \mathbf{C}_{\mathbf{J}}\in\mathcal{C}_{\mathbf{J},K_i}} \sum_{k=1}^{L}\left|\hat{y}_\eta(k) - \mathbf{C}_{\mathbf{J},K_i}(k)\right|^2, \tag{3.43}$$

for $1 \le \eta \le G$ and $1 \le i \le T$. Following the detection, the information bits are demodulated using the mapping table. The LLR detector is a near-optimal receiver

with a substantial computational advantage. The computational overhead of the LLR detector follows an order of $\mathcal{O}(LT(N_A+N_B))$, with an additional search of order $\mathcal{O}(L^2)$ for comparing LLR values within each subblock.

3.3.5 Spectral Efficiency of OTFS-GDM-IM

The SE of OTFS-GDM-IM is defined as the ratio of the information rate to the total bandwidth occupied. The total time span of an OTFS-GDM-IM frame is NT and the total bandwidth engaged by a frame is $M\Delta f$. The number of bits transmitted by a frame is $(g_1+g_2)G = \log_2(\sum_{i=1}^{T}\binom{L}{K_i}N_A^{K_i}N_B^{L-K_i})\times G$. The SE of OTFS-GDM-IM is therefore

$$\mathrm{SE}_{\text{OTFS-GDM-IM}} = \frac{\left\lfloor \log_2\left(\sum_{i=1}^{T}\binom{L}{K_i}N_A^{K_i}N_B^{L-K_i}\right)\right\rfloor}{L}, \tag{3.44}$$

where $G = MN/L$ and $T\Delta f = 1$. The SE of the OTFS, OTFS-IM [23], and OTFS-DM-IM systems can be represented using the same parameters as

$$\mathrm{SE}_{\text{OTFS}} = \log_2 M_{\text{mod}}, \tag{3.45}$$

$$\mathrm{SE}_{\text{OTFS-IM}} = \frac{\lfloor \log_2\binom{L}{K}\rfloor + K\log_2 M_{\text{mod}}}{L}, \tag{3.46}$$

$$\mathrm{SE}_{\text{OTFS-DM-IM}} = \frac{\lfloor \log_2\binom{L}{K}\rfloor + K\log_2 N_A + (L-K)\log_2 N_B}{L}, \tag{3.47}$$

where M_{mod} is the size of the modulation alphabet used. As an example, consider a scenario with two distinguishable QPSK alphabets used as primary and secondary constellations for OTFS-GDM-IM and OTFS-DM-IM. QPSK is the modulation used for OTFS and OTFS-IM. An OTFS subblock with $L=4$ and $K=2$ is considered for the calculation. The resulting spectral efficiencies are $\mathrm{SE}_{\text{OTFS}}=2$, $\mathrm{SE}_{\text{OTFS-IM}}=1.5$, $\mathrm{SE}_{\text{OTFS-DM-IM}}=2.5$, and $\mathrm{SE}_{\text{OTFS-GDM-IM}}=3$. There is a significant improvement in the SE of OTFS-GDM-IM compared to classical OTFS and other index modulations based on OTFS.

3.3.6 Computational Complexity of OTFS-GDM-IM

The signal detection algorithm at the receiver is composed of two distinct components that contribute to its overall complexity. The first part is the computational complexity of the MMSE algorithm used for equalization, which is of the order of $\mathcal{O}(MN \log_2 MN)$. The second part is the complexity of the demodulation algorithm. The ML detector has a computational complexity of $\mathcal{O}(\sum_{i=1}^{T} \binom{L}{K_i} N_A^{K_i} N_B^{L-K_i})$ for each OTFS subblock, which increases exponentially with the subblock size L, the constellation alphabet sizes N_A and N_B, and the size of $\mathcal{K}$. The computational complexity of the LLR detector is $\mathcal{O}(LT(N_A + N_B))$, with an additional search complexity of $\mathcal{O}(L^2)$ for the comparison of LLR values. The LLR detector therefore brings the demodulation cost of OTFS-GDM-IM from the exponential growth of the ML search to a linear scaling that is feasible for practical receivers.

3.4 Simulation Results

3.4.1 ESM-OTFS Performance

The findings from the simulations of the BER performance of ESM-OTFS compared to SM-OTFS and QSM-OTFS under different system configurations are discussed in this section. It is assumed that the receiver has the perfect channel state information and all the channels exhibit Rayleigh fading [7]. The main simulation parameters are a mobile user velocity of 120 km/h, a carrier frequency of 4 GHz, $M = 4$, $N = 4$, and a subcarrier spacing of 15 kHz.

The BER performance comparison of ESM-OTFS, QSM-OTFS, SM-OTFS, and SIMO-OTFS for 4 BPCU is given in Fig. 3.3. The constellation used in each scheme is indicated in the legend of the figure, and in the case of ESM-OTFS the primary constellation is indicated. A 2×4 MIMO setup is used for this simulation. ESM-OTFS outperforms the other schemes in BER performance. At a BER of 10^{-4}, ESM-OTFS outperforms QSM-OTFS by 2.1 dB, SM-OTFS by 3 dB, and

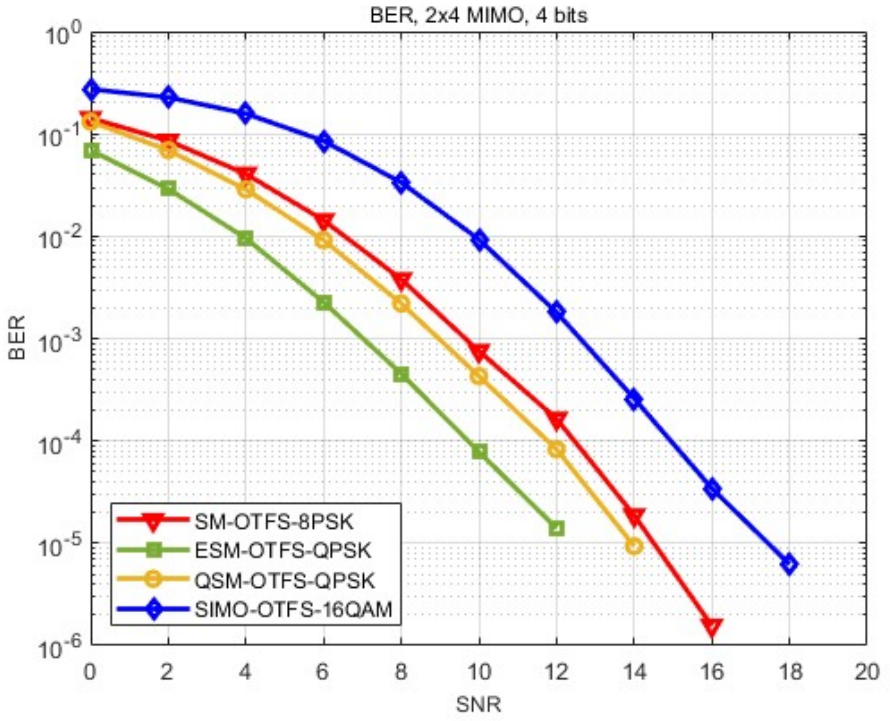


Figure 3.3: BER performance of ESM-OTFS, QSM-OTFS, SM-OTFS, and SIMO-OTFS systems based on MMSE detector with $M = 4$, $N = 4$ for 4 BPCU

SIMO-OTFS by 5.3 dB.

The BER performance comparison of ESM-OTFS, QSM-OTFS, SM-OTFS, and SIMO-OTFS for 6 BPCU is given in Fig. 3.4. A 4×4 MIMO setup is used for this simulation. At a BER of 10^{-3}, ESM-OTFS outperforms QSM-OTFS by 2 dB and SM-OTFS by 3.8 dB.

Fig. 3.5 depicts the BER performance of ESM-OTFS for 8 BPCU using various detectors. A 4×4 MIMO setup is used for this simulation and 16-QAM is used as the primary modulation. The VBI based detector outperforms the linear detectors. The ESM-OTFS VBI detector has a gain of 6.1 dB at a BER of 10^{-2} compared to the MMSE detector.

The BER performance of ESM-OTFS for 10 BPCU using various detectors is shown in Fig. 3.6. An 8×8 MIMO setup is used for this simulation and 16-QAM is used as the primary modulation. The VBI based detector has a gain of 7.8 dB over the MMSE based detector. It is observed from Fig. 3.5 and Fig. 3.6 that

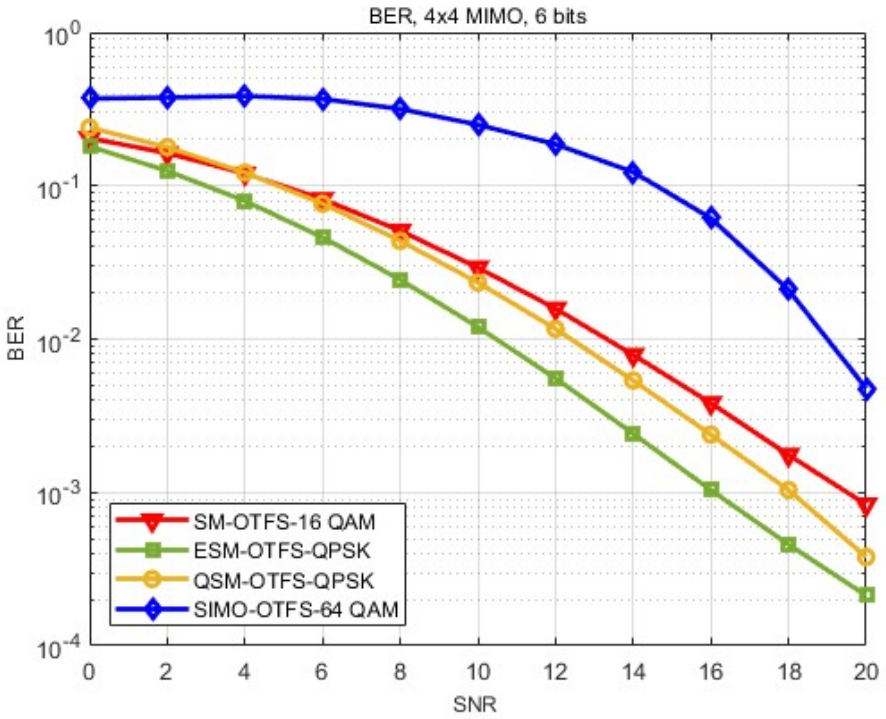


Figure 3.4: BER performance of ESM-OTFS, QSM-OTFS, SM-OTFS, and SIMO-OTFS systems based on MMSE detector with $M = 4$, $N = 4$ for 6 BPCU

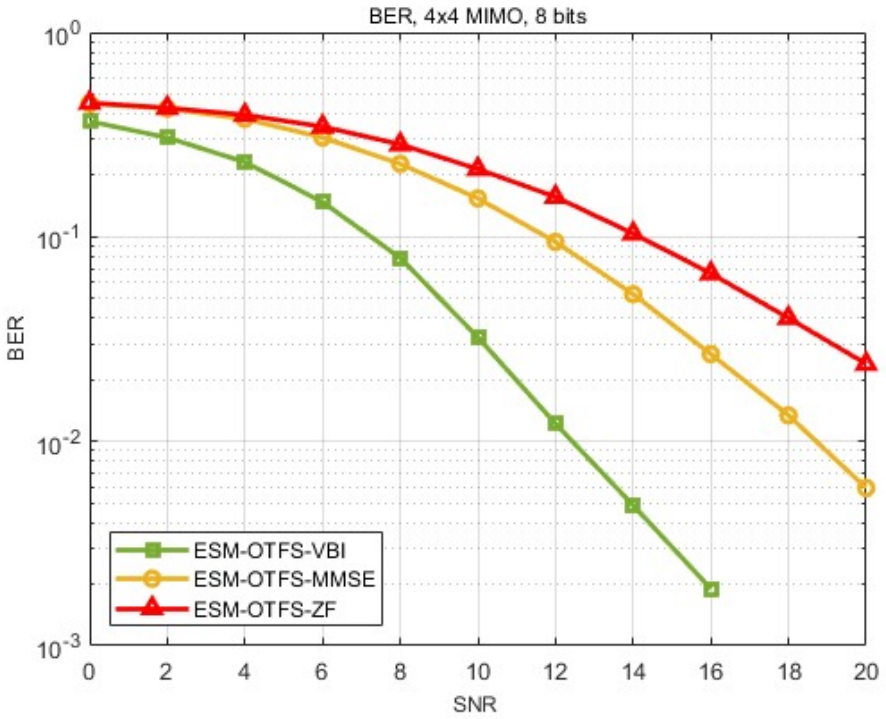


Figure 3.5: BER performance of ESM-OTFS using ZF, MMSE, and VBI detectors with $M = 4$, $N = 4$ for 8 BPCU

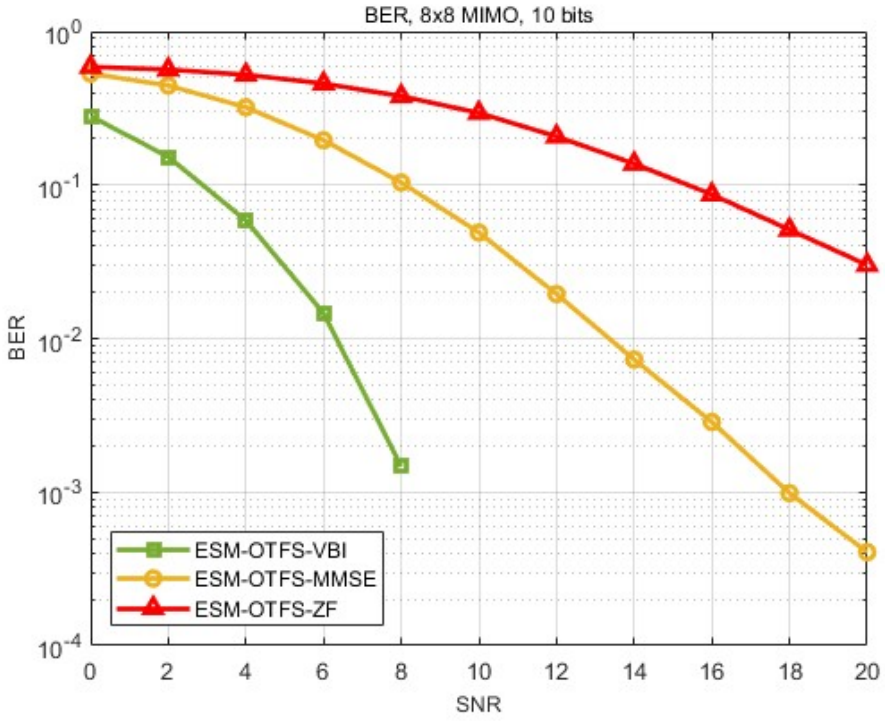


Figure 3.6: BER performance of ESM-OTFS using ZF, MMSE, and VBI detectors with $M = 4$, $N = 4$ for 10 BPCU

the performance of the VBI based detector improves as the transmit data matrix becomes more sparse.

ESM-OTFS is highly robust to Doppler shifts, which are prevalent in high mobility environments. Fig. 3.7 and Fig. 3.8 demonstrate the performance of ESM-OTFS at different velocities for 4 BPCU and 6 BPCU respectively. The BER performance of ESM-OTFS remains almost the same from a normal velocity of 30 km/h to a very high velocity of 500 km/h. There is only a slight performance degradation at higher velocities, and ESM-OTFS is highly immune to the Doppler shifts resulting from velocity variations.

To illustrate the computational complexity trade-off further, consider an ESM-OTFS system with $M = 4$, $N = 4$, and $N_T = 2$. In order to compare the receiver complexity at different BPCU, QPSK, 16-QAM, 64-QAM, and 256-QAM are used as the primary constellation to give BPCU of 4, 6, 8, and 10 respectively. Since the computational complexity of the equalization algorithms depends on

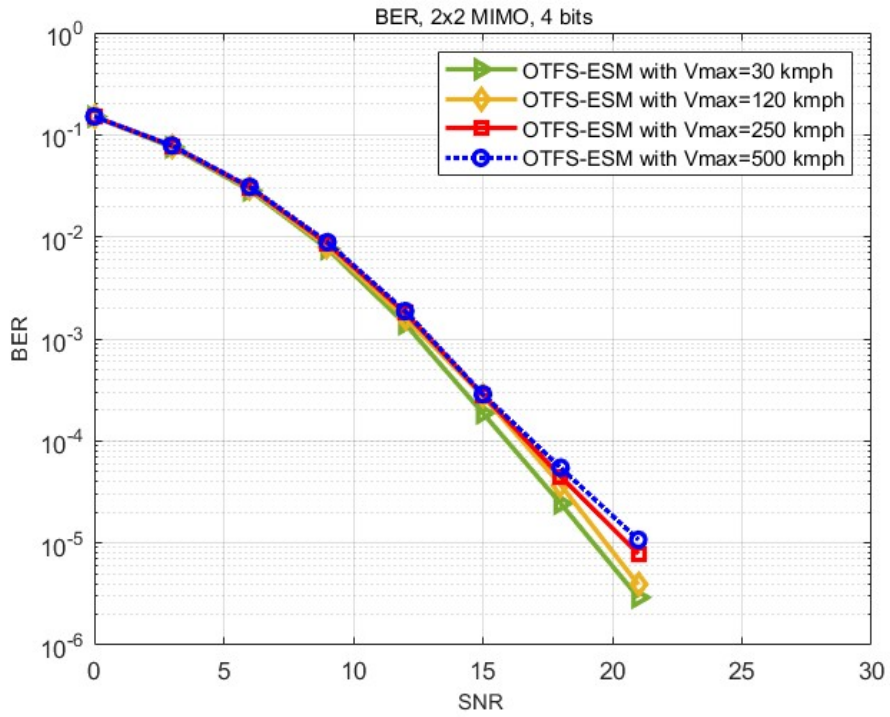


Figure 3.7: BER performance of ESM-OTFS at different velocities $M = 16$, $N = 16$ for 4 BPCU

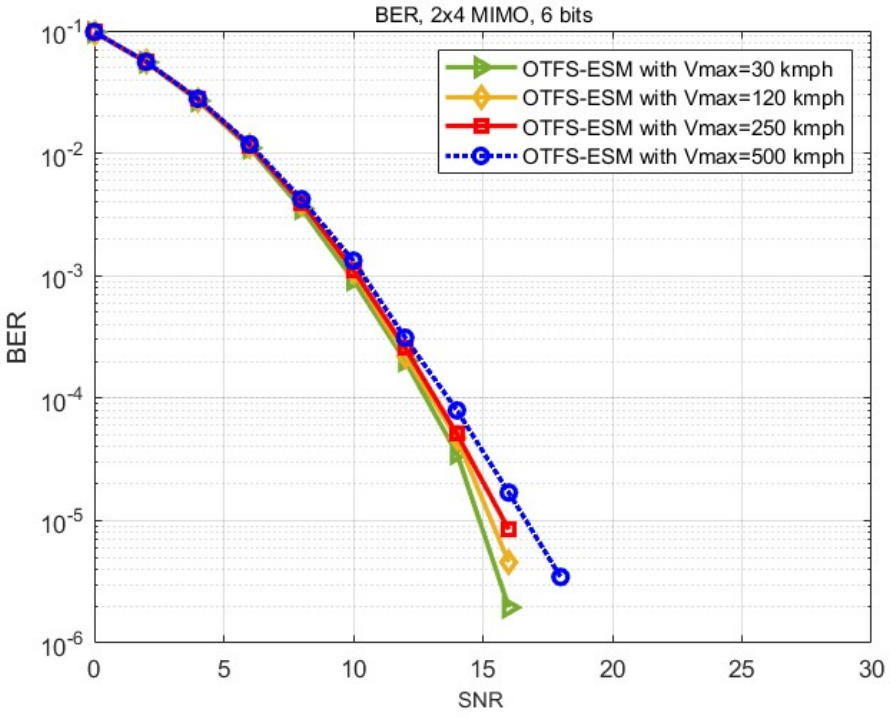


Figure 3.8: BER performance of ESM-OTFS at different velocities $M = 16$, $N = 16$ for 6 BPCU

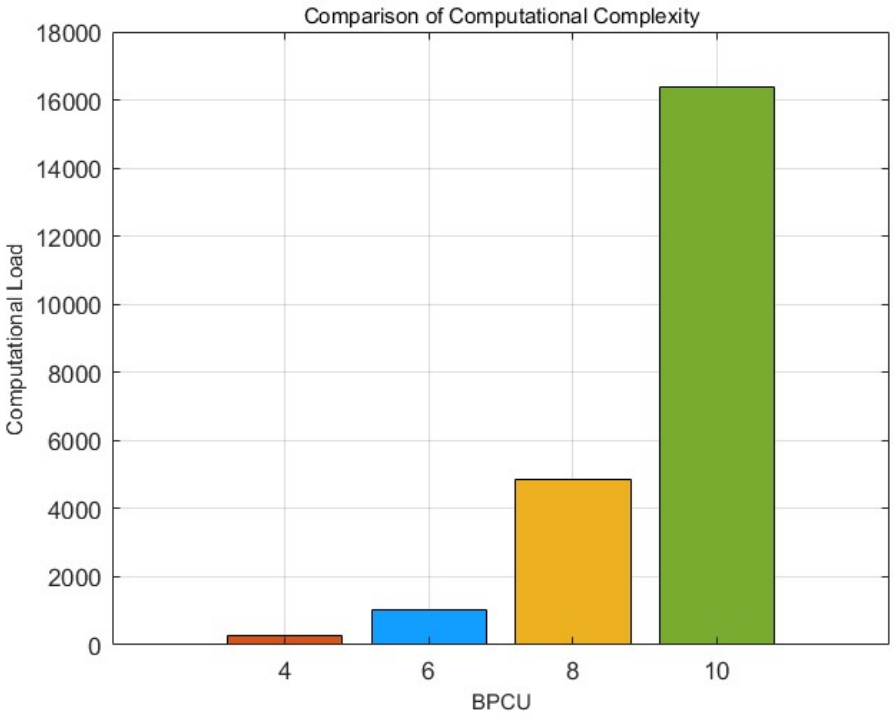


Figure 3.9: Trade-off between detector complexity and BPCU in ESM-OTFS systems

M, N, and N_T, the equalization complexity remains the same in all four cases of BPCU. Since the demodulation algorithm has a computational complexity of $\mathcal{O}(MN\mathbb{C}_{\text{ESM}})$, the computational load in terms of multiplications increases with the size of $\mathbb{C}_{\text{ESM}}$. As we know, the BPCU of the ESM-OTFS system is $\log_2(\mathbb{C}_{\text{ESM}})$, and the computational complexity of the detector increases with an increase in BPCU. This is highlighted in Fig. 3.9. As the modulation order increases, the receiver must perform more sophisticated signal processing to distinguish between closely spaced constellation points, thereby increasing the computational burden. This trade-off is critical in designing and optimizing communication systems for specific application scenarios, balancing the need for high data rates against the constraints of receiver complexity, power consumption, and real-time processing capabilities.

3.4.2 OTFS-GDM-IM Performance

The simulation of OTFS-GDM-IM is conducted assuming a time-varying multipath channel with integer delay and Doppler shifts and full channel state information at the receiver.

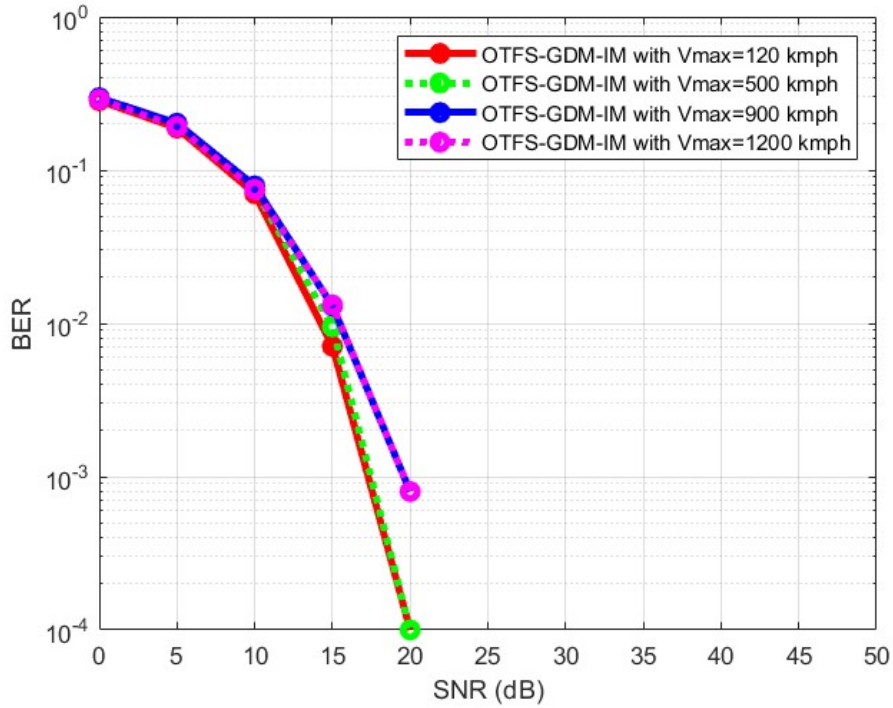


Figure 3.10: BER performance of OTFS-GDM-IM under high Doppler environments

The Monte Carlo simulation of OTFS-GDM-IM at various velocities of the scatterers is depicted in Fig. 3.10. From this figure, the proposed OTFS-GDM-IM system has good immunity under high Doppler environments. The simulation for Fig. 3.10 is performed with $M = 32$, $N = 32$, $N_A = N_B = 4$, and $L = 4$.

The simulations for Fig. 3.11, Fig. 3.12, and Fig. 3.13 are performed with $M = 4$, $N = 4$, $L = 4$, and $P = 2$, where P is the number of multipath scatterers. Fig. 3.11 highlights the performance of OTFS-GDM-IM with other OTFS based index modulation schemes under the same SE. OTFS-GDM-IM has superior BER performance compared to OTFS-IM [23] and OTFS-DM-IM [25].

Fig. 3.12 exhibits the performance of OTFS-GDM-IM with OTFS-DM-IM. OTFS-GDM-IM has a similar or comparable BER performance with OTFS-DM-IM

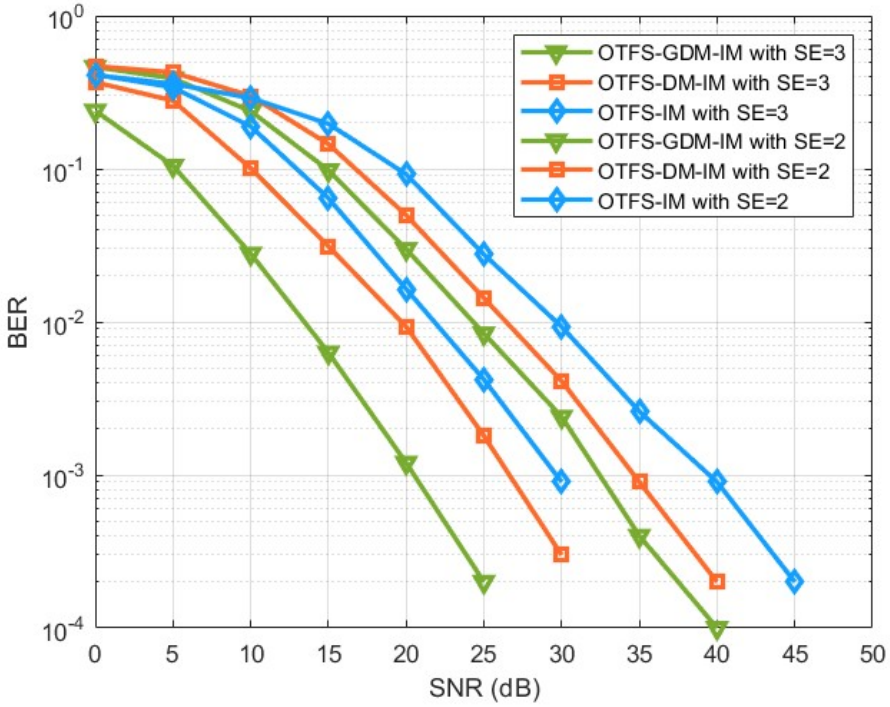


Figure 3.11: BER performance of OTFS-GDM-IM with other OTFS based index modulation systems

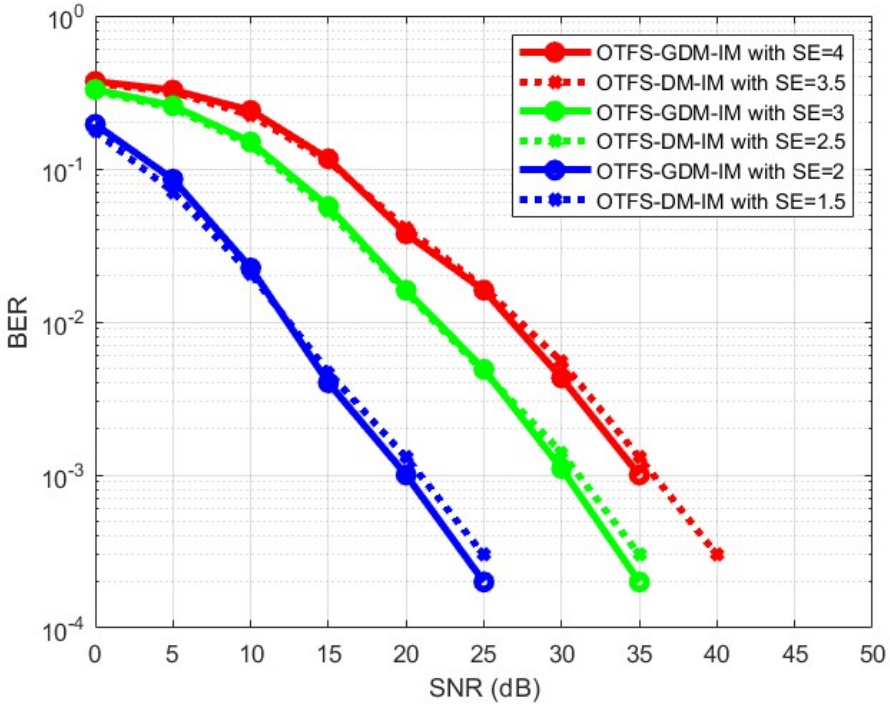


Figure 3.12: BER performance comparison of OTFS-GDM-IM with OTFS-DM-IM with the same system parameters

under the same system setting while delivering a higher spectral efficiency.

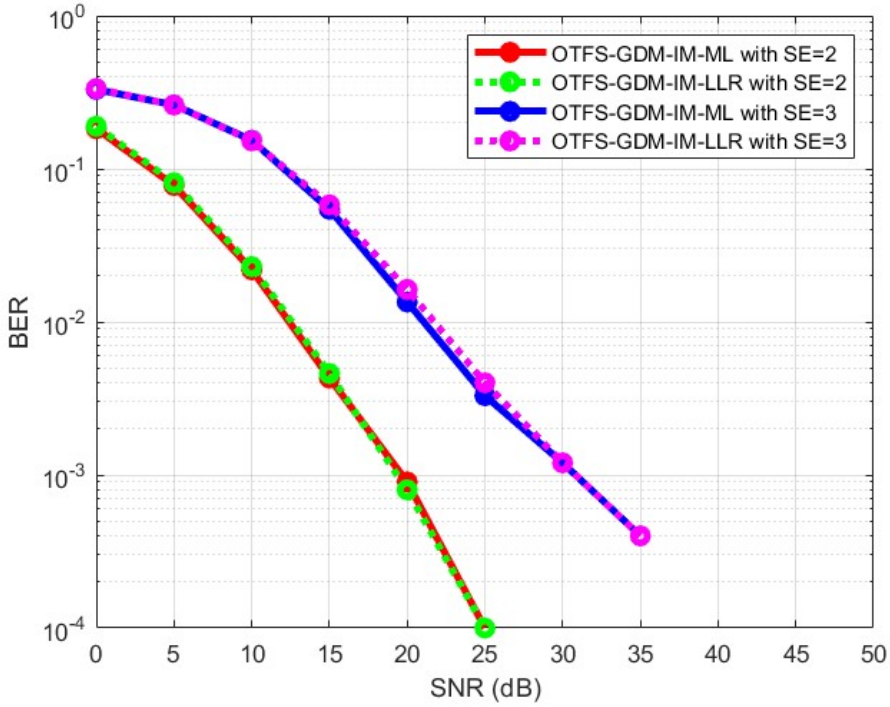


Figure 3.13: BER performance comparison of OTFS-GDM-IM detectors

Fig. 3.13 shows the performance of the proposed ML and LLR detectors with various SE. The ML detector and the LLR detector have similar or comparable BER performance while the ML detector has a computational complexity that grows exponentially. The BER performance deteriorates with the increase in SE, which reflects the reduced minimum Euclidean distance between admissible transmit vectors at higher rates.

3.5 Summary

This chapter developed two index modulation schemes built on OTFS for high mobility wireless communications. ESM-OTFS combines enhanced spatial modulation with OTFS in a MIMO setting and transmits information jointly through the antenna activation pattern, the choice of constellation set, and the modulated symbol on the active antennas. An MMSE based linear detector with

minimum Euclidean distance decoding was developed for ESM-OTFS, together with a Variational Bayesian Inference based detector that exploits the sparsity of the delay-Doppler transmit vector through a hierarchical Gaussian-Gamma prior, with the VBI detector showing the largest gains when the transmit vector becomes more sparse at higher antenna counts. OTFS-GDM-IM removed the fixed activation count of OTFS-DM-IM by allowing the number of grid points modulated by each constellation alphabet to vary across subblocks, which enlarged the set of admissible subblock realizations and raised the spectral efficiency over OTFS-IM and OTFS-DM-IM at matched parameters. An ML detector and a low complexity LLR detector were developed for OTFS-GDM-IM, and the LLR detector was shown to match the ML detector in BER while reducing the complexity from exponential growth with L, N_A, N_B, and the size of $\mathcal{K}$ to a linear scaling that is feasible for practical receivers. The OTFS system model, the MIMO-OTFS extension, the VBI detection framework, and the dual-mode index modulation construct introduced in this chapter recur in modified form in the AFDM based contributions.

Chapter 4

AFDM with Advanced Bayesian and Message Passing Detectors

This chapter develops the canonical AFDM system model [16,17] that the remaining chapters of the thesis build upon, and proposes three low-complexity detectors for AFDM in doubly dispersive channels. The system model section formalizes the Discrete Affine Fourier Transform (DAFT), the chirp-periodic prefix (CPP), the doubly dispersive channel, the DAFT-domain effective channel matrix, and the chirp-parameter selection rule that ensures path separability in the transformed domain. We then propose a low-complexity Vector Approximate Message Passing (VAMP) detector that replaces the singular value decomposition of the standard VAMP with a preconditioned conjugate gradient (CG) solver, reducing the per-iteration complexity from cubic to quadratic in the number of subcarriers. We then propose a Multi-Path Parallel Interference Cancellation (MP-PIC) detector that exploits the complete path separation property of AFDM by performing independent Bayesian inference on each resolvable delay-Doppler path and combining the path-wise estimates through reliability-weighted decision statistics combining (RWDSC). We then propose a Variational Bayesian (VB) detector for AFDM with low-resolution Analog-to-Digital Converters (ADCs) that incorporates the quantization constraints through a truncated Gaussian likelihood and exploits the sparse delay-Doppler

structure of the AFDM channel under a mean-field factorization of the posterior. Computational complexity and simulation results are presented for each detector at the end of the chapter.

4.1 AFDM System Model

4.1.1 Discrete Affine Fourier Transform

Let $\mathbf{x} \in \mathbb{C}^N$ denote the transmitted symbol vector drawn from a constellation alphabet $\mathcal{A}$. The DAFT transformation matrix $\mathbf{A} \in \mathbb{C}^{N \times N}$ is defined as

$$\mathbf{A} = \mathbf{\Lambda}_{c_2} \mathbf{F} \mathbf{\Lambda}_{c_1}, \tag{4.1}$$

where $\mathbf{F}$ is the normalized DFT matrix with entries

$$[\mathbf{F}]_{m,n} = \frac{1}{\sqrt{N}} \exp\left(-j\frac{2\pi mn}{N}\right), \quad m,n = 0,\ldots,N-1, \tag{4.2}$$

and $\mathbf{\Lambda}_c$ is the diagonal chirp modulation matrix

$$\mathbf{\Lambda}_c = \operatorname{diag}\left(\exp\left(-j2\pi c n^2\right)\right), \quad n = 0,\ldots,N-1. \tag{4.3}$$

The inverse DAFT satisfies $\mathbf{A}^{-1} = \mathbf{A}^H = \mathbf{\Lambda}_{c_1}^H \mathbf{F}^H \mathbf{\Lambda}_{c_2}^H$ due to the unitary property of both $\mathbf{F}$ and the diagonal chirp matrices.

4.1.2 AFDM Modulation

The time-domain transmitted signal is obtained through the inverse DAFT as

$$\mathbf{s} = \mathbf{A}^H \mathbf{x}. \tag{4.4}$$

A chirp-periodic prefix of length L_{cp} is appended before transmission, defined by

$$\begin{aligned} s[n] &= s[N+n]\exp\left(-j2\pi c_1(N^2+2Nn)\right), \\ n &= -L_{\text{cp}},\ldots,-1. \end{aligned} \tag{4.5}$$

The CPP makes the multipath channel effectively circular for the DAFT, preserves quadratic-phase continuity and symbol orthogonality. With $L_{\text{cp}} \geq L_{\max}$, it prevents inter-block interference and enables low-complexity detection in the DAFT domain.

4.1.3 Doubly Dispersive Channel

We consider a doubly dispersive channel with P resolvable paths [17]. The time-varying impulse response is

$$g_n(l) = \sum_{i=1}^{P} h_i \exp(-j2\pi f_i n)\,\delta(l-l_i), \tag{4.6}$$

where $h_i \sim \mathcal{CN}(0,\sigma_h^2/P)$ is the complex path gain with Rayleigh fading statistics, f_i is the normalized Doppler frequency, and $l_i \in \{0,1,\ldots,L_{\max}\}$ is the path delay in samples. The normalized Doppler shift of the ith path is

$$\nu_i = N f_i = \alpha_i + a_i, \tag{4.7}$$

where $\alpha_i \in \mathbb{Z}$ is the integer part and $a_i \in (-1/2, 1/2]$ is the fractional part.

After removing the chirp-periodic prefix, the discrete-time baseband channel model in matrix form is

$$\mathbf{r} = \mathbf{H}_{\text{td}}\,\mathbf{s} + \mathbf{w}, \tag{4.8}$$

where $\mathbf{H}_{\text{td}} \in \mathbb{C}^{N\times N}$ is the time-domain channel matrix

$$\mathbf{H}_{\text{td}} = \sum_{i=1}^{P} h_i\,\mathbf{\Gamma}_{\text{CPP},i}\,\mathbf{\Delta}_{\nu_i}\,\mathbf{\Pi}^{l_i}, \tag{4.9}$$

with $\mathbf{\Pi}$ the cyclic forward-shift matrix, $\mathbf{\Delta}_{\nu_i} = \mathrm{diag}(\exp(-j2\pi f_i n))$ the Doppler modulation operator, and $\mathbf{\Gamma}_{\mathrm{CPP},i}$ the CPP correction matrix. The cyclic forward-shift matrix is

$$\mathbf{\Pi} = \begin{bmatrix} 0 & \cdots & 0 & 1 \\ 1 & \cdots & 0 & 0 \\ \vdots & \ddots & \vdots & \vdots \\ 0 & \cdots & 1 & 0 \end{bmatrix}, \tag{4.10}$$

and the CPP correction matrix is $\mathbf{\Gamma}_{\mathrm{CPP},i} = \mathrm{diag}(\gamma_i[n])_{n=0}^{N-1}$ with

$$\gamma_i[n] = \begin{cases} \exp\Big(-j2\pi c_1(N^2 - 2N(l_i - n))\Big) & n < l_i, \\ 1 & n \geq l_i. \end{cases} \tag{4.11}$$

The additive noise vector $\mathbf{w} \in \mathbb{C}^N$ follows the distribution

$$\mathbf{w} \sim \mathcal{CN}(\mathbf{0}, \gamma_w^{-1}\mathbf{I}_N), \tag{4.12}$$

where $\gamma_w > 0$ is the noise precision parameter, equivalently $\sigma^2 = \gamma_w^{-1}$.

4.1.4 DAFT-Domain Representation

Applying DAFT demodulation at the receiver yields

$$\mathbf{y} = \mathbf{A}\,\mathbf{r} = \mathbf{A}\,\mathbf{H}_{\mathrm{td}}\,\mathbf{A}^H\,\mathbf{x} + \mathbf{A}\,\mathbf{w}. \tag{4.13}$$

Define the effective DAFT-domain channel matrix as

$$\mathbf{H}_{\mathrm{eff}} = \mathbf{A}\,\mathbf{H}_{\mathrm{td}}\,\mathbf{A}^H = \sum_{i=1}^{P} h_i\,\mathbf{H}_i, \tag{4.14}$$

where $\mathbf{H}_i = \mathbf{A}\,\mathbf{\Gamma}_{\mathrm{CPP},i}\,\mathbf{\Delta}_{\nu_i}\,\mathbf{\Pi}^{l_i}\,\mathbf{A}^H$. Since $\mathbf{A}$ is unitary, the transformed noise maintains the same statistical properties

$$\tilde{\mathbf{w}} = \mathbf{A}\,\mathbf{w} \sim \mathcal{CN}(\mathbf{0}, \gamma_w^{-1}\mathbf{I}_N), \tag{4.15}$$

and the measurement model becomes

$$\mathbf{y} = \mathbf{H}_{\text{eff}}\,\mathbf{x} + \tilde{\mathbf{w}}. \tag{4.16}$$

For integer Doppler shifts ($a_i = 0$), each row of $\mathbf{H}_i$ has exactly one non-zero entry. The (p,q)th entry of $\mathbf{H}_i$ is

$$[\mathbf{H}_i]_{p,q} = \begin{cases} \exp\left(j\frac{2\pi}{N}(Nc_1l_i^2 - ql_i + Nc_2(q^2-p^2))\right) & q = [p+\mathrm{loc}_i]_N, \\ 0 & \text{otherwise}, \end{cases} \tag{4.17}$$

where $\mathrm{loc}_i = [\alpha_i + 2Nc_1l_i]_N$ is the location offset of the ith path. For fractional Doppler, the entries spread over $2\xi_\nu + 1$ columns due to spectral leakage

$$[\mathbf{H}_i]_{p,q} = \begin{cases} \dfrac{\exp(j\psi_{i,p,q})}{N}\,\mathcal{F}_i(p,q), & (p+\mathrm{loc}_i-\xi_\nu)_N \le q \le (p+\mathrm{loc}_i+\xi_\nu)_N, \\ 0, & \text{otherwise}, \end{cases} \tag{4.18}$$

where

$$\mathcal{F}_i(p,q) = \frac{\exp(j2\pi(p-q+a_i+\mathrm{loc}_i))-1}{\exp\left(j\frac{2\pi}{N}(p-q+a_i+\mathrm{loc}_i)\right)-1}. \tag{4.19}$$

4.1.5 Parameter Selection

For a channel with maximum delay $L_{\max}$ and maximum integer Doppler $\alpha_{\max}$, the DAFT parameter c_1 is selected to ensure path separability in the transformed domain [17]. For integer Doppler shifts,

$$c_1 = \frac{2\alpha_{\max}+1}{2N\min_{i\neq j}(l_j - l_i)}, \tag{4.20}$$

and for fractional Doppler shifts,

$$c_1 = \frac{2(\alpha_{\max} + \xi_\nu) + 1}{2N \min_{i \neq j}(l_j - l_i)}, \tag{4.21}$$

where $\xi_\nu \leq k_\nu$ accounts for fractional Doppler spreading. These choices ensure $\text{loc}_i \neq \text{loc}_j$ for all $i \neq j$ when $2(\alpha_{\max} + \xi_\nu) l_{\max} + 2(\alpha_{\max} + \xi_\nu) + l_{\max} < N$. The second chirp parameter is chosen as

$$c_2 = \frac{1}{N^2 \pi}, \tag{4.22}$$

which is a sufficiently small irrational number to prevent path overlap in the DAFT domain. With proper parameter selection, each transmitted symbol $x[q]$ affects L_p received symbols, where

$$L_p = \begin{cases} P & \text{integer Doppler,} \\ (2\xi_\nu + 1)P & \text{fractional Doppler.} \end{cases} \tag{4.23}$$

4.1.6 Right Orthogonal Invariance of AFDM Channel

The VAMP algorithm [30, 70] requires the measurement matrix to satisfy approximate right orthogonal invariance, meaning $\mathbf{H}_{\text{eff}}\mathbf{V} \overset{d}{\approx} \mathbf{H}_{\text{eff}}$ for any unitary matrix $\mathbf{V}$. While the AFDM effective channel matrix $\mathbf{H}_{\text{eff}}$ does not exhibit strict right orthogonal invariance, it possesses sufficient randomness through the channel path gains $\{h_i\}_{i=1}^{P}$ to enable effective VAMP operation. Recall from (4.14) that

$$\mathbf{H}_{\text{eff}} = \sum_{i=1}^{P} h_i \mathbf{H}_i, \tag{4.24}$$

where $h_i \sim \mathcal{CN}(0, \sigma_h^2/P)$ are independent complex Gaussian random variables and $\mathbf{H}_i$ are deterministic matrices depending on the path delays $\{l_i\}$ and Doppler shifts $\{f_i\}$. Under the assumption of rich scattering with propagation paths having distinct delay-Doppler coordinates, the random linear combination structure ensures

that $\mathbf{H}_{\text{eff}}$ exhibits approximate distributional invariance under right multiplication by unitary matrices. This property has been empirically validated for doubly dispersive channels and forms the basis for applying VAMP to AFDM detection problems.

4.2 Standard VAMP Detector with SVD

The detection problem addressed in this chapter is stated as follows. Given the observation model $\mathbf{y} = \mathbf{H}_{\text{eff}}\,\mathbf{x} + \tilde{\mathbf{w}}$ with known $\mathbf{H}_{\text{eff}}$, the objective is the minimum mean square error estimate $\hat{\mathbf{x}} = \mathbb{E}[\mathbf{x} \mid \mathbf{y}]$ under the separable prior $p(\mathbf{x}) = \prod_m p(x[m])$ supported on the constellation $\mathcal{A}$, with the symbol decision obtained by slicing the posterior mean. Exact evaluation of this expectation is intractable for $|\mathcal{A}|^N$ candidate vectors, and the AMP, VAMP and variational algorithms developed in the remainder of the chapter are alternative tractable approximations to it. The MAP formulation is not pursued, since the sliced MMSE estimate minimizes symbol error rate under the assumed prior.

4.2.1 VAMP Framework

The VAMP iteration alternates between two modules. The linear module reconciles the estimate with the observation through an LMMSE step that inverts the channel, while the denoising module reconciles it with the discrete constellation prior. The Onsager-corrected messages exchanged between them keep the effective noise seen by each module approximately Gaussian and independent of the estimate, which is what allows the pair to converge to the replica-predicted MMSE.

VAMP solves the estimation problem by alternating between two modules [30]. The first module performs element-wise denoising exploiting prior information about signal structure. The second module implements linear minimum mean-squared error estimation incorporating measurement information. These operations are connected through Onsager correction terms [29].

Let $\mathbf{r}_k \in \mathbb{C}^N$ denote the iteration-k input to the denoiser with associated precision parameter $\gamma_k > 0$. The denoiser output is

$$\hat{\mathbf{x}}_k = g_1(\mathbf{r}_k, \gamma_k), \tag{4.25}$$

where g_1 operates element-wise on vector components. The divergence of the denoiser is

$$\alpha_k = \frac{1}{N} \sum_{n=1}^{N} \frac{\partial g_1(r_{k,n}, \gamma_k)}{\partial r_{k,n}}, \tag{4.26}$$

which measures the average sensitivity of the denoiser output to input perturbations. The Onsager-corrected estimate is

$$\tilde{\mathbf{r}}_k = \frac{\hat{\mathbf{x}}_k - \alpha_k \mathbf{r}_k}{1 - \alpha_k}, \tag{4.27}$$

with corresponding precision

$$\tilde{\gamma}_k = \frac{\gamma_k (1 - \alpha_k)}{\alpha_k}. \tag{4.28}$$

4.2.2 MMSE Denoising

For a finite constellation $\mathcal{A} = \{a_1, \ldots, a_M\}$, the MMSE denoiser implements

$$g_1(r, \gamma) = \frac{\sum_{m=1}^{M} a_m \exp\left(-\gamma |r - a_m|^2\right)}{\sum_{m=1}^{M} \exp(-\gamma |r - a_m|^2)} = \mathbb{E}[x | r, \gamma], \tag{4.29}$$

under the posterior distribution

$$p(x | r, \gamma) \propto \exp\left(-\gamma |r - x|^2\right) p(x), \tag{4.30}$$

where $p(x) = M^{-1}\sum_{m=1}^{M}\delta(x-a_m)$ for uniform priors. The denoiser derivative follows from the variance formula

$$g_1'(r,\gamma) = \frac{\partial g_1(r,\gamma)}{\partial r} = \gamma\,\mathrm{var}[x|r,\gamma], \tag{4.31}$$

where the conditional variance is

$$\mathrm{var}[x|r,\gamma] = \frac{\sum_{m=1}^{M}|a_m|^2\exp\left(-\gamma|r-a_m|^2\right)}{\sum_{m=1}^{M}\exp(-\gamma|r-a_m|^2)} - |g_1(r,\gamma)|^2. \tag{4.32}$$

4.2.3 SVD-Based LMMSE Estimation

The linear estimation step solves the regularized least-squares problem

$$\hat{\mathbf{x}}_{2,k} = \arg\min_{\mathbf{z}}\gamma_w\|\mathbf{y}-\mathbf{H}_{\text{eff}}\mathbf{z}\|_2^2 + \tilde{\gamma}_k\|\mathbf{z}-\tilde{\mathbf{r}}_k\|_2^2. \tag{4.33}$$

The solution is given by

$$\hat{\mathbf{x}}_{2,k} = (\gamma_w\mathbf{H}_{\text{eff}}^H\mathbf{H}_{\text{eff}} + \tilde{\gamma}_k\mathbf{I})^{-1}(\gamma_w\mathbf{H}_{\text{eff}}^H\mathbf{y} + \tilde{\gamma}_k\tilde{\mathbf{r}}_k). \tag{4.34}$$

Compute the economy singular value decomposition

$$\mathbf{H}_{\text{eff}} = \mathbf{U}\,\mathrm{Diag}(\mathbf{s})\,\mathbf{V}^H, \tag{4.35}$$

where $\mathbf{U}\in\mathbb{C}^{N\times R}$ and $\mathbf{V}\in\mathbb{C}^{N\times R}$ satisfy $\mathbf{U}^H\mathbf{U} = \mathbf{V}^H\mathbf{V} = \mathbf{I}_R$ with $R = \mathrm{rank}(\mathbf{H}_{\text{eff}})$, and $\mathbf{s}\in\mathbb{R}_+^R$ contains the singular values. Define the preconditioned measurement vector

$$\tilde{\mathbf{y}} = \mathrm{Diag}(\mathbf{s})^{-1}\,\mathbf{U}^H\,\mathbf{y}. \tag{4.36}$$

The LMMSE estimate can be computed efficiently as

$$\hat{\mathbf{x}}_{2,k} = \mathbf{V}\,\mathbf{d}_k, \tag{4.37}$$

where the coefficient vector is

$$\mathbf{d}_k = \gamma_w(\gamma_w \mathbf{s}^2 + \tilde{\gamma}_k \mathbf{1})^{-1} \odot [\mathbf{s}^2 \odot \tilde{\mathbf{y}} + \tilde{\gamma}_k \gamma_w^{-1} \mathbf{V}^H \tilde{\mathbf{r}}_k], \tag{4.38}$$

and $\odot$ denotes element-wise multiplication. The divergence of the LMMSE estimator is

$$\alpha_{2,k} = \frac{\tilde{\gamma}_k}{N} \operatorname{Tr}\left[(\gamma_w \mathbf{H}_{\text{eff}}^H \mathbf{H}_{\text{eff}} + \tilde{\gamma}_k \mathbf{I})^{-1}\right] = \frac{\tilde{\gamma}_k}{N} \sum_{n=1}^{R} \frac{1}{\gamma_w s_n^2 + \tilde{\gamma}_k}. \tag{4.39}$$

The updated parameters follow

$$\gamma_{k+1} = \frac{\tilde{\gamma}_k \, \alpha_{2,k}}{1 - \alpha_{2,k}}, \qquad \mathbf{r}_{k+1} = \frac{\hat{\mathbf{x}}_{2,k} - \alpha_{2,k} \tilde{\mathbf{r}}_k}{1 - \alpha_{2,k}}. \tag{4.40}$$

Algorithm 4.1 VAMP with SVD for AFDM

Require: $\mathbf{H}_{\text{eff}}$, $\mathbf{y}$, γ_w, $g_1(\cdot, \gamma)$, K_{it}
1: Compute $\mathbf{H}_{\text{eff}} = \mathbf{U} \operatorname{Diag}(\mathbf{s}) \mathbf{V}^H$, $\tilde{\mathbf{y}} = \operatorname{Diag}(\mathbf{s})^{-1} \mathbf{U}^H \mathbf{y}$
2: Initialize $\mathbf{r}_0$, γ_0
3: **for** $k = 0$ to $K_{\text{it}} - 1$ **do**
4: $\quad \hat{\mathbf{x}}_k = g_1(\mathbf{r}_k, \gamma_k)$, $\alpha_k = N^{-1} \sum_n g_1'(r_{k,n}, \gamma_k)$
5: $\quad \tilde{\mathbf{r}}_k = (\hat{\mathbf{x}}_k - \alpha_k \mathbf{r}_k)/(1 - \alpha_k)$, $\tilde{\gamma}_k = \gamma_k (1 - \alpha_k)/\alpha_k$
6: $\quad \mathbf{d}_k = \gamma_w(\gamma_w \mathbf{s}^2 + \tilde{\gamma}_k)^{-1} \odot \mathbf{s}^2$
7: $\quad \gamma_{k+1} = \tilde{\gamma}_k N^{-1} \sum_n d_{k,n} / (R/N - N^{-1} \sum_n d_{k,n})$
8: $\quad \mathbf{r}_{k+1} = \tilde{\mathbf{r}}_k + (N/R) \mathbf{V} \operatorname{Diag}(\mathbf{d}_k / \langle \mathbf{d}_k \rangle)(\tilde{\mathbf{y}} - \mathbf{V}^H \tilde{\mathbf{r}}_k)$
9: **end for**
10: **return** $\hat{\mathbf{x}}_{K_{\text{it}}}$

4.3 Low-Complexity VAMP Detector with Conjugate Gradient

4.3.1 Problem Formulation

The LMMSE estimation step in VAMP requires solving the regularized least-squares problem

$$\hat{\mathbf{x}}_{2,k} = \arg\min_{\mathbf{z}} \gamma_w \|\mathbf{y} - \mathbf{H}_{\text{eff}} \mathbf{z}\|_2^2 + \tilde{\gamma}_k \|\mathbf{z} - \tilde{\mathbf{r}}_k\|_2^2, \tag{4.41}$$

which is equivalent to solving the linear system

$$\mathbf{Q}_k \mathbf{z} = \mathbf{b}_k, \tag{4.42}$$

where the system matrix is

$$\mathbf{Q}_k = \gamma_w \mathbf{H}_{\text{eff}}^H \mathbf{H}_{\text{eff}} + \tilde{\gamma}_k \mathbf{I}_N, \tag{4.43}$$

and the right-hand side vector is

$$\mathbf{b}_k = \gamma_w \mathbf{H}_{\text{eff}}^H \mathbf{y} + \tilde{\gamma}_k \tilde{\mathbf{r}}_k. \tag{4.44}$$

The matrix $\mathbf{Q}_k$ is Hermitian positive definite since $\mathbf{z}^H \mathbf{Q}_k \mathbf{z} = \gamma_w \|\mathbf{H}_{\text{eff}} \mathbf{z}\|_2^2 + \tilde{\gamma}_k \|\mathbf{z}\|_2^2 > 0$ for any non-zero vector $\mathbf{z}$. Direct matrix inversion requires $\mathcal{O}(N^3)$ operations, while the conjugate gradient method provides an iterative alternative using only $\mathcal{O}(N^2)$ matrix-vector products per iteration.

4.3.2 Diagonal Preconditioning

We employ a diagonal preconditioner defined as $\mathbf{M} = \text{Diag}(\text{diag}(\mathbf{Q}_k))$ with the nth diagonal entry

$$M_{nn} = \gamma_w \sum_{m=1}^{N} |[\mathbf{H}_{\text{eff}}]_{m,n}|^2 + \tilde{\gamma}_k, \quad n = 1, \ldots, N. \tag{4.45}$$

In vector notation, the diagonal preconditioner is

$$\mathbf{m} = \gamma_w \, \text{diag}(\mathbf{H}_{\text{eff}}^H \mathbf{H}_{\text{eff}}) + \tilde{\gamma}_k \mathbf{1}, \tag{4.46}$$

where $\mathbf{M} = \mathrm{Diag}(\mathbf{m})$ and the inverse preconditioner is applied as $\mathbf{M}^{-1}\mathbf{v} = \mathbf{m}^{-1} \odot \mathbf{v}$. The preconditioned system

$$\mathbf{M}^{-1}\mathbf{Q}_k\,\mathbf{z} = \mathbf{M}^{-1}\mathbf{b}_k, \tag{4.47}$$

has substantially improved conditioning compared to the original system.

4.3.3 Preconditioned Conjugate Gradient Solver

The conjugate gradient solver replaces the explicit inverse by a sequence of matrix-vector products. Since $\mathbf{H}_{\text{eff}}$ is banded, each product costs $O(N \log N)$ rather than $O(N^2)$, and the preconditioner keeps the number of iterations required for a fixed residual tolerance essentially independent of N.

The preconditioned CG algorithm maintains approximations $\mathbf{z}^{(i)}$ with residual vector

$$\mathbf{r}_{\text{CG}}^{(i)} = \mathbf{b}_k - \mathbf{Q}_k\,\mathbf{z}^{(i)}, \tag{4.48}$$

and preconditioned residual

$$\mathbf{z}_{\text{pre}}^{(i)} = \mathbf{M}^{-1}\mathbf{r}_{\text{CG}}^{(i)} = \mathbf{m}^{-1} \odot \mathbf{r}_{\text{CG}}^{(i)}. \tag{4.49}$$

Initialize with $\mathbf{z}^{(0)} = \mathbf{0}$, $\mathbf{r}_{\text{CG}}^{(0)} = \mathbf{b}_k$, $\mathbf{z}_{\text{pre}}^{(0)} = \mathbf{m}^{-1} \odot \mathbf{b}_k$, and $\mathbf{p}^{(1)} = \mathbf{z}_{\text{pre}}^{(0)}$. For iterations $i = 1, 2, \ldots, K_{\text{CG}}$, compute the matrix-vector product

$$\mathbf{q}^{(i)} = \mathbf{Q}_k\,\mathbf{p}^{(i)} = \gamma_w \mathbf{H}_{\text{eff}}^H(\mathbf{H}_{\text{eff}}\mathbf{p}^{(i)}) + \tilde{\gamma}_k \mathbf{p}^{(i)}, \tag{4.50}$$

followed by the step size

$$s^{(i)} = \frac{(\mathbf{r}_{\text{CG}}^{(i-1)})^H \mathbf{z}_{\text{pre}}^{(i-1)}}{(\mathbf{p}^{(i)})^H \mathbf{q}^{(i)}}. \tag{4.51}$$

Update the solution and residual as

$$\mathbf{z}^{(i)} = \mathbf{z}^{(i-1)} + s^{(i)}\mathbf{p}^{(i)}, \qquad \mathbf{r}_{\text{CG}}^{(i)} = \mathbf{r}_{\text{CG}}^{(i-1)} - s^{(i)}\mathbf{q}^{(i)}. \tag{4.52}$$

Terminate if $\|\mathbf{r}_{\mathrm{CG}}^{(i)}\|_2 < \epsilon_{\mathrm{tol}}\|\mathbf{b}_k\|_2$ with $\epsilon_{\mathrm{tol}} = 10^{-7}$. Otherwise, compute the preconditioned residual $\mathbf{z}_{\mathrm{pre}}^{(i)} = \mathbf{m}^{-1} \odot \mathbf{r}_{\mathrm{CG}}^{(i)}$ and the conjugate coefficient

$$\beta^{(i)} = \frac{(\mathbf{r}_{\mathrm{CG}}^{(i)})^H \mathbf{z}_{\mathrm{pre}}^{(i)}}{(\mathbf{r}_{\mathrm{CG}}^{(i-1)})^H \mathbf{z}_{\mathrm{pre}}^{(i-1)}}, \tag{4.53}$$

and update the search direction as

$$\mathbf{p}^{(i+1)} = \mathbf{z}_{\mathrm{pre}}^{(i)} + \beta^{(i)} \mathbf{p}^{(i)}. \tag{4.54}$$

The final solution $\mathbf{z}^{(K_{\mathrm{CG}})}$ provides the LMMSE estimate $\hat{\mathbf{x}}_{2,k}$.

4.3.4 Simultaneous Trace Estimation

The Onsager correction parameter requires computing

$$\alpha_{2,k} = \frac{\tilde{\gamma}_k}{N} \mathrm{Tr}[\mathbf{Q}_k^{-1}]. \tag{4.55}$$

The CG iterations provide trace estimation through the Lanczos decomposition property, where search directions $\{\mathbf{p}^{(i)}\}$ span the Krylov subspace. Accumulating

$$\tau_k = \sum_{i=1}^{K_{\mathrm{CG}}} \frac{1}{(\mathbf{p}^{(i)})^H \mathbf{q}^{(i)}}, \tag{4.56}$$

approximates $\mathrm{Tr}[\mathbf{Q}_k^{-1}] \approx \tau_k$ with increasing accuracy as K_{CG} grows. For numerical stability, only the real part is accumulated

$$\tau_k \leftarrow \tau_k + \mathrm{Re}\left(\frac{1}{(\mathbf{p}^{(i)})^H \mathbf{q}^{(i)}}\right). \tag{4.57}$$

The Onsager parameter η corresponding to $\alpha_{2,k}$ is estimated as

$$\eta = \min\left(\frac{\tilde{\gamma}_k \tau_k}{N}, 0.95\right), \tag{4.58}$$

where the threshold 0.95 ensures $1-\eta$ remains bounded away from zero.

4.3.5 VAMP Parameter Updates

After obtaining $\hat{\mathbf{x}}_{2,k} = \mathbf{z}$ and Onsager parameter η, the VAMP parameters are updated as

$$\gamma_{k+1} = \frac{\tilde{\gamma}_k \eta}{1-\eta}, \qquad \mathbf{r}_{k+1}^{\text{raw}} = \frac{\mathbf{z} - \eta \tilde{\mathbf{r}}_k}{1-\eta}. \tag{4.59}$$

Damping is applied to mitigate oscillations

$$\mathbf{r}_{k+1} = \rho \mathbf{r}_{k+1}^{\text{raw}} + (1-\rho)\mathbf{r}_k, \tag{4.60}$$

where $\rho = 0.97$ provides momentum-like smoothing.

4.3.6 Denoiser Module

The denoiser processes $\mathbf{r}_k$ with precision γ_k to produce $\hat{\mathbf{x}}_k$ and divergence α_k. For constellation $\mathcal{A} = \{a_1, \ldots, a_M\}$ with uniform prior, the MMSE denoiser operates element-wise as

$$[\hat{\mathbf{x}}_k]_n = g_1([r_k]_n, \gamma_k) = \frac{\sum_{m=1}^{M} a_m \exp\Big(-\gamma_k |[r_k]_n - a_m|^2\Big)}{\sum_{m=1}^{M} \exp(-\gamma_k |[r_k]_n - a_m|^2)}, \tag{4.61}$$

for $n = 1, \ldots, N$, representing the posterior mean under $p(x|r,\gamma_k) \propto \exp\Big(-\gamma_k |r-x|^2\Big) p(x)$. The divergence is computed as

$$\alpha_k = \frac{1}{N} \sum_{n=1}^{N} \frac{\partial g_1([r_k]_n, \gamma_k)}{\partial [r_k]_n}, \tag{4.62}$$

where the derivative is

$$\frac{\partial g_1(r,\gamma_k)}{\partial r} = \gamma_k \operatorname{var}[x|r,\gamma_k], \tag{4.63}$$

$$\mathrm{var}[x|r,\gamma_k] = \frac{\sum_{m=1}^{M} |a_m|^2 \exp\Big(-\gamma_k |r-a_m|^2\Big)}{\sum_{m=1}^{M} \exp(-\gamma_k |r-a_m|^2)} - |g_1(r,\gamma_k)|^2. \tag{4.64}$$

The Onsager-corrected quantities are

$$\tilde{\mathbf{r}}_k = \frac{\hat{\mathbf{x}}_k - \alpha_k \mathbf{r}_k}{1-\alpha_k}, \qquad \tilde{\gamma}_k = \frac{\gamma_k(1-\alpha_k)}{\alpha_k}, \tag{4.65}$$

which serve as the effective prior for the LMMSE step. The algorithm initializes with $\mathbf{r}_0 = \mathbf{0}_N$ and $\gamma_0 = 1$.

Precision parameters are clipped to $[\gamma_{\min}, \gamma_{\max}]$ with $\gamma_{\min} = 10^{-11}$ and $\gamma_{\max} = 10^{11}$ via

$$\gamma = \mathrm{clip}(\gamma, \gamma_{\min}, \gamma_{\max}) = \max(\min(\gamma, \gamma_{\max}), \gamma_{\min}), \tag{4.66}$$

applied to both $\tilde{\gamma}_k$ and γ_{k+1}.

4.3.7 Convergence Properties

The CG error satisfies

$$\|\mathbf{z}^{(i)} - \mathbf{z}^*\|_{\mathbf{Q}_k} \leq 2\left(\frac{\sqrt{\kappa}-1}{\sqrt{\kappa}+1}\right)^i \|\mathbf{z}^{(0)} - \mathbf{z}^*\|_{\mathbf{Q}_k}, \tag{4.67}$$

where $\kappa = \lambda_{\max}(\mathbf{M}^{-1}\mathbf{Q}_k)/\lambda_{\min}(\mathbf{M}^{-1}\mathbf{Q}_k)$ is the condition number. The diagonal preconditioner ensures convergence within $K_{\mathrm{CG}} = 10$ to 20 iterations for typical AFDM channels.

4.3.8 Complexity of VAMP-CG

Each VAMP iteration performs MMSE denoising with $\mathcal{O}(MN)$ complexity, where M is the constellation size, followed by K_{CG} conjugate gradient iterations. Each CG iteration requires two matrix-vector products with $\mathbf{H}_{\mathrm{eff}}$, each costing $\mathcal{O}(N^2)$

Algorithm 4.2 VAMP with Conjugate Gradient for AFDM

Require: $\mathbf{H}_{\text{eff}}$, $\mathbf{y}$, γ_w, g_1, K_{it}, K_{CG}

Initialize $\mathbf{r}_0 = \mathbf{0}$, $\gamma_0 = 1$, $\rho = 0.97$
for $k = 0$ to $K_{\text{it}} - 1$ **do**
  $\hat{\mathbf{x}}_k = g_1(\mathbf{r}_k, \gamma_k)$, $\alpha_k = N^{-1} \sum_n g_1'(r_{k,n}, \gamma_k)$
  $\tilde{\mathbf{r}}_k = (\hat{\mathbf{x}}_k - \alpha_k \mathbf{r}_k)/(1 - \alpha_k)$
  $\tilde{\gamma}_k = \text{clip}(\gamma_k(1 - \alpha_k)/\alpha_k, \gamma_{\min}, \gamma_{\max})$
  $\mathbf{m} = \gamma_w \,\text{diag}(\mathbf{H}_{\text{eff}}^H \mathbf{H}_{\text{eff}}) + \tilde{\gamma}_k \mathbf{1}$
  $\mathbf{b} = \gamma_w \mathbf{H}_{\text{eff}}^H \mathbf{y} + \tilde{\gamma}_k \tilde{\mathbf{r}}_k$
  Initialize $\mathbf{z} = \mathbf{0}$, $\mathbf{r}_{\text{CG}} = \mathbf{b}$, $\mathbf{z}_{\text{pre}} = \mathbf{m}^{-1} \odot \mathbf{r}_{\text{CG}}$, $\mathbf{p} = \mathbf{z}_{\text{pre}}$, $\tau = 0$
  for $i = 1$ to K_{CG} **do**
    $\mathbf{q} = \gamma_w \mathbf{H}_{\text{eff}}^H (\mathbf{H}_{\text{eff}} \mathbf{p}) + \tilde{\gamma}_k \mathbf{p}$
    $s = (\mathbf{r}_{\text{CG}}^H \mathbf{z}_{\text{pre}})/(\mathbf{p}^H \mathbf{q})$
    $\mathbf{z} \leftarrow \mathbf{z} + s\mathbf{p}$, $\mathbf{r}_{\text{CG}} \leftarrow \mathbf{r}_{\text{CG}} - s\mathbf{q}$
    $\tau \leftarrow \tau + \text{Re}(1/(\mathbf{p}^H \mathbf{q}))$
    if $\|\mathbf{r}_{\text{CG}}\|_2 < 10^{-7} \|\mathbf{b}\|_2$ **then**
      break
    end if
    $\mathbf{z}_{\text{pre}}^{\text{new}} \leftarrow \mathbf{m}^{-1} \odot \mathbf{r}_{\text{CG}}$
    $\beta = (\mathbf{r}_{\text{CG}}^H \mathbf{z}_{\text{pre}}^{\text{new}})/(\mathbf{r}_{\text{CG}}^H \mathbf{z}_{\text{pre}})$
    $\mathbf{p} \leftarrow \mathbf{z}_{\text{pre}}^{\text{new}} + \beta \mathbf{p}$, $\mathbf{z}_{\text{pre}} \leftarrow \mathbf{z}_{\text{pre}}^{\text{new}}$
  end for
  $\eta = \min(\tau \tilde{\gamma}_k / N, 0.95)$
  $\gamma_{k+1} = \text{clip}(\tilde{\gamma}_k \eta/(1 - \eta), \gamma_{\min}, \gamma_{\max})$
  $\mathbf{r}_{k+1}^{\text{raw}} = (\mathbf{z} - \eta \tilde{\mathbf{r}}_k)/(1 - \eta)$
  $\mathbf{r}_{k+1} = \rho \mathbf{r}_{k+1}^{\text{raw}} + (1 - \rho)\mathbf{r}_k$
end for
return $\hat{\mathbf{x}}_{K_{\text{it}}}$

operations. For K_{it} VAMP iterations, the total complexity of VAMP-CG is

$$\mathcal{C}_{\text{VAMP-CG}} = \mathcal{O}(K_{\text{it}} K_{\text{CG}} N^2 + K_{\text{it}} MN). \tag{4.68}$$

In contrast, VAMP-SVD requires singular value decomposition with $\mathcal{O}(N^3)$ complexity as preprocessing, while direct LMMSE detection requires matrix inversion with the same cubic complexity. For typical parameters $K_{\text{it}} = 10$ and $K_{\text{CG}} = 10$, the proposed method achieves $\mathcal{O}(100N^2)$ complexity, yielding a reduction factor of approximately $N/100$ compared to cubic methods. For $N = 512$ subcarriers, this translates to roughly $5\times$ speedup, while for $N = 1024$ the speedup exceeds $10\times$, making the method highly suitable for real-time implementation in large-scale AFDM systems.

4.4 Multi-Path Parallel Interference Cancellation Detector

The Multi-Path Parallel Interference Cancellation (MP-PIC) detector exploits the complete path separation property of AFDM in the DAFT domain [17]. With proper chirp parameter selection, each transmitted symbol $x[q]$ creates distinct, non-overlapping observations at the receiver corresponding to different delay-Doppler paths. The detector performs Bayesian inference across these independent path observations and combines them through reliability-weighted decision statistics combining.

4.4.1 Problem Formulation

The optimal MAP detector is formulated as

$$\hat{\mathbf{x}}_{\text{MAP}} = \arg\max_{\mathbf{x}\in\mathcal{A}^N} p(\mathbf{x}|\mathbf{y}) = \arg\max_{\mathbf{x}\in\mathcal{A}^N} \frac{p(\mathbf{y}|\mathbf{x})\, p(\mathbf{x})}{p(\mathbf{y})}, \tag{4.69}$$

with the likelihood function $p(\mathbf{y}|\mathbf{x})$ taken as Gaussian and represented by

$$p(\mathbf{y}|\mathbf{x}) = \frac{1}{(\pi\sigma^2)^N} \exp\left(-\frac{\|\mathbf{y}-\mathbf{H}_{\text{eff}}\mathbf{x}\|^2}{\sigma^2}\right). \tag{4.70}$$

Assuming a uniform prior, the MAP solution reduces to ML with exponential complexity $\mathcal{O}(|\mathcal{A}|^N)$, which is impractical.

4.4.2 Factorized Gaussian Approximation

We approximate the posterior probability by a factorizable distribution that exploits the path structure of AFDM

$$p(\mathbf{x}|\mathbf{y}) \approx \prod_{q=0}^{N-1} \prod_{i=1}^{L_q} \mathcal{N}\left(x[q]; x^{(t)}_{\text{PIC},q,i}, \Sigma^{(t)}_{q,i}\right), \tag{4.71}$$

where L_q is the number of paths affecting symbol q, $x^{(t)}_{\text{PIC},q,i}$ is the soft estimate of $x[q]$ from path i at iteration t and $\Sigma^{(t)}_{q,i}$ is the variance of the estimate from path i. This factorization is motivated by three properties of the AFDM effective channel [48]. Path separation ensures independent observations per path. Residual noise after interference cancellation is approximately Gaussian. The product form enables efficient computation.

4.4.3 Multi-Path Parallel Interference Cancellation

For symbol q, let $\mathcal{R}_q = \{r_q^1, r_q^2, \ldots, r_q^{L_q}\}$ denote the set of received symbol indices affected by $x[q]$, where $r_q^i = [q - \text{loc}_i]_N$. Conversely, for received symbol $y[p]$, let $\mathcal{C}_p = \{c_p^1, c_p^2, \ldots, c_p^{L_p}\}$ denote the transmitted symbol indices contributing to $y[p]$, where $c_p^i = [p + \text{loc}_i]_N$. The PIC estimate of $x[q]$ from path i at iteration t is

formulated as

$$x^{(t)}_{\mathrm{PIC},q,i} = \frac{1}{|[\mathbf{H}_i]_{r^i_q,q}|^2}\,[\mathbf{H}_i]^*_{r^i_q,q} \times \left(y[r^i_q] - \sum_{j \in \mathcal{C}_{r^i_q} \setminus \{q\}} [\mathbf{H}_{\mathrm{eff}}]_{r^i_q,j}\, \hat{x}^{(t-1)}[j] \right). \quad (4.72)$$

Under the assumption that interference is perfectly canceled, the variance of $x^{(t)}_{\mathrm{PIC},q,i}$ is

$$\Sigma^{(t)}_{q,i} = \frac{\sigma^2}{|[\mathbf{H}_i]_{r^i_q,q}|^2}. \quad (4.73)$$

After interference cancellation, $\tilde{y}[r^i_q] = [\mathbf{H}_i]_{r^i_q,q}\, x[q] + \tilde{w}[r^i_q]$. Applying matched filtering and noting $\tilde{w}[r^i_q] \sim \mathcal{CN}(0, \sigma^2)$ yields the result.

4.4.4 Bayesian Symbol Estimation

Under the factorized approximation, the posterior for symbol q is given by

$$p(x[q]|\mathbf{y}) \propto \prod_{i=1}^{L_q} \exp\left(-\frac{|x[q] - x^{(t)}_{\mathrm{PIC},q,i}|^2}{2\Sigma^{(t)}_{q,i}} \right). \quad (4.74)$$

For the discrete signal constellation $\mathcal{A}$, the probability $p(x[q] = a|\mathbf{y})$ can be expanded as

$$p(x[q] = a|\mathbf{y}) = \frac{\prod_{i=1}^{L_q} \exp\left(-\frac{|a - x^{(t)}_{\mathrm{PIC},q,i}|^2}{2\Sigma^{(t)}_{q,i}} \right)}{\sum_{b \in \mathcal{A}} \prod_{i=1}^{L_q} \exp\left(-\frac{|b - x^{(t)}_{\mathrm{PIC},q,i}|^2}{2\Sigma^{(t)}_{q,i}} \right)}. \quad (4.75)$$

The MAP estimate is reformulated as

$$\hat{x}_{\mathrm{MAP}}[q] = \arg\max_{a \in \mathcal{A}} p(x[q] = a|\mathbf{y}), \quad (4.76)$$

with the conditional mean (MMSE estimate)

$$\hat{x}_{\mathrm{MMSE}}[q] = \mathbb{E}[x[q]|\mathbf{y}] = \sum_{a\in\mathcal{A}} a \cdot p(x[q] = a|\mathbf{y}), \tag{4.77}$$

and the posterior variance

$$V_q^{(t)} = \sum_{a\in\mathcal{A}} |a - \hat{x}_{\mathrm{MMSE}}[q]|^2 \cdot p(x[q] = a|\mathbf{y}). \tag{4.78}$$

For numerical stability, we use log-domain computation

$$\log p(x[q] = a|\mathbf{y}) = -\sum_{i=1}^{L_q} \frac{|a - x_{\mathrm{PIC},q,i}^{(t)}|^2}{2\Sigma_{q,i}^{(t)}} - \log Z_q, \tag{4.79}$$

where $\log Z_q$ is the log-sum-exp normalization constant.

4.4.5 Reliability-Weighted Decision Statistics Combining

4.4.5.1 Inter-Path Combining

Before computing the Bayesian estimate, we first combine the L_q PIC estimates as

$$\bar{x}_{\mathrm{PIC},q}^{(t)} = \sum_{i=1}^{L_q} w_{q,i}^{(t)}\, x_{\mathrm{PIC},q,i}^{(t)}. \tag{4.80}$$

The weights that minimize $\mathbb{E}[|x[q] - \bar{x}_{\mathrm{PIC},q}^{(t)}|^2]$ are

$$w_{q,i}^{(t)} = \frac{(\Sigma_{q,i}^{(t)})^{-1}}{\sum_{j=1}^{L_q} (\Sigma_{q,j}^{(t)})^{-1}}. \tag{4.81}$$

The variance of the combined estimate is

$$\bar{\Sigma}_q^{(t)} = \left(\sum_{i=1}^{L_q} \frac{1}{\Sigma_{q,i}^{(t)}} \right)^{-1}. \tag{4.82}$$

4.4.5.2 Inter-Iteration Combining

To accelerate convergence, we combine estimates across iterations

$$\tilde{x}^{(t)}[q] = \rho_q^{(t)}\, \hat{x}^{(t)}[q] + (1 - \rho_q^{(t)})\, \tilde{x}^{(t-1)}[q], \tag{4.83}$$

where the weighting coefficient is

$$\rho_q^{(t)} = \frac{e_q^{(t-1)}}{e_q^{(t)} + e_q^{(t-1)}}, \tag{4.84}$$

with instantaneous squared error

$$e_q^{(t)} = \left\| \frac{[\mathbf{H}_{\text{eff}}]_{:,q}^H}{\|[\mathbf{H}_{\text{eff}}]_{:,q}\|^2} (\mathbf{y} - \mathbf{H}_{\text{eff}} \hat{\mathbf{x}}^{(t)}) \right\|^2. \tag{4.85}$$

Algorithm 4.3 summarizes the complete MP-PIC detector. The per-iteration complexity is $\mathcal{O}(|\mathcal{A}|L_p N)$.

4.4.6 Computational Complexity of MP-PIC

The computational complexity of the MP-PIC algorithm consists of initialization and iterative components. The initialization requires computing $\hat{\mathbf{x}}^{(0)} = (\mathbf{H}_{\text{eff}}^H \mathbf{H}_{\text{eff}} + \sigma^2 \mathbf{I})^{-1} \mathbf{H}_{\text{eff}}^H \mathbf{y}$, which involves matrix inversion with complexity $\mathcal{O}(N^3)$. This can be optimized to $\mathcal{O}(N^2)$ by exploiting the sparse banded structure of $\mathbf{H}_{\text{eff}}$ using band matrix algorithms. The per-iteration complexity is dominated by three operations. MP-PIC computation requires $\mathcal{O}(NL_p^2)$ operations for interference cancellation across all symbols and paths. Bayesian symbol estimation involves evaluating $|\mathcal{A}|$ constellation points for each of N symbols with L_p paths, yielding $\mathcal{O}(N|\mathcal{A}|L_p)$. RWDSC requires $\mathcal{O}(NL_p)$ operations. The overall per-iteration complexity is therefore

$$\mathcal{C}_{\text{iter}} = \mathcal{O}(N|\mathcal{A}|L_p + NL_p^2) = \mathcal{O}(N|\mathcal{A}|L_p), \tag{4.86}$$

Algorithm 4.3 MP-PIC Detector for AFDM

Input: $\mathbf{y}$, $\mathbf{H}_{\text{eff}}$, σ^2, $\mathcal{A}$, $t_{\max}$, ε
Output: $\hat{\mathbf{x}}$
Initialize:
  $\hat{\mathbf{x}}^{(0)} = (\mathbf{H}_{\text{eff}}^H \mathbf{H}_{\text{eff}} + \sigma^2 \mathbf{I})^{-1} \mathbf{H}_{\text{eff}}^H \mathbf{y}$
  Extract path structure $\mathcal{R}_q$, $\mathcal{C}_p$ for all q, p
  $\tilde{\mathbf{x}}^{(0)} = \hat{\mathbf{x}}^{(0)}$, $t = 1$
while $t \leq t_{\max}$ **do**
  Step 1: Multi-Path Parallel Interference Cancellation
  for each symbol $q = 0, \ldots, N-1$ **do**
    for each path $i = 1, \ldots, L_q$ **do**
      $r_i^q \leftarrow [q - \text{loc}_i]_N$
      $\text{int} \leftarrow \sum_{j \in \mathcal{C}_{r_i^q} \setminus \{q\}} [\mathbf{H}_{\text{eff}}]_{r_i^q, j} \hat{x}^{(t-1)}[j]$
      $x_{\text{PIC},q,i}^{(t)} \leftarrow \frac{[\mathbf{H}_i]_{r_i^q, q}^* (y[r_i^q] - \text{int})}{|[\mathbf{H}_i]_{r_i^q, q}|^2}$
      $\Sigma_{q,i}^{(t)} \leftarrow \frac{\sigma^2}{|[\mathbf{H}_i]_{r_i^q, q}|^2}$
    end for
  end for
  Step 2: Bayesian Symbol Estimation
  for each symbol $q = 0, \ldots, N-1$ **do**
    for each $a \in \mathcal{A}$ **do**
      $\text{logprob}[a] \leftarrow -\sum_{i=1}^{L_q} \frac{|a - x_{\text{PIC},q,i}^{(t)}|^2}{2\Sigma_{q,i}^{(t)}}$
    end for
    $\text{prob} \leftarrow \exp(\text{logprob} - \text{logsumexp}(\text{logprob}))$
    $\hat{x}^{(t)}[q] \leftarrow \sum_{a \in \mathcal{A}} a \cdot \text{prob}[a]$
    $V_q^{(t)} \leftarrow \sum_{a \in \mathcal{A}} |a - \hat{x}^{(t)}[q]|^2 \cdot \text{prob}[a]$
  end for
  Step 3: Reliability-Weighted Decision Statistics Combining
  for each symbol $q = 0, \ldots, N-1$ **do**
    $\text{residual} \leftarrow \mathbf{y} - \mathbf{H}_{\text{eff}} \hat{\mathbf{x}}^{(t)}$
    $e_q^{(t)} \leftarrow \frac{|[\mathbf{H}_{\text{eff}}]_{:,q}^H \, \text{residual}|^2}{\|[\mathbf{H}_{\text{eff}}]_{:,q}\|^4}$
    $\rho_q^{(t)} \leftarrow \frac{e_q^{(t-1)}}{e_q^{(t)} + e_q^{(t-1)}}$
    $\tilde{x}^{(t)}[q] \leftarrow \rho_q^{(t)} \hat{x}^{(t)}[q] + (1 - \rho_q^{(t)}) \tilde{x}^{(t-1)}[q]$
  end for
  Step 4: Convergence Check
  if $\|\tilde{\mathbf{x}}^{(t)} - \tilde{\mathbf{x}}^{(t-1)}\| < \varepsilon$ **then**
    break
  end if
  $\hat{\mathbf{x}}^{(t)} \leftarrow \tilde{\mathbf{x}}^{(t)}$
  $t \leftarrow t + 1$
end while
Return: Hard decision $\hat{\mathbf{x}} = \arg\min_{a \in \mathcal{A}} |a - \tilde{x}^{(t)}[q]|$ for each q

since typically $|\mathcal{A}| \gg L_p$ for practical modulation schemes. With t_{last} iterations required for convergence, the total complexity is

$$\mathcal{C}_{\text{total}} = \mathcal{O}(N^3 + t_{\text{last}}\, N|\mathcal{A}|L_p). \tag{4.87}$$

For properly tuned AFDM parameters ensuring strong diagonal dominance, convergence occurs within $t_{\text{last}} = 3$ to 5 iterations, making the iterative cost comparable to a single LMMSE matrix inversion while achieving superior performance through path diversity exploitation.

4.4.7 Convergence Analysis

4.4.7.1 Matrix Formulation

Define $\mathbf{R} = \mathbf{H}_{\text{eff}}^H \mathbf{H}_{\text{eff}} + \sigma^2 \mathbf{I}$ and $\mathbf{b} = \mathbf{H}_{\text{eff}}^H \mathbf{y}$. The LMMSE solution satisfies

$$\mathbf{R}\,\mathbf{x}_{\text{LMMSE}} = \mathbf{b}. \tag{4.88}$$

Decompose $\mathbf{R} = \mathbf{D} + \mathbf{L} + \mathbf{L}^H$, where $\mathbf{D}$ is diagonal and $\mathbf{L}$ is strictly lower triangular. The MP-PIC update (without inter-iteration combining) can be written as

$$\hat{\mathbf{x}}^{(t)} = -(\mathbf{D} + \mathbf{L})^{-1}\mathbf{L}^H \hat{\mathbf{x}}^{(t-1)} + (\mathbf{D} + \mathbf{L})^{-1}\mathbf{b}. \tag{4.89}$$

This is equivalent to the Gauss-Seidel iteration for solving $\mathbf{R}\mathbf{x} = \mathbf{b}$. The MP-PIC detector converges to the LMMSE solution if and only if the spectral radius of the iteration matrix satisfies

$$\rho(\mathbf{M}_{\text{GS}}) = \rho\left(-(\mathbf{D} + \mathbf{L})^{-1}\mathbf{L}^H\right) < 1. \tag{4.90}$$

From the update equation,

$$\hat{\mathbf{x}}^{(t)} - \mathbf{x}_{\text{LMMSE}} = \mathbf{M}_{\text{GS}}(\hat{\mathbf{x}}^{(t-1)} - \mathbf{x}_{\text{LMMSE}}). \tag{4.91}$$

By induction, $\hat{\mathbf{x}}^{(t)} - \mathbf{x}_{\text{LMMSE}} = \mathbf{M}_{\text{GS}}^{t}(\hat{\mathbf{x}}^{(0)} - \mathbf{x}_{\text{LMMSE}})$. Convergence occurs iff $\lim_{t\to\infty} \mathbf{M}_{\text{GS}}^{t} = \mathbf{0}$, which requires $\rho(\mathbf{M}_{\text{GS}}) < 1$.

If $\mathbf{R} = \mathbf{H}_{\text{eff}}^{H}\mathbf{H}_{\text{eff}} + \sigma^2\mathbf{I}$ is a positive definite Hermitian matrix, then $\rho(\mathbf{M}_{\text{GS}}) < 1$ and the detector converges. For any eigenvector $\mathbf{v}$ of $\mathbf{M}_{\text{GS}}$ with eigenvalue λ,

$$-(\mathbf{D}+\mathbf{L})^{-1}\mathbf{L}^{H}\mathbf{v} = \lambda\mathbf{v}. \tag{4.92}$$

Multiplying both sides by $\mathbf{v}^{H}(\mathbf{D}+\mathbf{L})$,

$$-\mathbf{v}^{H}\mathbf{L}^{H}\mathbf{v} = \lambda\mathbf{v}^{H}(\mathbf{D}+\mathbf{L})\mathbf{v}. \tag{4.93}$$

Since $\mathbf{R}$ is positive definite,

$$\mathbf{v}^{H}\mathbf{R}\mathbf{v} = \mathbf{v}^{H}(\mathbf{D}+\mathbf{L}+\mathbf{L}^{H})\mathbf{v} > 0. \tag{4.94}$$

Let $a = \text{Re}(\mathbf{v}^{H}\mathbf{L}^{H}\mathbf{v})$ and $b = \text{Im}(\mathbf{v}^{H}\mathbf{L}^{H}\mathbf{v})$. Then

$$\mathbf{v}^{H}\mathbf{D}\mathbf{v} + 2a > 0 \Rightarrow a > -\frac{\mathbf{v}^{H}\mathbf{D}\mathbf{v}}{2}. \tag{4.95}$$

From the eigenvalue equation,

$$\lambda = \frac{a - jb}{\mathbf{v}^{H}\mathbf{D}\mathbf{v} + a - jb}, \tag{4.96}$$

and the eigenvalue magnitude is

$$|\lambda|^2 = \frac{a^2 + b^2}{(\mathbf{v}^{H}\mathbf{D}\mathbf{v} + a)^2 + b^2} < 1, \tag{4.97}$$

since $\mathbf{v}^H\mathbf{D}\mathbf{v} + a > 0$. Thus $|\lambda| < 1$ for all eigenvalues. For well-conditioned AFDM channels where $\mathbf{H}_{\text{eff}}$ has full column rank and $\sigma^2 > 0$, $\mathbf{R}$ is always positive definite, guaranteeing convergence.

4.4.7.2 Rate of Convergence

The error at iteration t satisfies

$$\|\hat{\mathbf{x}}^{(t)} - \mathbf{x}_{\text{LMMSE}}\| \leq \rho(\mathbf{M}_{\text{GS}})^t \, \|\hat{\mathbf{x}}^{(0)} - \mathbf{x}_{\text{LMMSE}}\|. \tag{4.98}$$

For ε-accuracy, the required number of iterations is

$$t_\varepsilon = \left\lceil \frac{\log\left(\varepsilon / \|\hat{\mathbf{x}}^{(0)} - \mathbf{x}_{\text{LMMSE}}\|\right)}{\log \rho(\mathbf{M}_{\text{GS}})} \right\rceil. \tag{4.99}$$

For AFDM with proper parameter selection, the banded structure of $\mathbf{H}_{\text{eff}}$ leads to strong diagonal dominance in $\mathbf{R}$, resulting in $\rho(\mathbf{M}_{\text{GS}}) \ll 1$ and fast convergence (typically 3 to 5 iterations).

4.5 Variational Bayesian Detector for Quantized AFDM

The practical realization of AFDM systems must account for hardware-induced impairments, particularly the quantization distortion arising from finite-resolution analog-to-digital converters [34,35,77]. Quantization noise differs from thermal noise in critical ways. It is signal dependent, has non-Gaussian statistics, and introduces nonlinear distortions that violate the assumptions underlying conventional linear detection. We propose a Variational Bayesian detection framework [32, 33] that explicitly incorporates the quantization constraints through a truncated Gaussian likelihood while exploiting the sparse delay-Doppler structure of the AFDM channel.

Three families of detectors are mainly available for the quantized observation

model. Bussgang-based linear receivers replace the quantizer by an equivalent linear gain plus uncorrelated distortion, which is analytically convenient but discards the interval information carried by each quantized sample. Generalized AMP handles the nonlinearity exactly through a component wise output channel, but its convergence relies on the measurement matrix being sufficiently close to i.i.d. Gaussian, a condition the banded $\mathbf{H}_{\text{eff}}$ of AFDM does not satisfy. The mean-field variational approach adopted here retains the exact quantization likelihood while imposing no distributional assumption on $\mathbf{H}_{\text{eff}}$, and it guarantees monotone convergence of the evidence lower bound. This combination motivates its selection.

4.5.1 Quantization Model

The uniform b_q-bit scalar quantizer operates on real and imaginary parts separately

$$r^q[k] = \mathcal{Q}_{\mathcal{R}}(\mathcal{R}\{r[k]\}) + j\mathcal{Q}_{\mathcal{I}}(\mathcal{I}\{r[k]\}). \tag{4.100}$$

For input $z \in \mathbb{R}$, the quantizer is defined by thresholds $\{u_j\}_{j=0}^{2^{b_q}}$ and output levels $\{c_j\}_{j=1}^{2^{b_q}}$ as

$$\mathcal{Q}(z) = \sum_{j=1}^{2^{b_q}} c_j \mathbb{1}(u_{j-1} < z \leq u_j), \tag{4.101}$$

where $\mathbb{1}(\cdot)$ denotes the indicator function, equal to unity when its argument is true and zero otherwise, so that $\mathbb{1}(u_{j-1} < z \leq u_j)$ selects the output level c_j associated with the interval $(u_{j-1}, u_j]$, $c_j = (u_{j-1} + u_j)/2$ and the step size is

$$\Delta_q = \frac{2\max_k(|\mathcal{R}\{r[k]\}|, |\mathcal{I}\{r[k]\}|)}{2^{b_q}}. \tag{4.102}$$

For symmetric quantization, $u_j = -2^{b_q-1}\Delta_q + j\Delta_q$, with $u_0 = -\infty$ and $u_{2^{b_q}} = \infty$. The quantization error is $e^q[k] = r^q[k] - r[k]$, with statistics $\mathbb{E}[e^q[k]] = 0$ and

$\mathbb{E}[|e^q[k]|^2] = \Delta_q^2/12$. The complete quantized observation is written as

$$\mathbf{r}^q = \mathcal{Q}(\mathbf{H}_{\text{td}}\mathbf{s} + \mathbf{w}) = \mathbf{r} + \mathbf{e}^q. \tag{4.103}$$

Applying DAFT at the receiver, the DAFT-domain quantized observation is

$$\mathbf{y}^q = \mathbf{A}\,\mathbf{r}^q = \mathbf{A}\,\mathcal{Q}(\mathbf{H}_{\text{td}}\mathbf{A}^H\mathbf{x} + \mathbf{w}), \tag{4.104}$$

which can be written as $\mathbf{y}^q = \mathcal{Q}(\mathbf{H}_{\text{eff}}\mathbf{x} + \tilde{\mathbf{w}})$ when the quantization is applied in the DAFT domain after the unitary transform.

4.5.2 Probabilistic Model Construction

We formulate the detection problem in a Bayesian framework by modeling all unknown quantities as random variables with appropriate priors, where the transmitted symbol vector $\mathbf{x}$ is the primary variable of interest and the joint distribution incorporates the symbol prior, the conditional likelihood of received samples given the symbols and channel, and the quantization likelihood relating analog and quantized observations

$$p(\mathbf{y}^q, \mathbf{r}, \mathbf{x}|\mathbf{H}_{\text{eff}}) = p(\mathbf{y}^q|\mathbf{r})\,p(\mathbf{r}|\mathbf{x}, \mathbf{H}_{\text{eff}})\,p(\mathbf{x}). \tag{4.105}$$

The quantization likelihood decomposes as

$$p(\mathbf{y}^q|\mathbf{r}) = \prod_{k=0}^{N-1} p(y^q[k]|r[k]). \tag{4.106}$$

For each observation component, the quantization likelihood is determined by the quantization interval. Given the quantized value $y^q[k]$ with real part in interval

$[u_{j_r}, u_{j_r+1})$ and imaginary part in $[u_{j_i}, u_{j_i+1})$,

$$\begin{aligned} p(y^q[k]|r[k]) = &\mathbb{1}(u_{j_r} < \mathcal{R}\{r[k]\} \leq u_{j_r+1}) \\ &\times \mathbb{1}(u_{j_i} < \mathcal{I}\{r[k]\} \leq u_{j_i+1}). \end{aligned} \tag{4.107}$$

The channel output likelihood follows a complex Gaussian distribution

$$p(\mathbf{r}|\mathbf{x}, \mathbf{H}_{\text{eff}}) = \mathcal{CN}(\mathbf{r}; \mathbf{H}_{\text{eff}}\mathbf{x}, N_0\mathbf{I}_N). \tag{4.108}$$

We assume uniform priors over the discrete constellation

$$p(\mathbf{x}) = \prod_{m=0}^{N-1} p(x[m]) = \prod_{m=0}^{N-1} \frac{1}{|\mathcal{A}|}. \tag{4.109}$$

The detection objective is to compute the posterior marginals $p(x[m]|\mathbf{y}^q, \mathbf{H}_{\text{eff}})$ for each symbol. Exact computation requires evaluating an intractable marginalization over the continuous latent variables $\mathbf{r}$ and summing over all possible symbol configurations.

4.5.3 Mean-Field Variational Approximation

The mean-field approximation restricts the variational family to distributions that factorize completely across the symbol indices, so that each symbol is treated as *a posteriori* independent of the others. The dependence induced by the channel is not discarded but is retained in an averaged form, since each factor is updated against the expectation of the joint log-likelihood taken over all the remaining factors. The name reflects this: every symbol responds to the mean field exerted by its neighbors rather than to their joint realization.

We approximate the posterior using a factorized distribution [32]

$$q(\mathbf{x}) = \prod_{m=0}^{N-1} q_m(x[m]) = \prod_{m=0}^{N-1} \sum_{a \in \mathcal{A}} \pi_{m,a}\, \delta(x[m] - a), \tag{4.110}$$

where $\pi_{m,a}$ represents the probability that symbol m takes value $a \in \mathcal{A}$. The variational objective is to maximize the Evidence Lower Bound (ELBO)

$$\mathcal{L}(q) = \mathbb{E}_q[\log p(\mathbf{y}^q, \mathbf{x}|\mathbf{H}_{\text{eff}})] - \mathbb{E}_q[\log q(\mathbf{x})]. \tag{4.111}$$

By decomposing the ELBO and isolating terms involving $q_m(x[m])$, we obtain the standard mean-field update

$$\log q_m^*(x[m]) = \mathbb{E}_{q_{-m}}[\log p(\mathbf{y}^q, \mathbf{x}|\mathbf{H}_{\text{eff}})] + \text{const}, \tag{4.112}$$

where $q_{-m} = \prod_{m' \neq m} q_{m'}(x[m'])$ denotes the approximate posterior with the mth factor excluded. Due to the sparsity of $\mathbf{H}_{\text{eff}}$, each observation $y^q[k]$ depends only on symbols in a neighborhood

$$\mathcal{M}(k) = \{m \mid h_{k,m} \neq 0\}. \tag{4.113}$$

Conversely, each symbol $x[m]$ affects observations in

$$\mathcal{N}(m) = \{k \mid h_{k,m} \neq 0\}. \tag{4.114}$$

The ELBO is framed as

$$\log q_m^*(x[m]) = \sum_{k \in \mathcal{N}(m)} \mathbb{E}_{q_{-m}}[\log p(y^q[k]|r[k])] + \text{const}. \tag{4.115}$$

4.5.4 Gaussian Approximation of Interference

For fixed $x[m] = a$, the received signal at observation k is

$$r[k] = h_{k,m}\, a + \sum_{m' \in \mathcal{M}(k) \setminus \{m\}} h_{k,m'}\, x[m'] + w[k]. \tag{4.116}$$

We approximate the interference-plus-noise term as a complex Gaussian random variable. We define the interference statistics as

$$\mu_k^{(-m)} = \sum_{m' \in \mathcal{M}(k) \setminus \{m\}} h_{k,m'} \, \bar{x}_{m'}, \tag{4.117}$$

$$\sigma_k^{2(-m)} = \sum_{m' \in \mathcal{M}(k) \setminus \{m\}} |h_{k,m'}|^2 \, v_{m'}, \tag{4.118}$$

where the moments under q are

$$\bar{x}_m = \mathbb{E}_{q_m}[x[m]] = \sum_{a \in \mathcal{A}} a \, \pi_{m,a}, \tag{4.119}$$

$$v_m = \mathbb{E}_{q_m}[|x[m] - \bar{x}_m|^2] = \sum_{a \in \mathcal{A}} |a|^2 \, \pi_{m,a} - |\bar{x}_m|^2. \tag{4.120}$$

Under this approximation, the received signal component is modeled as

$$r[k] \, | \, x[m] = a \sim$$

$$\mathrm{CN}(\mu_k^{(-m)} + h_{k,m} \, a, \, \sigma_k^{2(-m)} + N_0). \tag{4.121}$$

This Gaussian approximation is key to deriving tractable closed-form updates, as it reduces the complex integrals over latent variables to evaluations of Gaussian cumulative distribution functions.

4.5.5 Truncated Gaussian Likelihood Evaluation

The quantization likelihood $p(y^q[k]|r[k])$ is an indicator function over quantization intervals [76]. For Gaussian $r[k]$, the expectation becomes

$$\begin{aligned} \mathbb{E}_{r[k]|x[m]=a}[p(y^q[k]|r[k])] = P\Big(\ell_r^{(k)} < \mathcal{R}\{r[k]\} \leq u_r^{(k)}, \\ \ell_i^{(k)} < \mathcal{I}\{r[k]\} \leq u_i^{(k)} \, \Big| \, x[m] = a\Big). \end{aligned} \tag{4.122}$$

Since real and imaginary parts are independent Gaussians with variance $(\sigma_k^{2(-m)} + N_0)/2$, this factorizes as

$$\begin{aligned}
&\mathbb{E}_{r[k]|x[m]=a}[p(y^q[k]|r[k])] \\
&= \Phi_c\left(\frac{u_r^{(k)} - \mathcal{R}\{\mu_k^{(-m)} + h_{k,m}a\}}{\tilde{\sigma}_k}, \frac{\ell_r^{(k)} - \mathcal{R}\{\mu_k^{(-m)} + h_{k,m}a\}}{\tilde{\sigma}_k}\right) \\
&\quad \times \Phi_c\left(\frac{u_i^{(k)} - \mathcal{I}\{\mu_k^{(-m)} + h_{k,m}a\}}{\tilde{\sigma}_k}, \frac{\ell_i^{(k)} - \mathcal{I}\{\mu_k^{(-m)} + h_{k,m}a\}}{\tilde{\sigma}_k}\right),
\end{aligned} \tag{4.123}$$

where $\Phi_c(a,b) = \Phi(a) - \Phi(b)$ is the cumulative Gaussian probability over the interval $(b,a]$ and $\tilde{\sigma}_k = \sqrt{(\sigma_k^{2(-m)} + N_0)/2}$. Taking logarithms provides the log-likelihood contribution

$$\begin{aligned}
\Lambda_{k,m}(a) = &\log \Phi_c\left(\frac{u_r^{(k)} - \mathcal{R}\{\mu_k^{(-m)} + h_{k,m}a\}}{\tilde{\sigma}_k}, \frac{\ell_r^{(k)} - \mathcal{R}\{\mu_k^{(-m)} + h_{k,m}a\}}{\tilde{\sigma}_k}\right) \\
&+ \log \Phi_c\left(\frac{u_i^{(k)} - \mathcal{I}\{\mu_k^{(-m)} + h_{k,m}a\}}{\tilde{\sigma}_k}, \frac{\ell_i^{(k)} - \mathcal{I}\{\mu_k^{(-m)} + h_{k,m}a\}}{\tilde{\sigma}_k}\right).
\end{aligned} \tag{4.124}$$

4.5.6 Symbol Probability Update

Aggregating contributions from all affected observations, the unnormalized probability for symbol m taking value a is

$$\tilde{\pi}_{m,a} = \exp\left(\sum_{k \in \mathcal{N}(m)} \Lambda_{k,m}(a)\right). \tag{4.125}$$

Normalization yields the updated probability distribution

$$\pi_{m,a}^{\text{new}} = \frac{\tilde{\pi}_{m,a}}{\sum_{a' \in \mathcal{A}} \tilde{\pi}_{m,a'}}. \tag{4.126}$$

The first and second moments required for subsequent iterations are

$$\bar{x}_m^{\text{new}} = \sum_{a \in \mathcal{A}} a\, \pi_{m,a}^{\text{new}}, \tag{4.127}$$

$$v_m^{\text{new}} = \sum_{a\in\mathcal{A}} |a|^2 \pi_{m,a}^{\text{new}} - |\bar{x}_m^{\text{new}}|^2. \tag{4.128}$$

These moments fully characterize the approximate posterior for each symbol and are used to compute interference statistics in the next iteration.

Algorithm 4.4 summarizes the VB detector for quantized AFDM. The algorithm iteratively refines the symbol probabilities by alternating between computing interference statistics from current beliefs and updating beliefs based on quantized observations. The convergence criterion ensures that the probability estimates have stabilized before making final detection decisions.

Algorithm 4.4 VB Detection for Quantized AFDM

Input: Effective channel $\mathbf{H}_{\text{eff}}$, quantized samples $\mathbf{y}^q$, constellation $\mathcal{A}$, maximum iterations $T_{\max}$, tolerance ϵ
Initialize: $\pi_m^{(0)}(a) = 1/|\mathcal{A}|$ for all symbols m and $a \in \mathcal{A}$
Compute initial moments $\bar{x}_m^{(0)}$, $v_m^{(0)}$
for $t = 1$ to $T_{\max}$ **do**
    for each symbol $m = 0, \ldots, N-1$ **do**
        Compute interference statistics for all $k \in \mathcal{N}(m)$
        $\mu_k^{(-m)} = \sum_{m'\in\mathcal{M}(k)\setminus\{m\}} h_{k,m'} \bar{x}_{m'}^{(t-1)}$
        $\sigma_k^{2(-m)} = \sum_{m'\in\mathcal{M}(k)\setminus\{m\}} |h_{k,m'}|^2 v_{m'}^{(t-1)}$
        For each $a \in \mathcal{A}$, compute $\Lambda_{k,m}^{(t)}(a)$ using (4.124)
        Update unnormalized probability $\tilde{\pi}_m^{(t)}(a) = \exp\left(\sum_{k\in\mathcal{N}(m)} \Lambda_{k,m}^{(t)}(a)\right)$
        Normalize $\pi_m^{(t)}(a) = \tilde{\pi}_m^{(t)}(a) / \sum_{a'\in\mathcal{A}} \tilde{\pi}_m^{(t)}(a')$
        Update posterior moments $\bar{x}_m^{(t)} = \sum_{a\in\mathcal{A}} a\, \pi_m^{(t)}(a)$, $v_m^{(t)} = \sum_{a\in\mathcal{A}} |a|^2 \pi_m^{(t)}(a) - |\bar{x}_m^{(t)}|^2$
    end for
    if $\max_{m,a} |\pi_m^{(t)}(a) - \pi_m^{(t-1)}(a)| < \epsilon$ **then**
        break
    end if
end for
Output: Hard decisions $\hat{x}_m = \arg\max_a \pi_m^{(T)}(a)$ or soft estimates $\hat{x}_m = \bar{x}_m^{(T)}$

4.5.7 ELBO Monotonicity

Define the ELBO at iteration t as

$$\begin{aligned}\mathcal{L}^{(t)} = &\sum_m \sum_a \pi_{m,a}^{(t)} \sum_{k\in\mathcal{N}(m)} \mathbb{E}_{q_{-m}^{(t)}} \left[\log p(y^q[k]|x[m]=a, \mathbf{x}_{-m})\right] \\ &- \sum_m \sum_a \pi_{m,a}^{(t)} \log \pi_{m,a}^{(t)}.\end{aligned} \tag{4.129}$$

Since each update maximizes the ELBO with respect to one factor while holding others fixed,

$$\mathcal{L}^{(t+1)} \geq \mathcal{L}^{(t)}. \tag{4.130}$$

The sequence $\{\mathcal{L}^{(t)}\}$ is bounded above by $\log p(\mathbf{y}^q|\mathbf{H}_{\text{eff}})$, thus convergence is guaranteed. This theoretical guarantee ensures that the algorithm will not oscillate indefinitely and provides confidence in the iterative approach.

4.5.8 Computational Complexity of VB-Quantized AFDM

For each symbol m at iteration t, the algorithm performs three main operations. Computing interference statistics using (4.117) and (4.118) requires $\mathcal{O}(L_p)$ complex multiplications, where L_p is the channel sparsity level. Evaluating log-likelihood contributions $\Lambda_{k,m}(a)$ for each $a \in \mathcal{A}$ involves $|\mathcal{A}| \cdot |\mathcal{N}(m)|$ cumulative distribution function evaluations, yielding $\mathcal{O}(|\mathcal{A}|L_p)$ operations. Probability normalization and moment updates require $\mathcal{O}(|\mathcal{A}|)$ operations. The per-symbol complexity is dominated by $\mathcal{O}(|\mathcal{A}|L_p)$. Aggregating over all N symbols, the complexity per iteration is

$$\mathcal{C}_{\text{iter}} = \mathcal{O}(N|\mathcal{A}|L_p), \tag{4.131}$$

and for $T_{\max}$ iterations, the total complexity is

$$\mathcal{C}_{\text{total}} = \mathcal{O}(T_{\max}N|\mathcal{A}|L_p), \tag{4.132}$$

which scales linearly in all system parameters.

4.6 Simulation Results

4.6.1 VAMP-CG Performance

The proposed VAMP-CG detector is evaluated through Monte Carlo simulations over doubly dispersive channels with $N = 64$ subcarriers, subcarrier spacing $\Delta f = 1$ MHz, and carrier frequency $f_c = 4$ GHz. The wireless channel consists of $P = 4$ propagation paths with maximum delay spread $L_{\max} = 3$ samples and a maximum UE velocity of 800 km/h. Complex path gains follow $h_i \sim \mathcal{CN}(0, \sigma_h^2/P)$ with $\sigma_h^2 = 1$, path delays are uniformly distributed over $\{0, 1, \ldots, L_{\max}\}$, and Doppler frequencies over $[-f_{\max}, f_{\max}]$. The DAFT parameters are computed as $c_1 = (2\alpha_{\max} + 1)/(2N)$ where $\alpha_{\max} = \lceil N f_{\max} \rceil$ and $c_2 = 1/\sqrt{\pi N^2}$, with chirp-periodic prefix length $L_{\text{cp}} = L_{\max} + 1$. Both VAMP-CG and VAMP-SVD employ $K_{\text{it}} = 15$ outer iterations with the conjugate gradient solver using $K_{\text{CG}} = 10$ inner iterations, convergence tolerance $\epsilon_{\text{tol}} = 10^{-7}$, damping factor $\rho = 0.97$, and precision clipping $[\gamma_{\min}, \gamma_{\max}] = [10^{-11}, 10^{11}]$.

Fig. 4.1 compares the BER performance of VAMP-CG, VAMP-SVD, and LMMSE detectors across BPSK, QPSK and 16-QAM modulation. The proposed VAMP-CG achieves virtually identical performance to VAMP-SVD with degradation less than 0.2 dB across all modulation orders and SNR values, confirming that the conjugate gradient approach maintains detection accuracy while eliminating expensive matrix decomposition. Both VAMP detectors significantly outperform linear MMSE, providing gains of 2 to 3 dB for QPSK and 4 to 5 dB for 16-QAM at moderate BER levels due to iterative exploitation of constellation structure.

Fig. 4.2 demonstrates the scalability of VAMP-CG across modulation orders from QPSK to 256-QAM, showing consistent convergence and robust performance even for high-order constellations.

Fig. 4.3 examines the relationship between system dimension and detection performance. AFDM requires a minimum number of subcarriers $N_{\min} = 2\alpha_{\max}(l_{\max} +$

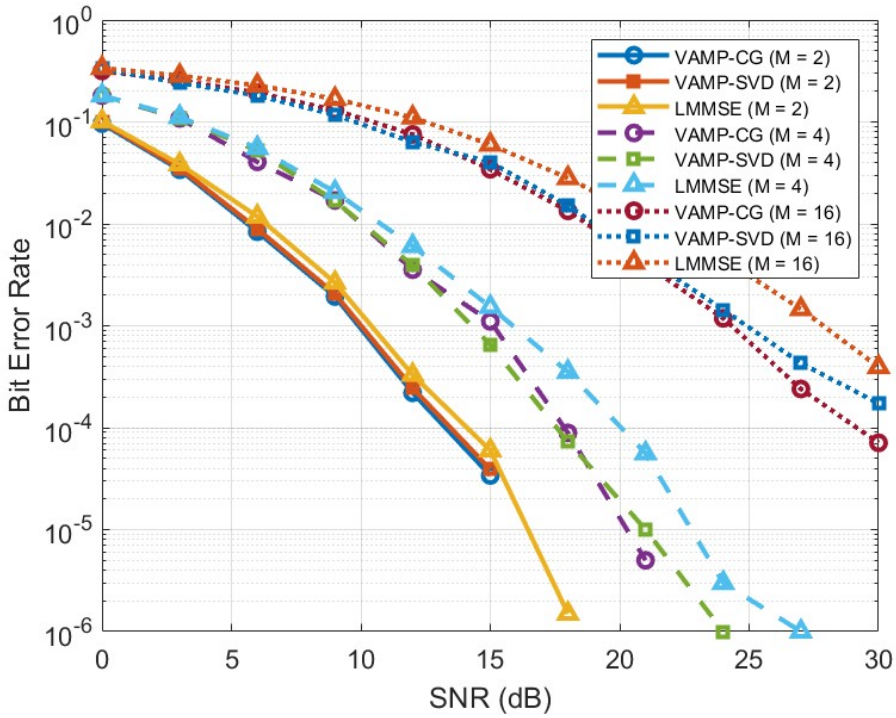


Figure 4.1: BER performance comparison of VAMP-CG, VAMP-SVD, and MMSE detectors

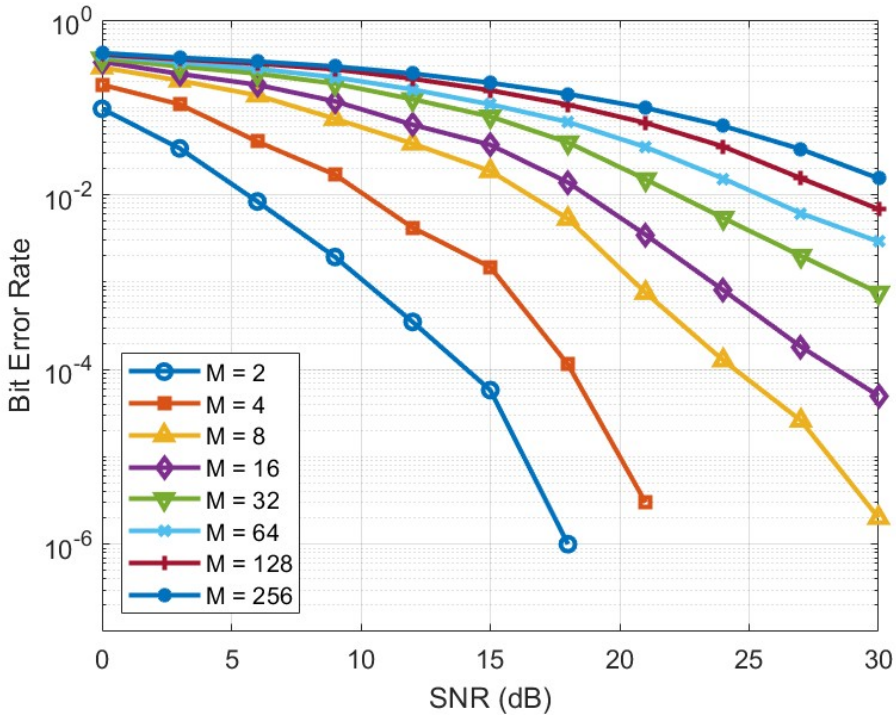


Figure 4.2: BER performance of the proposed VAMP-CG detector across multiple modulation orders

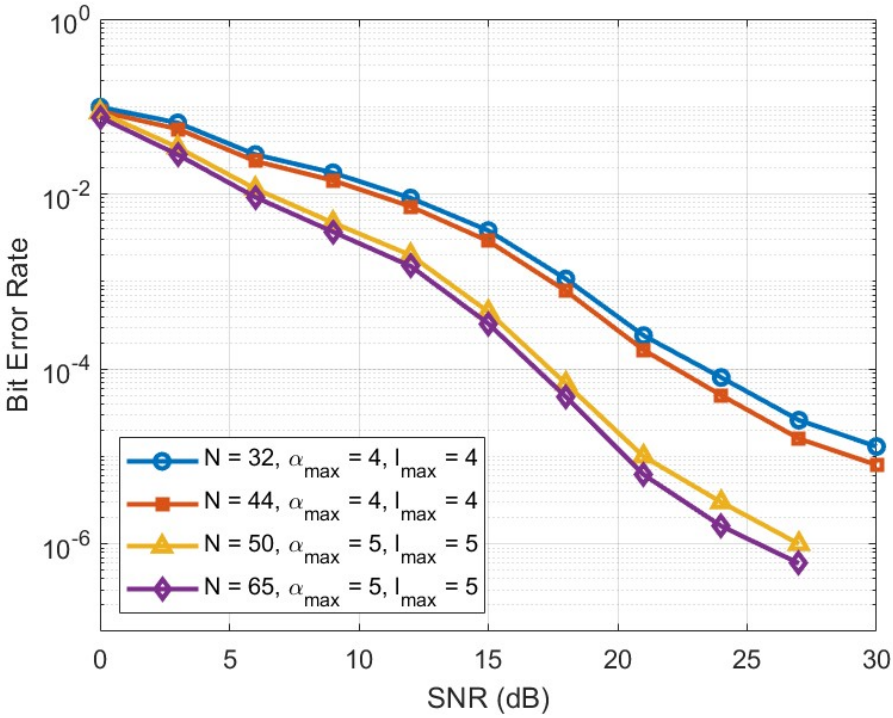


Figure 4.3: Impact of system dimension on VAMP-CG detector performance with varying number of subcarriers and channel parameters

$1)+l_{\max}$ to preserve chirp orthogonality in the DAFT domain. Configurations with $N < N_{\min}$ violate this condition, causing severe performance degradation due to inter-path interference. The proposed VAMP-CG detector is particularly valuable for such minimal-dimension systems where the $\mathcal{O}(N^2)$ complexity advantage over SVD-based methods becomes critical for resource-constrained implementations. The results confirm that $N = 32$ with $(l_{\max}, \alpha_{\max}) = (4,4)$ yields $N_{\min} = 44$, exhibiting error floors above BER $= 10^{-3}$, while $N = 65$ with $(l_{\max}, \alpha_{\max}) = (5,5)$ satisfies the orthogonality constraint and achieves BER below 10^{-6} at 30 dB SNR.

Fig. 4.4 examines the sensitivity of VAMP-CG to fractional Doppler for $N = 64$ subcarriers with $P = 2$ paths, maximum normalised delay and Doppler $l_{\max} = \alpha_{\max} = 2$, and $K_{\text{it}} = 15$ outer iterations. The on-grid case, in which each path Doppler is an exact multiple of the Doppler resolution, is compared with the off-grid case, in which the shifts are drawn continuously over $[-\alpha_{\max}, \alpha_{\max}]$ so that their energy leaks across neighbouring DAFT bins. The two cases yield nearly coincident

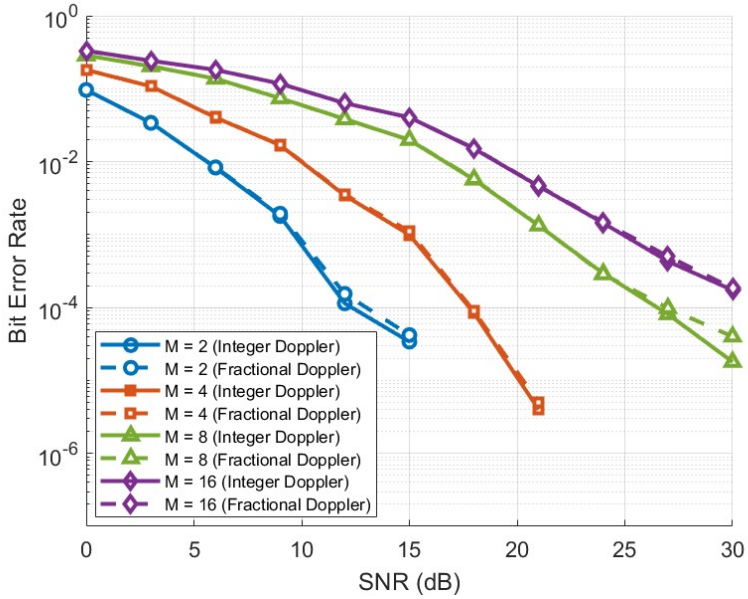


Figure 4.4: BER of the proposed VAMP-CG detector under integer and fractional Doppler for AFDM with $N = 64$ and modulation orders $M = 2, 4, 8, 16$

BER curves for all modulation orders from $M = 2$ to $M = 16$, the gap staying within a fraction of a decibel even at high SNR. This follows from the detector operating directly on $\mathbf{H}_{\text{eff}}$ as realised, so the off-grid coupling is absorbed into the channel matrix and handled by the same LMMSE and denoising updates, with no dedicated cancellation or grid-refinement step.

Fig. 4.5 relaxes the perfect-CSI assumption for QPSK AFDM with the same $N = 64$, $P = 2$ and $l_{\max} = \alpha_{\max} = 2$. The detector is supplied with an imperfect estimate of the effective channel, $\hat{\mathbf{H}}_{\text{eff}} = \mathbf{H}_{\text{eff}} + \mathbf{E}$, where the error term $\mathbf{E} \sim \mathcal{CN}(\mathbf{0}, \beta\sigma_h^2\mathbf{I})$ is zero-mean complex Gaussian with variance $\beta\sigma_h^2$ and $\beta \geq 0$ scales the error power relative to the channel power σ_h^2. This additive Gaussian model is the standard abstraction for pilot-based least-squares and MMSE channel estimation, whose residual error is asymptotically Gaussian and whose variance scales inversely with pilot SNR; β therefore acts as a single, estimator-agnostic knob that spans the range from perfect CSI ($\beta = 0$) to severe mismatch without committing the analysis to one particular estimator. For $\beta \leq 10^{-3}$ the BER is indistinguishable from perfect CSI; for $\beta \geq 10^{-2}$ a residual error floor emerges at high SNR, reaching about 10^{-2} at

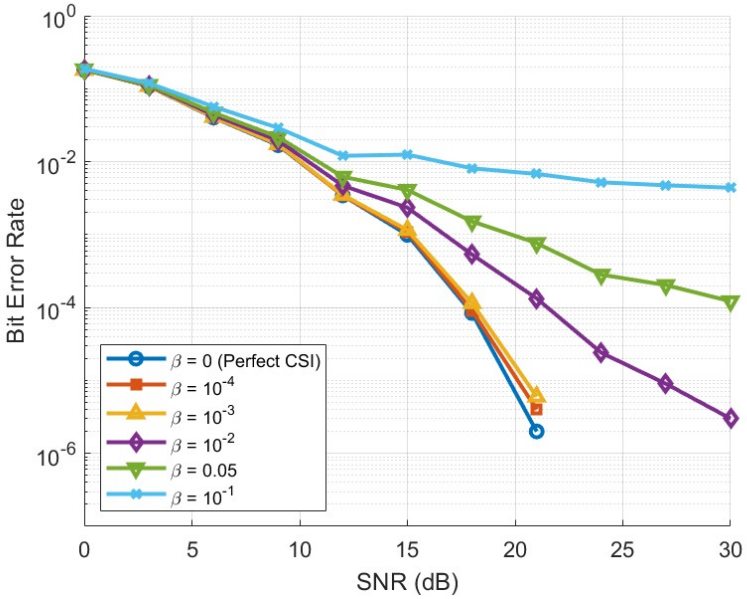


Figure 4.5: BER of the proposed VAMP-CG detector under imperfect CSI for QPSK AFDM with $N = 64$, with change in the estimation error variance scaled by β

$\beta = 10^{-1}$, since the mismatch term acts as an SNR-independent noise contribution that eventually dominates. This is the expected effect of channel mismatch and delineates the estimation accuracy needed to preserve the reported gains. A joint channel-estimation-and-detection scheme addressing this is noted as future work.

4.6.2 MP-PIC Performance

The simulation setup considers N subcarriers, subcarrier spacing $\Delta f = 1$ MHz, and a carrier frequency $f_c = 4$ GHz. The wireless channel is modeled with P multipath components and a maximum delay spread of $L_{\max} = 3$ samples, corresponding to an Extended Vehicular A (EVA) profile. The UE velocity is assumed to be 800 km/h. Each channel tap is generated as $h_i \sim \mathcal{CN}(0, \sigma_h^2/P)$. For AFDM, the system parameters are $c_1 = (2\alpha_{\max} + 1)/(2N)$ and $c_2 = 1/\sqrt{\pi N^2}$.

Fig. 4.6 and Fig. 4.7 compare the BER performance of the MP-PIC detector against baseline schemes including MMSE, standard message passing (MP) [49], and variational Bayesian (VB) detectors [74] for $N = 20$ subcarriers with $P = 5$ and $P = 10$ paths. The results demonstrate that MP-PIC achieves significant performance

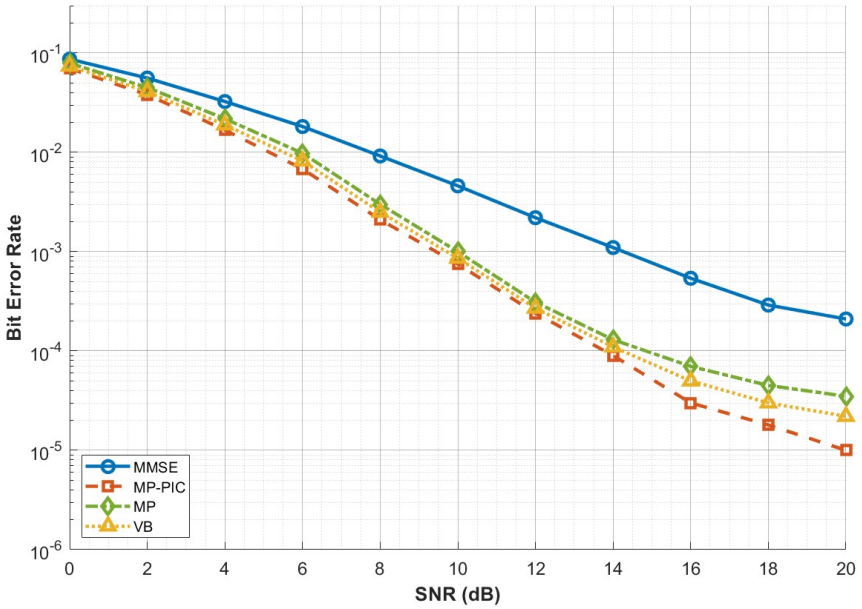


Figure 4.6: BER performance of the MP-PIC detector with $N = 20$ and $P = 5$ paths

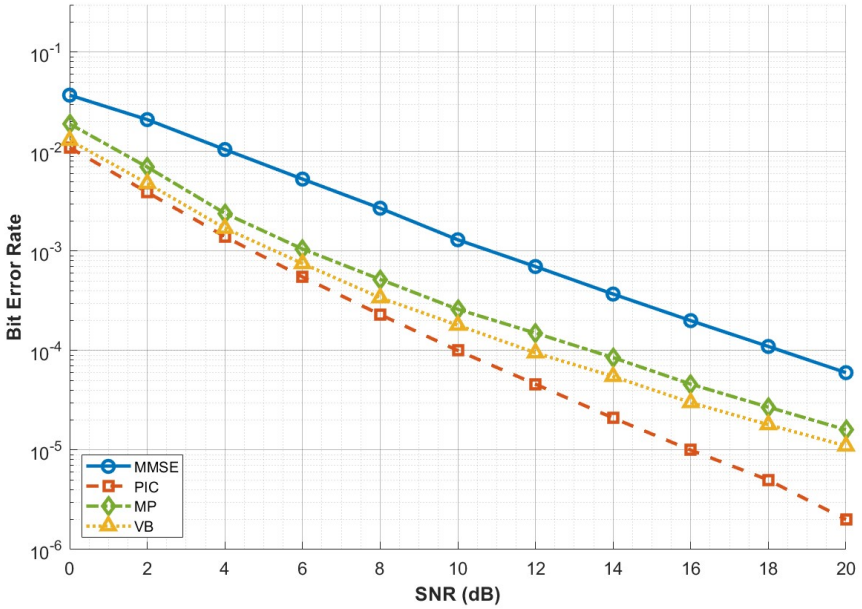


Figure 4.7: BER performance of the MP-PIC detector with $N = 20$ and $P = 10$ paths

gains over MMSE across all SNR values, with improvements of approximately 4 to 5 dB at BER $= 10^{-4}$. The MP-PIC detector consistently outperforms both MP and VB approaches, validating the effectiveness of exploiting path diversity through parallel interference cancellation combined with reliability-weighted combining.

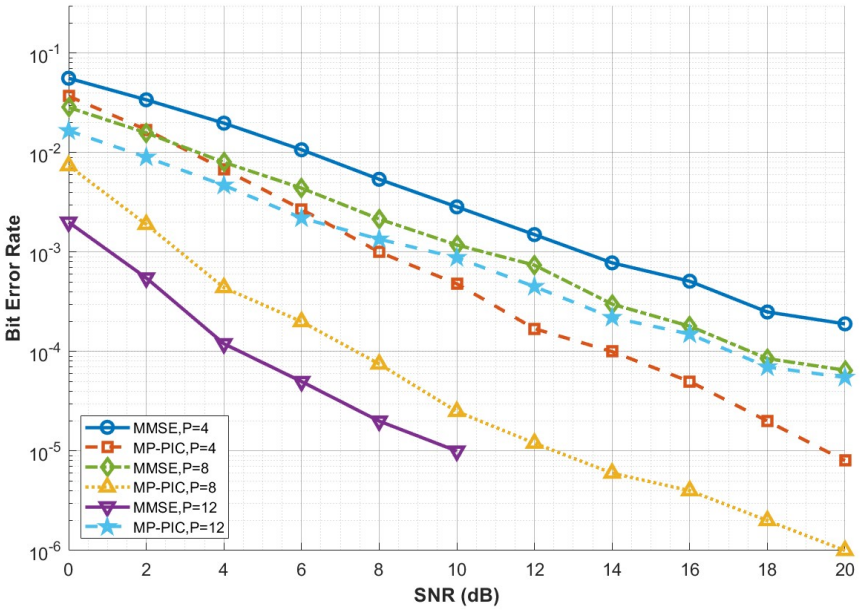


Figure 4.8: BER performance comparison of the MP-PIC detector at $N = 20$ across different path counts $P = 4, 8, 10, 12$

Fig. 4.8 and Fig. 4.9 illustrate the impact of path diversity on detection performance by comparing MMSE and MP-PIC for varying numbers of paths ($P = 4, 8, 10, 12$) at $N = 20$ and $N = 40$ subcarriers. The performance gap between MMSE and MP-PIC widens substantially as the number of paths increases, with gains reaching 6 to 8 dB for $P = 12$ at BER $= 10^{-5}$. This trend confirms that the proposed detector effectively harnesses path diversity, since more resolvable paths provide additional independent observations that improve symbol estimation accuracy. Increasing the frame size from $N = 20$ to $N = 40$ enhances performance for both detectors due to improved DAFT resolution, though MP-PIC maintains consistent superiority across all configurations.

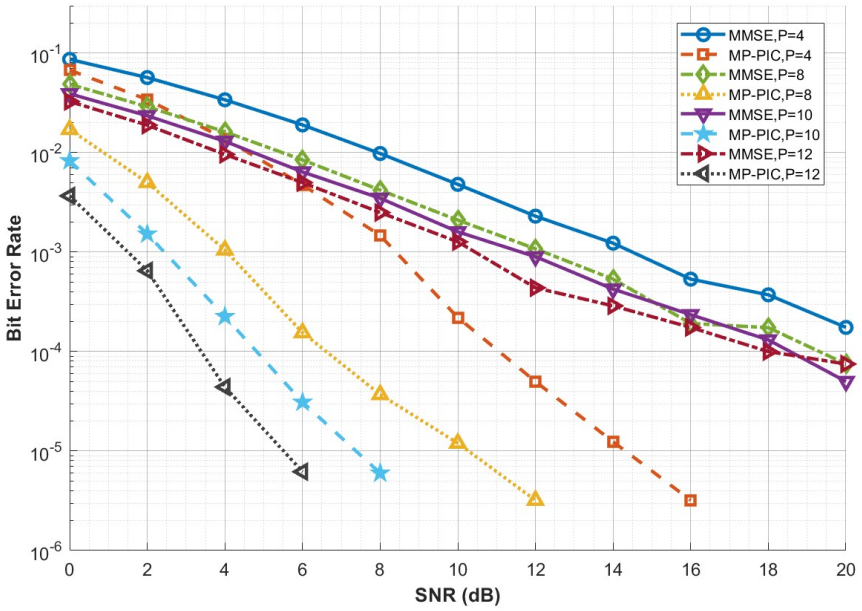


Figure 4.9: BER performance comparison of the MP-PIC detector at $N = 40$ across different path counts $P = 4, 8, 10, 12$

4.6.3 VB Detector for Quantized AFDM Performance

Simulation parameters for the VB detector include $N \in \{8, 12\}$, $\Delta f = 1$ MHz, $f_c = 4$ GHz, $P = 4$ paths, $L_{\max} = 3$ samples, maximum UE velocity of 800 km/h, and Extended Vehicular A power delay profile with $h_i \sim \mathcal{CN}(0, \sigma_h^2/P)$. Quantization resolution $b_q \in \{3, 4, 5, 6, 7, 8\}$ bits is considered for uniform scalar quantization. AFDM parameters are $c_1 = (2\alpha_{\max} + 1)/(2N)$ and $c_2 = 1/\sqrt{\pi N^2}$, and algorithm parameters are $T_{\max} = 30$ and $\epsilon = 10^{-10}$.

Fig. 4.10 and Fig. 4.11 present the VB detector NMSE for $N = 8$ subcarriers using BPSK and QPSK modulation respectively. The NMSE decreases monotonically with SNR across $b_q \in \{3, 4, 5, 6, 7, 8\}$ bits and achieves below -10 dB even at $b_q = 3$ bits, validating the truncated Gaussian modeling. Performance convergence beyond $b_q = 6$ bits indicates the optimal resolution where quantization becomes negligible.

Fig. 4.12 demonstrates exponential BER improvement, with $b_q = 8$ bit BPSK reaching 10^{-5} at 18 dB SNR. Four-bit quantization achieves a practical BER below 10^{-3} at 12 dB, enabling energy-efficient operation with moderate degradation.

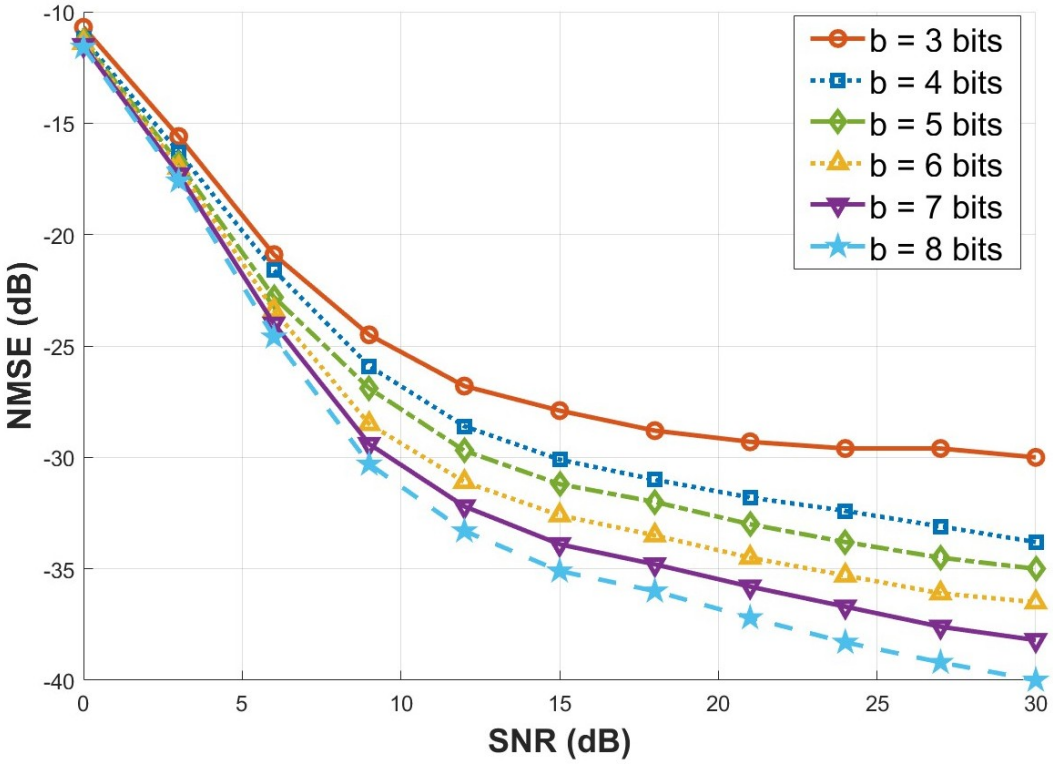


Figure 4.10: NMSE performance of the VB detector for quantized AFDM using BPSK

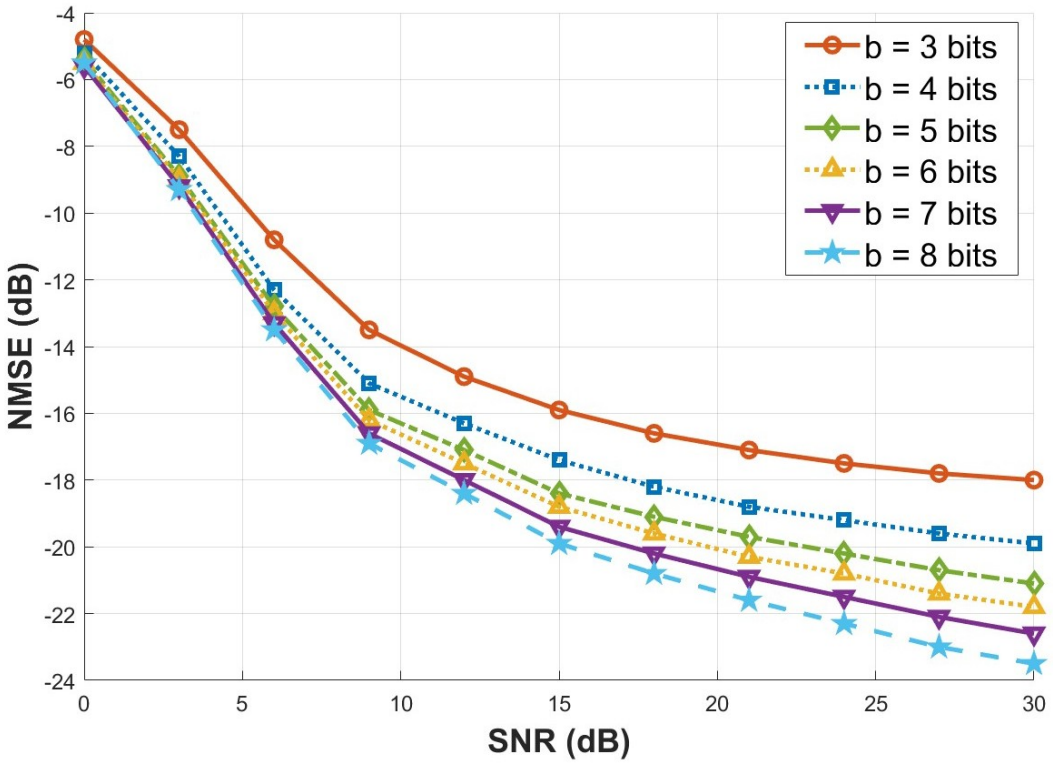


Figure 4.11: NMSE performance of the VB detector for quantized AFDM using QPSK

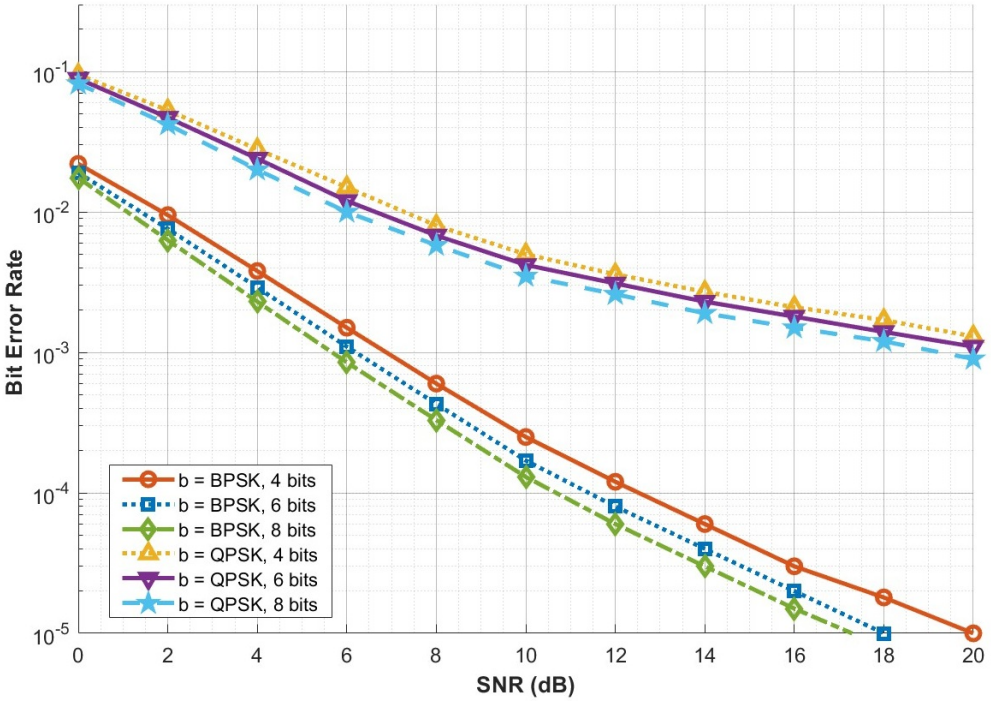


Figure 4.12: BER performance of the VB detector for quantized AFDM using BPSK and QPSK modulation

QPSK exhibits the expected 3 dB penalty versus BPSK.

Fig. 4.13, Fig. 4.14, and Fig. 4.15 demonstrate the superiority of the proposed VB detector over baseline methods, simulated with $N = 12$. The VB approach consistently delivers the best NMSE and BER performance across all SNRs and quantization levels, with the advantages becoming significant at low bit resolutions where quantization effects dominate. Bussgang MMSE (B-MMSE) [36, 75] saturates at high SNR due to unmodelled quantization distortion, while modified message passing (B-MP) methods [78] offer only partial improvements. In contrast, VB accurately captures the truncated Gaussian statistics and achieves the lowest NMSE. The BER comparison confirms large gains, with VB approaching the unquantized bound at higher resolutions and delivering an order-of-magnitude improvement at very low resolutions.

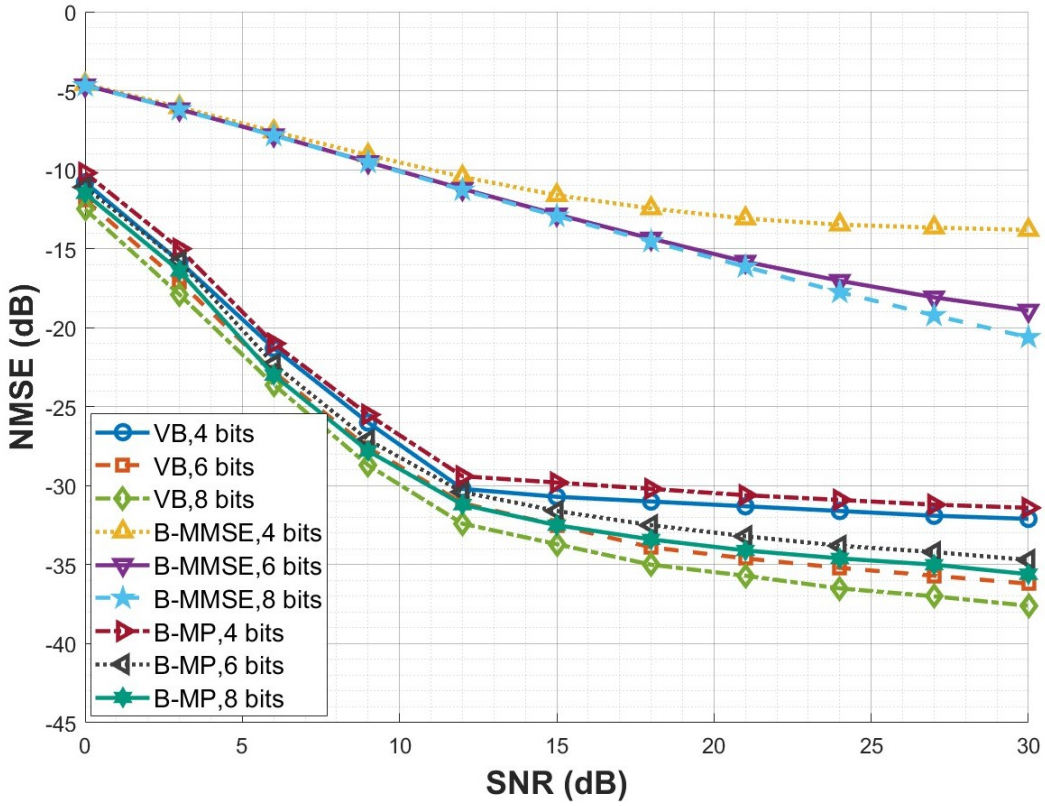


Figure 4.13: NMSE performance comparison of various detectors for quantized AFDM using BPSK

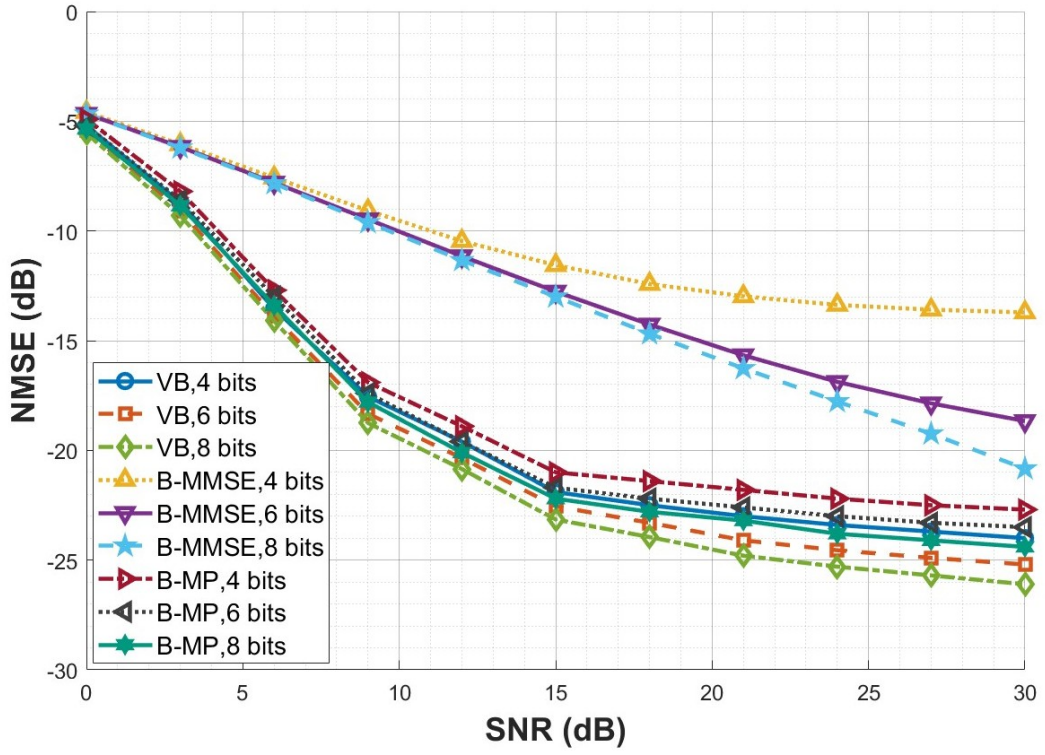


Figure 4.14: NMSE performance comparison of various detectors for quantized AFDM using QPSK

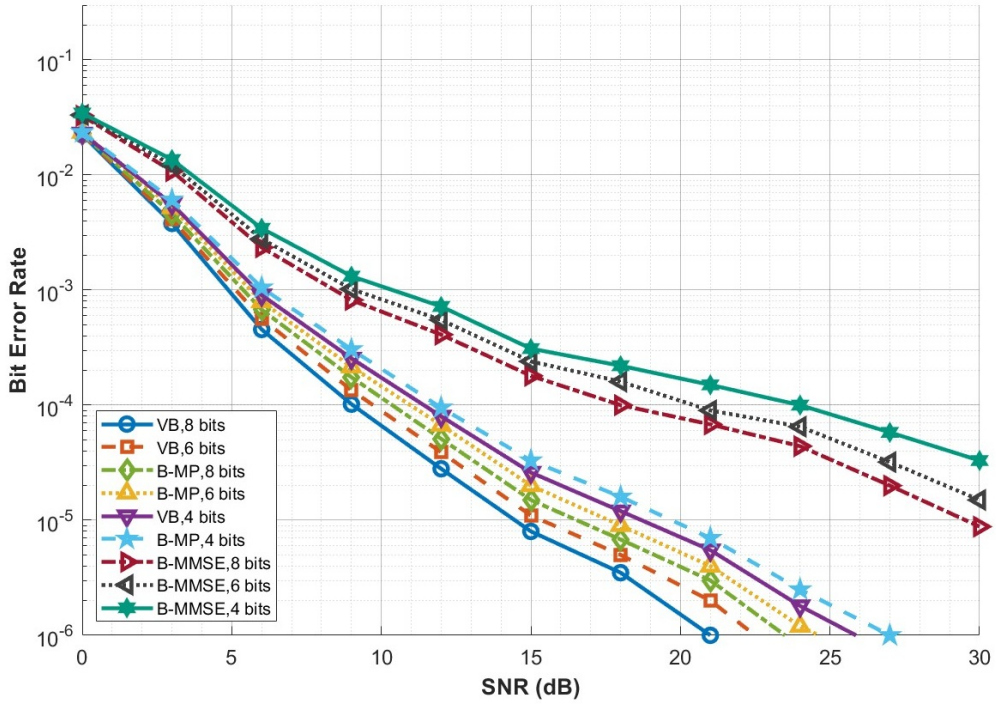


Figure 4.15: BER performance comparison of various detectors for quantized AFDM using BPSK

4.7 Complexity Comparison

Table 4.1 compares the computational complexity of the three proposed detectors in chapter 4 with the direct LMMSE and standard VAMP-SVD baselines. Direct LMMSE and VAMP-SVD both incur a cubic $\mathcal{O}(N^3)$ cost, from matrix inversion and singular value decomposition respectively. The proposed VAMP-CG removes this cubic term by replacing the SVD with K_{CG} conjugate gradient iterations, each of $\mathcal{O}(N^2)$, reducing the per-iteration cost to quadratic in N at negligible loss in BER. MP-PIC retains a one-time $\mathcal{O}(N^3)$ initialization but its iterative stage scales only as $\mathcal{O}(N|\mathcal{A}|L_p)$ by exploiting the path-separation structure, and the quantized-ADC VB detector is fully quadratic-free of any cubic term, scaling as $\mathcal{O}(T_{\max}N|\mathcal{A}|L_p)$ across its iterations. The proposed detectors therefore span a range of complexity–performance operating points while all avoiding the cubic scaling of the conventional baselines except for the single initialization step of MP-PIC.

Table 4.1: Computational complexity comparison of AFDM detectors with N subcarriers, $|\mathcal{A}|$ constellation size, L_p effective channel taps per symbol, K_{it} outer VAMP iterations, K_{CG} inner CG iterations, $t_{\max}$ MP-PIC iterations, and $T_{\max}$ VB iterations.

Detector	Complexity
Direct LMMSE	$\mathcal{O}(N^3)$
VAMP-SVD	$\mathcal{O}(N^3 + K_{\text{it}}\lvert\mathcal{A}\rvert N)$
VAMP-CG	$\mathcal{O}(K_{\text{it}}K_{\text{CG}}N^2 + K_{\text{it}}\lvert\mathcal{A}\rvert N)$
MP-PIC	$\mathcal{O}(N^3 + t_{\max}N\lvert\mathcal{A}\rvert L_p)$
VB-Quantized AFDM	$\mathcal{O}(T_{\max}N\lvert\mathcal{A}\rvert L_p)$

4.8 Summary

This chapter established the canonical AFDM system model used throughout the remainder of the thesis and developed three detectors that target different operating regimes of AFDM. The system model formalized the DAFT, the chirp-periodic prefix, the doubly dispersive channel, the DAFT-domain effective channel matrix $\mathbf{H}_{\text{eff}}$, and the chirp-parameter selection rule that separates the P propagation paths in the transformed domain. A low-complexity VAMP detector was developed that replaces the singular value decomposition of standard VAMP with a preconditioned conjugate gradient solver and a simultaneous trace estimator for the Onsager correction, reducing the per-iteration cost from $\mathcal{O}(N^3)$ to $\mathcal{O}(K_{\text{CG}}N^2)$ without measurable loss in BER. A Multi-Path Parallel Interference Cancellation detector was developed that exploits the complete path separation property of AFDM, performs independent Bayesian inference on each of the L_p resolvable paths, and combines the path-wise estimates through reliability-weighted decision statistics combining, achieving 4 to 8 dB BER gains over MMSE while remaining provably convergent through a Gauss-Seidel equivalence. A Variational Bayesian detector for quantized AFDM was developed that incorporates the truncated Gaussian likelihood induced by uniform scalar quantization into a mean-field factorized posterior over the discrete constellation, achieving near-unquantized BER at moderate ADC resolutions and large NMSE and BER gains over Bussgang-based linear receivers

and message-passing baselines at 3 to 4 bits where nonlinear quantization effects dominate. The DAFT-domain channel model, the chirp-parameter selection rule, and the detector families introduced in this chapter recur in modified form in the index modulation contributions of following Chapters.

Chapter 5

AFDM with Index Modulation Schemes and Sparse Bayesian Detection

This chapter develops three index modulation schemes built on the AFDM waveform and a sparse Bayesian detector tailored to the structured sparsity of AFDM with index modulation. The AFDM system model, the chirp-parameter selection rule, and the DAFT-domain effective channel matrix $\mathbf{H}_{\text{eff}}$ that this chapter relies on are those established in Section 4.1, and are not repeated here. We first review the AFDM with Index Modulation (AFDM-IM) baseline that is the common building block of all three schemes. We then propose AFDM with Generalized Index Modulation (AFDM-GIM), which relaxes the fixed active-subcarrier constraint of AFDM-IM by allowing the number of active subcarriers per subblock to vary across a permitted set, and develop energy detection (ED) and log-likelihood ratio (LLR) based detectors. We then propose AFDM with Quadrature Index Modulation (AFDM-QIM), which extends subcarrier index modulation in AFDM to operate independently on the in-phase and quadrature components, and develop both MMSE-ML and ML detectors together with a pairwise error probability (PEP) based analysis of the average bit error rate. We then propose a Variational

Bayesian Sparse Bayesian Learning (VB-SBL) detector for AFDM-IM that exploits the structured sparsity of the AFDM-IM transmit vector through a hierarchical Gaussian-Gamma prior. Spectral efficiency and computational complexity are derived alongside each contribution, and simulation results are presented together at the end of the chapter.

5.1 AFDM-IM Baseline

In AFDM with index modulation [27, 28], the N subcarriers of an AFDM frame are partitioned into G subblocks of length $L = N/G$. The incoming bit stream is split into G groups, each of p bits, with one group assigned to each subblock. Within each subblock, the p bits are split into two parts. The first part of p_1 bits selects which K of the L subcarriers in the subblock are active, and the second part of p_2 bits modulates the active subcarriers with symbols drawn from an M-ary constellation $\mathcal{A}$. The subcarriers that are not selected remain inactive and are set to zero.

The set of active subcarrier indices for the gth subblock is denoted

$$\mathcal{J}^{(g)} = \{j_{g,1}, j_{g,2}, \ldots, j_{g,K}\}, \quad j_{g,k} \in \{1, 2, \ldots, L\}. \tag{5.1}$$

The total bit load per subblock is

$$p = p_1 + p_2 = \left\lfloor \log_2 \binom{L}{K} \right\rfloor + K \log_2 M. \tag{5.2}$$

The modulated symbol vector for the gth subblock is

$$\mathbf{m}_g = [m_{g,1}, m_{g,2}, \ldots, m_{g,K}]^T, \tag{5.3}$$

where each $m_{g,k} \in \mathcal{A}$. The subblock transmit vector $\mathbf{x}_g \in \mathbb{C}^{L \times 1}$ is sparse and

contains the modulated symbols only at positions indexed by $\mathcal{J}^{(g)}$

$$x_g[n] = \begin{cases} m_{g,k}, & n = j_{g,k} \text{ for some } k \in \{1, \ldots, K\}, \\ 0, & \text{otherwise}, \end{cases} \tag{5.4}$$

for $n = 1, 2, \ldots, L$. Equivalently,

$$\mathbf{x}_g = \sum_{k=1}^{K} m_{g,k} \, \mathbf{e}_{j_{g,k}}, \tag{5.5}$$

where $\mathbf{e}_{j_{g,k}}$ is the standard unit vector of length L with a one at position $j_{g,k}$ and zeros elsewhere. Once all G subblocks are constructed, they are concatenated to form the full DAFT-domain AFDM-IM transmit vector

$$\mathbf{x} = [\mathbf{x}_1^T, \mathbf{x}_2^T, \ldots, \mathbf{x}_G^T]^T \in \mathbb{C}^{N \times 1}. \tag{5.6}$$

This vector is then processed by the AFDM modulator of Section 4.1.2 and transmitted across the doubly dispersive channel. At the receiver, after CPP removal and DAFT demodulation, the received signal follows the DAFT-domain input-output relation (4.16), with effective channel matrix $\mathbf{H}_{\text{eff}}$ given by (4.14). The AFDM-IM scheme thus inherits the doubly dispersive channel resilience of AFDM [17] while injecting an additional information dimension through subcarrier indexing.

5.2 AFDM with Generalized Index Modulation

5.2.1 Generalization of AFDM-IM

In the AFDM-IM scheme of Section 5.1, the number of active subcarriers per subblock is fixed at K. Fixing the number of active subcarriers per subblock is not necessary, and relaxing this restriction enlarges the set of admissible subblock

realizations and raises the spectral efficiency at matched parameters [51].

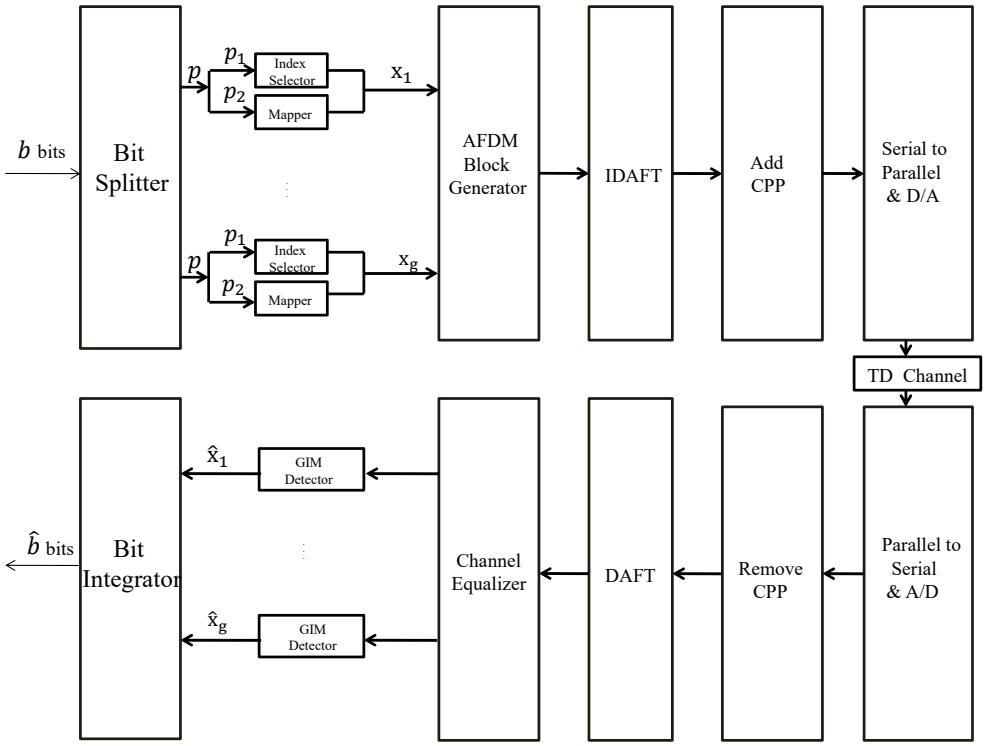


Figure 5.1: Block diagram of the AFDM-GIM system

To enhance flexibility, the AFDM scheme with generalized index modulation (AFDM-GIM) is introduced, allowing varying numbers of active subcarriers per subblock as illustrated in Fig. 5.1. Let L be the total number of subcarriers in an AFDM subblock, and let T denote the number of permitted values for active subcarriers. For instance, if an AFDM subblock allows either one or three active subcarriers, then $T = 2$. The set of permitted values for the number of active subcarriers is

$$\mathcal{K} = \{K_1, K_2, \ldots, K_T\}. \tag{5.7}$$

For a given $K_\phi \in \mathcal{K}$ with $\phi = 1, \ldots, T$, the indices of the K_ϕ active subcarriers in the gth subblock are

$$\mathcal{J}^{(g,\phi)} = \{j_g^\phi(1), j_g^\phi(2), \ldots, j_g^\phi(K_\phi)\}, \tag{5.8}$$

where $j_g^{\phi}(\eta) \in \{1,\ldots,L\}$ for $g = 1,\ldots,G$ and $\eta = 1,\ldots,K_\phi$, with $j_g^{\phi}(\eta_1) \neq j_g^{\phi}(\eta_2)$ for $\eta_1 \neq \eta_2$. The corresponding signal constellation symbols assigned to these active subcarriers are

$$\mathbf{s}_g^{\phi} = [s_g^{\phi}(1),\ldots,s_g^{\phi}(K_\phi)]. \tag{5.9}$$

The original AFDM-IM scheme of Section 5.1 is the special case in which K_ϕ is fixed for all subblocks, making AFDM-IM a particular instance of the proposed AFDM-GIM scheme.

For a given $K_\phi \in \mathcal{K}$, the number of bits transmitted per AFDM-GIM subblock is

$$m^g(\phi) = \left\lfloor \log_2\left(M^{K_\phi} \binom{L}{K_\phi} \right) \right\rfloor. \tag{5.10}$$

Summing over all permitted values of K_ϕ, the total number of bits transmitted per subblock is

$$\sum_{K_\phi \in \mathcal{K}} m^g(\phi) = \left\lfloor \log_2\left(\sum_{K_\phi \in \mathcal{K}} M^{K_\phi} \binom{L}{K_\phi} \right) \right\rfloor. \tag{5.11}$$

For the extreme case $\mathcal{K} = \{0,1,\ldots,L\}$,

$$\sum_{\phi=1}^{L+1} m^g(\phi) = \left\lfloor \log_2\left(\sum_{\phi=1}^{L+1} M^{K_\phi} \binom{L}{K_\phi} \right) \right\rfloor = \log_2((M+1)^L). \tag{5.12}$$

Since $\log_2((M+1)^L)$ significantly exceeds $m^g(\phi)$ for a fixed K_ϕ, permitting multiple K_ϕ values allows more flexible active subcarrier selection. The AFDM-GIM scheme therefore achieves higher spectral efficiency than conventional AFDM-IM.

5.2.2 Example Implementation

An example implementation of the generalized index modulation scheme is demonstrated for parameters $L = 4$, $\mathcal{K} = \{1,2,3\}$, and $M = 4$ (QPSK modulation). Each AFDM subblock consists of four subcarriers, with a varying number of active subcarriers permitted. The set $\mathcal{K}$ specifies the allowable numbers of active subcarriers per subblock, with indices selected from $\{1,2,3\}$.

The decimal representations of the incoming bit sequences D_p are segmented into three ranges corresponding to each value of K_ϕ:

- $D_p \in [0,15]$, corresponding to $K_\phi = 1$ active subcarrier,
- $D_p \in [16,111]$, corresponding to $K_\phi = 2$ active subcarriers,
- $D_p \in [112,319]$, corresponding to $K_\phi = 3$ active subcarriers.

Offsets are applied to each subcarrier combination so that each range begins at zero. The offset values applied are

$$\text{Offsets} = \{0,1,1\} \quad \text{for} \quad K_\phi = \{1,2,3\}, \tag{5.13}$$

respectively. These offsets are essential for aligning each D_p within the correct integer range required by the combinational selection method. Once the appropriate range of D_p is determined, the number of bits allocated to constellation mapping (p_2 bits) varies according to the generalized rule

$$p_2 = \begin{cases} K_1 \log_2 M, & D_p \in [0, M^{K_1}\binom{L}{K_1} - 1], \\ K_2 \log_2 M, & D_p \in [M^{K_1}\binom{L}{K_1}, M^{K_2}\binom{L}{K_2} - 1], \\ K_3 \log_2 M, & D_p \in [M^{K_2}\binom{L}{K_2}, M^{K_3}\binom{L}{K_3} - 1]. \end{cases} \tag{5.14}$$

For the considered parameters,

$$p_2 = \begin{cases} 2, & D_p \in [0,15], \\ 4, & D_p \in [16,111], \\ 6, & D_p \in [112,319]. \end{cases} \tag{5.15}$$

The remaining bits $p_1 = p - p_2$ are passed to the index selector that determines the active subcarrier indices. The least significant p_2 bits are then mapped onto QPSK symbols and transmitted via the selected active subcarriers. Through this generalized approach, AFDM-GIM achieves higher flexibility and spectral efficiency

compared to AFDM-IM by dynamically adjusting the number of active subcarriers and the corresponding bit allocations within each AFDM subblock.

5.2.3 AFDM-GIM Receiver and Equalization

The DAFT-domain AFDM-GIM transmit vector $\mathbf{x} \in \mathbb{C}^{N\times 1}$ is constructed from the G subblocks and passes through the AFDM modulator and the doubly dispersive channel. At the receiver, the DAFT-domain input-output relation

$$\mathbf{y} = \mathbf{H}_{\text{eff}}\,\mathbf{x} + \tilde{\mathbf{w}}, \tag{5.16}$$

holds with $\mathbf{H}_{\text{eff}}$ given by (4.14). The AFDM scheme distributes symbols across N subcarriers in the DAFT domain, leading to interference between the G AFDM-GIM subblocks. To mitigate this, MMSE equalization is applied

$$\hat{\mathbf{x}} = \left(\mathbf{H}_{\text{eff}}^{H}\mathbf{H}_{\text{eff}} + \sigma^2\mathbf{I}_N\right)^{-1}\mathbf{H}_{\text{eff}}^{H}\,\mathbf{y}, \tag{5.17}$$

where $\mathbf{I}_N$ is the $N \times N$ identity matrix. The equalized signal is then partitioned into G subblocks of length L and passed to the detector. Bit estimation is then performed using one of two detection strategies, energy detection or log-likelihood ratio detection, both of which assume a varying number of active subcarriers within subblocks.

5.2.4 Energy Detection Based Detector

The energy detection based approach [20] identifies the active subcarriers by measuring the energy of each equalized received symbol. For each permitted number of active subcarriers $K_\phi \in \mathcal{K}$, the detector selects the K_ϕ indices with the highest energy. Let $\mathbf{Y} = [Y_1, Y_2, \ldots, Y_L]^T$ be the received equalized AFDM-GIM subblock. The detection procedure follows these steps.

1. Compute energies $E_i = |Y_i|^2$, $i = 1, \ldots, L$.

2. Select the top K_ϕ indices $\mathcal{I}_{K_\phi}$ corresponding to the highest energies.

3. For the selected active subcarriers, detect the transmitted symbols via minimum Euclidean distance decoding

$$\hat{s}_i = \arg\min_{s\in\mathcal{A}} |Y_i - s|^2, \quad i \in \mathcal{I}_{K_\phi}, \tag{5.18}$$

where $\mathcal{A}$ denotes the constellation symbols.

4. Reconstruct the candidate subblock and compute the Euclidean distance metric

$$\text{Metric} = \|\mathbf{Y} - \hat{\mathbf{X}}_{K_\phi}\|^2, \tag{5.19}$$

where $\hat{X}_i = \hat{s}_i$ for $i \in \mathcal{I}_{K_\phi}$ and zero otherwise.

5. Repeat steps 1 to 4 for all values of $K_\phi \in \mathcal{K}$.

The number of active subcarriers K_ϕ yielding the minimum distance metric is selected as the final estimate. Detected symbols are then directly mapped to their corresponding bits.

5.2.5 LLR Based Detector

The LLR based detector incorporates probabilistic computations to determine the active subcarriers. For each candidate $K_\phi \in \mathcal{K}$, LLR values for each subcarrier are computed as

$$\begin{aligned}\zeta_i^{(K_\phi)} =& \ln\left(\frac{\sum_{s\in\mathcal{A}} \exp\left(-\frac{|Y_i-s|^2}{\sigma^2}\right)}{\sum_{s\in\{0\}} \exp\left(-\frac{|Y_i-s|^2}{\sigma^2}\right)}\right) \\ &+ \ln\left(\frac{K_\phi}{L-K_\phi}\right), \quad i = 1,\ldots,L,\end{aligned} \tag{5.20}$$

where σ^2 is the noise variance. The indices of the active subcarriers $\mathcal{I}_{K_\phi}$ are chosen based on the highest LLR values. Symbols at these indices are detected through minimum Euclidean distance decoding. The candidate subblocks are evaluated

using (5.19) for all $K_\phi \in \mathcal{K}$, and the configuration yielding the minimum metric is selected. The final detected bits are estimated from the indices of the optimal subcarrier set and the detected symbols, resulting in higher accuracy through the probabilistic weighting inherent in the LLR approach.

5.2.6 Spectral Efficiency of AFDM-GIM

The spectral efficiency of AFDM-GIM is the number of bits transmitted per subcarrier. For the AFDM-IM baseline of Section 5.1, with K active subcarriers in a subblock of length L and modulation order M,

$$\mathrm{SE}_{\text{AFDM-IM}} = \frac{\lfloor \log_2 \binom{L}{K} \rfloor + K \log_2 M}{L}. \tag{5.21}$$

AFDM-GIM with permitted set $\mathcal{K} = \{K_1, K_2, \ldots, K_T\}$ raises the number of admissible subblock realizations and the bits per subblock to

$$\mathrm{SE}_{\text{AFDM-GIM}} = \frac{\left\lfloor \log_2 \left(\sum_{K_\phi \in \mathcal{K}} M^{K_\phi} \binom{L}{K_\phi} \right) \right\rfloor}{L}. \tag{5.22}$$

The spectral efficiency of conventional AFDM is $\mathrm{SE}_{\text{AFDM}} = \log_2 M$. As an illustration, with $L = 4$, QPSK modulation, $K = 2$ for AFDM-IM, and $\mathcal{K} = \{1, 2, 3\}$ for AFDM-GIM, we obtain $\mathrm{SE}_{\text{AFDM-IM}} = 1.5$ and $\mathrm{SE}_{\text{AFDM-GIM}} = 2$ bits per subcarrier, while conventional AFDM at the same QPSK alphabet attains $\mathrm{SE}_{\text{AFDM}} = 2$. AFDM-GIM matches conventional AFDM in spectral efficiency at $L = 4$ and grows beyond it for larger permitted sets and longer subblocks.

5.2.7 Computational Complexity of AFDM-GIM

The AFDM-GIM receiver consists of two stages, MMSE equalization followed by demodulation. The equalization stage involves the inversion of an $N \times N$ matrix at a complexity of $\mathcal{O}(N^3)$. The energy detection based demodulator scans the T

permitted active-count values across G subblocks of length L and selects the K_ϕ subcarriers with the largest received energy, at a cost of $\mathcal{O}(GLT(M+1))$. The LLR based demodulator replaces the energy comparison with a log-likelihood ratio evaluated against the M constellation points, at a cost of $\mathcal{O}(GLTM)$. The total complexity of AFDM-GIM is therefore $\mathcal{O}(N^3+GLT(M+1))$ with the ED detector and $\mathcal{O}(N^3+GLTM)$ with the LLR detector. Both detectors are substantially less expensive than joint ML detection across the G subblocks, which would grow exponentially with L and M.

5.3 AFDM with Quadrature Index Modulation

5.3.1 AFDM-QIM Transmitter

The block diagram of the AFDM-QIM transmitter is shown in Fig. 5.2. Incoming data bits are processed for transmission over N subcarriers. Each AFDM block of N subcarriers carries $b = 2pG$ bits, partitioned into $2G$ groups of p bits each. Each group of p bits is used to generate the in-phase and quadrature components of an AFDM-QIM subblock, which consists of $L = N/G$ subcarriers. In contrast to conventional OFDM, where data is mapped onto all subcarriers, AFDM-QIM divides each p bit group into two parts [52]. The first part, with $p_1 = \lfloor \log_2 \binom{L}{K} \rfloor$ bits, is used for index modulation, selecting which subcarriers will be active. These bits are sent to the index selector, which activates K subcarriers out of L for both the in-phase and quadrature components using a look-up table, while the remaining subcarriers remain inactive. The second part of $p_2 = K \log_2 M$ bits is used for symbol modulation, where data symbols are assigned to the active subcarriers.

A distinctive feature of this system is that the selection of the active subcarriers for the in-phase and quadrature components is performed independently. For each AFDM-QIM subblock g, the indices of the K active subcarriers are selected separately for the I and Q components, enabling disjoint modulation. This boosts

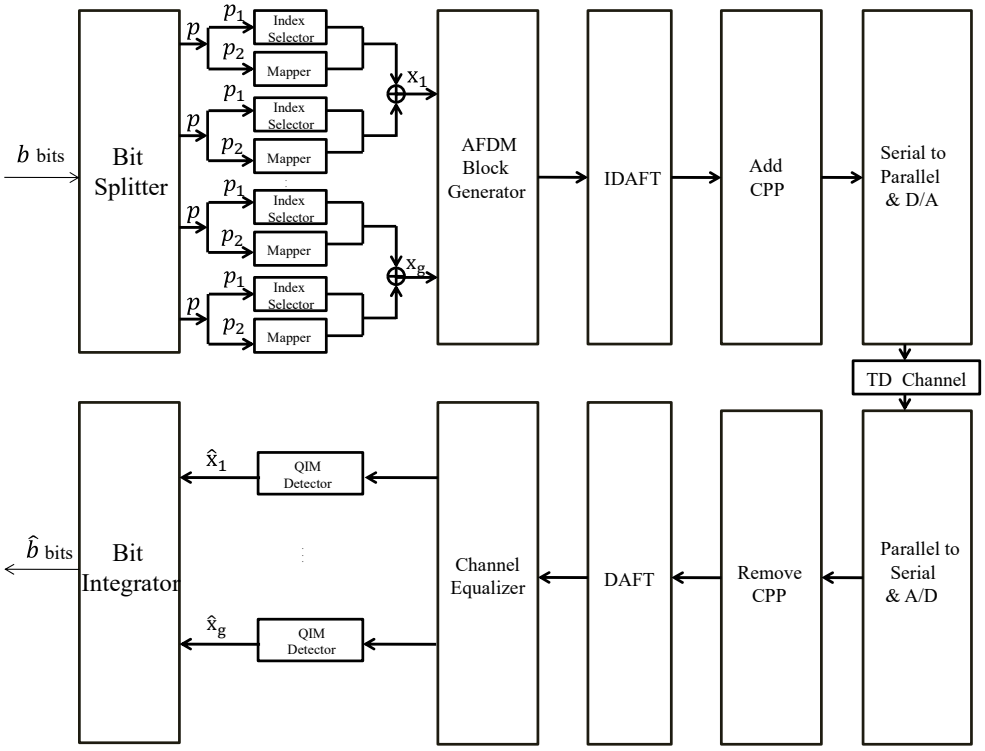


Figure 5.2: Block diagram of the AFDM-QIM system

spectral efficiency by using two activation patterns to transmit additional bits while simultaneously modulating symbols on the active subcarriers, offering higher data rates compared to AFDM-IM. In the gth AFDM-QIM subblock ($1 \leq g \leq G$), the in-phase and quadrature components are assigned to K active subcarriers, with their indices chosen independently in each dimension

$$\mathcal{J}^{(g,I)} = \{j^I_{g,1}, \ldots, j^I_{g,K}\}, \quad \mathcal{J}^{(g,Q)} = \{j^Q_{g,1}, \ldots, j^Q_{g,K}\}, \tag{5.23}$$

where $j^I_{g,k}, j^Q_{g,k} \in \{1, \ldots, L\}$. The remaining $p_2 = K \log_2 M$ bits are encoded using an M-ary pulse amplitude modulation scheme, represented by the alphabets $\mathcal{A}_I$ and $\mathcal{A}_Q$, to generate the transmitted symbols for the I and Q dimensions on the K active subcarriers in the gth AFDM-QIM subblock

$$x^I_{g,\eta} = \begin{cases} s^I_{g,\eta}, & \eta \in \mathcal{J}^{(g,I)}, \\ 0, & \text{otherwise}, \end{cases} \quad x^Q_{g,\eta} = \begin{cases} s^Q_{g,\eta}, & \eta \in \mathcal{J}^{(g,Q)}, \\ 0, & \text{otherwise}, \end{cases} \tag{5.24}$$

where $s^I_{g,\eta} \in \mathcal{A}_I$ and $s^Q_{g,\eta} \in \mathcal{A}_Q$. Each AFDM-QIM subblock is constructed by merging the I and Q components from (5.24)

$$x_{g,\eta} = x^I_{g,\eta} + j\, x^Q_{g,\eta}, \quad g = 1, \ldots, G, \eta = 1, \ldots, L. \tag{5.25}$$

After collecting all the AFDM-QIM subblocks, the AFDM block generator creates a DAFT-domain transmit vector $\mathbf{x} \in \mathbb{C}^{N\times 1}$

$$\mathbf{x} = [\mathbf{x}_1, \mathbf{x}_2, \ldots, \mathbf{x}_G]^T. \tag{5.26}$$

The DAFT-domain vector $\mathbf{x}$ is then processed by the AFDM modulator of Section 4.1.2.

5.3.2 AFDM-QIM Receiver Model

After transmission across the doubly dispersive channel and CPP removal, the DAFT-domain received vector follows the input-output relation

$$\mathbf{y} = \mathbf{H}_{\text{eff}}\, \mathbf{x} + \tilde{\mathbf{w}}, \tag{5.27}$$

with $\mathbf{H}_{\text{eff}}$ given by (4.14) and $\tilde{\mathbf{w}} \sim \mathcal{CN}(\mathbf{0}, \sigma^2 \mathbf{I}_N)$. Two detection strategies are developed for AFDM-QIM, an MMSE-ML detector and a full ML detector.

5.3.3 MMSE-ML Detector

The AFDM scheme distributes symbols across N subcarriers in the DAFT domain, leading to interference between the G AFDM-QIM subblocks. To address this, MMSE equalization is first applied

$$\hat{\mathbf{x}}_{\text{MMSE}} = \left(\mathbf{H}^H_{\text{eff}} \mathbf{H}_{\text{eff}} + \sigma^2 \mathbf{I}_N\right)^{-1} \mathbf{H}^H_{\text{eff}}\, \mathbf{y}. \tag{5.28}$$

The equalized signal is divided into G subgroups, with each subgroup further separated into real and imaginary components, forming the I and Q parts. After these divisions, a total of $2G$ subgroups are obtained. The in-phase and quadrature subgroups are independently subjected to ML detection

$$\begin{aligned}(\hat{\mathbf{x}}_g^I, \hat{\mathcal{J}}^{(g,I)}) &= \arg \min_{\mathbf{x}_g^I, \mathcal{J}^{(g,I)}} \left\| \hat{\mathbf{x}}_{\text{MMSE}}^I - \mathbf{x}^I \right\|^2, \\ (\hat{\mathbf{x}}_g^Q, \hat{\mathcal{J}}^{(g,Q)}) &= \arg \min_{\mathbf{x}_g^Q, \mathcal{J}^{(g,Q)}} \left\| \hat{\mathbf{x}}_{\text{MMSE}}^Q - \mathbf{x}^Q \right\|^2,\end{aligned} \tag{5.29}$$

where $\mathbf{x}^I$ and $\mathbf{x}^Q$ represent all possible combinations of the in-phase and quadrature subgroups in the AFDM-QIM scheme.

5.3.4 ML Detector

The maximum likelihood detector is the optimal detector for the AFDM-QIM system

$$(\hat{\mathbf{x}}_g^I, \hat{\mathcal{J}}^{(g,I)}, \hat{\mathbf{x}}_g^Q, \hat{\mathcal{J}}^{(g,Q)}) = \arg \min_{\mathbf{x} \in \mathbb{X}} \|\mathbf{y} - \mathbf{H}_{\text{eff}}\, \mathbf{x}\|_F^2, \tag{5.30}$$

where $\mathbb{X}$ is the set of all possible representations of $\mathbf{x}$. The computational complexity of the ML detector grows significantly with the size of $\mathbb{X}$. After estimating the indices and modulated symbols of the in-phase and quadrature subblocks using the MMSE-ML or ML detector, the original bit stream $\hat{\mathbf{b}}$ is recovered using an index pattern mapping table together with the two constellation alphabets of the in-phase and quadrature components.

5.3.5 Spectral Efficiency of AFDM-QIM

The spectral efficiency of AFDM-QIM is the number of bits transmitted per subcarrier. For the AFDM-IM baseline of Section 5.1, with K active subcarriers in a subblock of length L and modulation order M, SE is formulated as $\text{SE}_{\text{AFDM-IM}} = \frac{\lfloor \log_2 \binom{L}{K} \rfloor + K \log_2 M}{L}$.

AFDM-QIM activates subcarriers independently on the in-phase and quadrature

components of the chirp subcarriers, doubling the index-modulation contribution to spectral efficiency

$$\mathrm{SE}_{\text{AFDM-QIM}} = \frac{2\left(\lfloor \log_2 \binom{L}{K} \rfloor + K \log_2 M\right)}{L}. \tag{5.31}$$

The spectral efficiency of conventional AFDM is $\mathrm{SE}_{\text{AFDM}} = \log_2 M$. As an illustration, with $L = 4$, $K = 2$, and QPSK modulation, $\mathrm{SE}_{\text{AFDM-IM}} = 1.5$, $\mathrm{SE}_{\text{AFDM-QIM}} = 3$, and $\mathrm{SE}_{\text{AFDM}} = 2$ bits per subcarrier. AFDM-QIM doubles the spectral efficiency of AFDM-IM at the same subblock length and active-subcarrier count, and exceeds conventional AFDM by exploiting the index-modulation gain on both signal-space components.

5.3.6 Computational Complexity of AFDM-QIM

The AFDM-QIM receiver consists of two stages, MMSE equalization followed by joint detection of the in-phase and quadrature index patterns and constellation symbols. The equalization stage costs $\mathcal{O}(N^3)$. The MMSE-ML detector performs an independent ML search per subblock and per signal-space component, evaluating $\binom{L}{K} M^K$ candidate vectors for each of the G subblocks on both components, at a cost of $\mathcal{O}(2G\binom{L}{K} M^K)$. The total complexity of the MMSE-ML detector is therefore $\mathcal{O}(N^3 + 2G\binom{L}{K} M^K)$. The joint ML detector searches the full Cartesian product of index patterns and symbol vectors across all G subblocks and both I/Q components, with complexity $\mathcal{O}\left(\binom{L}{K}^{2G} M^{2KG}\right)$. The exponential scaling of joint ML with G makes it impractical for any realistic frame size, which motivates the per-subblock MMSE-ML decomposition.

5.4 Pairwise Error Probability Analysis for AFDM-QIM

5.4.1 Conditional Pairwise Error Probability

The received signal $\mathbf{y}$ in (5.27) can be restated as [17, 39]

$$\mathbf{y} = \sum_{i=1}^{P} h_i \mathbf{H}_i \mathbf{x} + \tilde{\mathbf{w}} = \mathbf{\Phi}(\mathbf{x})\,\mathbf{\Psi} + \tilde{\mathbf{w}}, \tag{5.32}$$

where $\mathbf{\Psi} = [h_1, h_2, \ldots, h_P]^T \in \mathbb{C}^{P\times 1}$, $\mathbf{H}_i = \mathbf{A}\,\mathbf{\Gamma}_{\mathrm{CPP},i}\,\mathbf{\Delta}_{\nu_i}\,\mathbf{\Pi}^{l_i}\,\mathbf{A}^H \in \mathbb{C}^{N\times N}$ is defined as in (4.14), and

$$\mathbf{\Phi}(\mathbf{x}) = [\mathbf{H}_1\mathbf{x}\,|\,\cdots\,|\,\mathbf{H}_P\mathbf{x}] \in \mathbb{C}^{N\times P}. \tag{5.33}$$

The conditional pairwise error probability for the AFDM-QIM scheme can be computed as

$$\begin{aligned} &P(\mathbf{x}\to\hat{\mathbf{x}}\,|\,\mathbf{\Psi}) \\ &= P\left(\|\mathbf{y}-\mathbf{\Phi}(\hat{\mathbf{x}})\mathbf{\Psi}\|^2 < \|\mathbf{y}-\mathbf{\Phi}(\mathbf{x})\mathbf{\Psi}\|^2\right) \\ &= Q\left(\sqrt{\frac{\delta}{2P\sigma^2}}\right), \end{aligned} \tag{5.34}$$

where the Gaussian Q-function is defined as

$$Q(x) = \frac{1}{\pi}\int_0^{\pi/2} \exp\left(-\frac{x^2}{2\sin^2\rho}\right) d\rho, \tag{5.35}$$

and the conditional squared distance δ is

$$\delta = \|(\mathbf{\Phi}(\hat{\mathbf{x}}) - \mathbf{\Phi}(\mathbf{x}))\mathbf{\Psi}\|^2 = \mathbf{\Psi}^H\mathbf{K}\mathbf{\Psi}, \tag{5.36}$$

with

$$\mathbf{K} = (\mathbf{\Phi}(\hat{\mathbf{x}}) - \mathbf{\Phi}(\mathbf{x}))^H(\mathbf{\Phi}(\hat{\mathbf{x}}) - \mathbf{\Phi}(\mathbf{x})). \tag{5.37}$$

5.4.2 Unconditional Pairwise Error Probability

The unconditional pairwise error probability is obtained by averaging the conditional pairwise error probability over the distribution of $\mathbf{\Psi}$

$$\begin{aligned} P(\mathbf{x} \to \hat{\mathbf{x}}) &= \int_0^{+\infty} P(\mathbf{x} \to \hat{\mathbf{x}} \,|\, \mathbf{\Psi})\, p_\delta(\delta)\, d\delta \\ &= \frac{1}{\pi} \int_0^{\pi/2} \int_0^{+\infty} \exp\left(-\frac{\delta}{4P\sigma^2 \sin^2\rho}\right) p_\delta(\delta)\, d\delta\, d\rho \\ &= \frac{1}{\pi} \int_0^{\pi/2} F_\delta\left(-\frac{1}{4P\sigma^2 \sin^2\rho}\right) d\rho, \end{aligned} \tag{5.38}$$

where $F_\delta(\cdot)$ is the moment generating function of δ

$$F_\delta(t) = |\mathbf{I} - t\mathbf{K}|^{-1} = \prod_{i=1}^{q} (1 - t\lambda_i)^{-1}, \tag{5.39}$$

with q the number of distinct nonzero eigenvalues λ_i of $\mathbf{K}$. Substituting (5.39) into (5.38),

$$P(\mathbf{x} \to \hat{\mathbf{x}}) = \frac{1}{\pi} \int_0^{\pi/2} \prod_{i=1}^{q} \left(\frac{1}{1 + \frac{\lambda_i}{4P\sigma^2 \sin^2\rho}}\right) d\rho. \tag{5.40}$$

5.4.3 Chernoff Bound and Average Bit Error Rate

Applying the Chernoff bound inequality, the upper bound of the pairwise error probability is

$$P(\mathbf{x} \to \hat{\mathbf{x}}) \le \prod_{i=1}^{q} \left(1 + \frac{\lambda_i}{4P\sigma^2}\right)^{-1}. \tag{5.41}$$

The theoretical upper bound on the average bit error rate (ABER) of the proposed AFDM-QIM scheme is

$$P_{\text{ABER}} \le \frac{1}{p\, 2^p} \sum_{\mathbf{x}} \sum_{\hat{\mathbf{x}}} P(\mathbf{x} \to \hat{\mathbf{x}})\, d_H(\mathbf{x}, \hat{\mathbf{x}}), \tag{5.42}$$

where $d_H(\mathbf{x}, \hat{\mathbf{x}})$ is the Hamming distance between the respective bit sequences and $p = 2(p_1 + p_2)$ is the total number of bits per AFDM-QIM subblock.

5.5 Variational Bayesian Sparse Bayesian Learning Detector for AFDM-IM

The AFDM-IM transmit vector $\mathbf{x} \in \mathbb{C}^{N\times 1}$ constructed in (5.6) is sparse, since at most KG of its N entries are nonzero. This structured sparsity can be exploited at the detector through a sparse signal recovery formulation based on Variational Bayesian Inference [32, 33], leading to a detector that significantly outperforms conventional MMSE-based detection of AFDM-IM under severe Doppler conditions.

5.5.1 Sparse Signal Recovery Formulation

The AFDM-IM detection problem can be cast as the linear inverse problem

$$\mathbf{y} = \mathbf{H}_{\text{eff}}\,\mathbf{x} + \tilde{\mathbf{w}}, \tag{5.43}$$

where $\mathbf{x} \in \mathbb{C}^{N\times 1}$ and $\mathbf{y} \in \mathbb{C}^{N\times 1}$ are the transmitted and received signals in the DAFT domain, $\mathbf{H}_{\text{eff}} \in \mathbb{C}^{N\times N}$ is the effective DAFT-domain channel matrix from (4.14), and $\tilde{\mathbf{w}}$ is white Gaussian noise with zero mean and variance σ^2.

5.5.2 Hierarchical Gaussian-Gamma Prior

To promote sparsity in $\mathbf{x}$, a two-layer hierarchical prior is imposed. The vector $\mathbf{x}$ is assumed to follow a zero-mean Gaussian distribution parameterized by the inverse-variance parameters $\boldsymbol{\alpha} = [\alpha_1, \ldots, \alpha_N]$

$$p(\mathbf{x}\,|\,\boldsymbol{\alpha}) = \prod_{i=1}^{N} \mathcal{N}(x_i\,|\,0, \alpha_i^{-1}). \tag{5.44}$$

Each α_i is independently drawn from a Gamma distribution with hyperparameters a and b

$$p(\boldsymbol{\alpha}) = \prod_{i=1}^{N} \frac{b^a}{\Gamma(a)}\,\alpha_i^{a-1}\exp(-b\,\alpha_i). \tag{5.45}$$

Assuming known noise variance σ^2 and perfect channel state information at the receiver, the likelihood is

$$p(\mathbf{y}\,|\,\mathbf{x}) = \frac{1}{(2\pi\sigma^2)^{N/2}} \exp\left(-\frac{1}{2\sigma^2}\|\mathbf{y}-\mathbf{H}_{\text{eff}}\mathbf{x}\|^2\right). \tag{5.46}$$

5.5.3 Mean-Field Variational Approximation

Direct computation of the posterior $p(\mathbf{x},\boldsymbol{\alpha}\,|\,\mathbf{y})$ is intractable. A variational approximation is used

$$q(\mathbf{x},\boldsymbol{\alpha}) = \prod_{i=1}^{N} q_{x_i}(x_i) \prod_{i=1}^{N} q_{\alpha_i}(\alpha_i). \tag{5.47}$$

The variational factors are optimized by minimizing the Kullback-Leibler divergence

$$\text{KL}_{\text{VB}} = \text{KL}\left(p(\mathbf{x},\boldsymbol{\alpha}\,|\,\mathbf{y})\,\|\,q(\mathbf{x},\boldsymbol{\alpha})\right). \tag{5.48}$$

Minimizing this KL divergence is equivalent to maximizing the evidence lower bound (ELBO). With $\boldsymbol{\theta} = \{\mathbf{x},\boldsymbol{\alpha}\}$, the KL can be written as

$$\begin{aligned} \text{KL}_{\text{VB}} &= -\int q(\boldsymbol{\theta}) \ln \frac{p(\boldsymbol{\theta}\,|\,\mathbf{y})}{q(\boldsymbol{\theta})}\, d\boldsymbol{\theta} \\ &= -\int q(\boldsymbol{\theta}) \ln \frac{p(\mathbf{y},\boldsymbol{\theta})}{p(\mathbf{y})\,q(\boldsymbol{\theta})}\, d\boldsymbol{\theta}, \end{aligned} \tag{5.49}$$

which yields

$$\text{KL}_{\text{VB}} = \ln p(\mathbf{y}) - \int q(\boldsymbol{\theta}) \ln \frac{p(\mathbf{y},\boldsymbol{\theta})}{q(\boldsymbol{\theta})}\, d\boldsymbol{\theta}, \tag{5.50}$$

and simplifies to

$$\ln p(\mathbf{y}) = \text{KL}_{\text{VB}} + \mathcal{L}(q). \tag{5.51}$$

Since $\text{KL}_{\text{VB}} \geq 0$, the ELBO $\mathcal{L}(q)$ is a lower bound on $\ln p(\mathbf{y})$. As $\ln p(\mathbf{y})$ is constant with respect to $q(\boldsymbol{\theta})$, minimizing KL_{VB} is equivalent to maximizing $\mathcal{L}(q)$. The maximization of the ELBO leads to the following update for each variational factor

$$\ln q_i(\theta_i) = \langle \ln p(\mathbf{y},\boldsymbol{\theta}) \rangle_{k\neq i} + c_i, \tag{5.52}$$

where θ_i is an individual component of $\boldsymbol{\theta}$ and $\langle\cdot\rangle_{k\neq i}$ denotes the expectation with respect to all q_k for $k \neq i$.

5.5.4 Iterative VB Updates

The joint distribution factorizes as

$$p(\mathbf{y},\boldsymbol{\theta}) = p(\mathbf{y}\,|\,\mathbf{x})\,p(\mathbf{x}\,|\,\boldsymbol{\alpha})\,p(\boldsymbol{\alpha}). \tag{5.53}$$

Expanding $\ln p(\mathbf{y},\boldsymbol{\theta})$ gives

$$\begin{aligned}\ln p(\mathbf{y},\boldsymbol{\theta}) = {}& \frac{N}{2}\ln\gamma_w - \frac{\gamma_w}{2}\|\mathbf{y}-\mathbf{H}_{\text{eff}}\mathbf{x}\|^2 \\ & + \sum_{i=1}^{N}\left(\frac{1}{2}\ln\alpha_i - \frac{\alpha_i}{2}x_i^2\right) \\ & + \sum_{i=1}^{N}\left((a-1)\ln\alpha_i + a\ln b - b\alpha_i\right) \\ & + \text{constants},\end{aligned} \tag{5.54}$$

where $\gamma_w = 1/\sigma^2$ is the noise precision. Using (5.52) and (5.54), the update for the ith component of $\mathbf{x}$ is

$$\begin{aligned}\ln q_{x_i}(x_i) = {}& -\frac{\gamma_w}{2}\Big\{\langle\|\mathbf{y}-\mathbf{H}_{\bar{i}}\mathbf{x}_{\bar{i}}\|^2\rangle - (\mathbf{y}-\mathbf{H}_{\bar{i}}\langle\mathbf{x}_{\bar{i}}\rangle)^H\mathbf{H}_i x_i \\ & - x_i\mathbf{H}_i^H(\mathbf{y}-\mathbf{H}_{\bar{i}}\langle\mathbf{x}_{\bar{i}}\rangle) + \|\mathbf{H}_i\|^2 x_i^2\Big\} \\ & - \frac{\langle\alpha_i\rangle}{2}x_i^2 + c_{x_i} \\ = {}& -\frac{1}{2\sigma_i^2}(x_i-\mu_i)^2 + c'_{x_i},\end{aligned} \tag{5.55}$$

where the product $\mathbf{H}_{\text{eff}}\mathbf{x}$ is decomposed as $\mathbf{H}_{\text{eff}}\mathbf{x} = \mathbf{H}_i x_i + \mathbf{H}_{\bar{i}}\mathbf{x}_{\bar{i}}$, with $\mathbf{H}_i$ the ith column of $\mathbf{H}_{\text{eff}}$ and $\mathbf{H}_{\bar{i}}$ the matrix formed by removing the ith column from $\mathbf{H}_{\text{eff}}$. The expression is quadratic in x_i, so $q_{x_i}(x_i)$ is Gaussian with mean and variance

$$\sigma_i^2 = \frac{1}{\gamma_w\,\|\mathbf{H}_i\|^2 + \langle\alpha_i\rangle}, \qquad \langle x_i\rangle = \mu_i = \sigma_i^2\,\mathbf{H}_i^H\,(\mathbf{y}-\mathbf{H}_{\bar{i}}\langle\mathbf{x}_{\bar{i}}\rangle)\,\gamma_w. \tag{5.56}$$

The update for $\ln q_{\alpha_i}(\alpha_i)$ is

$$\begin{aligned} \ln q_{\alpha_i}(\alpha_i) &= \left(a-1+\frac{1}{2}\right)\ln\alpha_i - \alpha_i\left(\frac{\langle x_i^2\rangle}{2}+b\right)+c_{\alpha_i}, \\ q_{\alpha_i}(\alpha_i) &\propto \alpha_i^{a+1/2-1}\exp\left(-\alpha_i\left(\frac{\langle x_i^2\rangle}{2}+b\right)\right), \end{aligned} \tag{5.57}$$

which is the log of a Gamma distribution with mean

$$\langle \alpha_i \rangle = \frac{a+\frac{1}{2}}{\frac{\langle x_i^2\rangle}{2}+b}, \qquad \langle x_i^2\rangle = \mu_i^2+\sigma_i^2. \tag{5.58}$$

By iteratively updating the parameters of the Gaussian and Gamma distributions, the variational Bayesian framework provides an efficient solution for sparse signal estimation in AFDM-IM detection. Each element of the estimated signal $\hat{\mathbf{x}}$ is deduced as the point estimate using (5.56) and (5.58).

5.5.5 Energy Detection Based Demodulation

Following the estimation of $\hat{\mathbf{x}}$, an energy detection based demodulation technique is used to recover the transmitted bits. The ED method determines the active subcarriers by evaluating the power of each estimated received symbol and identifies the K positions with the highest energy. Let the estimated AFDM-IM subblock be $\mathbf{Y} = [Y_1, Y_2, \ldots, Y_L]^T$. The detection algorithm proceeds as follows.

1. Compute energies $E_i = |Y_i|^2$, $i = 1, \ldots, L$.

2. Identify the indices $\mathcal{J}_K$ corresponding to the K largest energy values.

3. For each identified active subcarrier, estimate the transmitted symbol using minimum Euclidean distance decoding

$$\hat{m}_i = \arg\min_{m\in\mathcal{A}} |Y_i - m|^2, \quad i \in \mathcal{J}_K, \tag{5.59}$$

where $\mathcal{A}$ is the modulation constellation.

4. Form a reconstructed subblock $\hat{\mathbf{X}}_K$ by assigning $\hat{X}_i = \hat{m}_i$ for $i \in \mathcal{J}_K$ and zeros elsewhere, and compute the metric

$$\text{Metric} = \|\mathbf{Y} - \hat{\mathbf{X}}_K\|^2. \tag{5.60}$$

The detected symbols are then demapped to recover the transmitted bit sequence.

5.5.6 Computational Complexity of VB-SBL Detector

The VB-SBL detector replaces the MMSE-based equalization of the AFDM-IM baseline with iterative variational updates that avoid matrix inversion [48]. Each iteration evaluates the variance and mean updates derived in Section **??** at a cost dominated by the matrix-vector products with $\mathbf{H}_{\text{eff}}$, which scales as $\mathcal{O}(N^2)$ per iteration. With I iterations required for convergence, the equalization stage has complexity $\mathcal{O}(I\,N^2)$. The energy detection based demodulator scans G subblocks of length L and identifies the K subcarriers with the largest posterior energy at a cost of $\mathcal{O}(MKG+GL)$. The total complexity of AFDM-IM with the VB-SBL detector is therefore $\mathcal{O}(I\,N^2+MKG+GL)$, compared with $\mathcal{O}(N^3+MKG+GL)$ for the MMSE plus ED baseline. For typical AFDM-IM systems with N between 64 and 256 and I between 10 and 20, the quadratic-in-N scaling of VB-SBL is substantially cheaper than the cubic scaling of MMSE.

5.6 Simulation Results

5.6.1 AFDM-GIM Performance

The simulation parameters for AFDM-GIM are a carrier frequency $f_c = 4$ GHz, a subcarrier spacing $\Delta f = 1$ MHz, two or four propagation paths ($P = 2, 4$), and a maximum UE velocity of 800 km/h. The DAFT parameters are set to $c_1 = (2\alpha_{\max}+1)/(2N)$ and $c_2 = 1/(\pi N^2)$, and simulations are conducted under an

integer Doppler channel.

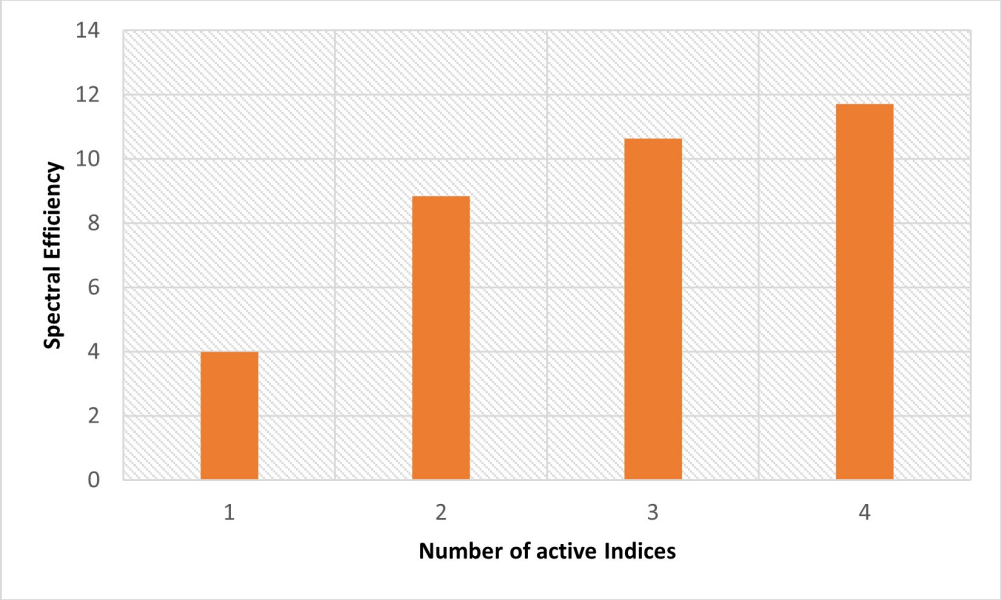


Figure 5.3: Spectral efficiency variation with the permitted active subcarriers in AFDM-GIM

The spectral efficiency of AFDM-GIM is evaluated using (5.11) for varying numbers of active subcarriers in an AFDM subblock. As illustrated in Fig. 5.3, the spectral efficiency increases as the number of permitted active indices grows. For an AFDM subblock of size $L = 8$, the configurations $\mathcal{K} = \{1\}$, $\{1,3\}$, $\{1,3,4\}$, and $\{1,3,4,5\}$ result in spectral efficiencies of 4, 8.858, 10.629, and 11.721 bits/s/Hz respectively. This demonstrates that a higher number of permitted active subcarriers leads to improved spectral efficiency, highlighting the potential of AFDM-GIM in optimizing data transmission.

Fig. 5.4 illustrates the BER performance comparison of AFDM-GIM, AFDM-IM [27], and conventional AFDM under the same spectral efficiency. The AFDM-GIM scheme employs a permitted active set $\mathcal{K} = \{1,2,3\}$ with subblock length $L = 4$, AFDM frame length $N = 64$, and $G = 16$ subblocks. QPSK is used for symbol modulation in AFDM-GIM. AFDM-IM uses $K = 1$ with 16-QAM modulation, while conventional AFDM uses 64-QAM. The BER curves indicate that AFDM-GIM outperforms both AFDM-IM and conventional AFDM across the entire SNR range. This improvement is due to the additional diversity gain provided by

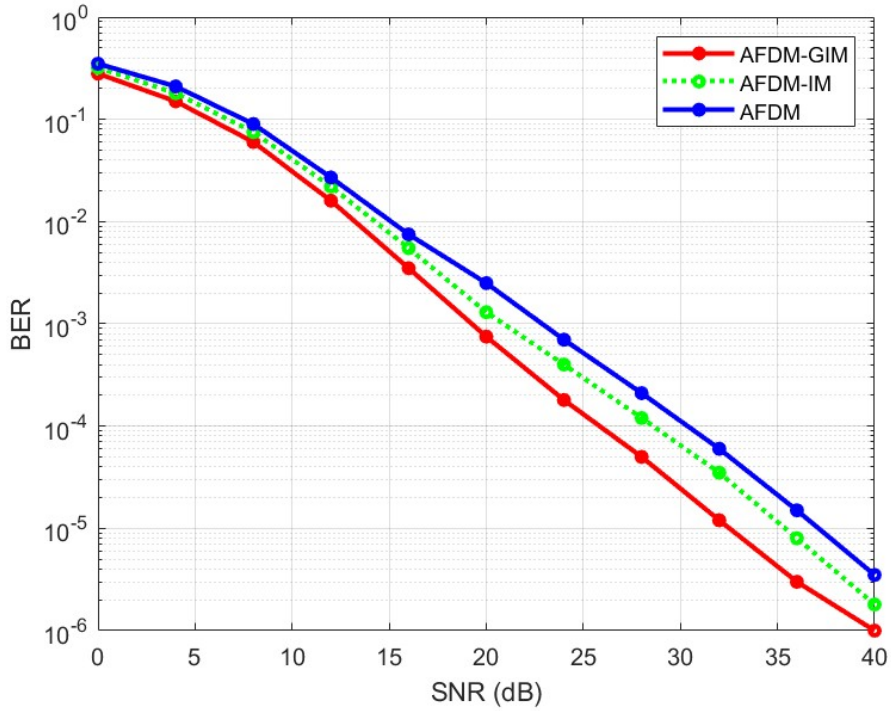


Figure 5.4: BER performance comparison of AFDM-GIM with AFDM-IM and conventional AFDM at the same spectral efficiency

the generalized index modulation technique, which leverages both index selection and symbol modulation. At BER $= 10^{-4}$, AFDM-GIM achieves an SNR gain of approximately 2 dB over AFDM-IM and 4 dB over conventional AFDM.

Fig. 5.5 reports the BER performance of AFDM-GIM at two different spectral efficiency values of 11.139 bits/s/Hz and 6.906 bits/s/Hz. The scheme uses a permitted active set $\mathcal{K} = \{1, 3, 5\}$, with QPSK modulation for the higher spectral efficiency and BPSK modulation for the lower spectral efficiency. The AFDM frame consists of $N = 16$ subcarriers divided into $G = 16$ subblocks. Performance is evaluated using both ED and LLR based detection. The results demonstrate the impact of spectral efficiency and detection technique on the BER performance of AFDM-GIM, with both detectors exhibiting similar performance across the evaluated SNR range.

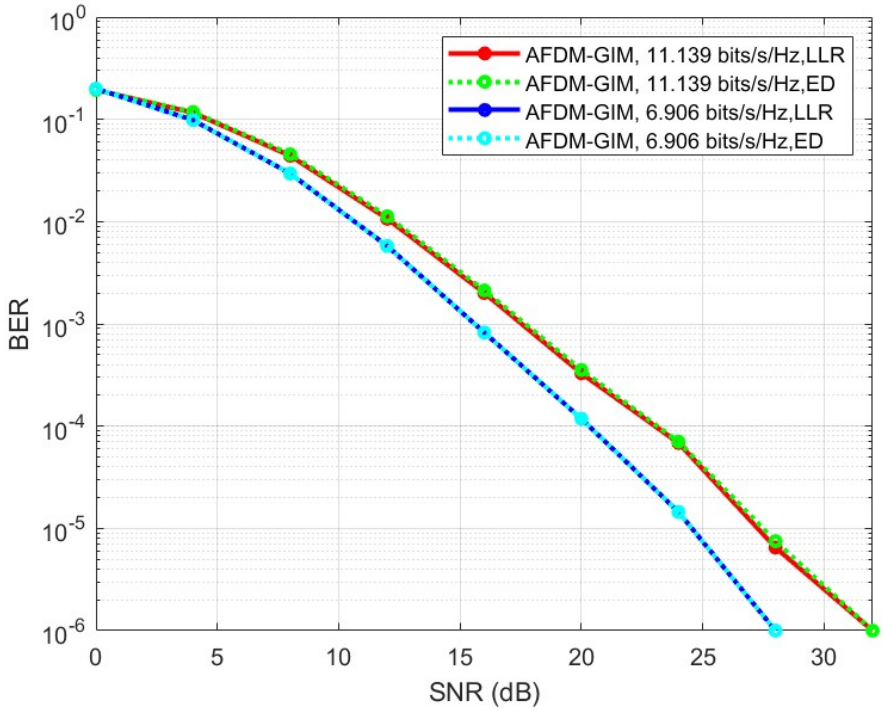


Figure 5.5: BER performance of AFDM-GIM with different spectral efficiencies and detection techniques

5.6.2 AFDM-QIM Performance

The simulation parameters for AFDM-QIM are $f_c = 4$ GHz, $\Delta f = 1$ MHz, a two-path channel ($P = 2$), and a maximum UE velocity of 750 km/h. The DAFT parameters are $c_1 = (2\alpha_{\max} + 1)/(2N)$ and $c_2 = 1/(\pi N^2)$, and simulations are conducted under an integer Doppler channel.

Fig. 5.6 illustrates the BER performance comparison of AFDM-QIM obtained from simulation and from the theoretical PEP analysis of Section 5.4. The system parameters are $N = 4$, $K = 2$, and $M = 4$ for both the in-phase and quadrature components, with $L_{\max} = 0$ and $\alpha_{\max} = 1$. As the SNR increases, the theoretical BER values gradually converge with the simulation results. This alignment becomes particularly noticeable beyond 17 dB, where the theoretical predictions closely match the simulated data points. The strong correlation between the two curves at higher SNR levels validates the accuracy of the upper bound in (5.42) in predicting the BER performance of AFDM-QIM under the specified conditions.

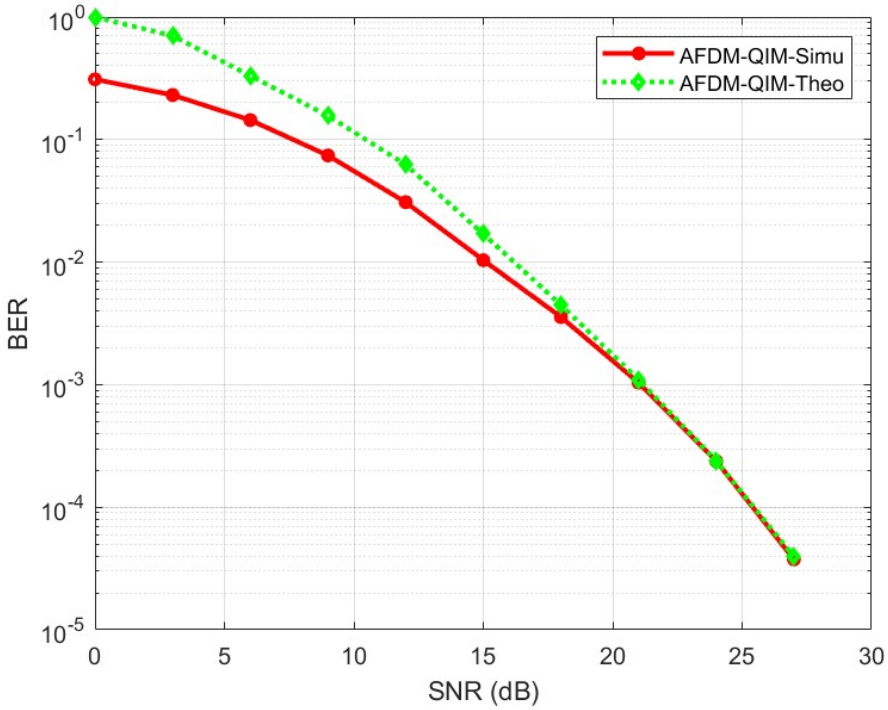


Figure 5.6: Comparison between the theoretical BER analysis and the simulated BER performance for AFDM-QIM using ML detector

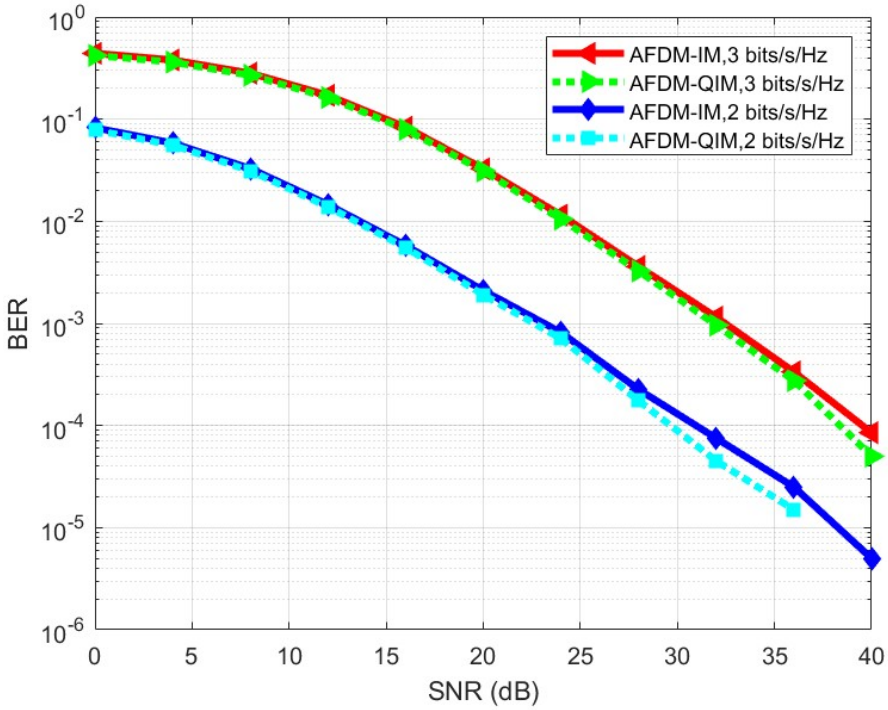


Figure 5.7: BER performance comparison of AFDM-QIM and AFDM-IM under two different spectral efficiency values

The BER performance of AFDM-QIM and AFDM-IM [28] under spectral efficiencies of 2 bits/s/Hz and 3 bits/s/Hz is illustrated in Fig. 5.7. The simulations use $N = 16$, $G = 4$, $K = 2$, $L_{\max} = 1$ and $\alpha_{\max} = 1$. For the spectral efficiency of 2 bits/s/Hz, AFDM-QIM uses $M = 2$ for both the in-phase and quadrature dimensions while AFDM-IM uses a symbol modulation order of eight. For the spectral efficiency of 3 bits/s/Hz, AFDM-QIM uses $M = 4$ for both dimensions and AFDM-IM uses 32-QAM. For both spectral efficiency levels, AFDM-QIM demonstrates better BER performance than AFDM-IM, especially at higher SNR values. At BER $= 10^{-3}$, AFDM-QIM with spectral efficiency 3 bits/s/Hz attains an SNR gain of approximately 2 dB over AFDM-IM at the same spectral efficiency. At BER $= 10^{-4}$, AFDM-QIM operating at 2 bits/s/Hz shows an SNR gain of approximately 1.5 dB over AFDM-IM. The results emphasize the inherent trade-off between spectral efficiency and error performance, since systems with higher spectral efficiency exhibit higher BER than those with lower spectral efficiency at the same SNR.

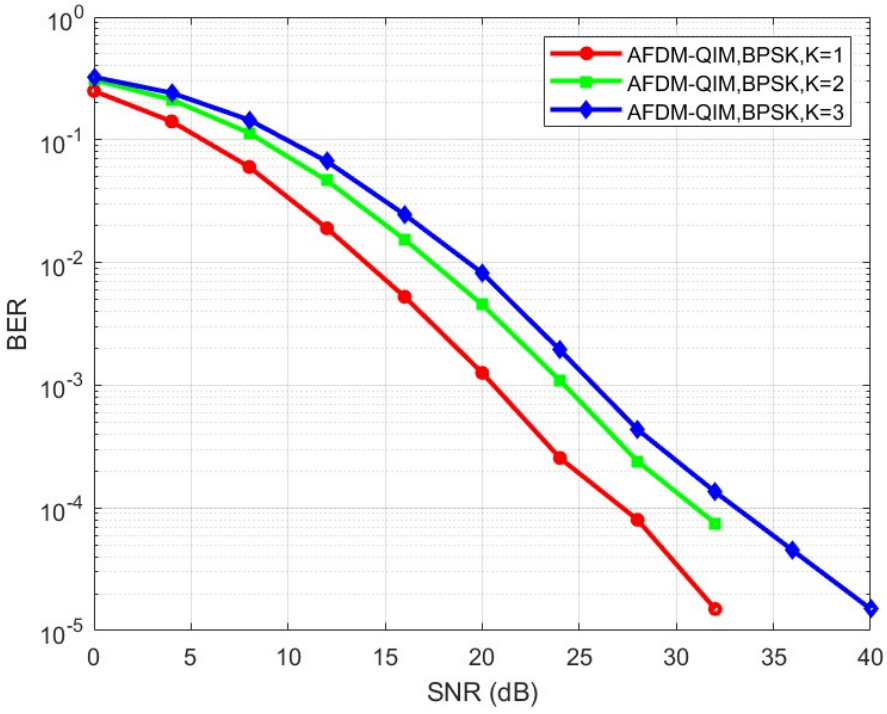


Figure 5.8: BER performance comparison of AFDM-QIM under different values of $K = \{1, 2, 3\}$ and $M = 2$

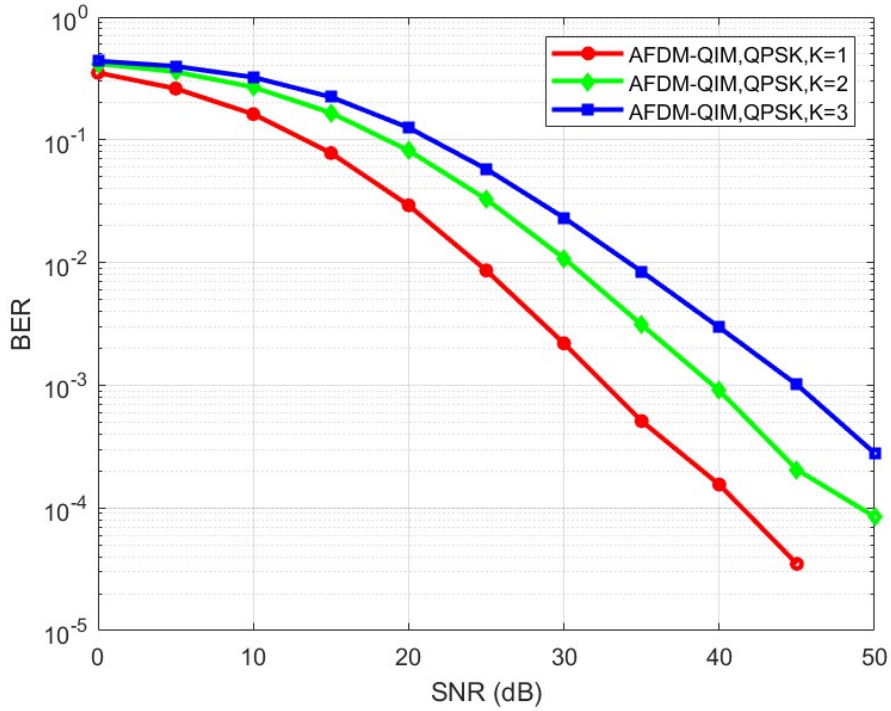


Figure 5.9: BER performance comparison of AFDM-QIM under different values of $K = \{1,2,3\}$ and $M = 4$

Fig. 5.8 and Fig. 5.9 report the BER performance of AFDM-QIM under different values of $K \in \{1,2,3\}$ with $M = 2$ and $M = 4$ respectively. The system parameters are $N = 16$, $G = 4$, $L_{\max} = 1$, and $\alpha_{\max} = 1$. For the BPSK case, AFDM-QIM achieves BER $= 10^{-4}$ at approximately 26 dB for $K = 1$, 29 dB for $K = 2$, and 32 dB for $K = 3$, indicating an SNR gain of approximately 3 dB between $K = 1$ and $K = 2$, and approximately 6 dB between $K = 1$ and $K = 3$. For QPSK modulation, AFDM-QIM reaches BER $= 10^{-4}$ at approximately 36 dB for $K = 1$, 40 dB for $K = 2$, and 44 dB for $K = 3$, with an SNR gain of approximately 4 dB between $K = 1$ and $K = 2$, and approximately 8 dB between $K = 1$ and $K = 3$. These results demonstrate that lower values of K lead to better BER performance in AFDM-QIM regardless of the modulation order, with the trade-off that higher K enables greater data throughput at the expense of degraded BER. This trade-off becomes more significant as the modulation order increases from BPSK to QPSK.

5.6.3 VB-SBL Detector Performance

The simulation setup for the VB-SBL detector considers a high-Doppler Rayleigh fading channel with a maximum UE velocity of 800 km/h, $N = 64$, QPSK modulation, and $P = 3$ multipath components. The VB-SBL detector uses 100 iterations.

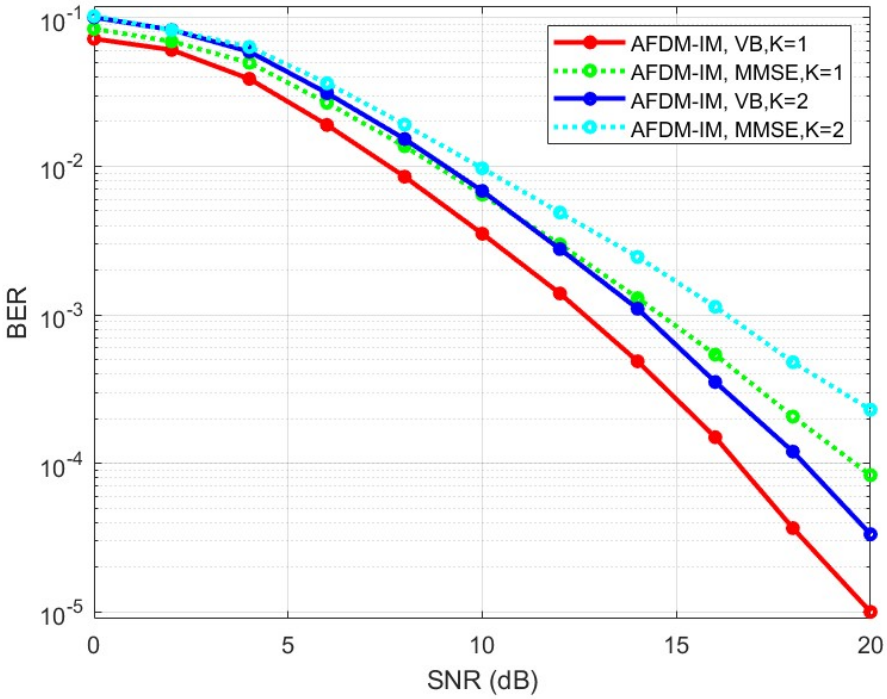


Figure 5.10: BER performance comparison of MMSE and VB-SBL detector for AFDM-IM with $L = 4$

Fig. 5.10 and Fig. 5.11 compare the BER performance of AFDM-IM with the MMSE detector and the proposed VB-SBL detector. Fig. 5.10 uses subblock length $L = 4$ with two sparsity levels $K = 1$ and $K = 2$, while Fig. 5.11 uses $L = 8$ with $K = 1$ and $K = 3$. Across both configurations, the VB-SBL detector consistently outperforms the MMSE-based approach [74], particularly in the high-SNR regime, due to its ability to exploit the structured sparsity of the AFDM-IM transmit vector. A lower value of K yields better BER performance, since fewer active subcarriers reduce inter-symbol interference and improve detection accuracy. Increasing the subblock length from $L = 4$ to $L = 8$ also improves BER performance, due to increased symbol diversity and reduced index collision probability.

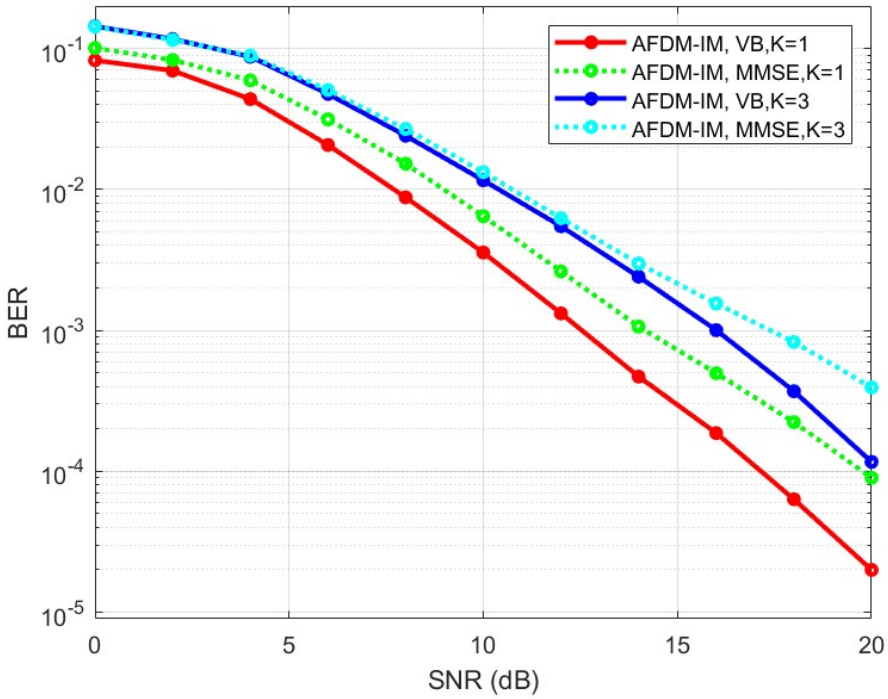


Figure 5.11: BER performance comparison of MMSE and VB-SBL detector for AFDM-IM with $L = 8$

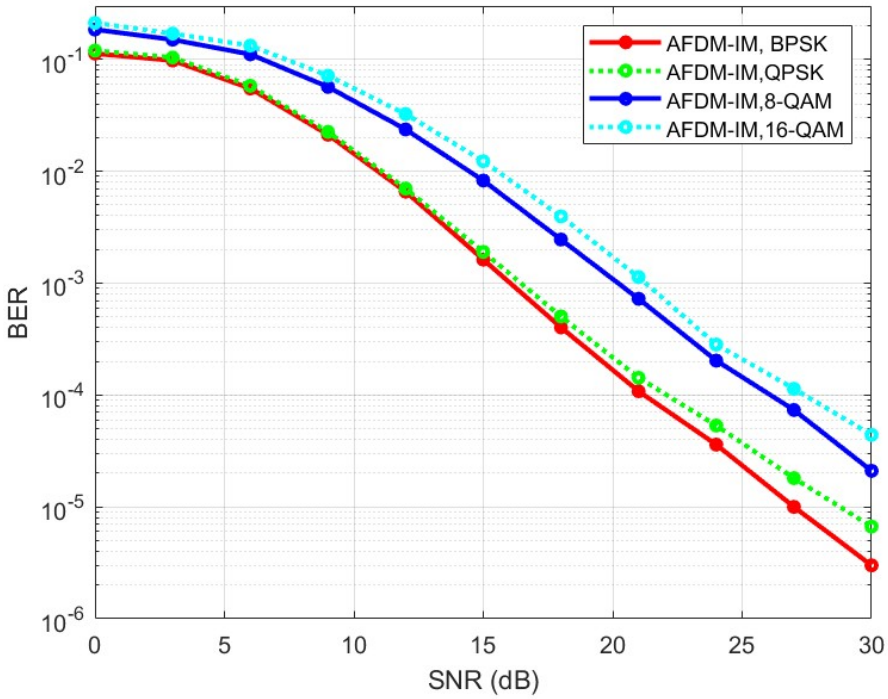


Figure 5.12: BER performance of the VB-SBL based AFDM-IM detector across different modulation schemes

Fig. 5.12 illustrates the BER performance of the VB-SBL based AFDM-IM detector for BPSK, QPSK, 8-QAM, and 16-QAM modulation under the configuration $L = 4$ and $K = 1$. Lower-order modulation schemes such as BPSK and QPSK demonstrate superior BER performance across the SNR range due to their higher noise resilience, with BPSK achieving the lowest BER followed closely by QPSK. The higher-order modulations 8-QAM and 16-QAM suffer from increased error rates, especially at low and moderate SNR. All modulation schemes show significant BER improvement as SNR increases, validating the effectiveness of the VB-SBL detection approach across modulation orders.

5.7 Summary

This chapter developed three index modulation schemes built on the AFDM waveform together with a sparse Bayesian detector tailored to the structured sparsity of AFDM-IM. AFDM-GIM relaxed the fixed active-subcarrier constraint of AFDM-IM by allowing the number of active subcarriers per subblock to vary across a permitted set $\mathcal{K} = \{K_1, \ldots, K_T\}$, which enlarged the set of admissible subblock realizations and raised the spectral efficiency over both AFDM-IM and conventional AFDM at matched SNR. Energy detection and LLR based detectors were developed for AFDM-GIM, with both detectors achieving comparable BER. AFDM-QIM extended subcarrier index modulation in AFDM to operate independently on the in-phase and quadrature components, doubling the index-modulation contribution to spectral efficiency at matched subblock length. MMSE-ML and ML detectors were developed for AFDM-QIM, and a complete PEP based analysis of the average bit error rate was derived using the moment generating function of the codeword difference correlation matrix and the Chernoff bound, with the theoretical upper bound closely matching the simulated BER in the high-SNR regime. A Variational Bayesian Sparse Bayesian Learning detector was developed for AFDM-IM that exploits the structured sparsity of the AFDM-IM transmit vector through a two-

layer hierarchical Gaussian-Gamma prior, with closed-form iterative updates derived from the ELBO that avoid matrix inversion and reduce the equalization cost from $\mathcal{O}(N^3)$ to $\mathcal{O}(IN^2)$ per iteration while delivering substantial BER gains over conventional MMSE detection of AFDM-IM in high-Doppler channels. The AFDM-IM construction, the generalized and quadrature variants, and the sparse Bayesian detection framework introduced in this chapter form the basis for the dual-mode and multi-mode index modulation schemes developed in following Chapters .

Chapter 6

AFDM with Dual-Mode Index Modulation and Message Passing Detection

This chapter develops AFDM with Dual-Mode Index Modulation (AFDM-DM-IM), a scheme that activates every subcarrier of a subblock and modulates it with one of two disjoint constellation alphabets [21, 25], achieving full resource utilization and higher spectral efficiency than the AFDM-IM scheme of Chapter 5. The AFDM system model, the chirp-parameter selection rule, and the DAFT-domain effective channel matrix $\mathbf{H}_{\text{eff}}$ that this chapter relies on are those established in Section 4.1, and are not repeated here. We first present the AFDM-DM-IM transmitter and the dual-mode index modulation structure. We then develop three baseline detectors, an optimal maximum likelihood (ML) detector, an MMSE-ML detector, and a low-complexity MMSE-LLR detector. We then propose two message passing detectors that jointly infer the transmitted symbols and the subblock activation patterns through an inline belief propagation module, a Vector Approximate Message Passing detector with preconditioned conjugate gradient linear estimation termed VAMP-DMDIM, and a Generalized Approximate Message Passing detector termed GAMP-DMDIM. A pairwise error probability analysis of the average bit error rate

is derived, and spectral efficiency, computational complexity, and simulation results are presented at the end of the chapter.

6.1 AFDM-DM-IM System Model

In the AFDM-DM-IM system as in [53], the N chirp subcarriers separated by a subcarrier spacing of Δf carry a total of b bits per frame. These bits are divided into G groups, each containing g bits that are further split into g_1 index bits and g_2 information bits. Each group corresponds to an AFDM subblock of length $L = N/G$. The index selector uses the first g_1 bits to segregate the subcarriers of the subblock into two index subsets, $\mathcal{J}_A^{(g)}$ and $\mathcal{J}_B^{(g)}$. Two distinct constellation alphabets, $\mathcal{A}$ and $\mathcal{B}$, each of size M_A and M_B with no overlapping elements ($\mathcal{A} \cap \mathcal{B} = \varnothing$), are used to modulate the two subsets. For instance, $\mathcal{A} = \{-1-j, 1-j, 1+j, -1+j\}$ and $\mathcal{B} = \{3, 3j, -3, -3j\}$ are two distinguishable QPSK alphabets. The subcarriers associated with $\mathcal{J}_A^{(g)}$ and $\mathcal{J}_B^{(g)}$ are modulated by mappers $\mathcal{A}$ and $\mathcal{B}$ respectively, with K subcarriers modulated by $\mathcal{A}$ and the remaining $L-K$ subcarriers modulated by $\mathcal{B}$. The number of index bits and information bits per subblock are

$$g_1 = \left\lfloor \log_2 \binom{L}{K} \right\rfloor, \qquad g_2 = K \log_2 M_A + (L-K) \log_2 M_B, \tag{6.1}$$

where $\binom{L}{K}$ denotes the binomial coefficient and $\lfloor \cdot \rfloor$ is the floor function. An AFDM subblock is represented as $\mathbf{x}^{(g)} = \{x^{(g)}(1), x^{(g)}(2), \ldots, x^{(g)}(L)\}$ for $1 \leq g \leq G$. After collecting all subblocks, the AFDM block generator forms the DAFT-domain transmit vector

$$\mathbf{x} = \{\mathbf{x}^{(1)}, \ldots, \mathbf{x}^{(g)}, \ldots, \mathbf{x}^{(G)}\} \in \mathbb{C}^{N \times 1}. \tag{6.2}$$

The operation of the index selector is detailed in Table 6.1 for the specific values $g_1 = 2$, $L = 4$, and $K = 2$. The index bits select the subset $\mathcal{J}_A^{(g)}$ of subcarriers modulated by alphabet $\mathcal{A}$, and the remaining subcarriers form $\mathcal{J}_B^{(g)}$, modulated by alphabet $\mathcal{B}$.

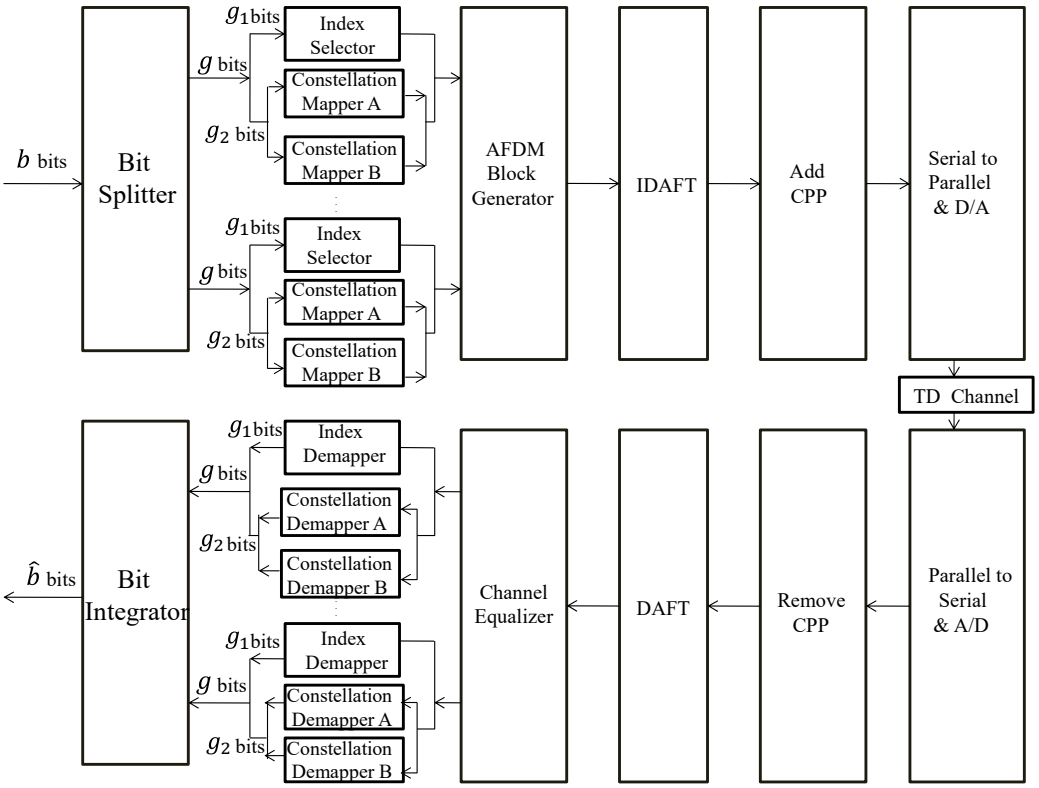


Figure 6.1: Block diagram of the AFDM-DM-IM system

Table 6.1: Look-up table for dual-mode index modulation with $g_1 = 2$, $L = 4$, $K = 2$

Index bits	Indices	Subblock
$[0,0]$	$[1,2]$	$[\eta_A^{(1)}, \eta_A^{(2)}, \eta_B^{(1)}, \eta_B^{(2)}]$
$[0,1]$	$[1,3]$	$[\eta_A^{(1)}, \eta_B^{(1)}, \eta_A^{(2)}, \eta_B^{(2)}]$
$[1,0]$	$[2,3]$	$[\eta_B^{(1)}, \eta_A^{(1)}, \eta_A^{(2)}, \eta_B^{(2)}]$
$[1,1]$	$[3,4]$	$[\eta_B^{(1)}, \eta_B^{(2)}, \eta_A^{(1)}, \eta_A^{(2)}]$

The DAFT-domain transmit vector $\mathbf{x}$ is processed by the AFDM modulator of Section 4.1.2, which applies the inverse DAFT and prepends a chirp-periodic prefix of length L_{cp}. After transmission across the doubly dispersive channel and CPP removal, the DAFT-domain received vector follows the input-output relation

$$\mathbf{y} = \mathbf{H}_{\text{eff}}\,\mathbf{x} + \tilde{\mathbf{w}}, \tag{6.3}$$

where the effective DAFT-domain channel matrix $\mathbf{H}_{\text{eff}}$ is given by (4.14), repeated here for the P-path channel as

$$\mathbf{H}_{\text{eff}} = \sum_{i=1}^{P} h_i\,\mathbf{A}\,\boldsymbol{\Gamma}_{\text{CPP},i}\,\boldsymbol{\Delta}_{\nu_i}\,\boldsymbol{\Pi}^{l_i}\,\mathbf{A}^{H}, \tag{6.4}$$

with h_i the complex gain, l_i the integer delay, and ν_i the normalized Doppler shift of the ith path. The noise $\tilde{\mathbf{w}} \sim \mathcal{CN}(\mathbf{0}, \sigma^2\mathbf{I}_N)$ retains the same statistics as the time-domain noise because $\mathbf{A}$ is unitary. The chirp parameter c_1 is selected per the path-separability rule of (4.21).

6.2 Baseline Detectors for AFDM-DM-IM

6.2.1 ML Detector

The ML detector is the optimal detector for the AFDM-DM-IM system and is given by

$$\hat{\mathbf{x}}^{\text{ML}} = \arg\min_{\mathbf{x}\in\mathbb{X}} \|\mathbf{y} - \mathbf{H}_{\text{eff}}\mathbf{x}\|_F^2, \tag{6.5}$$

where $\mathbb{X}$ is the set of all possible realizations of the AFDM-DM-IM transmit vector $\mathbf{x}$. The computational complexity of the ML detector increases drastically with the size of $\mathbb{X}$, which makes it infeasible for practical implementation at large frame sizes.

6.2.2 MMSE-ML Detector

To reduce the computational complexity of the ML detector, the MMSE-ML detector first applies MMSE equalization to the received signal

$$\hat{\mathbf{x}}^{\mathrm{MMSE}} = \left(\mathbf{H}_{\mathrm{eff}}^{H}\mathbf{H}_{\mathrm{eff}} + \sigma^2\mathbf{I}_N\right)^{-1}\mathbf{H}_{\mathrm{eff}}^{H}\mathbf{y}, \tag{6.6}$$

where $\mathbf{I}_N$ is the identity matrix of order N. The equalized signal $\hat{\mathbf{x}}^{\mathrm{MMSE}}$ is partitioned into G subblocks $\mathbf{u}^{(\zeta)}$, $\zeta = 1, \ldots, G$, and each subblock is demodulated using an ML algorithm. For the ζth subblock, the optimal index sequence and transmitted symbols are obtained by evaluating every possible subblock configuration by exploring all index patterns $\mathbf{J} \in \mathcal{J}$ and their corresponding symbol combinations $\mathbf{C}_{\mathbf{J}} \in \mathcal{C}_{\mathbf{J}}$

$$\left\{\hat{\mathbf{J}}^{(\zeta)}, \hat{\mathbf{x}}^{(\zeta)}\right\} = \arg \min_{\mathbf{J}\in\mathcal{J}, \mathbf{C}_{\mathbf{J}}\in\mathcal{C}_{\mathbf{J}}} \sum_{k=1}^{L} \left|\mathbf{u}^{(\zeta)}(k) - \mathbf{C}_{\mathbf{J}}(k)\right|^2, \quad 1 \le \zeta \le G, \tag{6.7}$$

where $\hat{\mathbf{J}}^{(\zeta)}$ is the estimated index pattern of the ζth subblock and $\hat{\mathbf{x}}^{(\zeta)}$ is the estimated symbol vector. The information bits are recovered using an index pattern mapping table together with the two constellation alphabets.

6.2.3 MMSE-LLR Detector

After equalization of the received signal using (6.6) and partitioning into subblocks, an LLR based algorithm demodulates each subblock [20]. Since each subcarrier is modulated by either alphabet $\mathcal{A}$ or alphabet $\mathcal{B}$, the natural logarithm of the ratio of the posterior probabilities of the two cases identifies the constellation mode of the subcarrier. For the nth subcarrier of the ζth subblock, the log-likelihood ratio is

$$\zeta_n = \ln\left(\frac{\sum_{j=1}^{M_A} \Pr\left(x_n^{(\eta)} = C_A(j) \mid u_n^{(\zeta)}\right)}{\sum_{q=1}^{M_B} \Pr\left(x_n^{(\eta)} = C_B(q) \mid u_n^{(\zeta)}\right)}\right), \quad 1 \le n \le L, \tag{6.8}$$

where $C_A(j) \in \mathcal{A}$ and $C_B(q) \in \mathcal{B}$. A positive ζ_n indicates that the nth subcarrier is more likely modulated by alphabet $\mathcal{A}$, and a negative ζ_n indicates that it is more likely modulated by alphabet $\mathcal{B}$. Relying solely on the sign of ζ_n can lead to incorrect index pattern estimates in the presence of channel noise. To mitigate this, the K largest LLR values in each subblock are identified, and the associated subcarriers are taken as modulated by alphabet $\mathcal{A}$. The transmitted symbols are estimated by hard decision, and the information bits are decoded using the mapping table. The LLR detector nearly matches the BER of the MMSE-ML detector while significantly reducing the computational complexity.

6.3 VAMP-DMDIM Detector

The baseline detectors decouple equalization from index detection and ignore the discrete constellation structure during the linear stage. The VAMP-DMDIM detector instead jointly infers the transmitted symbols $\mathbf{x}$ and the index patterns $\{\mathcal{J}_A^{(g)}\}_{g=1}^{G}$ by adapting the VAMP framework [30] with preconditioned conjugate gradient linear estimation of Chapter 4 to the dual-mode prior through an inline subblock belief propagation module.

6.3.1 Detection Problem and Dynamic Mixed Prior

Given the measurement (6.3), the prior on the symbol x_n within subblock g is a dynamically updated soft mixture of the two alphabets

$$p(x_n \mid \pi_{A,n}) = \frac{\pi_{A,n}}{M_A} \sum_{m=1}^{M_A} \delta(x_n - a_m) + \frac{\pi_{B,n}}{M_B} \sum_{m=1}^{M_B} \delta(x_n - b_m), \tag{6.9}$$

where $\pi_{B,n} = 1 - \pi_{A,n}$ and the type probability is initialized as $\pi_{A,n}^{(0)} = K/L$. The combined alphabet is $\mathcal{C} = \mathcal{A} \cup \mathcal{B}$ with $Q = M_A + M_B$ elements, and the type indicator is $t_q = \mathbf{1}[c_q \in \mathcal{A}]$.

6.3.2 MMSE Denoiser

At outer iteration k, the VAMP denoiser receives the effective input $\mathbf{r}_{1,k} \in \mathbb{C}^N$ with scalar precision $\gamma_{1,k} > 0$. For each subcarrier n, the log-posterior over the combined alphabet $\mathcal{C}$ is

$$\ell_q^{(n)} = \log \omega_q^{(n)} - \gamma_{1,k} \left| r_{1,k,n} - c_q \right|^2, \quad q = 1, \ldots, Q, \tag{6.10}$$

where $\omega_q^{(n)} = \pi_{A,n}/M_A$ for $c_q \in \mathcal{A}$ and $\omega_q^{(n)} = \pi_{B,n}/M_B$ for $c_q \in \mathcal{B}$. After log-sum-exp stabilization, the posterior weights are $\tilde{\omega}_q^{(n)} = e^{\ell_q^{(n)}} / \sum_{q'} e^{\ell_{q'}^{(n)}}$. The MMSE estimate, posterior variance, and soft type posterior are

$$\hat{x}_{1,k,n} = \sum_{q=1}^{Q} c_q \tilde{\omega}_q^{(n)}, \tag{6.11}$$

$$\alpha_{1,k,n} = \sum_{q=1}^{Q} \left| c_q - \hat{x}_{1,k,n} \right|^2 \tilde{\omega}_q^{(n)}, \tag{6.12}$$

$$q_{A,n} = \sum_{q=1}^{Q} t_q \tilde{\omega}_q^{(n)}. \tag{6.13}$$

The Onsager-corrected quantities passed to the linear stage are

$$\tilde{\mathbf{r}}_k = \frac{\hat{\mathbf{x}}_{1,k} - \alpha_{1,k} \mathbf{r}_{1,k}}{1 - \alpha_{1,k}}, \qquad \tilde{\gamma}_k = \frac{\gamma_{1,k}(1 - \alpha_{1,k})}{\alpha_{1,k}}, \tag{6.14}$$

where $\alpha_{1,k} = N^{-1} \sum_n \alpha_{1,k,n}$.

6.3.3 Subblock Belief Propagation

For the gth subblock, let $\mathcal{P}_1, \ldots, \mathcal{P}_{N_p}$ enumerate all $N_p = \binom{L}{K}$ valid index patterns, with binary indicator $t_{j,l} = \mathbf{1}[l \in \mathcal{P}_j]$ [29]. The log-likelihood of pattern j is

$$\Lambda_j^{(g)} = \sum_{l=1}^{L} \left[t_{j,l} \log q_{A,n_l} + (1 - t_{j,l}) \log\left(1 - q_{A,n_l}\right) \right], \tag{6.15}$$

where $n_l = (g-1)L + l$. After log-sum-exp normalization, the pattern posterior $\rho_j^{(g)}$ is obtained, and the updated soft type probability is

$$\pi_{A,n_l}^{\text{new}} = \sum_{j=1}^{N_p} t_{j,l}\, \rho_j^{(g)}. \tag{6.16}$$

The MAP index pattern estimate is $\hat{\mathcal{J}}_A^{(g)} = \mathcal{P}_{j^*}$ with $j^* = \arg\max_j \rho_j^{(g)}$.

6.3.4 CG-Based LMMSE Estimation

The linear stage solves the Hermitian positive definite system $\mathbf{Q}_k \hat{\mathbf{x}}_{2,k} = \mathbf{b}_k$, where

$$\mathbf{Q}_k = \gamma_w \mathbf{H}_{\text{eff}}^H \mathbf{H}_{\text{eff}} + \tilde{\gamma}_k \mathbf{I}_N, \qquad \mathbf{b}_k = \gamma_w \mathbf{H}_{\text{eff}}^H \mathbf{y} + \tilde{\gamma}_k \tilde{\mathbf{r}}_k. \tag{6.17}$$

This system is solved iteratively using preconditioned conjugate gradient with K_{CG} inner iterations and diagonal preconditioner $m_n = \gamma_w \sum_m |[\mathbf{H}_{\text{eff}}]_{m,n}|^2 + \tilde{\gamma}_k$, following the VAMP-CG construction of Section 4.3. The Onsager parameter $\alpha_{2,k} = (\tilde{\gamma}_k/N)\text{Tr}[\mathbf{Q}_k^{-1}]$ is estimated via a stochastic trace estimator using n_{probe} probe vectors $\mathbf{z}_j \sim \mathcal{CN}(\mathbf{0}, \mathbf{I}_N)$, with each $\mathbf{Q}_k^{-1}\mathbf{z}_j$ obtained via an additional CG solve. The VAMP state update is

$$\gamma_{k+1} = \frac{\tilde{\gamma}_k \alpha_{2,k}}{1-\alpha_{2,k}}, \qquad \mathbf{r}_{1,k+1} = \rho_d \frac{\hat{\mathbf{x}}_{2,k} - \alpha_{2,k}\tilde{\mathbf{r}}_k}{1-\alpha_{2,k}} + (1-\rho_d)\mathbf{r}_{1,k}, \tag{6.18}$$

with damping factor $\rho_d = 0.5$ and clipping. The type probability is damped as $\boldsymbol{\pi}_A \leftarrow 0.5\boldsymbol{\pi}_A^{\text{new}} + 0.5\boldsymbol{\pi}_A$.

6.3.5 Hard Decision

A voting buffer of depth $n_v = 3$ accumulates the per-iteration MAP pattern estimates, and the final index pattern is determined by majority vote to mitigate oscillation. Given the finalized type vector $\hat{\mathbf{t}}^{(g)} \in \{0,1\}^L$, the hard symbol decision

is

$$\hat{x}_n = \begin{cases} \arg\min_{a\in\mathcal{A}} |\hat{x}_{1,T,n} - a|, & \hat{t}_l^{(g)} = 1, \\ \arg\min_{b\in\mathcal{B}} |\hat{x}_{1,T,n} - b|, & \hat{t}_l^{(g)} = 0. \end{cases} \tag{6.19}$$

Index bits are recovered by table lookup of the matched valid pattern, and symbol bits by nearest-point indexing within the chosen alphabet. The complete VAMP-DMDIM detector is summarized in Algorithm 6.1.

Algorithm 6.1 VAMP-DMDIM Detector for AFDM-DM-IM

Require: $\mathbf{H}_{\text{eff}}, \mathbf{y}, \sigma_w^2, \mathcal{A}, \mathcal{B}, K, L, G, T, K_{\text{CG}}, n_{\text{probe}}$
Precompute: $\{(\mathcal{P}_j, \mathbf{t}_j)\}$, $\mathbf{H}_{\text{eff}}^H\mathbf{y}$, $\|\mathbf{h}_n\|^2$
Initialize: $\mathbf{r}_0 = \mathbf{0}$, $\gamma_0 = 1$, $\pi_{A,n}^{(0)} = K/L$, $\mathcal{V} = \varnothing$
for $k = 0$ to $T-1$ **do**
    Denoiser: compute $\hat{x}_{k,n}, \alpha_{k,n}, q_{A,n}$ via (6.10) to (6.13)
    Compute $\tilde{\mathbf{r}}_k, \tilde{\gamma}_k$ via (6.14) and clip
    Subblock BP: $\Lambda_j^{(g)}, \rho_j^{(g)}, \pi_{A,nl}^{\text{new}}$; $j^* = \arg\max_j \rho_j^{(g)}$
    Damped $\boldsymbol{\pi}_A$ update; push $\{j_g^*\}$ into $\mathcal{V}$
    CG-LMMSE: solve $\mathbf{Q}_k\hat{\mathbf{x}}_{2,k} = \mathbf{b}_k$ via PCG
    Estimate $\alpha_{2,k}$ via n_{probe} probes; update $\gamma_{k+1}, \mathbf{r}_{k+1}$
    if convergence reached and $k > 3$ **then**
        break
    end if
end for
Hard decision: majority-vote $\hat{t}_l^{(g)}$; enforce K ones; symbol decision via (6.19); decode bits
return $\hat{\mathbf{x}}$, decoded bits

6.4 GAMP-DMDIM Detector

The GAMP-DMDIM detector [31] replaces the conjugate gradient linear step of VAMP-DMDIM with direct output and input message updates, augmented by adaptive damping, variance flooring, an Onsager bypass at high SNR, and a divergence-detection reset. This eliminates the inner CG loop and the stochastic trace estimator, reducing the per-iteration cost to two matrix-vector products while retaining the joint symbol-index inference through the same subblock belief propagation module.

6.4.1 Output Linear Update

GAMP-DMDIM maintains output messages $\hat{\mathbf{s}} \in \mathbb{C}^N$ and input estimates $\hat{\mathbf{x}} \in \mathbb{C}^N$ with per-subcarrier variance $\mathbf{v}_x \in \mathbb{R}_+^N$. Define the variance floor $v_{\min} = \min_{c \in \mathcal{C}} |c|^2 \times 10^{-4}$ and the noise-safe variance $\sigma_{w,s}^2 = \max(\sigma_w^2, 10^{-10})$. The output variance is

$$v_{p,m} = \max\left(\sum_n |[\mathbf{H}_{\text{eff}}]_{m,n}|^2 v_{x,n}, v_{\min} \right). \tag{6.20}$$

The effective output, with Onsager bypass at high SNR, is

$$p_m = \begin{cases} [\mathbf{H}_{\text{eff}} \hat{\mathbf{x}}]_m - v_{p,m} \hat{s}_m, & \bar{v}_x > 10 v_{\min}, \\ [\mathbf{H}_{\text{eff}} \hat{\mathbf{x}}]_m, & \text{otherwise.} \end{cases} \tag{6.21}$$

The output residual and message variance are

$$\hat{s}_{\text{new},m} = \frac{y_m - p_m}{v_{p,m} + \sigma_{w,s}^2}, \qquad v_{s,m} = \frac{1}{v_{p,m} + \sigma_{w,s}^2}. \tag{6.22}$$

The output message is clipped element-wise to magnitude $s_{\max} = 10 \max_c |c| / \sqrt{\sigma_{w,s}^2}$.

6.4.2 Input Linear Update

The input message variance is $v_{r,n} = (\sum_m |[\mathbf{H}_{\text{eff}}]_{m,n}|^2 v_{s,m})^{-1}$, clipped to $2\mathbb{E}[|x|^2]$. The effective input observation is

$$r_n = \hat{x}_n + v_{r,n} \, [\mathbf{H}_{\text{eff}}^H \hat{\mathbf{s}}_{\text{new}}]_n, \tag{6.23}$$

clipped to magnitude $r_{\max} = 3 \max_c |c|$.

6.4.3 MMSE Denoiser with Dynamic Mixed Prior

The denoiser is identical in structure to the VAMP-DMDIM denoiser, but the scalar precision $\gamma_{1,k}$ is replaced by the per-subcarrier precision $v_{r,n}^{-1}$

$$\ell_q^{(n)} = \log \omega_q^{(n)} - \frac{|r_n - c_q|^2}{v_{r,n}}, \tag{6.24}$$

yielding the updated mean $\hat{x}_{n,\text{new}}$, the floored variance $v_{x,n,\text{new}}$, and the soft type posterior $q_{A,n}$ via (6.11) to (6.13).

6.4.4 Subblock Belief Propagation

The subblock belief propagation module is identical to that of Section 6.3.3. The pattern log-likelihoods $\{\Lambda_j^{(g)}\}$ are computed via (6.15), the pattern posteriors $\{\rho_j^{(g)}\}$ and soft type updates via (6.16), and the MAP pattern $\hat{\jmath}_A^{(g)}$ is taken as the most probable pattern.

6.4.5 Adaptive Damping Schedule

The damping coefficients are linearly scheduled over the T iterations

$$\beta_t = \beta_0 + \frac{t-1}{T-1}(\beta_f - \beta_0), \tag{6.25}$$

with $(\beta_0, \beta_f) = (0.3, 0.7)$ for the symbol estimates and $(\beta_{\pi,0}, \beta_{\pi,f}) = (0.2, 0.5)$ for the type probabilities. The damped updates are

$$\hat{\mathbf{x}} \leftarrow \beta_t \hat{\mathbf{x}}_{\text{new}} + (1-\beta_t)\hat{\mathbf{x}}, \tag{6.26}$$

$$\mathbf{v}_x \leftarrow \max\left(\beta_t \mathbf{v}_{x,\text{new}} + (1-\beta_t)\mathbf{v}_x, v_{\min}\right), \tag{6.27}$$

$$\boldsymbol{\pi}_A \leftarrow \text{clip}\left(\beta_{\pi,t} \boldsymbol{\pi}_A^{\text{new}} + (1-\beta_{\pi,t})\boldsymbol{\pi}_A, \epsilon, 1-\epsilon\right). \tag{6.28}$$

6.4.6 Divergence Detection and Reset

If $\|\hat{\mathbf{x}}_{\text{new}}\|_2 > x_{\text{ref}} = 5\sqrt{N}\max_c |c|$ or becomes non-finite, the output messages are reset and the symbol estimate is reverted

$$\hat{\mathbf{s}} \leftarrow \mathbf{0}, \qquad \hat{\mathbf{x}}_{\text{new}} \leftarrow \hat{\mathbf{x}}. \tag{6.29}$$

6.4.7 Hard Decision

After iteration T, the index pattern is taken as $\hat{\mathcal{J}}_A^{(g)} = \mathcal{P}_{j_T^*}$. The hard symbol decision uses the damped estimate

$$\hat{x}_n^{\text{hard}} = \begin{cases} \arg\min_{a\in\mathcal{A}} |\hat{x}_n - a|, & \hat{t}_l^{(g)} = 1, \\ \arg\min_{b\in\mathcal{B}} |\hat{x}_n - b|, & \hat{t}_l^{(g)} = 0. \end{cases} \tag{6.30}$$

If $\sum_l \hat{t}_l^{(g)} \neq K$, the type vector is corrected by retaining or adding the positions with the largest q_{A,n_l}. Index and symbol bits are decoded by table lookup and nearest-point indexing. The complete GAMP-DMDIM detector is summarized in Algorithm 6.2.

Algorithm 6.2 GAMP-DMDIM Detector for AFDM-DM-IM

Require: $\mathbf{H}_{\text{eff}}, \mathbf{y}, \sigma_w^2, \mathcal{A}, \mathcal{B}, K, L, G, T$
Precompute: $\{(\mathcal{P}_j, \mathbf{t}_j)\}$, $|[\mathbf{H}_{\text{eff}}]_{m,n}|^2$, constants
Initialize: $\hat{\mathbf{x}} = \mathbf{0}$, $\mathbf{v}_x = S_{\text{avg}}\mathbf{1}$, $\hat{\mathbf{s}} = \mathbf{0}$, $\pi_{A,n}^{(0)} = K/L$
for $t = 1$ to T **do**
    Adaptive damping $\beta_t, \beta_{\pi,t}$ via (6.25)
    Output update: $\mathbf{v}_p, \mathbf{p}, \hat{\mathbf{s}}_{\text{new}}, \mathbf{v}_s$ via (6.20) to (6.22)
    Input update: $\mathbf{v}_r, \mathbf{r}$ via (6.23) and clip
    Denoiser: $\hat{x}_{n,\text{new}}, v_{x,n,\text{new}}, q_{A,n}$ via (6.24), (6.11) to (6.13)
    Subblock BP: $\Lambda_j^{(g)}, \rho_j^{(g)}, \pi_{A,n_l}^{\text{new}}, j_t^*$
    Divergence check: reset via (6.29) if needed
    Damped update via (6.26) to (6.28)
    if convergence reached and $t > 3$ **then**
        break
    end if
end for
Hard decision: MAP pattern $\hat{t}_l^{(g)} \leftarrow t_{j_T^*,l}$; enforce K ones; symbol decision via (6.30); decode bits
return $\hat{\mathbf{x}}^{\text{hard}}$, decoded bits

6.5 Pairwise Error Probability Analysis

6.5.1 Conditional Pairwise Error Probability

The received signal (6.3) can be restated as [17, 39]

$$\mathbf{y} = \sum_{i=1}^{P} h_i \mathbf{H}_i \mathbf{x} + \tilde{\mathbf{w}} = \mathbf{\Phi}(\mathbf{x})\,\mathbf{\Psi} + \tilde{\mathbf{w}}, \tag{6.31}$$

where $\mathbf{\Psi} = [h_1, h_2, \ldots, h_P]^T \in \mathbb{C}^{P\times 1}$, $\mathbf{H}_i = \mathbf{A}\,\mathbf{\Gamma}_{\text{CPP},i}\,\mathbf{\Delta}_{\nu_i}\,\mathbf{\Pi}^{l_i}\,\mathbf{A}^H \in \mathbb{C}^{N\times N}$, and

$$\mathbf{\Phi}(\mathbf{x}) = [\mathbf{H}_1\mathbf{x}\,|\,\cdots\,|\,\mathbf{H}_P\mathbf{x}] \in \mathbb{C}^{N\times P}. \tag{6.32}$$

The conditional pairwise error probability for the AFDM-DM-IM scheme is

$$\begin{aligned} P(\mathbf{x} \to \hat{\mathbf{x}} \mid \mathbf{\Psi}) &= P\left(\|\mathbf{y} - \mathbf{\Phi}(\hat{\mathbf{x}})\mathbf{\Psi}\|^2 < \|\mathbf{y} - \mathbf{\Phi}(\mathbf{x})\mathbf{\Psi}\|^2\right) \\ &= Q\left(\sqrt{\frac{\delta}{2P\sigma^2}}\right), \end{aligned} \tag{6.33}$$

where the Gaussian Q-function is $Q(x) = \frac{1}{\pi}\int_0^{\pi/2} \exp\left(-\frac{x^2}{2\sin^2\rho}\right) d\rho$, and the conditional squared distance is

$$\delta = \|(\mathbf{\Phi}(\hat{\mathbf{x}}) - \mathbf{\Phi}(\mathbf{x}))\mathbf{\Psi}\|^2 = \mathbf{\Psi}^H \mathbf{K} \mathbf{\Psi}, \tag{6.34}$$

with $\mathbf{K} = (\mathbf{\Phi}(\hat{\mathbf{x}}) - \mathbf{\Phi}(\mathbf{x}))^H (\mathbf{\Phi}(\hat{\mathbf{x}}) - \mathbf{\Phi}(\mathbf{x}))$.

6.5.2 Unconditional Pairwise Error Probability

Averaging the conditional pairwise error probability over the distribution of $\mathbf{\Psi}$ gives

$$\begin{aligned} P(\mathbf{x} \to \hat{\mathbf{x}}) &= \frac{1}{\pi}\int_0^{\pi/2}\int_0^{+\infty} \exp\left(-\frac{\delta}{4P\sigma^2\sin^2\rho}\right) p_\delta(\delta)\, d\delta\, d\rho \\ &= \frac{1}{\pi}\int_0^{\pi/2} F_\delta\left(-\frac{1}{4P\sigma^2\sin^2\rho}\right) d\rho, \end{aligned} \tag{6.35}$$

where $F_\delta(\cdot)$ is the moment generating function of δ

$$F_\delta(t) = |\mathbf{I} - t\mathbf{K}|^{-1} = \prod_{i=1}^{q} (1 - t\lambda_i)^{-1}, \tag{6.36}$$

with q the number of distinct nonzero eigenvalues λ_i of $\mathbf{K}$. Substituting (6.36) into (6.35),

$$P(\mathbf{x} \to \hat{\mathbf{x}}) = \frac{1}{\pi}\int_0^{\pi/2} \prod_{i=1}^{q} \left(\frac{1}{1 + \frac{\lambda_i}{4P\sigma^2\sin^2\rho}}\right) d\rho. \tag{6.37}$$

6.5.3 Chernoff Bound and Average Bit Error Rate

Applying the Chernoff bound inequality, the upper bound on the pairwise error probability is

$$P(\mathbf{x} \to \hat{\mathbf{x}}) \le \prod_{i=1}^{q} \left(1 + \frac{\lambda_i}{4P\sigma^2}\right)^{-1}. \tag{6.38}$$

The theoretical upper bound on the average bit error rate of the AFDM-DM-IM scheme is

$$P_{\text{ABER}} \le \frac{1}{g\,2^g} \sum_{\mathbf{x}} \sum_{\hat{\mathbf{x}}} P(\mathbf{x} \to \hat{\mathbf{x}})\, d_H(\mathbf{x}, \hat{\mathbf{x}}), \tag{6.39}$$

where $d_H(\mathbf{x}, \hat{\mathbf{x}})$ is the Hamming distance between the bit sequences of the respective error events and $g = g_1 + g_2$ is the total number of bits per subblock.

6.6 Spectral Efficiency

The spectral efficiency of the AFDM-DM-IM scheme is the ratio of the information rate to the bandwidth occupied. An AFDM-DM-IM frame spans a duration T and a bandwidth $N\Delta f$, and conveys $(g_1 + g_2)G$ bits. With $G = N/L$ and $T\Delta f = 1$, the spectral efficiency is

$$\mathrm{SE}_{\text{AFDM-DM-IM}} = \frac{\lfloor \log_2 \binom{L}{K} \rfloor + K \log_2 M_A + (L-K) \log_2 M_B}{L}. \tag{6.40}$$

For comparison, the spectral efficiencies of conventional AFDM and AFDM-IM are

$$\mathrm{SE}_{\text{AFDM}} = \log_2 M_{\text{mod}}, \qquad \mathrm{SE}_{\text{AFDM-IM}} = \frac{\lfloor \log_2 \binom{L}{K} \rfloor + K \log_2 M_{\text{mod}}}{L}, \tag{6.41}$$

where M_{mod} is the size of the modulation alphabet. AFDM-DM-IM activates every subcarrier of a subblock through two disjoint alphabets, which achieves complete resource utilization and higher spectral efficiency than AFDM-IM while avoiding the higher-order constellations that would otherwise reduce the minimum distance and degrade reliability.

6.7 Computational Complexity Summary

Table 6.2 summarizes the computational complexity of the detectors developed in this chapter. The ML detector grows exponentially with the joint index-symbol search space and is infeasible for large frames. The MMSE-ML and MMSE-LLR detectors replace the joint search with MMSE equalization at $\mathcal{O}(N^3)$ followed by per-subblock demodulation. The VAMP-DMDIM detector performs $K_{\text{CG}} + n_{\text{probe}}$ conjugate gradient solves per outer iteration, each at $\mathcal{O}(N^2)$, plus the denoiser and

belief propagation module of cost $\mathcal{O}(QN + N_pG)$. The GAMP-DMDIM detector requires only two matrix-vector products per iteration at $\mathcal{O}(N^2)$, plus the same denoiser and belief propagation module. Since $K_{\mathrm{CG}} + n_{\mathrm{probe}} \gg 2$, GAMP-DMDIM achieves substantially lower per-iteration cost than VAMP-DMDIM while both retain quadratic scaling in N.

Table 6.2: Computational complexity of AFDM-DM-IM detectors with N subcarriers, G subblocks, L subblock length, K active subcarriers, alphabet sizes M_A and M_B, combined alphabet size $Q = M_A + M_B$, pattern count $N_p = \binom{L}{K}$, T message passing iterations, K_{CG} inner CG iterations, and n_{probe} trace probes

Detector	Complexity
ML	$\mathcal{O}\left((M_A^K M_B^{L-K})^G\right)$
MMSE-ML	$\mathcal{O}\left(N^3 + G(\lfloor \log_2 \binom{L}{K} \rfloor + K \log_2 M_A + (L-K)\log_2 M_B)\right)$
MMSE-LLR	$\mathcal{O}\left(N^3 + GL(M_A + M_B) + GL^2\right)$
VAMP-DMDIM	$\mathcal{O}\left(T(K_{\mathrm{CG}} + n_{\mathrm{probe}})N^2 + T(QN + N_pG)\right)$
GAMP-DMDIM	$\mathcal{O}\left(2TN^2 + T(QN + N_pG)\right)$

6.8 Simulation Results

6.8.1 AFDM-DM-IM Performance with Baseline Detectors

The simulation parameters for the AFDM-DM-IM baseline evaluation are a carrier frequency $f_c = 4$ GHz, a chirp subcarrier spacing $\Delta f = 4$ kHz, a three-path channel ($P = 3$) with a maximum UE speed of 1200 km/h, and chirp parameter $c_1 = (2(a_{\max} + k_\nu) + 1)/(2N)$ with $k_\nu = 1$.

Fig. 6.2 compares the BER of AFDM-DM-IM and AFDM-IM [27] with the configuration $\{N, G, L, K\} = \{16, 4, 4, 2\}$. AFDM-DM-IM achieves a spectral efficiency of 1.5 bits/s/Hz using two distinguishable BPSK alphabets, while AFDM-IM achieves the same spectral efficiency using QPSK with two of the four subcarriers modulated and the rest left inactive. At a BER of 10^{-4}, AFDM-DM-IM attains a 4 dB SNR gain over AFDM-IM. To reach a spectral efficiency of 2.5 bits/s/Hz, AFDM-DM-IM uses two distinguishable QPSK alphabets while AFDM-IM uses

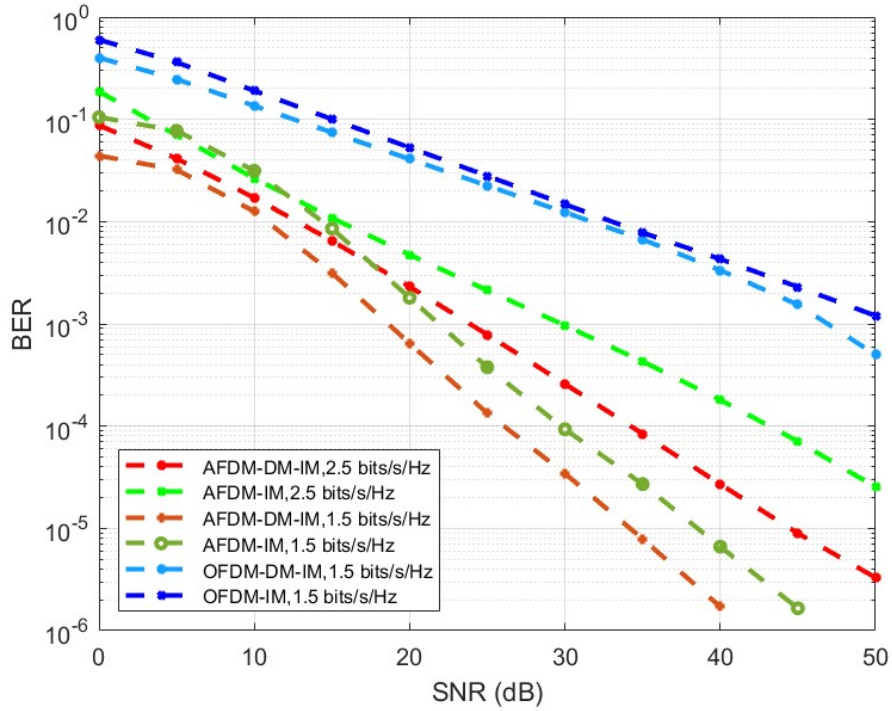


Figure 6.2: BER comparison of AFDM-DM-IM and AFDM-IM under high Doppler

16-QAM, and AFDM-DM-IM achieves almost 8 dB SNR gain over AFDM-IM. This larger gain arises because the minimum distance between the constellation symbols is smaller in 16-QAM than in the dual-mode QPSK and QPSK case.

Fig. 6.3 examines the effectiveness of the derived BER upper bound of (6.39). The system parameters are a spectral efficiency of 1.5 bits/s/Hz with $\{N, G, L, K\} = \{4, 1, 4, 2\}$, evaluated under three channel conditions with $P = 1, 2, 3$ paths. As the SNR increases, the theoretical upper bound converges with the simulation results, demonstrating excellent alignment particularly for SNR values above 10 dB. For all multipath scenarios, the theoretical bounds consistently track the simulation trends, confirming their reliability as performance indicators.

Fig. 6.4 illustrates the BER of AFDM-DM-IM for spectral efficiency values of 1.5, 2.5, and 4.5 bits/s/Hz with $\{N, G, L, K\} = \{16, 1, 4, 2\}$. The system with 1.5 bits/s/Hz using the BPSK and BPSK scheme exhibits the lowest BER, reaching 10^{-4} at around 30 dB SNR. The 2.5 bits/s/Hz configuration using QPSK and QPSK reaches a similar BER at around 35 dB SNR, and the 4.5 bits/s/Hz configuration

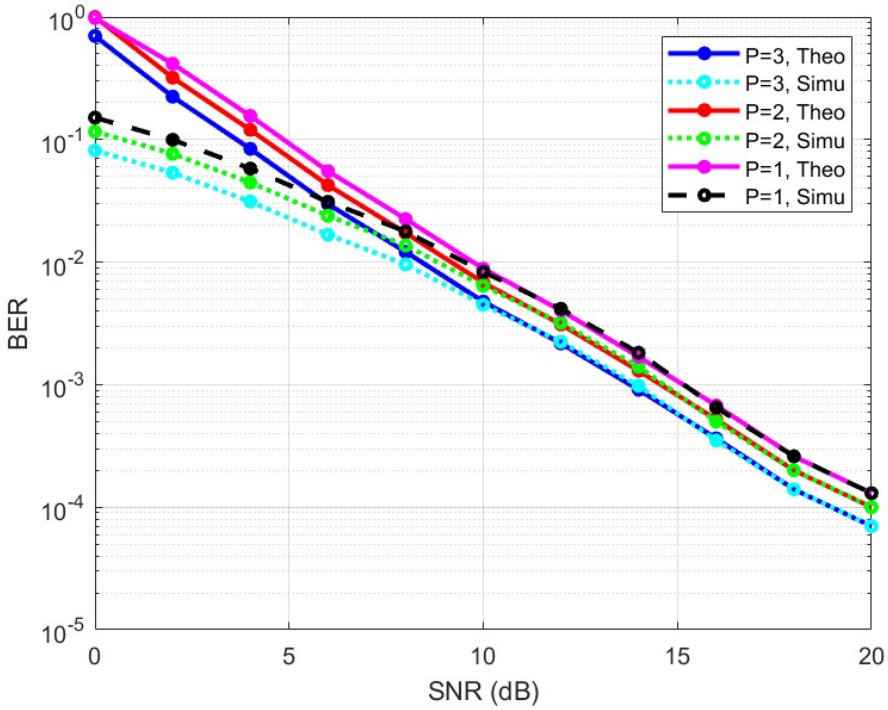


Figure 6.3: Comparison between the theoretical BER upper bound and the simulated BER for AFDM-DM-IM using the ML detector

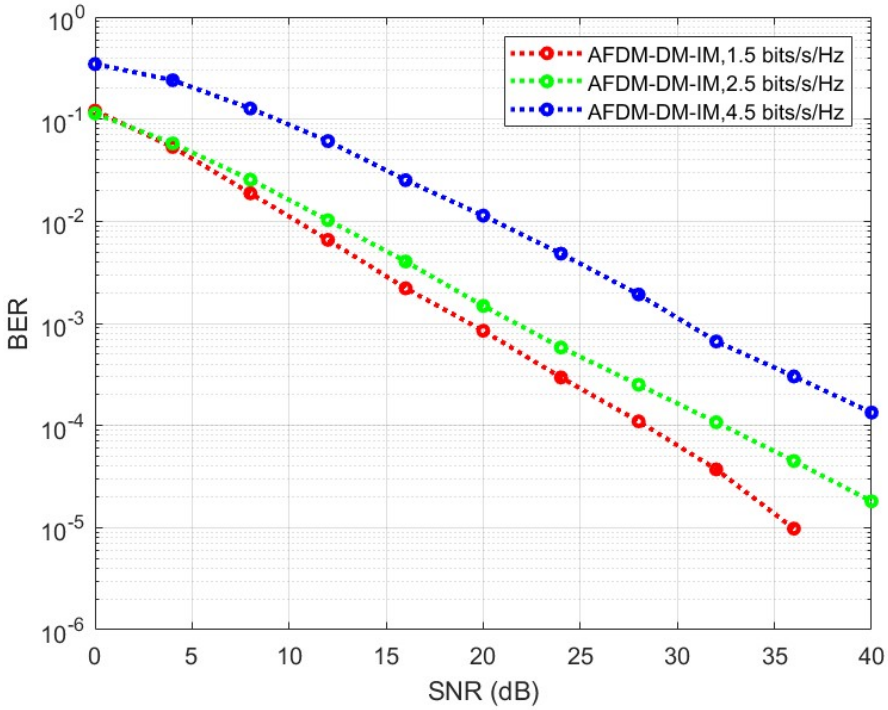


Figure 6.4: BER performance of AFDM-DM-IM under different spectral efficiency values

using 16-QAM and 16-QAM reaches it at approximately 40 dB SNR. Higher-order modulation schemes used to achieve higher spectral efficiency increase the BER for a given SNR, reflecting the trade-off between data rate and reliability.

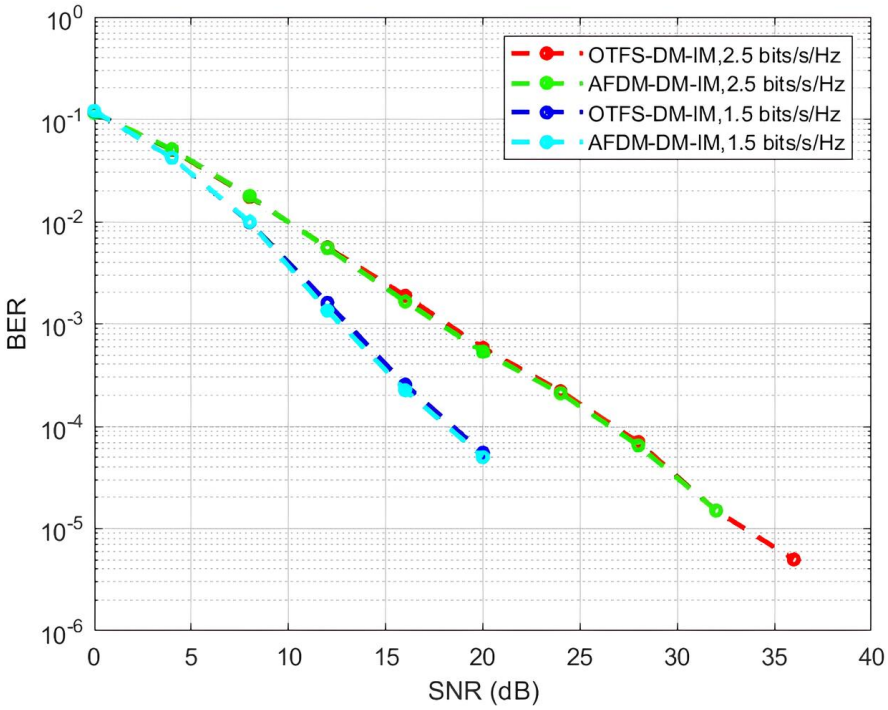


Figure 6.5: BER comparison of AFDM-DM-IM and OTFS-DM-IM

Fig. 6.5 compares AFDM-DM-IM and OTFS-DM-IM [25] with $\{N, G, L, K\} = \{16, 1, 4, 2\}$. At a spectral efficiency of 2.5 bits/s/Hz, both systems exhibit nearly identical BER across the SNR range. At a lower spectral efficiency of 1.5 bits/s/Hz, AFDM-DM-IM consistently outperforms OTFS-DM-IM, with the gap widening as SNR increases. AFDM-DM-IM therefore delivers better error performance than OTFS-DM-IM at lower spectral efficiency while matching it at higher spectral efficiency.

6.8.2 Message Passing Detector Performance

The message passing detectors are evaluated against the MMSE-LLR baseline over the 3GPP ITU EVA channel profile with Jake's Doppler model. The AFDM system uses a carrier frequency $f_c = 4$ GHz, a bandwidth $B_w = 4$ MHz with sampling period

$T_s = 1/B_w$, and integer tap delays obtained by rounding the standard ITU EVA delay table. The fading coefficients are drawn as $h_i \sim \mathcal{CN}(0, \sigma_i^2)$ with normalized tap powers, and the Doppler frequencies follow $\nu_i = \alpha_{\max} \cos\theta_i$ with $\theta_i \sim \mathcal{U}[-\pi, \pi]$. Both message passing detectors are run for $T = 12$ outer iterations, with $K_{\mathrm{CG}} = 15$ inner CG iterations and $n_{\mathrm{probe}} = 3$ probe vectors for the VAMP-DMDIM trace estimator. The number of subcarriers is fixed at $N = 256$, and Monte Carlo averaging is performed over independent channel realizations per SNR point.

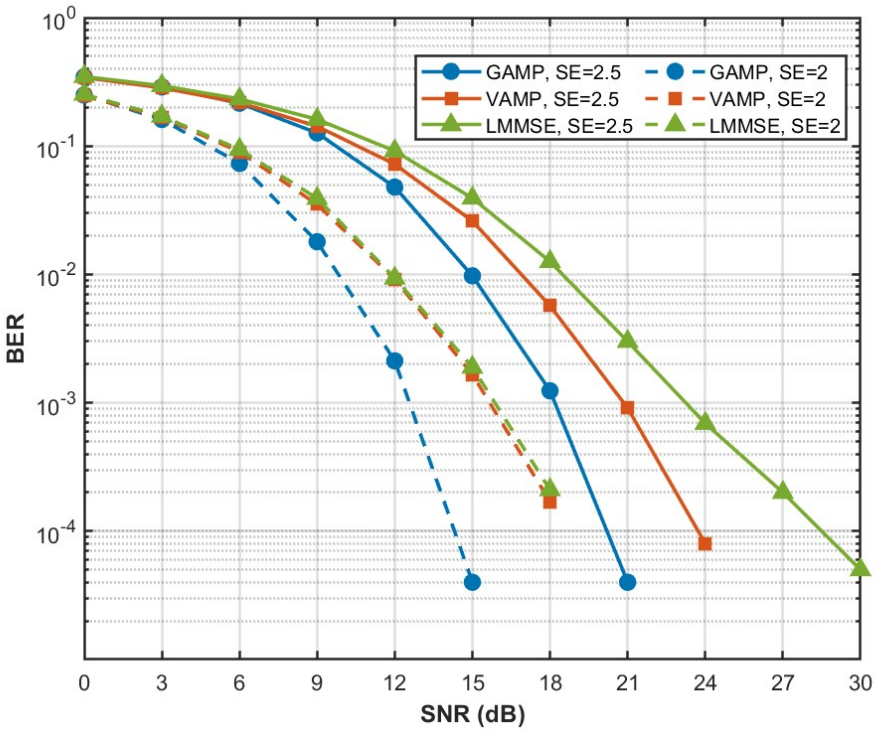


Figure 6.6: BER versus SNR for two spectral efficiency configurations with $L = 4$, $K = 2$ over the EVA channel

Fig. 6.6 shows the BER versus SNR for $\alpha_{\max} = 2$, $L = 4$, $K = 2$ at two spectral efficiencies. The 2.5 bits/s/Hz setting uses disjoint dual-mode QPSK alphabets, while the 2 bits/s/Hz setting uses disjoint BPSK alphabets on the real and imaginary axes, all normalized to unit power. GAMP-DMDIM attains the lowest BER in both cases, with gains of about 3 dB over MMSE-LLR and 1.5 dB over VAMP-DMDIM at a BER of 10^{-3} for the 2.5 bits/s/Hz setting, widening further at 2 bits/s/Hz where the reduced constellation density allows the joint symbol-index refinement

to exploit the dual-mode prior more effectively than the decoupled MMSE-LLR baseline.

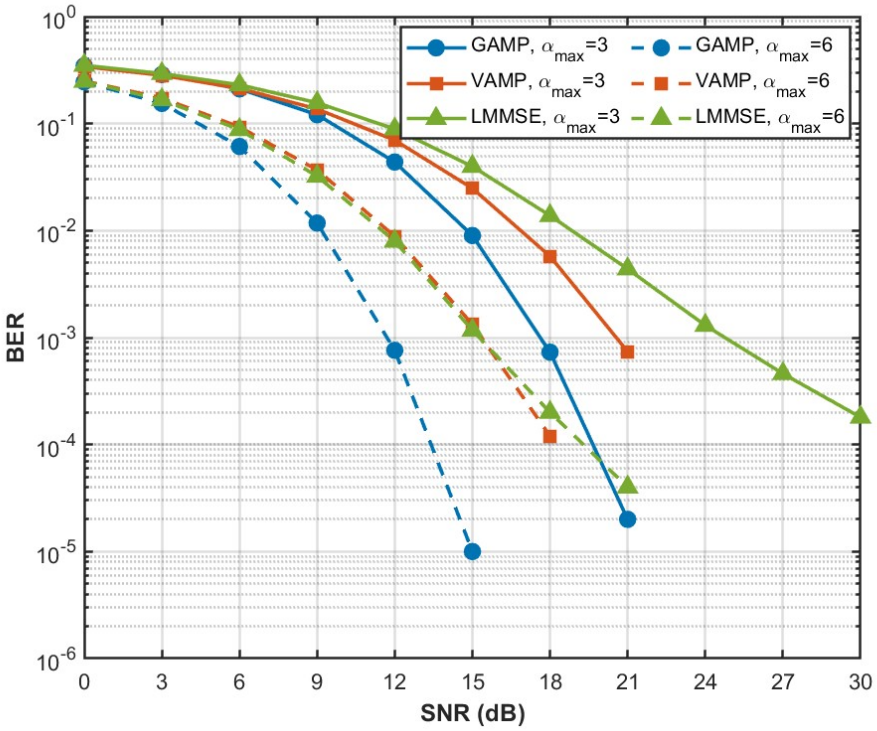


Figure 6.7: BER versus SNR for two values of $\alpha_{\max}$ over the EVA channel with disjoint BPSK dual-mode alphabets

Fig. 6.7 compares the BER for two values of the maximum normalized Doppler $\alpha_{\max}$, using disjoint BPSK alphabets with $L = 16$, $K = 3$. Increasing $\alpha_{\max}$ enriches the delay-Doppler diversity captured by the DAFT and yields a steeper BER waterfall for all three detectors. GAMP-DMDIM yields a gain of approximately 2 to 3 dB over MMSE-LLR and about 1 dB over VAMP-DMDIM at a BER of 10^{-3} for both Doppler values. The performance ordering is preserved across Doppler settings because the iterative output and input message updates of GAMP-DMDIM track the per-subcarrier diversity gain directly, whereas the linear MMSE-LLR baseline fails to exploit it.

Fig. 6.8 and Fig. 6.9 examine the impact of subblock length and activation density. Across both $L = 8$ and $L = 16$, GAMP-DMDIM achieves a gain of approximately 2.5 to 3 dB over MMSE-LLR and around 1 dB over VAMP-DMDIM

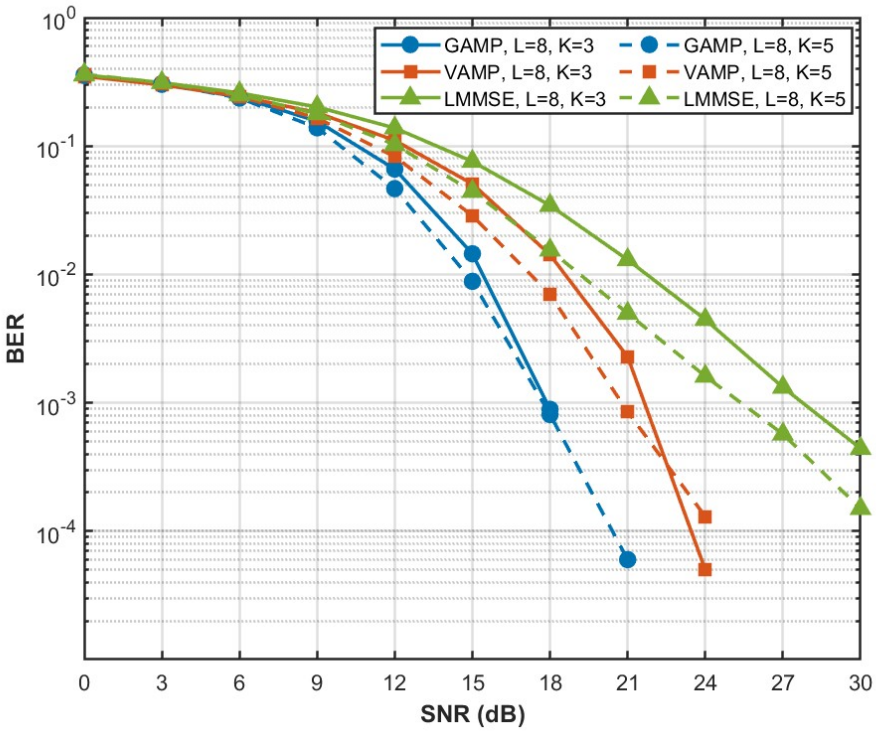


Figure 6.8: BER versus SNR for $L = 8$ over the EVA channel, comparing $K = 3$ and $K = 5$

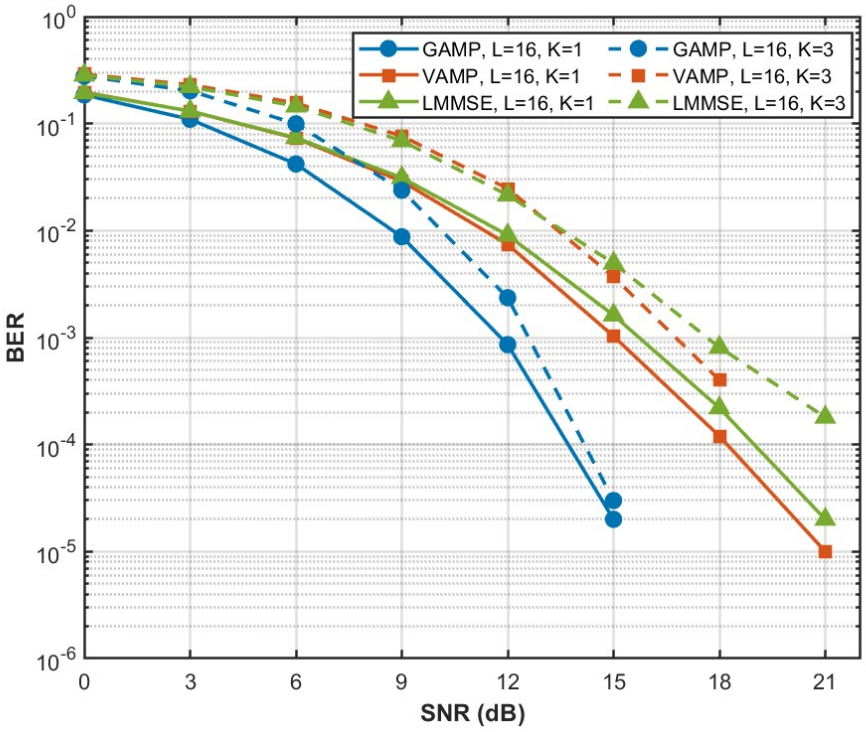


Figure 6.9: BER versus SNR for $L = 16$ over the EVA channel, comparing $K = 1$ and $K = 3$

at a BER of 10^{-3}, with sparser activation patterns yielding the lowest absolute BER due to sharper pattern likelihoods in the subblock belief propagation module. The consistent advantage at the larger pattern set $N_p = \binom{16}{3} = 560$ confirms that the inline belief propagation module scales effectively to denser configurations, while the elimination of the inner CG loop allows GAMP-DMDIM to reach this BER at lower per-iteration cost than VAMP-DMDIM.

6.9 Summary

This chapter developed AFDM-DM-IM, a dual-mode index modulation scheme that activates every subcarrier of a subblock through two disjoint constellation alphabets and thereby achieves complete resource utilization and higher spectral efficiency than the AFDM-IM scheme of Chapter 5. Three baseline detectors were developed, an optimal ML detector, an MMSE-ML detector, and a low-complexity MMSE-LLR detector, with the ML detector achieving the lowest BER at a complexity that grows exponentially with the joint index-symbol search space. A complete pairwise error probability analysis of the average bit error rate was derived using the moment generating function of the codeword difference correlation matrix and the Chernoff bound, with the theoretical upper bound closely matching the simulated BER above 10 dB. Two message passing detectors were then proposed that jointly infer the transmitted symbols and the subblock activation patterns through an inline belief propagation module enforcing the K-of-L index constraint. VAMP-DMDIM adapts the preconditioned conjugate gradient VAMP framework of Chapter 4 to the dual-mode prior with majority-vote hard decisions for index stability, while GAMP-DMDIM replaces the conjugate gradient linear step with direct output and input message updates augmented by adaptive damping, variance flooring, an Onsager bypass at high SNR, and a divergence-detection reset. Simulations over the 3GPP ITU EVA profile with Jake's Doppler model confirmed that GAMP-DMDIM consistently outperforms

MMSE-LLR and VAMP-DMDIM in BER while eliminating the inner conjugate gradient loop yields lower per-iteration computational cost. The dual-mode index modulation construct and the message passing detection framework introduced in this chapter extend to the multi-mode index modulation scheme developed in Chapter 7.

Chapter 7

AFDM with Multi-Mode Index Modulation and Permutation-Based Detection

This chapter develops AFDM with Multi-Mode Index Modulation (AFDM-MM-IM), an index modulation scheme that activates every subcarrier of a subblock and modulates it with a symbol drawn from one of n distinct constellation modes, with the permutation of modes across the subblock carrying index information [22, 26]. The AFDM system model, the chirp-parameter selection rule, and the DAFT-domain effective channel matrix $\mathbf{H}_{\text{eff}}$ that this chapter relies on are those established in Section 4.1, and are not repeated here. We first present the AFDM-MM-IM transmitter, the factorial permutation mapping that encodes the index bits, and the DAFT-domain signal model. We then develop three detectors, an LLR-based greedy detector that decouples mode assignment and symbol detection at low complexity, a Viterbi-based trellis detector that formulates the mode assignment as a shortest-path problem over a binomial-state trellis, and a sphere decoding based near-ML detector that jointly searches the mode-symbol space with branch-and-bound pruning. A pairwise error probability analysis of the average bit error probability is derived, and spectral efficiency, computational complexity, and simulation results

are presented at the end of the chapter.

The multi-mode scheme developed here is benchmarked not only against classical AFDM and AFDM-IM but also against the multi-mode variants of OFDM and OTFS (OFDM-MM and OTFS-MM), since the multi-mode setting is where a comparison across waveforms is most informative; these cross-waveform baselines are presented together in the performance comparison at the end of this chapter.

7.1 AFDM-MM-IM System Model

In the AFDM-MM-IM system as in [54], the N DAFT-domain subcarriers are organized into G subblocks of length $n = N/G$, and a stream of b incoming bits is divided into G groups of $g = b/G$ bits each. Since each group is processed identically, we focus on an arbitrary group $g \in \{1, 2, \ldots, G\}$. Each bit group of g bits is split into two segments. The first segment carries g_1 index bits, which determine the permutation of a predefined set of modulation constellations $\{\mathcal{M}_1, \mathcal{M}_2, \ldots, \mathcal{M}_n\}$ over the n subcarriers of the subblock. The second segment carries $g_2 = n \log_2 M$ modulation bits, which are mapped to n symbols $s_1^{(g)}, s_2^{(g)}, \ldots, s_n^{(g)}$, with each symbol drawn from the constellation assigned to the corresponding subcarrier.

To ensure distinct modulation modes across subcarriers, the g_1 index bits must encode one of the $n!$ full permutations of the n modes, so that

$$g_1 = \lfloor \log_2(n!) \rfloor. \tag{7.1}$$

The index set corresponding to the selected permutation is denoted as $\mathcal{P}^{(g)} = \{j_1^{(g)}, j_2^{(g)}, \ldots, j_n^{(g)}\}$, where $j_r^{(g)} \in \{1, 2, \ldots, n\}$ identifies the constellation assigned to the rth subcarrier of the gth subblock.

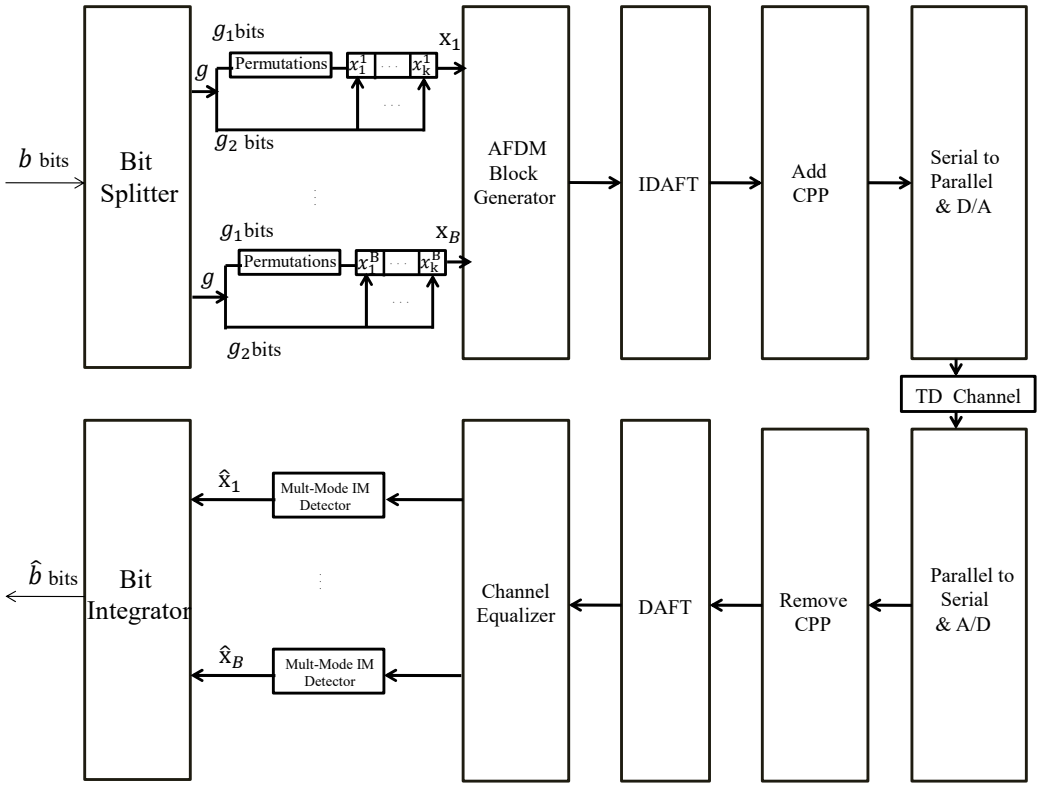


Figure 7.1: Block diagram of the AFDM-MM-IM system

7.1.1 Look-Up Table Method

A look-up table with 2^{g_1} entries is precomputed at both the transmitter and receiver. Each unique g_1-bit pattern maps to a selected permutation of $\{\mathcal{M}_1,\ldots,\mathcal{M}_n\}$. For instance, for $g_1 = 3$ and $n = 4$, only $2^3 = 8$ permutations out of $4! = 24$ are used. This approach is simple but becomes inefficient for large n due to the memory required to store the table.

7.1.2 Factorial Permutation Method

This method establishes a bijective mapping from integers in the range $[0, n!-1]$ to the permutations of $\mathcal{U} = \{1,2,\ldots,n\}$ based on lexicographic order. Each integer $\lambda \in [0, n!-1]$ is converted into a factorial-base representation

$$\lambda = (c_n - 1)(n-1)! + (c_{n-1} - 1)(n-2)! + \cdots + (c_2 - 1)\,1! + (c_1 - 1)\,0!, \qquad (7.2)$$

where $\mathcal{C} = \{c_n, c_{n-1}, \ldots, c_1\}$ and each c_i is the largest integer such that the accumulated sum does not exceed λ. Given $\mathcal{C}$, the permutation $\mathcal{P}^{(g)}$ is obtained by successively picking the c_ith smallest unused element from $\mathcal{U}$.

As an example, for $n = 4$ and $\lambda \in [0, 23]$, the corresponding permutations are listed in Table 7.1. For $\lambda = 2$, the factorial expansion yields $\mathcal{C} = \{1, 1, 2, 1\}$. The first index 1 selects the first smallest unused element (1), leaving $\{2, 3, 4\}$. The next index 1 selects 2, leaving $\{3, 4\}$. The next index 2 selects 4, leaving $\{3\}$. The final index 1 selects 3. Thus, $\mathcal{P}^{(g)} = \{1, 2, 4, 3\}$. This method avoids the memory cost of the look-up table and is preferred for large n.

Table 7.1: Permutation mapping for $n = 4$ using factorial expansion

λ	Factorial expansion	$\mathcal{C}$	$\mathcal{P}^{(g)}$
0	$0\cdot 6+0\cdot 2+0\cdot 1+0\cdot 0$	$\{1,1,1,1\}$	$\{1,2,3,4\}$
1	$0\cdot 6+0\cdot 2+0\cdot 1+1\cdot 0$	$\{1,1,1,2\}$	$\{1,2,4,3\}$
2	$0\cdot 6+0\cdot 2+1\cdot 1+0\cdot 0$	$\{1,1,2,1\}$	$\{1,3,2,4\}$
3	$0\cdot 6+0\cdot 2+1\cdot 1+1\cdot 0$	$\{1,1,2,2\}$	$\{1,3,4,2\}$
4	$0\cdot 6+0\cdot 2+2\cdot 1+0\cdot 0$	$\{1,1,3,1\}$	$\{1,4,2,3\}$
5	$0\cdot 6+0\cdot 2+2\cdot 1+1\cdot 0$	$\{1,1,3,2\}$	$\{1,4,3,2\}$
$\vdots$	$\vdots$	$\vdots$	$\vdots$
23	$3\cdot 6+1\cdot 2+1\cdot 1+1\cdot 0$	$\{4,2,2,2\}$	$\{4,3,2,1\}$

7.1.3 Transmit Signal and Channel Model

Once $\mathcal{P}^{(g)} = \{j_1^{(g)}, \ldots, j_n^{(g)}\}$ is identified, each symbol $s_r^{(g)}$ is drawn from the constellation $\mathcal{M}_{j_r^{(g)}}$. After processing all G groups, the resulting symbol vectors $\mathbf{x}^{(1)}, \mathbf{x}^{(2)}, \ldots, \mathbf{x}^{(G)}$ are arranged into the matrix

$$\mathcal{S} = [\mathbf{x}^{(1)}, \mathbf{x}^{(2)}, \ldots, \mathbf{x}^{(G)}]. \tag{7.3}$$

The matrix is read row-wise and written column-wise to form the DAFT-domain transmit vector

$$\mathbf{x} = [x_1^{(1)}, \ldots, x_n^{(1)}, x_1^{(2)}, \ldots, x_n^{(2)}, \ldots, x_1^{(G)}, \ldots, x_n^{(G)}]^T \in \mathbb{C}^{N\times 1}. \tag{7.4}$$

The DAFT-domain vector $\mathbf{x}$ is processed by the AFDM modulator of Section 4.1.2, which applies the inverse DAFT and prepends a chirp-periodic prefix of length L_{cp}. After transmission across the doubly dispersive channel and CPP removal, the DAFT-domain received vector follows the input-output relation

$$\mathbf{y} = \mathbf{H}_{\text{eff}}\,\mathbf{x} + \tilde{\mathbf{w}}, \tag{7.5}$$

where the effective DAFT-domain channel matrix $\mathbf{H}_{\text{eff}}$ is given by (4.14), with h_i the complex gain, l_i the integer delay, and $\nu_i = \alpha_i + a_i$ the normalized Doppler shift of the ith path. The chirp parameter c_1 is selected per the path-separability rule of (4.21), and the noise $\tilde{\mathbf{w}} \sim \mathcal{CN}(\mathbf{0}, \sigma^2\mathbf{I}_N)$.

7.1.4 MMSE Equalization and Joint ML Decoding

The DAFT-domain received signal is processed by an MMSE equalizer to mitigate the delay-Doppler spread of the channel

$$\hat{\mathbf{z}} = \left(\mathbf{H}_{\text{eff}}^H\mathbf{H}_{\text{eff}} + \sigma^2\mathbf{I}_N\right)^{-1}\mathbf{H}_{\text{eff}}^H\,\mathbf{y}, \tag{7.6}$$

where $\mathbf{I}_N$ is the identity matrix of order N. The equalized signal $\hat{\mathbf{z}}$ is partitioned into G subblocks $\mathbf{z}^{(g)} \in \mathbb{C}^{n\times 1}$ for $g = 1, \ldots, G$, and each subblock is processed independently because the encoding of each subblock is independent.

The receiver can jointly detect the transmitted symbol vector and the mode

permutation for the gth subblock by solving the maximum likelihood optimization

$$\left(\mathbf{s}_{\text{est}}^{(g)}, \mathcal{P}_{\text{est}}^{(g)}\right) = \arg \min_{\mathbf{s}^{(g)}, \mathcal{P}^{(g)}} \left\| \mathbf{z}^{(g)} - \mathbf{x}^{(g)} \right\|^2, \tag{7.7}$$

where $\mathcal{P}_{\text{est}}^{(g)}$ is the estimated permutation index vector and $\mathbf{s}_{\text{est}}^{(g)}$ is the estimated symbol vector. The computational complexity of (7.7) is approximately $\mathcal{O}(n!\, M^n)$ complex multiplications per subblock, which quickly becomes infeasible for large n and M. The next three sections develop low-complexity alternatives.

7.2 LLR-Based Greedy Detector

The detection of AFDM-MM-IM signals involves two intertwined tasks, identifying the active mode permutation for the subcarriers within a subblock and detecting the corresponding modulated symbols. An LLR-based greedy detector [20] reduces the factorial mode search to a per-subcarrier metric evaluation while preserving reliable detection performance.

For each subcarrier $i \in \{1, \ldots, n\}$ and each candidate mode $\tau \in \{1, \ldots, n\}$ of the gth subblock, the receiver computes a log-likelihood ratio that quantifies the likelihood that the symbol on subcarrier i was transmitted using mode $\mathcal{M}_\tau$

$$\Lambda(i, \tau) = \log \left(\frac{\sum_{s \in \mathcal{M}_\tau} \exp\left(-|z_i^{(g)} - s|^2 \right)}{\sum_{\gamma \neq \tau} \sum_{s \in \mathcal{M}_\gamma} \exp\left(-|z_i^{(g)} - s|^2 \right)} \right), \tag{7.8}$$

where $\mathcal{M}_\tau$ denotes the constellation of the τth mode. Since each subcarrier must be assigned a unique mode from $\{\mathcal{M}_1, \ldots, \mathcal{M}_n\}$, a greedy algorithm is used to maximize the overall LLR-based confidence. For each subcarrier i, the unassigned mode $\tau^*(i)$ that yields the highest LLR value is selected

$$\tau^*(i) = \arg \max_{\tau \in \mathcal{U}_i} \Lambda(i, \tau), \tag{7.9}$$

where $\mathcal{U}_i \subseteq \{1,\dots,n\}$ is the set of modes not yet assigned to any subcarrier. This ensures that each mode is used exactly once within the subblock, adhering to the permutation constraint.

Once the mode assignment $\{\tau^*(i)\}$ is finalized for all subcarriers, the symbol detection step compares the equalized symbol $z_i^{(g)}$ against all elements in the assigned mode $\mathcal{M}_{\tau^*(i)}$, and selects the closest one

$$\hat{s}_i = \arg\min_{s\in\mathcal{M}_{\tau^*(i)}} \left| z_i^{(g)} - s \right|^2 . \tag{7.10}$$

Each detected symbol $\hat{s}_i$ corresponds to a unique index $\ell_i \in \{0,\dots,M-1\}$ within the assigned mode and is mapped to a binary vector $\hat{\mathbf{b}}_i \in \{0,1\}^{\log_2 M}$ using most-significant-bit ordering. The recovered bits from all subcarriers and subblocks are concatenated to form the estimated bit stream $\hat{\mathbf{b}}$. The complete procedure is summarized in Algorithm 7.1.

Algorithm 7.1 LLR-Based Greedy Detection for AFDM-MM-IM

Require: Received DAFT-domain subblock $\mathbf{z}^{(g)} \in \mathbb{C}^n$, mode sets $\{\mathcal{M}_1,\dots,\mathcal{M}_n\}$, constellation size M

Compute LLR matrix $\Lambda(i,\tau)$ for all subcarriers i and modes τ via (7.8)
Initialize unassigned mode set $\mathcal{U} = \{1,2,\dots,n\}$
for $i = 1$ to n **do**
    Select mode $\tau^*(i) = \arg\max_{\tau\in\mathcal{U}} \Lambda(i,\tau)$
    Assign $\tau^*(i)$ to subcarrier i and update $\mathcal{U} \leftarrow \mathcal{U} \setminus \{\tau^*(i)\}$
end for
for $i = 1$ to n **do**
    Detect symbol $\hat{s}_i = \arg\min_{s\in\mathcal{M}_{\tau^*(i)}} |z_i^{(g)} - s|^2$
    Map $\hat{s}_i$ to bit vector $\hat{\mathbf{b}}_i \in \{0,1\}^{\log_2 M}$
end for
Concatenate bits $\hat{\mathbf{b}} = [\hat{\mathbf{b}}_1^T, \hat{\mathbf{b}}_2^T, \dots, \hat{\mathbf{b}}_n^T]^T$
return estimated permutation $\{\tau^*(i)\}$ and bit stream $\hat{\mathbf{b}}$

The LLR-based greedy detector reduces the computational cost from the $\mathcal{O}(n!\,M^n)$ of joint ML detection to a per-subblock metric evaluation that is quadratic in n and linear in M. By decoupling mode selection from symbol demodulation, it achieves reliable performance at moderate system sizes with tractable complexity.

7.3 Viterbi-Based Trellis Detector

Given the factorial number of possible permutations, joint ML detection over the mode space is computationally prohibitive. A trellis-based algorithm inspired by the Viterbi decoder [81] enables efficient detection of the optimal permutation with near-optimal performance.

7.3.1 Trellis Construction

A trellis is constructed with $n+1$ stages corresponding to n sequential decisions, one per subcarrier of the subblock. The initial state at stage 0 is the null set $\varnothing$, representing the condition in which no mode has yet been assigned. At stage $\gamma \in \{1,\ldots,n\}$, the number of valid states is the binomial coefficient $\binom{n}{\gamma}$, corresponding to all possible γ-element subsets of the available n modes. Each state represents the set of modes assigned to the first γ subcarriers, irrespective of ordering. A transition exists between two states if the mode set at stage $\gamma-1$ is a proper subset of that at stage γ differing by exactly one element. Each node at stage γ has γ incoming paths and $n-\gamma$ outgoing paths.

For $n=4$, the trellis comprises five stages as shown in Fig. 7.2. Stage 0 is initialized with $\varnothing$. Stage 1 consists of all singleton subsets $\{1\},\{2\},\{3\},\{4\}$. Stage 2 includes all two-element subsets $\{1,2\},\{1,3\},\{1,4\},\{2,3\},\{2,4\},\{3,4\}$. Stage 3 includes $\{1,2,3\},\{1,2,4\},\{1,3,4\},\{2,3,4\}$, and stage 4 includes all permutations of the four modes. Each path from the initial to the terminal stage represents a unique permutation of modes assigned across the four subcarriers.

7.3.2 Cost Matrix and Dynamic Programming

Let $\mathbf{z}^{(g)} = [z_1^{(g)},\ldots,z_n^{(g)}]^T \in \mathbb{C}^n$ denote the DAFT-domain equalized received vector corresponding to the gth subblock. The cost of assigning mode m to subcarrier i is the minimum Euclidean distance between the received symbol and the closest

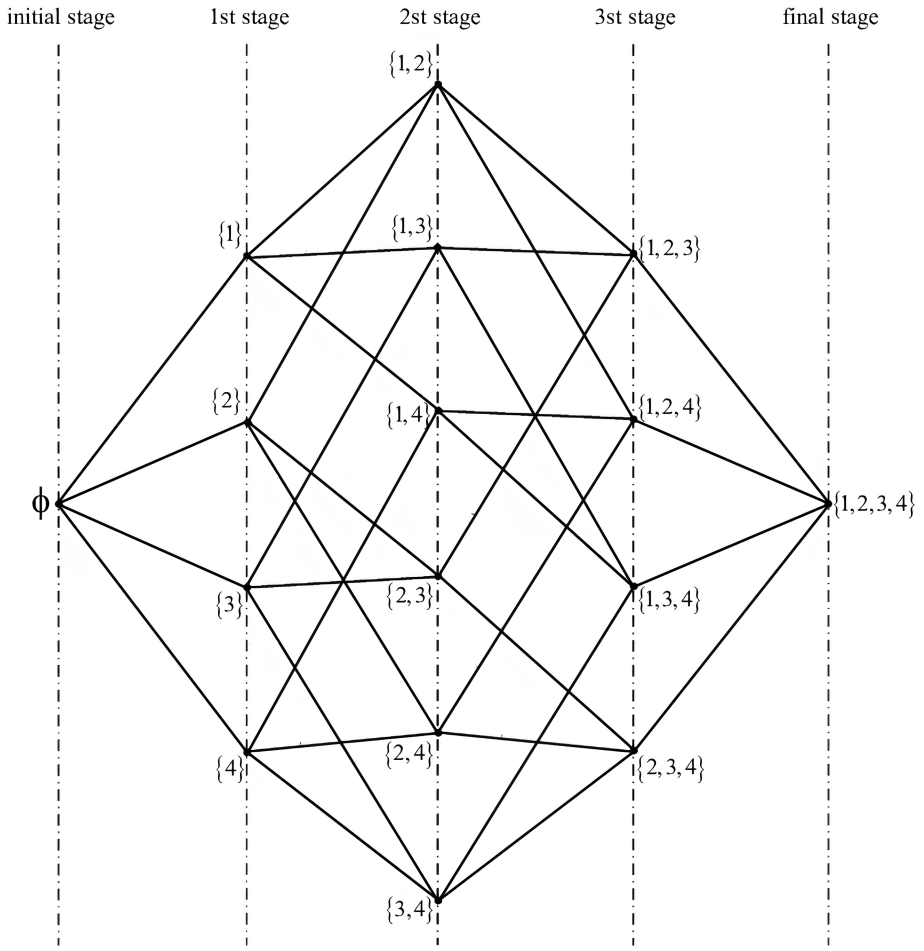


Figure 7.2: Trellis diagram for $n = 4$ used in mode-order detection for multi-mode index modulation

constellation point in $\mathcal{M}_m$

$$C(i,m) = \min_{s\in\mathcal{M}_m} \left| z_i^{(g)} - s \right|^2. \tag{7.11}$$

The detection task reduces to identifying the permutation $\mathcal{P}^{(g)} = [\tau^*(1),\ldots,\tau^*(n)]$ that minimizes the total assignment cost $\sum_{i=1}^{n} C(i,\tau^*(i))$, subject to $\tau^*(i) \neq \tau^*(j)$ for $i \neq j$.

We use a binary bitmask $s \in \{0,1\}^n$ to encode the set of modes assigned up to a given stage, compactly represented as an integer in $[0, 2^n - 1]$. Let $\mathrm{DP}(i,s)$ denote the minimum path cost to reach stage i under assignment state s. The recursion is initialized for all single-mode assignments as

$$\mathrm{DP}(1, 2^{m-1}) = C(1,m), \quad m \in \{1,\ldots,n\}. \tag{7.12}$$

At each subsequent stage $i = 2,\ldots,n$, we consider all valid previous states s with $i-1$ active bits and extend them by assigning one additional unallocated mode m. The updated state becomes $s' = s + 2^{m-1}$, and the recurrence is

$$\mathrm{DP}(i,s') = \min\left[\mathrm{DP}(i-1,s) + C(i,m)\right], \tag{7.13}$$

with a pointer matrix $\mathrm{Path}(i,s')$ recording the optimal transition at each step. After computing all entries, the minimum-cost full assignment corresponds to the state $s_{\text{full}} = 2^n - 1$, and the optimal path is recovered by backtracking through Path, yielding the permutation $\mathcal{P}^{(g)}$ that minimizes the total cost.

Following permutation detection, symbol demodulation is performed independently per subcarrier. For each index i, the received value $z_i^{(g)}$ is compared to all constellation points in the assigned mode $\mathcal{M}_{\tau^*(i)}$, and the closest symbol is selected

$$\hat{s}_i = \arg\min_{s\in\mathcal{M}_{\tau^*(i)}} \left| z_i^{(g)} - s \right|^2. \tag{7.14}$$

The detected symbol index is mapped to its binary representation $\hat{\mathbf{b}}_i$, and the bit streams across all subcarriers and subblocks are concatenated to reconstruct the estimated message vector. The complete trellis detector is summarized in Algorithm 7.2.

Algorithm 7.2 Viterbi-Based Trellis Detection for AFDM-MM-IM

Require: $\mathbf{z}^{(g)} = [z_1^{(g)}, \ldots, z_n^{(g)}]^T$, constellation modes $\{\mathcal{M}_1, \ldots, \mathcal{M}_n\}$, constellation size M

Construct cost matrix $C(i,m) = \min_{s \in \mathcal{M}_m} |z_i^{(g)} - s|^2$ for all i, m
Set $\mathrm{DP}(1, 2^{m-1}) = C(1,m)$ and $\mathrm{Path}(1, 2^{m-1}) = m$ for $m = 1, \ldots, n$
for $i = 2$ to n **do**
    for each previous state s with Hamming weight $i-1$ **do**
        for each unassigned mode $m \notin s$ **do**
            $s' \leftarrow s + 2^{m-1}$
            $\mathrm{DP}(i, s') \leftarrow \min[\mathrm{DP}(i-1, s) + C(i,m)]$
            $\mathrm{Path}(i, s') \leftarrow (s, m)$
        end for
    end for
end for
Recover optimal permutation $\mathcal{P}^{(g)}$ from Path by backtracking from $s_{\text{full}} = 2^n - 1$
for $i = 1$ to n **do**
    $\hat{s}_i = \arg\min_{s \in \mathcal{M}_{\tau^*(i)}} |z_i^{(g)} - s|^2$
    Map $\hat{s}_i$ to bit vector $\hat{\mathbf{b}}_i$
end for
Concatenate $\hat{\mathbf{b}} = [\hat{\mathbf{b}}_1^T, \ldots, \hat{\mathbf{b}}_n^T]^T$
return estimated permutation $\mathcal{P}^{(g)}$ and bit stream $\hat{\mathbf{b}}$

There are $\binom{n}{\gamma}$ nodes at stage γ, and each node requires the computation of γ path metrics, one per incoming transition. The total computational complexity of the trellis detector is $\mathcal{O}\left(\sum_{\gamma=1}^{n} \gamma \binom{n}{\gamma}\right) = \mathcal{O}(n\, 2^n)$, which is significantly lower than the brute-force ML complexity of $\mathcal{O}(n!\, M^n)$. This reduction makes the trellis-based Viterbi algorithm highly suitable for AFDM-MM-IM systems at moderate values of n, where a balance between detection performance and computational cost is essential.

7.4 Sphere Decoding Based Near-ML Detector

The sphere decoder [82] performs a depth-first, branch-and-bound tree search over the joint mode-symbol space, retaining near-ML accuracy while exploiting pruning to reduce the average complexity well below the exhaustive search. For the gth subblock, the joint detection problem is

$$\left(\hat{\mathcal{P}}, \hat{\mathbf{s}}\right) = \arg \min_{\mathcal{P} \in \mathfrak{P}_n} \min_{\mathbf{s} \in \mathcal{M}_{j_1} \times \cdots \times \mathcal{M}_{j_n}} \left\| \mathbf{z}^{(g)} - \mathbf{s} \right\|^2, \tag{7.15}$$

where $\mathfrak{P}_n$ denotes the set of all $n!$ permutations of $\{1, \ldots, n\}$. This combinatorial problem is formulated as a layered tree, where each level i corresponds to assigning a mode and a symbol to the ith subcarrier.

The sphere decoder performs a recursive depth-first search over this tree. At level i, it considers all mode indices not already used in previous levels and tries each constellation point in the current candidate mode. For a partial assignment with symbol vector $\mathbf{s}_{1:i}$, the cumulative metric is

$$\mathcal{T}_i = \sum_{j=1}^{i} \left| z_j^{(g)} - s_j \right|^2. \tag{7.16}$$

If $\mathcal{T}_i \geq \mathcal{T}_{\text{best}}$, where $\mathcal{T}_{\text{best}}$ is the minimum cost among previously found complete solutions, the path is pruned. Otherwise, the decoder proceeds to level $i+1$. Once a full path to level n is completed, the total cost is compared and retained if lower. The detector is summarized in Algorithm 7.3.

Branch-and-bound pruning lets the sphere decoder explore a significantly reduced search space compared to brute-force ML. Although its worst-case complexity is still $\mathcal{O}(n!\,M^n)$, the average complexity remains low at moderate to high SNR, where many paths are pruned early. This makes sphere decoding a practical trade-off between complexity and performance for AFDM-MM-IM.

Algorithm 7.3 Sphere Decoding Based Near-ML Detection for AFDM-MM-IM

Require: Received subblock $\mathbf{z}^{(g)} \in \mathbb{C}^n$, mode constellations $\{\mathcal{M}_1, \ldots, \mathcal{M}_n\}$

Initialize sphere radius $\mathcal{T}_{\text{best}} = \infty$ and best path $(\hat{\mathcal{P}}, \hat{\mathbf{s}}) = \varnothing$
for each starting mode $m \in \{1, \ldots, n\}$ **do**
    Call SphereDecode$(1, m, \varnothing, 0)$
end for
Procedure SphereDecode$(i, m, \mathbf{s}_{1:i-1}, \mathcal{T}_{i-1})$
for each $s_i \in \mathcal{M}_m$ **do**
    $\mathcal{T}_i \leftarrow \mathcal{T}_{i-1} + |z_i^{(g)} - s_i|^2$
    if $\mathcal{T}_i \geq \mathcal{T}_{\text{best}}$ **then**
        prune this path
    else if $i = n$ **then**
        $\mathcal{T}_{\text{best}} \leftarrow \mathcal{T}_i$
        Store $(\hat{\mathcal{P}}, \hat{\mathbf{s}}) = (\mathcal{P}, [s_1, \ldots, s_n])$
    else
        for each unused mode m' **do**
            Call SphereDecode$(i+1, m', \mathbf{s}_{1:i}, \mathcal{T}_i)$
        end for
    end if
end for
End Procedure
for $i = 1$ to n **do**
    $\hat{s}_i = \arg\min_{s \in \mathcal{M}_{\hat{\mathcal{P}}(i)}} |z_i^{(g)} - s|^2$
    Map $\hat{s}_i$ to bit vector $\hat{\mathbf{b}}_i$
end for
return estimated permutation $\hat{\mathcal{P}}$ and bit stream $\hat{\mathbf{b}} = [\hat{\mathbf{b}}_1^T, \ldots, \hat{\mathbf{b}}_n^T]^T$

7.5 Pairwise Error Probability Analysis

To analytically evaluate the error performance of AFDM-MM-IM under ML detection, we derive the BER through pairwise error probability (PEP) analysis [17, 39]. Unlike conventional subblock-wise analysis, we consider the entire transmitted vector $\mathbf{x} \in \mathbb{C}^{N\times 1}$ to capture the global error characteristics of the multi-mode index modulation scheme. The conditional pairwise error probability quantifies the likelihood that the ML detector decides in favor of an incorrect vector $\hat{\mathbf{x}}$ when the true transmitted vector is $\mathbf{x}$, given perfect knowledge of the effective channel matrix $\mathbf{H}_{\text{eff}}$.

7.5.1 Conditional Pairwise Error Probability

From the DAFT-domain received signal (7.5), the ML decision metric is

$$\hat{\mathbf{x}}_{\text{ML}} = \arg\min_{\mathbf{x}\in\mathcal{X}} \|\mathbf{y} - \mathbf{H}_{\text{eff}}\mathbf{x}\|^2, \tag{7.17}$$

where $\mathcal{X}$ denotes the set of all valid AFDM-MM-IM codewords. The conditional pairwise error probability, conditioned on the channel realization $\mathbf{H}_{\text{eff}}$, is

$$\Pr(\mathbf{x} \to \hat{\mathbf{x}} \mid \mathbf{H}_{\text{eff}}) = Q\left(\sqrt{\frac{E_s\,\delta^2}{2N_0}}\right), \tag{7.18}$$

where $Q(\cdot)$ is the Gaussian Q-function, E_s is the average symbol energy, and the effective squared Euclidean distance is

$$\delta^2 = \|\mathbf{H}_{\text{eff}}(\mathbf{x}-\hat{\mathbf{x}})\|^2 = (\mathbf{x}-\hat{\mathbf{x}})^H\,\mathbf{H}_{\text{eff}}^H\mathbf{H}_{\text{eff}}\,(\mathbf{x}-\hat{\mathbf{x}}). \tag{7.19}$$

Defining the error vector $\mathbf{e} = \mathbf{x} - \hat{\mathbf{x}}$ and the error correlation matrix $\mathbf{\Phi} = \mathbf{e}\mathbf{e}^H$, the effective distance can be expressed as

$$\delta^2 = \text{tr}(\mathbf{H}_{\text{eff}}^H\mathbf{H}_{\text{eff}}\mathbf{\Phi}) = \text{tr}(\mathbf{\Phi}\,\mathbf{H}_{\text{eff}}^H\mathbf{H}_{\text{eff}}), \tag{7.20}$$

where $\mathrm{tr}(\cdot)$ denotes the matrix trace.

To enable analytical tractability, we use the widely adopted exponential approximation of the Q-function

$$Q(x) \approx \frac{1}{12}\exp\left(-\frac{x^2}{2}\right) + \frac{1}{4}\exp\left(-\frac{2x^2}{3}\right). \tag{7.21}$$

Substituting (7.21) into (7.18),

$$\Pr\left(\mathbf{x} \to \hat{\mathbf{x}} \mid \mathbf{H}_{\text{eff}}\right) \approx \frac{1}{12}\exp\left(-\frac{E_s\,\delta^2}{4N_0}\right) + \frac{1}{4}\exp\left(-\frac{E_s\,\delta^2}{3N_0}\right). \tag{7.22}$$

7.5.2 Unconditional Pairwise Error Probability

The unconditional pairwise error probability is obtained by averaging the conditional pairwise error probability over the distribution of $\mathbf{H}_{\text{eff}}$

$$\begin{aligned}\Pr(\mathbf{x} \to \hat{\mathbf{x}}) &= \mathbb{E}_{\mathbf{H}_{\text{eff}}}\left\{\Pr\left(\mathbf{x} \to \hat{\mathbf{x}} \mid \mathbf{H}_{\text{eff}}\right)\right\} \\ &\approx \frac{1}{12}\mathbb{E}_{\mathbf{H}_{\text{eff}}}\left\{\exp\left(-\frac{E_s\,\delta^2}{4N_0}\right)\right\} + \frac{1}{4}\mathbb{E}_{\mathbf{H}_{\text{eff}}}\left\{\exp\left(-\frac{E_s\,\delta^2}{3N_0}\right)\right\}.\end{aligned} \tag{7.23}$$

For a Rayleigh fading channel where the effective channel coefficients follow a circularly symmetric complex Gaussian distribution, the channel correlation matrix is

$$\mathbf{C} = \mathbb{E}\left\{\mathrm{vec}(\mathbf{H}_{\text{eff}})\,\mathrm{vec}(\mathbf{H}_{\text{eff}})^H\right\}, \tag{7.24}$$

where $\mathrm{vec}(\cdot)$ is the vectorization operator. The eigenvalue decomposition $\mathbf{C} = \mathbf{Q}\mathbf{D}\mathbf{Q}^H$ provides the eigenvectors $\mathbf{Q}$ and the diagonal matrix $\mathbf{D} = \mathrm{diag}(\lambda_1, \lambda_2, \ldots, \lambda_r)$ of nonzero eigenvalues, with $r = \mathrm{rank}(\mathbf{C})$ the diversity order. Writing the effective channel matrix as $\mathbf{H}_{\text{eff}} = \mathbf{Q}\mathbf{D}^{1/2}\mathbf{U}$ with $\mathbf{U}$ an $r \times N$ matrix of i.i.d. $\mathcal{CN}(0,1)$ entries, the effective distance reduces to

$$\delta^2 = \mathbf{u}^H \mathbf{D}\,\mathbf{\Psi}\mathbf{u}, \tag{7.25}$$

where $\mathbf{u} = \mathbf{U}\mathbf{e}$ and $\mathbf{\Psi} = \mathbf{Q}^H \mathbf{\Phi} \mathbf{Q}$. Using the moment generating function approach, the expectation in (7.23) evaluates to

$$\mathbb{E}_{\mathbf{H}_{\text{eff}}} \left\{ \exp\left(-\alpha E_s \, \delta^2 \right) \right\} = \frac{1}{\det\left(\mathbf{I}_N + \alpha E_s \, \mathbf{\Phi} \mathbf{C} \right)}, \tag{7.26}$$

where $\alpha \in \{1/(4N_0), 1/(3N_0)\}$ for the two terms in (7.23). Therefore, the unconditional pairwise error probability for AFDM-MM-IM is

$$\Pr(\mathbf{x} \to \hat{\mathbf{x}}) \approx \frac{1}{12 \det\left(\mathbf{I}_N + \frac{E_s}{4N_0} \mathbf{\Phi} \mathbf{C} \right)} + \frac{1}{4 \det\left(\mathbf{I}_N + \frac{E_s}{3N_0} \mathbf{\Phi} \mathbf{C} \right)}. \tag{7.27}$$

7.5.3 Average Bit Error Probability

The average bit error probability is computed by averaging the unconditional pairwise error probability over all error events, weighted by the corresponding number of bit errors. Let $\mathcal{X}$ denote the set of all $W = 2^b$ valid AFDM-MM-IM codewords, where $b = Gg$ is the total number of bits transmitted per AFDM frame. The average bit error probability is

$$P_b \approx \frac{1}{bW} \sum_{\mathbf{x} \in \mathcal{X}} \sum_{\substack{\hat{\mathbf{x}} \in \mathcal{X} \\ \hat{\mathbf{x}} \neq \mathbf{x}}} \Pr(\mathbf{x} \to \hat{\mathbf{x}}) \, d_H(\mathbf{x}, \hat{\mathbf{x}}), \tag{7.28}$$

where $d_H(\mathbf{x}, \hat{\mathbf{x}})$ is the Hamming distance between the bit sequences corresponding to $\mathbf{x}$ and $\hat{\mathbf{x}}$. Equation (7.28) provides a tight analytical approximation to the BER of AFDM-MM-IM under ML detection over doubly dispersive channels, with the approximation becoming increasingly precise at high SNR where the exponential Q-function approximation in (7.21) is tight.

7.6 Spectral Efficiency

Spectral efficiency (SE) measures the number of information bits transmitted per DAFT-domain resource element per unit bandwidth. In classical AFDM, every one

of the n DAFT-domain subcarriers of a subblock carries a single symbol drawn from an M_{AFDM}-ary constellation, so

$$\mathrm{SE}_{\mathrm{AFDM}} = \log_2 M_{\mathrm{AFDM}}. \tag{7.29}$$

AFDM-IM activates only K out of n subcarriers and uses the choice of which K are active to convey $\lfloor \log_2 \binom{n}{K} \rfloor$ index bits, with each active subcarrier transmitting a symbol from an M_{mod}-ary constellation

$$\mathrm{SE}_{\mathrm{IM}} = \frac{\lfloor \log_2 \binom{n}{K} \rfloor + K \log_2 M_{\mathrm{mod}}}{n}. \tag{7.30}$$

AFDM-DM-IM uses all n subcarriers, assigning each to one of two distinguishable constellations of sizes M_A and M_B and carrying $\lfloor \log_2 \binom{n}{K} \rfloor$ index bits through the assignment pattern

$$\mathrm{SE}_{\mathrm{DM}} = \frac{\lfloor \log_2 \binom{n}{K} \rfloor + K \log_2 M_A + (n-K) \log_2 M_B}{n}. \tag{7.31}$$

The proposed AFDM-MM-IM maximizes the index-modulation flexibility by using a full permutation of n distinct M-ary constellations across the n subcarriers, carrying $\lfloor \log_2(n!) \rfloor$ index bits and $n \log_2 M$ modulation bits

$$\mathrm{SE}_{\mathrm{MM}} = \frac{\lfloor \log_2(n!) \rfloor + n \log_2 M}{n}. \tag{7.32}$$

By fully using every subcarrier and exploiting factorial-order indexing, AFDM-MM-IM matches or exceeds the spectral efficiency of AFDM-DM-IM, AFDM-IM, and classical AFDM, while delivering superior diversity and BER performance at the same spectral efficiency.

As an example, for $n = 4$, $K = 2$, $M_{\mathrm{AFDM}} = 4$, $M_{\mathrm{mod}} = 8$, $M_A = 4$, $M_B = 2$, and $M = 2$, all four schemes attain an average spectral efficiency of 2 bits/s/Hz. Classical AFDM reaches it via its 4-ary constellation, since $\log_2 4 = 2$. AFDM-IM

conveys $\lfloor \log_2 \binom{4}{2} \rfloor = 2$ index bits and two 8-ary symbols per subblock, yielding $(2+2\cdot 3)/4 = 2$. AFDM-DM-IM carries two index bits and two symbols each from $\mathcal{M}_A$ and $\mathcal{M}_B$, giving $(2+4+2)/4 = 2$. AFDM-MM-IM uses factorial indexing with $\lfloor \log_2 24 \rfloor = 4$ bits together with four BPSK symbols, giving $(4+4)/4 = 2$. Although the nominal spectral efficiencies coincide, only AFDM-MM-IM achieves it through full factorial indexing and full resource utilization, which underpins its superior diversity and BER performance without any increase in bandwidth.

7.7 Computational Complexity Summary

Table 7.2 summarizes the dominant complexity of the proposed detectors for AFDM-MM-IM with N subcarriers, subblock length n, and constellation size M for each mode.

Table 7.2: Computational complexity of AFDM-MM-IM detectors

Stage	Complexity
MMSE equalization	$\mathcal{O}(N^3)$
LLR-based greedy detection	$\mathcal{O}(n^2 M)$
Viterbi-based trellis detection	$\mathcal{O}(n\,2^n + nM)$
Sphere decoding (worst case)	$\mathcal{O}(n!\,M^n)$
Sphere decoding (average)	$\mathcal{O}(n^\alpha)$, $1 < \alpha < n$

The MMSE equalization stage is dominated by the inversion of the $N \times N$ matrix $\mathbf{H}_{\text{eff}}^H \mathbf{H}_{\text{eff}} + \sigma^2 \mathbf{I}_N$, with the matrix-vector products that follow incurring $\mathcal{O}(N^2)$ each. The LLR-based greedy detector evaluates $|z_i^{(g)} - s|^2$ for all s in each of the n modes for each of the n subcarriers, yielding $\mathcal{O}(n^2 M)$ per subblock. The Viterbi-based trellis detector precomputes the cost matrix at $\mathcal{O}(nM)$ and updates path metrics over the trellis at $\mathcal{O}(n\,2^n)$, plus symbol demodulation at $\mathcal{O}(nM)$. The sphere decoder has worst-case complexity $\mathcal{O}(n!\,M^n)$ when no pruning occurs, but the average complexity scales as $\mathcal{O}(\kappa n^\alpha)$ with $1 < \alpha < n$, with the constant κ dependent on SNR and channel statistics. Enumeration strategies such

as Schnorr-Euchner and radius adaptation heuristics further reduce the average sphere decoding complexity.

7.8 Simulation Results

The simulation results assess the performance of the proposed AFDM-MM-IM system. The carrier frequency is $f_c = 4$ GHz and the chirp subcarrier spacing is $\Delta f = 4$ MHz. The channel includes scenarios with different multipath conditions, with $P = 4$ representing a four-tap channel at a maximum user velocity of 1200 km/h. The chirp parameter is $c_1 = (2(\alpha_{\max} + \xi_\nu) + 1)/(2N)$.

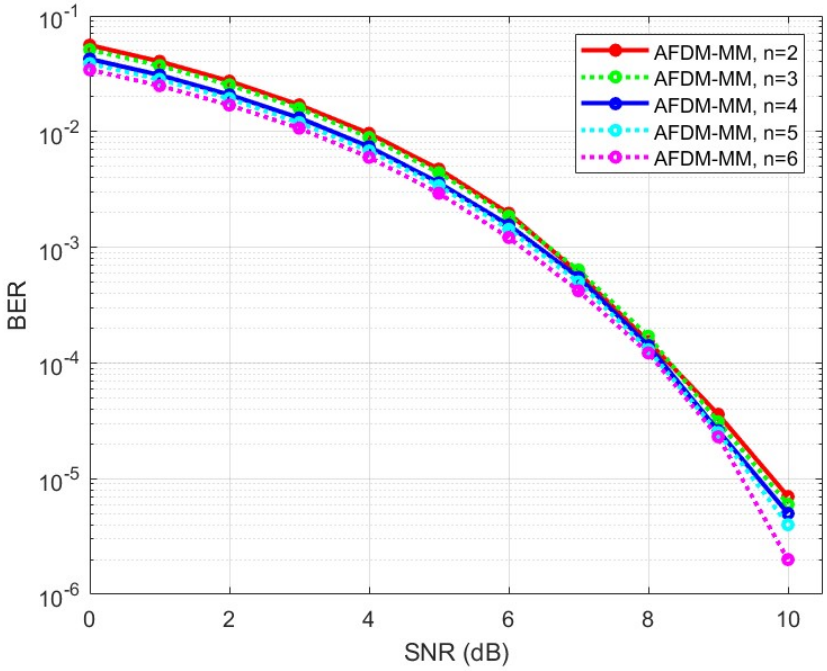


Figure 7.3: BER performance of AFDM-MM-IM using n-mode constellations under the AWGN channel with BPSK

Fig. 7.3 illustrates the BER of AFDM-MM-IM with BPSK constellations under an AWGN channel for $N = 120$. In MM-IM, each subcarrier within a subblock is modulated using a symbol from one of the n distinct constellations, so varying n from 2 to 6 effectively changes the number of modes within each subblock and enhances the diversity of the symbol mapping. The BER decreases consistently

with n. At 10 dB SNR, the BER reduces from approximately 10^{-5} for $n = 2$ to about $10^{-5.8}$ for $n = 6$, indicating an SNR gain of approximately 0.8 to 1 dB. The improvement arises because additional mode permutations enhance the ability of the system to separate transmitted symbols even under BPSK modulation, leading to better error resilience.

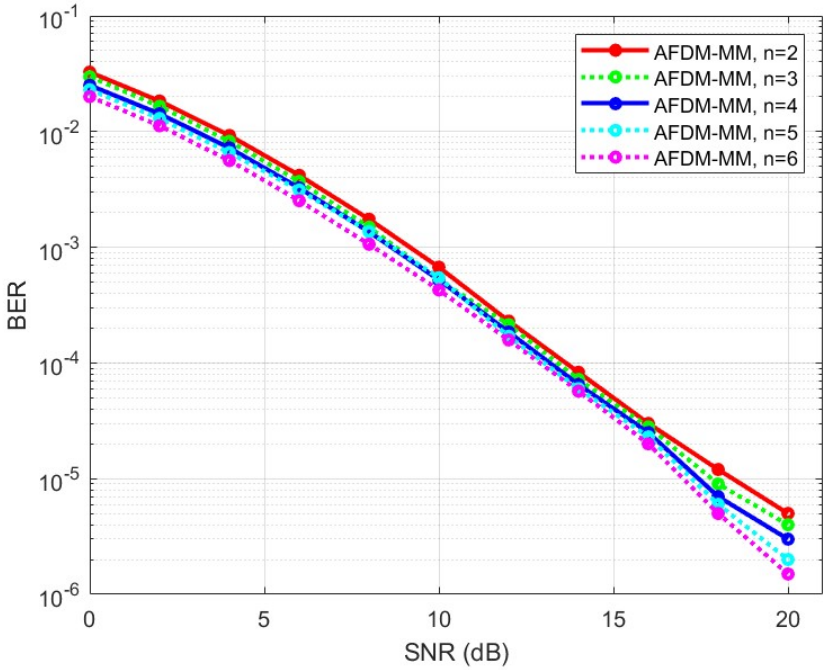


Figure 7.4: BER performance of AFDM-MM-IM using n-mode constellations under the doubly dispersive channel with BPSK

Fig. 7.4 and Fig. 7.5 report the BER performance of AFDM-MM-IM with BPSK and QPSK modulation under a high-Doppler doubly dispersive channel with $N = 120$, $\lambda_{\max} = 4$, and $\nu_{\max} = 2$. The detector uses MMSE equalization followed by LLR-based greedy detection. For BPSK, the BER decreases consistently with n, demonstrating the effectiveness of multi-mode index modulation in exploiting diversity. At 20 dB SNR, the BER drops from approximately 2×10^{-5} for $n = 2$ to below 5×10^{-6} for $n = 6$, an SNR gain of about 1.5 to 2 dB at a target BER of 10^{-4}. The MMSE equalizer mitigates channel-induced distortion and the LLR-based detector provides soft metrics over all mode-symbol combinations, ensuring robust performance under Doppler. For QPSK the trend is similar but the mode-diversity

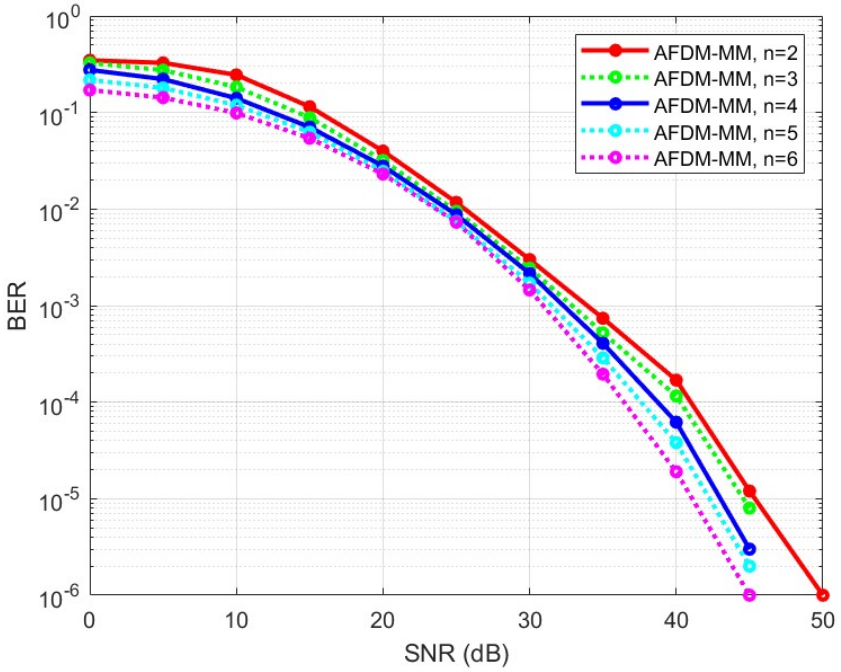


Figure 7.5: BER performance of AFDM-MM-IM using n-mode constellations under the doubly dispersive channel with QPSK

gains become more pronounced at higher SNR. At 40 dB, the BER improves from approximately 1.5×10^{-4} for $n = 2$ to about 3×10^{-5} for $n = 6$, with an SNR gain of 3 to 4 dB at a target BER of 10^{-4}.

Fig. 7.6 and Fig. 7.7 report the BER performance of the three detectors at $n = 4$ for BPSK and QPSK respectively. All schemes apply MMSE equalization first. For BPSK, the Viterbi-based detector consistently outperforms the others across the SNR range, achieving approximately 1.2 dB gain over the LLR-based detector and around 0.6 dB over the sphere decoder at a BER of 10^{-4}. The trellis-based optimization captures the best permutation path at manageable complexity, while the sphere decoder is slightly behind due to early pruning at lower SNR and the LLR-based approach incurs a penalty from its greedy mode assignment. For QPSK, the gains are more pronounced due to the denser constellation. At a BER of 10^{-5}, the Viterbi detector provides approximately 4 dB gain over the LLR-based detector and about 2 dB over the sphere decoder, with the sphere decoder approaching the Viterbi performance near 35 dB. The Viterbi and sphere decoding detectors are

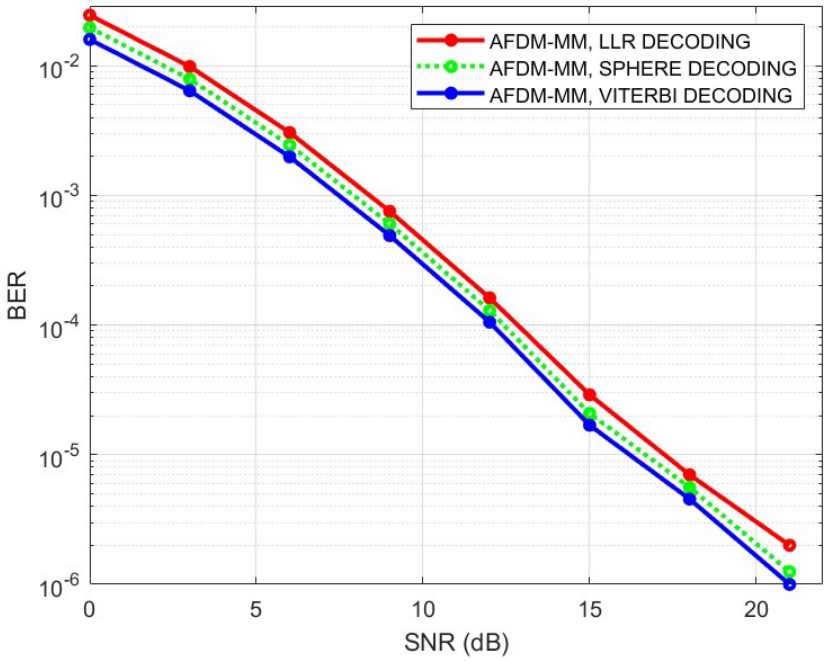


Figure 7.6: BER performance of AFDM-MM-IM with $n = 4$ under different detection schemes with BPSK modulation

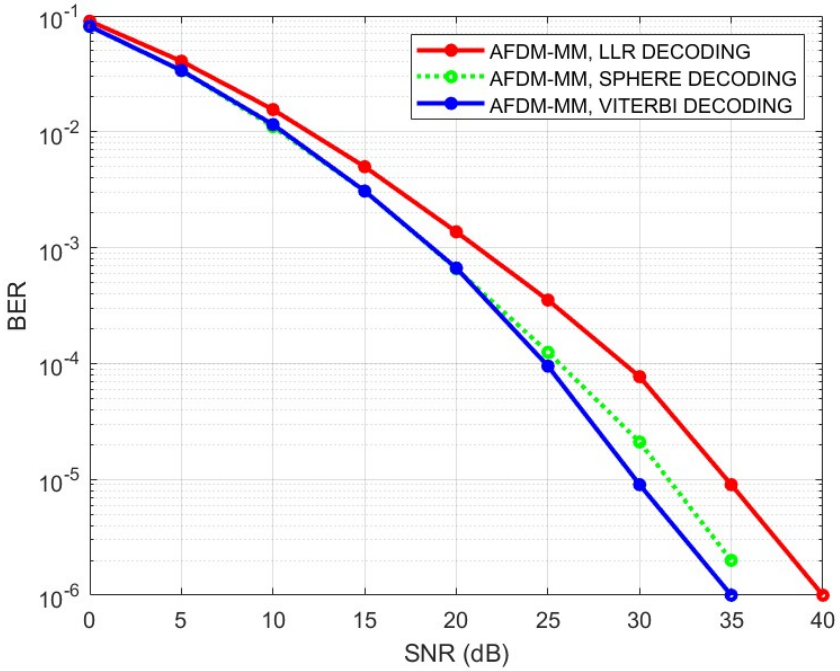


Figure 7.7: BER performance of AFDM-MM-IM with $n = 4$ under different detection schemes with QPSK modulation

therefore the preferred choices for AFDM-MM-IM in highly dispersive channels, especially at higher modulation orders.

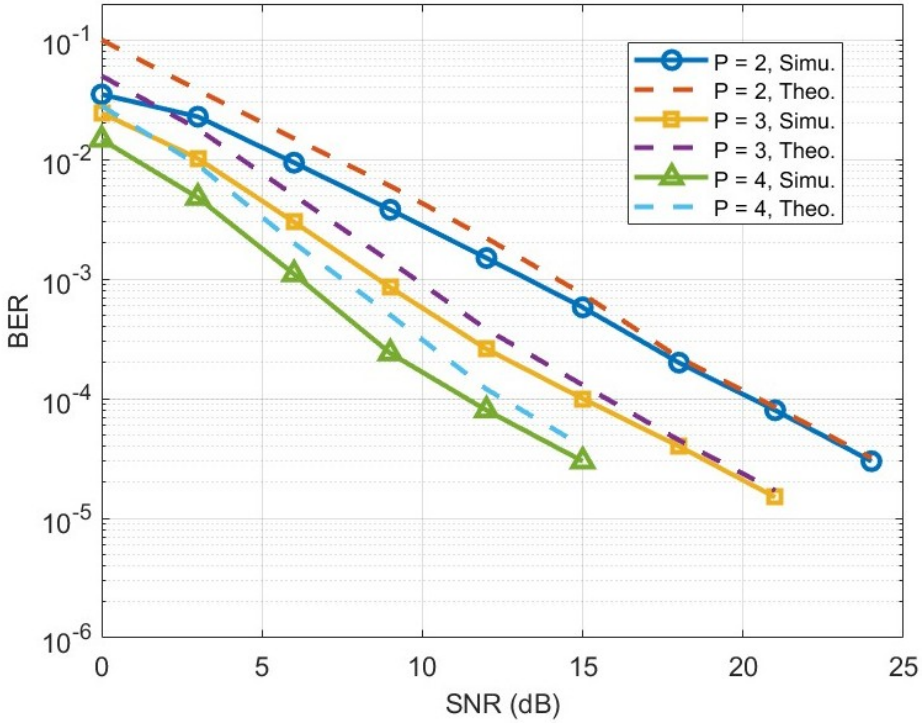


Figure 7.8: Comparison of the theoretical BER upper bound and the simulated BER of AFDM-MM-IM with $n = 3$, BPSK, and ML detection for different P

Fig. 7.8 demonstrates the agreement between the theoretical BER derived in Section 7.5 and the simulated BER of AFDM-MM-IM under ML detection. The system parameters are $N = 6$, $\lambda_{\max} = 1$, $\nu_{\max} = 1$, with $n = 3$ modes using distinct BPSK constellations evaluated for $P = 2, 3$, and 4 multipath components. The theoretical curves computed using the moment generating function framework of (7.27) and (7.28) exhibit excellent agreement with the Monte Carlo simulations across all SNR values. As P increases from 2 to 4, both the simulated and theoretical curves show improved BER due to enhanced multipath diversity. At a BER of 10^{-4}, the $P = 4$ configuration achieves approximately 3 dB gain over $P = 2$, validating the diversity benefits captured by the theoretical model.

Fig. 7.9 compares AFDM-MM-IM, AFDM-DM-IM [21], and classical AFDM at the same compact system size $N = 6$. The configurations are AFDM-MM-IM

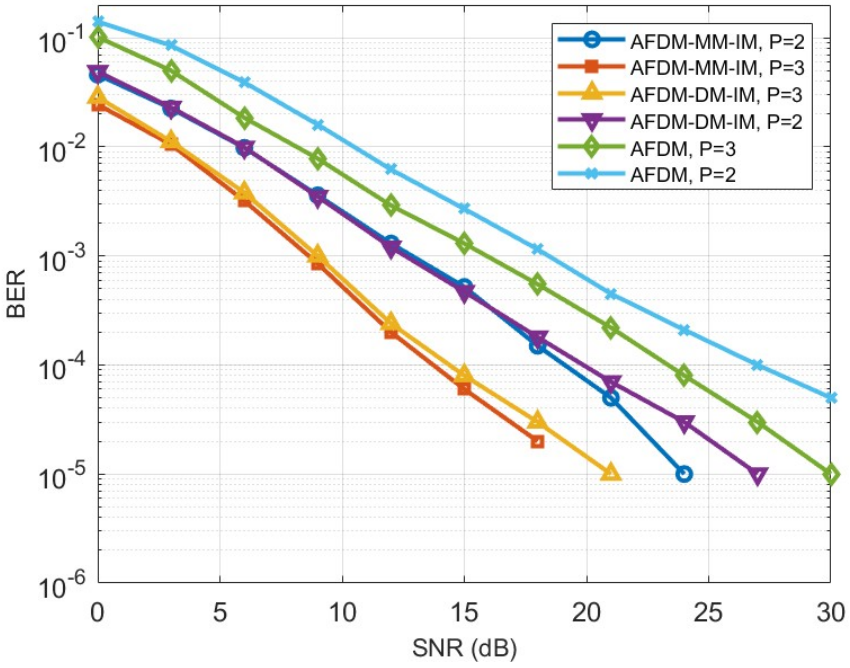


Figure 7.9: Comparison of AFDM-MM-IM, AFDM-DM-IM, and classical AFDM at comparable spectral efficiencies

with $n = 3$ and distinct BPSK modes giving 1.67 bits/s/Hz, AFDM-DM-IM with $n = 2$ and dual distinct BPSK constellations giving 1.5 bits/s/Hz, and classical AFDM with QPSK giving 2 bits/s/Hz. AFDM-MM-IM demonstrates superior error performance across all multipath scenarios. For $P = 2$, AFDM-MM-IM reaches a BER of 10^{-4} at approximately 14 dB, with gains of about 3 dB over AFDM-DM-IM and 5.5 dB over classical AFDM. The advantage grows with multipath diversity, with AFDM-MM-IM reaching a BER of 10^{-5} at approximately 20 dB for $P = 3$ while the baselines require significantly higher SNR. The factorial-order indexing of AFDM-MM-IM with $\lfloor \log_2(3!) \rfloor = 2$ index bits and full subcarrier utilization gives an enhanced minimum Euclidean distance and better exploitation of both multipath and mode diversity, compared to the dual-mode indexing of AFDM-DM-IM and the absence of indexing in classical AFDM.

Fig. 7.10 compares the BER of AFDM-MM with OTFS-MM [26] for subblock lengths $n = 2, 3$, and 6 using distinguishable BPSK modulation across all modes, with $N = 120$, $\lambda_{\max} = 4$, and $\nu_{\max} = 2$. The BER improves as the subblock length

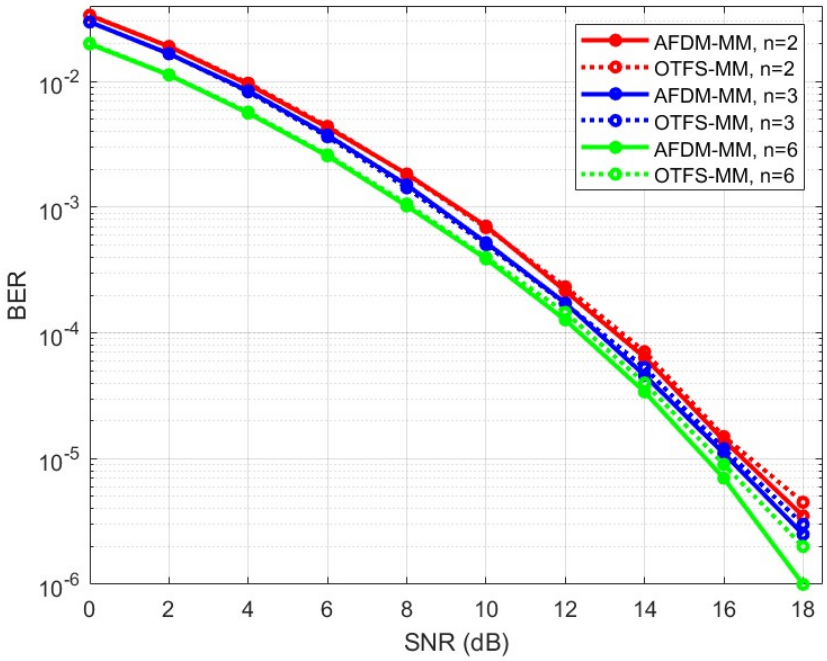


Figure 7.10: BER performance comparison of AFDM-MM and OTFS-MM for different subblock lengths under the high-Doppler channel

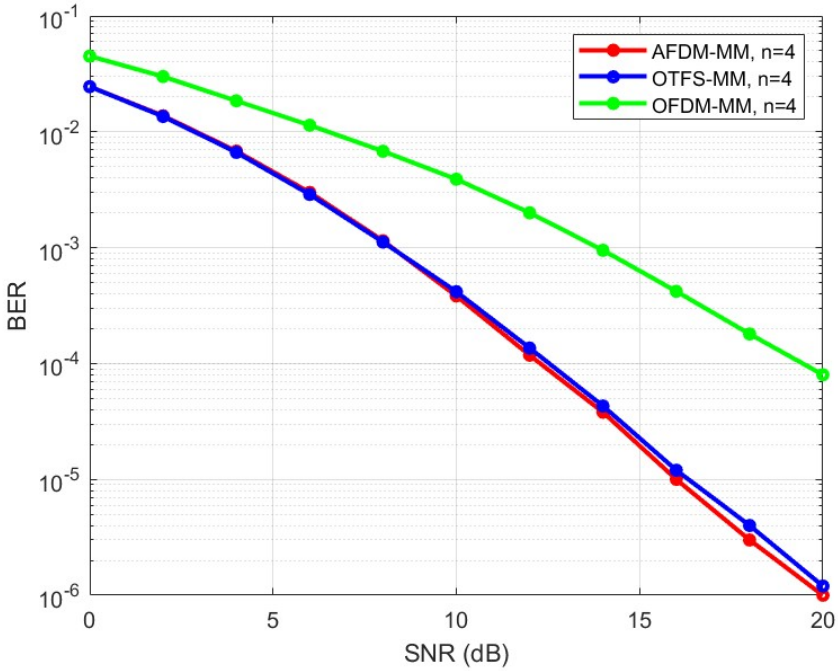


Figure 7.11: BER performance comparison of AFDM-MM, OTFS-MM, and OFDM-MM for $n = 4$ under the high-Doppler channel

increases due to enhanced index diversity and better utilization of the permutation space. Across all values of n, AFDM-MM consistently outperforms OTFS-MM, owing to the superior delay-Doppler localization and Doppler robustness of the DAFT-domain representation of AFDM compared to the symplectic delay-Doppler grid of OTFS. The advantage becomes more evident as n increases, with AFDM-MM reaching a BER of 10^{-5} at approximately 16 dB for $n = 6$ while OTFS-MM lags slightly behind.

Fig. 7.11 compares AFDM-MM, OTFS-MM, and OFDM-MM [22] at a fixed subblock length $n = 4$. AFDM-MM and OTFS-MM both significantly outperform OFDM-MM across the entire SNR range. OFDM suffers in doubly dispersive channels due to its lack of delay-Doppler diversity, whereas both AFDM-MM and OTFS-MM exploit the delay-Doppler structure of the channel. AFDM-MM slightly outperforms OTFS-MM in the medium-to-high SNR regime due to its affine basis functions that offer better orthogonality and reduced inter-symbol interference under high Doppler. At a BER of 10^{-4}, AFDM-MM and OTFS-MM reach the target at approximately 11 dB while OFDM-MM requires more than 17 dB, reflecting a 6 dB gain.

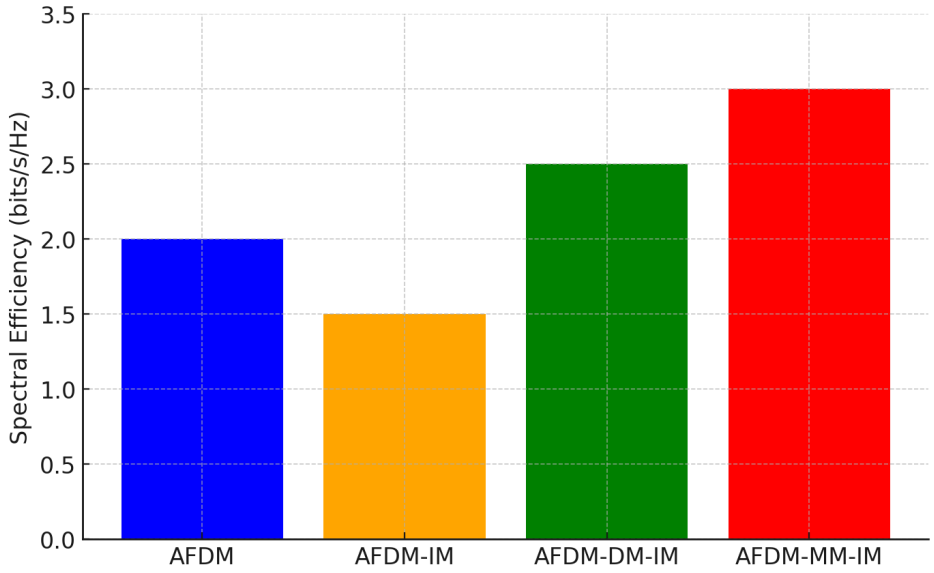


Figure 7.12: Spectral efficiency comparison for AFDM-based schemes with $n = 4$, $K = 2$, and constellation size 4

Fig. 7.12 illustrates the spectral efficiency comparison among the AFDM-based schemes. For $n = 4$, $K = 2$, and a common constellation size of 4, classical AFDM achieves $\log_2 4 = 2$ bits/s/Hz. AFDM-IM with $K = 2$ active subcarriers conveys $\lfloor \log_2 \binom{4}{2} \rfloor = 2$ index bits and $2 \log_2 4 = 4$ modulation bits, giving $(2+4)/4 = 1.5$ bits/s/Hz, suffering from the inactive carriers. AFDM-DM-IM uses all four subcarriers with two constellations of equal size, carrying 2 index bits and $4+4 = 8$ modulation bits, giving $(2+8)/4 = 2.5$ bits/s/Hz. AFDM-MM-IM uses factorial indexing with $\lfloor \log_2 24 \rfloor = 4$ bits together with four $M = 4$ symbols (another 8 bits), giving $(4+8)/4 = 3$ bits/s/Hz. AFDM-MM-IM thus achieves the highest spectral efficiency without any increase in bandwidth, by fully using every subcarrier and exploiting factorial-order indexing.

7.9 Summary

This chapter developed AFDM-MM-IM, a multi-mode index modulation scheme that activates every subcarrier of a subblock and modulates it with a symbol drawn from one of n distinct constellations, with the full permutation of modes across the subblock carrying $\lfloor \log_2(n!) \rfloor$ index bits. Both a look-up table method and a factorial-base permutation method were presented for the index-to-permutation mapping, with the factorial method preferred at large n due to its memory efficiency. Three detectors of increasing accuracy and decreasing efficiency were developed. The LLR-based greedy detector decoupled mode assignment from symbol detection through subcarrier-wise log-likelihood metrics, with a per-subblock cost quadratic in n and linear in M. The Viterbi-based trellis detector formulated the mode assignment as a shortest-path problem over a binomial-state trellis using a dynamic programming recursion, with a per-subblock cost of $\mathcal{O}(n\,2^n)$ that is significantly lower than the factorial cost of joint ML detection. The sphere decoding based near-ML detector performed a depth-first branch-and-bound tree search over the joint mode-symbol space, achieving near-ML accuracy at a sub-exponential

average complexity. A pairwise error probability analysis of the average bit error probability was derived using the moment generating function of the codeword difference correlation matrix and the exponential Q-function approximation, and the theoretical bound was shown to match the simulated BER closely. Simulations over the doubly dispersive channel with Jake's Doppler model confirmed that AFDM-MM-IM significantly outperforms both classical AFDM and AFDM-DM-IM in BER at comparable spectral efficiencies, and outperforms OFDM-MM and OTFS-MM in high-Doppler regimes. The factorial permutation construct and the trellis and sphere decoding detection frameworks introduced in this chapter close out the family of index-modulated AFDM schemes developed in Chapters 5, 6, and 7.

Chapter 8

Conclusion and Future Work

This chapter summarizes the work carried out in this thesis and outlines directions for further research.

8.1 Conclusions

This thesis has addressed the design of waveforms and receivers for high-mobility wireless communication, with particular emphasis on index modulation schemes built on the AFDM waveform and the Bayesian and message-passing detectors that recover information from them. The motivation throughout has been the observation that AFDM, despite its strong fundamentals as a delay-Doppler waveform, has received considerably less attention than OTFS in the context of index modulation, and that several well-established techniques from the OFDM-IM and OTFS-IM literatures have not been carried over to AFDM in any systematic way. The work was organized in three phases, each building on the previous one.

The first phase developed two index modulation schemes built on OTFS as foundational work for the AFDM chapters that follow. ESM-OTFS was proposed in a MIMO setting, combining the delay-Doppler diversity of OTFS with the spectral and energy efficiency of spatial modulation, supported by an MMSE based baseline detector and a VBI detector that exploits the sparsity of the delay-Doppler transmit

vector through a hierarchical Gaussian-Gamma prior. OTFS-GDM-IM was also proposed with ML and LLR detectors. The MIMO-OTFS extension and the VBI detection framework introduced in this phase recur in modified form in the AFDM contributions of the later chapters.

The second phase established the canonical AFDM system model used throughout the remainder of the thesis and developed three detectors that target different operating regimes of AFDM. A low-complexity VAMP-CG detector was developed that replaces the SVD step of standard VAMP, reducing the per-iteration complexity from cubic to quadratic in the number of subcarriers without measurable loss in BER. An MP-PIC detector was developed that exploits the complete delay-Doppler separation of propagation paths in the DAFT-domain channel matrix, constructing independent Bayesian estimates from each resolvable path and combining them through reliability-weighted decision statistics combining. A VB detector for AFDM with low-resolution ADCs was also developed, incorporating the truncated Gaussian likelihood induced by quantization directly and maintaining effective operation at 3-bit and 4-bit resolutions where Bussgang-based linear receivers exhibit a pronounced BER floor.

The third phase developed four AFDM-based index modulation schemes together with the detectors required to support them. AFDM-GIM relaxed the fixed-activation constraint of AFDM-IM by permitting the active-subcarrier count per subblock to vary across a permitted set, while AFDM-QIM extended subcarrier indexing to the in-phase and quadrature components independently. A VB-SBL detector was developed for the AFDM-IM family, exploiting the structured sparsity of the transmit vector through a hierarchical Gaussian-Gamma prior. AFDM-DM-IM was proposed that activates every subcarrier with one of two disjoint constellations, supported by MMSE-ML and MMSE-LLR baselines together with the VAMP-DMDIM and GAMP-DMDIM message-passing detectors that jointly infer symbols and mode assignments through an inline belief propagation module.

AFDM-MM-IM used full permutations of distinct constellations across subblock subcarriers and was supported by an LLR-greedy detector, a Viterbi-style trellis detector, and a sphere decoder. Closed-form BER bounds based on the pairwise error probability framework were derived and shown to match the simulated BER closely at moderate to high SNR. Together, these contributions establish AFDM as a strong candidate waveform for 6G high-mobility communication.

8.2 Future Directions

While the schemes and detectors developed in this thesis demonstrate strong performance under idealized channel and parameter settings, several practical and methodological challenges remain.

A primary direction is the integration of channel estimation with detection. The detectors proposed in this thesis assume perfect CSI at the receiver, and developing joint channel-estimation-and-detection frameworks under fractional Doppler will be an important next step. The variational Bayesian and message-passing machinery used in the present work extends naturally to this setting, allowing the channel, the noise statistics, and the symbols to be estimated within the same inference loop.

Another direction is the extension of the AFDM index modulation schemes to MIMO settings. The MIMO-OTFS work in Chapter 3 was developed for ESM-OTFS, but AFDM-GIM, AFDM-QIM, AFDM-DM-IM, and AFDM-MM-IM have so far been studied only in single-antenna configurations. Extending these schemes to MIMO raises additional design questions around antenna selection, spatial diversity, and joint detection across antenna streams.

The integration of AFDM with RIS is a third area of interest. RIS-assisted AFDM combines the delay-Doppler resilience of AFDM with the propagation control offered by passive reflecting surfaces, and the index modulation schemes proposed here can be combined with RIS-based phase configurations for both communication and joint localization in high-mobility scenarios.

A further direction lies in ISAC using AFDM index modulation. The path-separation property of AFDM that the MP-PIC detector of Chapter 4 exploits is also useful for delay-Doppler sensing of targets, and combining AFDM-IM with ISAC would deliver simultaneous data transmission and target sensing within a single waveform, which is particularly relevant for vehicular and UAV applications.

Model-based deep learning enhancements of the detectors developed in this thesis offer a final promising direction. Deep unfolding of VAMP-CG, VB-SBL, and the message-passing detectors can adapt denoiser parameters and damping schedules to specific channel statistics while preserving the convergence guarantees of the underlying inference framework.

List of Publications

Journals

- Anoop, A., Christo Kurisummoottil Thomas, S. Kala, JV Bibal Benifa, and Walid Saad. "Multi-mode index modulation based on affine frequency division multiplexing." Physical Communication 76 (2026): 103059. https://doi.org/10.1016/j.phycom.2026.103059
- Anoop, A., Christo Kurisummoottil Thomas, S. Kala, JV Bibal Benifa, and Walid Saad. "Dual-mode index modulation based on affine frequency division multiplexing." Physical Communication 70 (2025): 102628. https://doi.org/10.1016/j.phycom.2025.102628
- Anoop, A., Christo Kurisummoottil Thomas and Kala S, "Enhanced Spatial Modulation Based Orthogonal Time Frequency Space System," in IEICE Transactions on Communications, vol. E107-B, no. 11, pp. 785-796, November 2024. https://doi.org/10.23919/transcom.2023EBP3206

Conferences

- A. Anoop, C. K. Thomas, J. V. Bibal Benifa, Rony Thomas and S. Kala, “A GAMP Detector for Dual-Mode Index Modulated AFDM in High-Mobility Channels,” TENCON 2026 - 2026 IEEE Region 10 Conference (TENCON), Bali, Indonesia, 2026.
- A. Anoop, C. K. Thomas, J. V. Bibal Benifa and S. Kala, “Variational Bayesian Detection for Quantized AFDM Systems,” 2026 IEEE Wireless Communications and Networking Conference Workshops (WCNCW), KUALA LUMPUR, Malaysia, 2026, pp. 1-6. https://doi.org/10.1109/WCNCW67598.2026.11555710

- A. Anoop, C. K. Thomas, J. V. Bibal Benifa and S. Kala, "Low-Complexity VAMP Detector for Affine Frequency Division Multiplexing Systems," 2026 IEEE Wireless Communications and Networking Conference Workshops (WCNCW), KUALA LUMPUR, Malaysia, 2026, pp. 1-6.
  https://doi.org/10.1109/WCNCW67598.2026.11555324
- A. Anoop, C. K. Thomas, J. V. Bibal Benifa and S. Kala, "Multi-Path Bayesian Inference for Symbol Detection in Affine Frequency Division Multiplexing," 2026 National Conference on Communications (NCC), Hyderabad, India, 2026.
  https://doi.org/10.1109/NCC68160.2026.11479015
- A. A., C. K. Thomas, J. V. B. Benifa and S. Kala, "Variational Bayesian Detection for Sparse AFDM-IM in High-Doppler Wireless Channels," 2025 International Conference on Networks & Advances in Computational Technologies (NetACT), Trivandrum, India, 2025, pp. 1–6.
  https://doi.org/10.1109/NetACT65906.2025.11188158
- A. Anoop, C. K. Thomas, J. V. Bibal Benifa and S. Kala, "Affine Frequency Division Multiplexing With Generalized Index Modulation," 2025 11th International Conference on Smart Computing and Communications (ICSCC), Kochi, India, 2025, pp. 1–5.
  https://doi.org/10.1109/ICSCC66177.2025.11233736
- A. A., C. K. Thomas and S. Kala, "Affine Frequency Division Multiplexing with Quadrature Index Modulation," 2025 Emerging Technologies for Intelligent Systems (ETIS), Trivandrum, India, 2025, pp. 1–6.
  https://doi.org/10.1109/ETIS64005.2025.10961678
- A. A., C. K. Thomas and S. Kala, "Generalized Dual-Mode Index Modulation Based on OTFS," 2024 IEEE International Conference on Electronics, Computing and Communication Technologies (CONECCT), Bangalore, India, 2024, pp. 1–6.

https://doi.org/10.1109/CONECCT62155.2024.10677134

- A. Anoop, C. K. Thomas, J. V. Bibal Benifa and S. Kala, "Variational Bayesian Spectrum Sensing over AFDM Waveforms in Doubly-Dispersive Channels," 2026 IEEE International Symposium on Spectrum Innovation (DySPAN), Washington, DC, USA, 2026, pp. 5-11. https://doi.org/10.1109/DySPAN69846.2026.11571145

References

[1] B. Li, T. Xiao, K. Zhou, L. Xu, G. Liu, B. Wang, J. Gao, J. Guan, and Z. Di, "2022 ieee international conference on trust, security and privacy in computing and communications (trustcom)," in *Research on OTFS Systems for 6G*, 2022, pp. 1498–1503.

[2] C. De Alwis, A. Kalla, Q.-V. Pham, P. Kumar, K. Dev, W.-J. Hwang, and M. Liyanage, "Survey on 6G frontiers: Trends, applications, requirements, technologies and future research," *IEEE Open Journal of the Communications Society*, vol. 2, pp. 836–886, 2021.

[3] T. Hwang, C. Yang, G. Wu, S. Li, and G. Y. Li, "OFDM and its wireless applications: A survey," *IEEE Transactions on Vehicular Technology*, vol. 58, no. 4, pp. 1673–1694, 2009.

[4] M. Marchese and P. Savazzi, "Robust 6g ofdm high-mobility communications using delay-doppler superimposed pilots," *IEEE Transactions on Vehicular Technology*, pp. 1–13, 2026.

[5] R. Hadani, S. Rakib, M. Tsatsanis, A. Monk, A. J. Goldsmith, A. F. Molisch, and R. Calderbank, "Orthogonal time frequency space modulation," in *IEEE Wireless Communications and Networking Conference (WCNC)*, 2017, pp. 1–6.

[6] R. Hadani and A. Monk, "OTFS: A new generation of modulation addressing the challenges of 5G," *arXiv preprint arXiv:1802.02623*, 2018.

[7] P. Raviteja, K. T. Phan, Y. Hong, and E. Viterbo, "Interference cancellation and iterative detection for orthogonal time frequency space modulation," *IEEE Transactions on Wireless Communications*, vol. 17, no. 10, pp. 6501–6515, 2018.

[8] R. Hadani, S. Rakib, A. F. Molisch, C. Ibars, A. Monk, M. Tsatsanis, J. Delfeld, A. Goldsmith, and R. Calderbank, "OTFS: A new modulation scheme for multi-user millimeter-wave systems," in *IEEE Vehicular Technology Conference (VTC)*, 2017.

[9] M. K. Ramachandran and A. Chockalingam, "MIMO-OTFS in high-doppler fading channels: Signal detection and channel estimation," *IEEE Global Communications Conference (GLOBECOM)*, 2018.

[10] S. Das, R. Prasad, and R. Murch, "Time-domain channel estimation for OTFS systems," *IEEE Transactions on Wireless Communications*, 2021.

[11] P. Raviteja, K. T. Phan, Y. Hong, and E. Viterbo, "Practical pulse-shaping waveforms for reduced-cyclic-prefix OTFS," *IEEE Transactions on Vehicular Technology*, vol. 68, no. 1, pp. 957–961, 2018.

[12] G. D. Surabhi, R. M. Augustine, and A. Chockalingam, "Peak-to-average power ratio of OTFS modulation," *IEEE Communications Letters*, vol. 23, no. 6, pp. 999–1002, 2019.

[13] W. Shen, L. Dai, J. An, P. Fan, and R. W. Heath, "Channel estimation for orthogonal time frequency space (OTFS) massive MIMO," *IEEE Transactions on Signal Processing*, vol. 67, no. 16, pp. 4204–4217, 2019.

[14] Y. Liu, S. Zhang, F. Gao, J. Tang, and O. A. Dobre, "Uplink-aided high mobility downlink channel estimation over massive MIMO-OTFS system," *IEEE Journal on Selected Areas in Communications*, vol. 38, no. 9, pp. 1994–2009, 2020.

[15] Y. Shan and F. Wang, "Low-complexity and low-overhead receiver for OTFS via large-scale antenna array," *IEEE Transactions on Vehicular Technology*, vol. 70, no. 6, pp. 5703–5718, 2021.

[16] A. Bemani, N. Ksairi, and M. Kountouris, "AFDM: A full diversity next generation waveform for high mobility communications," in *IEEE International Conference on Communications Workshops (ICC Workshops)*, 2021, pp. 1–6.

[17] A. Bemani, N. Ksairi, and M.Kountouris, "Affine frequency division multiplexing for next generation wireless communications," *IEEE Transactions on Wireless Communications*, vol. 22, no. 11, pp. 8214–8229, 2023.

[18] T. Mao, Q. Wang, Z. Wang, and S. Chen, "Novel index modulation techniques: A survey," *IEEE Communications Surveys & Tutorials*, vol. 21, no. 1, pp. 315–348, 2019.

[19] E. Basar, M. Wen, R. Mesleh, M. Di Renzo, Y. Xiao, and H. Haas, "Index modulation techniques for next-generation wireless networks," *IEEE Access*, vol. 5, pp. 16 693–16 746, 2017.

[20] E. Basar, U. Aygolu, E. Panayirci, and H. V. Poor, "Orthogonal frequency division multiplexing with index modulation," *IEEE Transactions on Signal Processing*, vol. 61, no. 22, pp. 5536–5549, 2013.

[21] T. Mao, Z. Wang, Q. Wang, S. Chen, and L. Hanzo, "Dual-mode index modulation aided OFDM," *IEEE Access*, vol. 5, pp. 50–60, 2017.

[22] M. Wen, E. Basar, Q. Li, B. Zheng, and M. Zhang, "Multiple-mode orthogonal frequency division multiplexing with index modulation," *IEEE Transactions on Communications*, vol. 65, no. 9, pp. 3892–3906, 2017.

[23] Y. Liang, L. Li, P. Fan, and Y. Guan, "Doppler resilient orthogonal time-frequency space (OTFS) systems based on index modulation," *IEEE Vehicular Technology Conference (VTC)*, 2020.

[24] W. Ren, L. Li, and P. Fan, "Improved index modulation based on OTFS systems," *IEEE Communications Letters*, 2021.

[25] H. Zhao, D. He, Z. Kang, and H. Wang, "Orthogonal time frequency space (OTFS) with dual-mode index modulation," *IEEE Wireless Communications Letters*, 2021.

[26] Q. Cheng, Z. Shi, J. Yuan, M.-M. Zhao, and Y. Liu, "Multi-mode index modulation for orthogonal time frequency space," *IEEE Transactions on Wireless Communications*, 2023.

[27] Y. Zhu, W. Yuan, M. Wen, Y. Liu, and J. Yuan, "Index modulation for affine frequency division multiplexing," *IEEE Transactions on Vehicular Technology*, 2024.

[28] Y. Tao, M. Wen, Y. Ge, and J. Li, "Affine frequency division multiplexing with index modulation," *IEEE Wireless Communications Letters*, 2024.

[29] D. L. Donoho, A. Maleki, and A. Montanari, "Message-passing algorithms for compressed sensing," *Proceedings of the National Academy of Sciences*, vol. 106, no. 45, pp. 18 914–18 919, 2009.

[30] S. Rangan, P. Schniter, and A. K. Fletcher, "Vector approximate message passing," *IEEE Transactions on Information Theory*, vol. 65, no. 10, pp. 6664–6684, 2019.

[31] S. Rangan, "Generalized approximate message passing for estimation with random linear mixing," in *IEEE International Symposium on Information Theory (ISIT)*, 2011, pp. 2168–2172.

[32] C. K. Thomas and D. Slock, "SAVE - space alternating variational estimation for sparse Bayesian learning," in *IEEE Data Science Workshop (DSW)*, 2018, pp. 11–15.

[33] M. E. Tipping, "Sparse Bayesian learning and the relevance vector machine," *Journal of Machine Learning Research*, vol. 1, pp. 211–244, 2001.

[34] J. Zhang, L. Dai, Z. He, S. Jin, and X. Li, "Performance analysis of mixed-ADC massive MIMO systems over Rician fading channels," *IEEE Journal on Selected Areas in Communications*, vol. 35, no. 6, pp. 1327–1338, 2016.

[35] S. Jacobsson, G. Durisi, M. Coldrey, U. Gustavsson, and C. Studer, "Throughput analysis of massive MIMO uplink with low-resolution ADCs," *IEEE Transactions on Wireless Communications*, vol. 16, no. 6, pp. 4038–4051, 2017.

[36] J. J. Bussgang, "Crosscorrelation functions of amplitude-distorted Gaussian signals," *MIT Research Laboratory of Electronics Technical Report*, no. 216, 1952.

[37] Y. Zhang, X. Wang, and J. Zhang, "Precoding and decision-feedback equalization for OFDM in high-mobility channels," *IEEE Transactions on Vehicular Technology*, 2014.

[38] X. Ouyang and J. Zhao, "Orthogonal chirp division multiplexing," *IEEE Transactions on Communications*, vol. 64, no. 9, pp. 3946–3957, 2016.

[39] G. D. Surabhi, R. M. Augustine, and A. Chockalingam, "On the diversity of uncoded OTFS modulation in doubly-dispersive channels," *IEEE Transactions on Wireless Communications*, vol. 18, no. 6, pp. 3049–3063, 2019.

[40] P. Raviteja, K. T. Phan, and Y. Hong, "Embedded pilot-aided channel estimation for OTFS in delay-Doppler channels," in *IEEE Transactions on Vehicular Technology*, vol. 68, no. 5, 2019, pp. 4906–4917.

[41] X. Li *et al.*, "Channel estimation for AFDM systems with fractional Doppler," *IEEE Transactions on Wireless Communications*, 2024.

[42] Y. Ge, W. Yuan, and M. Wen, "Fractional Doppler estimation for AFDM," *IEEE Communications Letters*, 2024.

[43] T. Zhou, L. Yang, L. Liu, and H. Jiang, "An overview of AFDM waveform design for 6G wireless communications," *IEEE Wireless Communications*, 2024.

[44] Y. Tao, M. Wen, and Y. Ge, "AFDM-SCMA: A promising waveform for massive connectivity over high mobility channels," *IEEE Transactions on Wireless Communications*, 2024.

[45] Y. Ni, Z. Wang, W. Yuan, and P. Fan, "An AFDM-based integrated sensing and communications," *IEEE Transactions on Communications*, 2024.

[46] J. Zhang *et al.*, "Sensing with AFDM waveforms: Performance analysis and optimization," *IEEE Transactions on Vehicular Technology*, 2024.

[47] W. Yuan, M. Wen, and Y. Ge, "DFT-based AFDM for backward compatibility with OFDM," *IEEE Communications Letters*, 2024.

[48] A. Bemani, N. Ksairi, and M. Kountouris, "Low-complexity equalization for AFDM in doubly dispersive channels," *IEEE International Conference on Acoustics, Speech and Signal Processing (ICASSP)*, 2022.

[49] J. Wu *et al.*, "Matched-filter-based message passing detection for AFDM systems," *IEEE Transactions on Wireless Communications*, 2024.

[50] Y. Xu *et al.*, "Multi-block UAMP detector for AFDM systems," *IEEE Transactions on Communications*, 2025.

[51] R. Fan, Y. J. Yu, and Y. Guan, "Generalization of orthogonal frequency division multiplexing with index modulation," *IEEE Transactions on Wireless Communications*, vol. 14, no. 10, pp. 5350–5359, 2014.

[52] E. Ozturk, E. Basar, and H. A. Cirpan, "Generalized frequency division multiplexing with index modulation," *IEEE GLOBECOM Workshops*, 2017.

[53] Z. Zhang, H. Lu, Y. Xiao, and W. Xiang, "Dual-mode index modulation aided OFDM with constellation power allocation," *IEEE Vehicular Technology Conference (VTC)*, 2017.

[54] E. Aydin and H. Ilhan, "Composite multi-mode OFDM with index modulation," *IEEE Transactions on Vehicular Technology*, 2018.

[55] Q. Li, M. Wen, and E. Basar, "Index modulation multiple access," *IEEE Transactions on Wireless Communications*, 2022.

[56] R. Y. Mesleh, H. Haas, S. Sinanovic, C. W. Ahn, and S. Yun, "Spatial modulation," *IEEE Transactions on Vehicular Technology*, vol. 57, no. 4, pp. 2228–2241, 2008.

[57] J. Jeganathan, A. Ghrayeb, L. Szczecinski, and A. Ceron, "Space shift keying modulation for MIMO channels," *IEEE Transactions on Wireless Communications*, vol. 8, no. 7, pp. 3692–3703, 2009.

[58] C.-C. Cheng, H. Sari, S. Sezginer, and Y. T. Su, "Enhanced spatial modulation with multiple signal constellations," *IEEE Transactions on Communications*, vol. 63, no. 6, pp. 2237–2248, 2015.

[59] R. Mesleh, S. S. Ikki, and H. M. Aggoune, "Quadrature spatial modulation," *IEEE Transactions on Vehicular Technology*, vol. 64, no. 6, pp. 2738–2742, 2015.

[60] X. Liu *et al.*, "Multi-UAV cooperative NOMA with index modulation for air-ground networks," *IEEE Transactions on Vehicular Technology*, 2022.

[61] J. Francis and A. Chockalingam, "Diversity and PAPR enhancement in OTFS via indexing," *IEEE Wireless Communications Letters*, 2021.

[62] H. Zhao, D. He, and Z. Kang, "Dual-mode index modulation for OTFS over fractional Doppler channels," *IEEE Transactions on Vehicular Technology*, 2024.

[63] E. Ozturk, E. Basar, and H. A. Cirpan, "OTFS with subcarrier number modulation," *IEEE Communications Letters*, 2020.

[64] T. Wang, F. Yang, J. Song, and Z. Han, "Deep learning-based detection scheme for OFDM-IM," *IEEE Wireless Communications Letters*, vol. 8, no. 4, pp. 1159–1162, 2019.

[65] F. Yang, T. Wang, and J. Song, "DeepDM: Deep learning-based detection for dual-mode OFDM-IM," *IEEE Wireless Communications Letters*, 2020.

[66] Y. Tao, M. Wen, and Y. Ge, "Index modulation with repetition coding for AFDM systems," *IEEE Communications Letters*, 2024.

[67] Y. Zhu, W. Yuan, and M. Wen, "Pre-chirp index modulation for AFDM," *IEEE Transactions on Vehicular Technology*, 2024.

[68] Y. Wang *et al.*, "CDD-AFDM-IM: Cyclic delay diversity AFDM with index modulation," *IEEE Transactions on Wireless Communications*, 2024.

[69] M. Bayati and A. Montanari, "The dynamics of message passing on dense graphs, with applications to compressed sensing," *IEEE Transactions on Information Theory*, vol. 57, no. 2, pp. 764–785, 2011.

[70] A. K. Fletcher, S. Rangan, and P. Schniter, "Inference in deep networks in high dimensions," *IEEE International Symposium on Information Theory (ISIT)*, 2018.

[71] J. Ma and L. Ping, "Orthogonal AMP," *IEEE Access*, vol. 5, pp. 2020–2033, 2017.

[72] Z. Yuan, F. Liu, W. Yuan, Q. Guo, Z. Wang, and J. Yuan, "Iterative detection for orthogonal time frequency space modulation with unitary approximate message passing," *IEEE Transactions on Wireless Communications*, vol. 21, no. 2, pp. 714–725, 2022.

[73] S. S. Sharma *et al.*, "Expectation propagation detector for OTFS with fractional Doppler," *IEEE Transactions on Vehicular Technology*, 2022.

[74] W. Liu *et al.*, "Variational Bayesian joint channel estimation and signal detection for MIMO-OTFS," *IEEE Transactions on Vehicular Technology*, 2022.

[75] Y. Li, C. Tao, G. Seco-Granados, A. Mezghani, A. L. Swindlehurst, and L. Liu, "Channel estimation and performance analysis of one-bit massive MIMO systems," *IEEE Transactions on Signal Processing*, vol. 65, no. 15, pp. 4075–4089, 2017.

[76] L. V. Nguyen, A. L. Swindlehurst, and D. H. N. Nguyen, "Variational Bayesian inference for few-bit massive MIMO systems," *IEEE Transactions on Wireless Communications*, 2024.

[77] R. H. Walden, "Analog-to-digital converter survey and analysis," *IEEE Journal on Selected Areas in Communications*, vol. 17, no. 4, pp. 539–550, 1999.

[78] J. Mo, P. Schniter, and R. W. Heath, "Channel estimation in broadband millimeter wave MIMO systems with few-bit ADCs," *IEEE Transactions on Signal Processing*, vol. 66, no. 5, pp. 1141–1154, 2018.

[79] S. Rao, A. Mezghani, and A. L. Swindlehurst, "Massive MIMO channel estimation with 1-bit spatial sigma-delta ADCs," *IEEE International Conference on Acoustics, Speech and Signal Processing (ICASSP)*, 2019.

[80] S. Mehrotra *et al.*, "Sparse channel estimation for MIMO-OTFS and OTSM systems with finite-resolution ADCs," *IEEE Transactions on Wireless Communications*, 2025.

[81] A. J. Viterbi, "Error bounds for convolutional codes and an asymptotically optimum decoding algorithm," *IEEE Transactions on Information Theory*, vol. 13, no. 2, pp. 260–269, Apr. 1967.

[82] E. Viterbo and J. Boutros, "A universal lattice code decoder for fading channels," *IEEE Transactions on Information Theory*, vol. 45, no. 5, pp. 1639–1642, Jul. 1999.

Curriculum Vitae

Anoop A obtained his B.Tech degree in Electronics and Communication Engineering from National Institute of Technology Calicut, Kerala, India in 2010. He is currently pursuing his Ph.D in the area of delay-Doppler waveforms, index modulation, and Bayesian and message passing detection for 6G high-mobility communication at IIIT Kottayam, Kerala, India. He worked as Senior Telecom Engineer at ZTE Telecom India Pvt. Ltd, Hyderabad from August 14, 2010 to July 2, 2012. He is currently working as Superintendent Engineer (Electronics) at Oil and Natural Gas Corporation Limited, a Maharatna Public Sector Enterprise under the Ministry of Petroleum and Natural Gas, Government of India, since June 18, 2013.

His research interests include affine frequency division multiplexing, orthogonal time frequency space modulation, index modulation, variational Bayesian inference, message passing detection, and 6G high-mobility wireless communication.

He has secured several national-level academic distinctions, including All India Rank 4 in the Graduate Aptitude Test in Engineering (GATE) 2013 in the Electronics and Communication Engineering paper, All India Rank 85 in GATE 2017, All India Rank 37 in GATE 2018, and All India Rank 29 in GATE 2021, all in the Instrumentation Engineering paper. He has also secured All India Rank 30 in the CSIR National Eligibility Test in Engineering Sciences, and All India Rank 36 in the Engineering Services Examination 2014 in Electronics and Telecommunication stream.

1. **Bio-data**

   - *Name*: Anoop A
   - *Roll No.*: 2022PHD22006
   - *Permanent Address*: Ambattu House
     Malakunnam P.O.
     Changanacherry
     Kottayam, Kerala
     India
     686535